NONLINEAR FINITE ELEMENT ANALYSIS OF REINFORCED CONCRETE STRUCTURES SUBJECTED TO BLAST LOADING

by

Fouad Bakheet Aboud Beshara

Thesis submitted for the Degree
of
Doctor of Philosophy

City University
Department of Civil Engineering
London

April, 1991

ERRATA

Page 80, Line 10: equation (3-53) should read equation (3-55)

Page 84, equation (3-64): C_p should read C_r

Page 131, Line 17: when should read where

Page 137, Equation (5-39) should read

$$\dot{\sigma} + E\gamma(\dot{\varepsilon})\ (\sigma - \tau) = E\ \dot{\varepsilon}$$

Page 137, Equation (5-42) should read

$$t = 2\ \eta\ C_c\ (\varepsilon'_{cd} - C_c\ t)$$

Page 142, Line 23: equation (5-9) should read equation (5-11)

Page 149, Line 5: radical should read radial

Page 166, Equation (5-14) should read

$$\dot{\sigma} + E\ \gamma_s\ (\sigma - \tau^s) - C_s\ E = 0$$

Page 172, Table 5-2: Values of coefficient B_2 should read 0.915, 0.904, 0.943, 0.863

Page 182, Figure 5.9: ε_{vp} should read ε'_{vp}

Page 183, Figure 5.10: ε_{vp} should read ε'_{vp}

Page 201, Equation (6-21) should read

$$\ddot{d}_n = \frac{1}{\Delta t^2}\ (d_{n+1} - 2d_n + d_{n-1})$$

Page 201, Line 2: d_{n+1} should read $\ddot{d}_{n+1}$

Page 255, Line 7: overpressure should read load

Page 270, Table 8-2: Steel Young's modulus should read 205940.7 MN/m^2

ACKNOWLEDGEMENTS

The research described in this thesis was made at City University under the supervision of Professor K S Virdi, to whom the author wishes to express his profound gratitude for his invaluable advice and constructive guidance throughout the entire course of this study.

Sincere thanks go to the author's friend Dr S El-Shorbani for the initial instigation for pursuing the research studies and his continuous patronage in my endeavours to finish this project.

The author also wishes to express his appreciation to his friend, Ronald Wilkins for his encouragement and useful discussions on many occasions.

The author is grateful to the staff of City University Library, especially Mrs Sheila Munton and Mr John Adams, for their help in obtaining many of the papers referenced herein. Thanks are also due to the operating and advisory staff of the Computer Centre at City University for their assistance in computational matters.

Special thanks are also extended to Mrs Pat Walker for her care, skill and patience in typing this thesis.

The author acknowledges the partial financial support of the Overseas Research Students Awards Scheme during the period October 1987 to June 1989 of this investigation.

Most of all, his sincere thanks are reserved for his parents. But for their constant affection, sacrifices and unlimited patience, this work would still be a faraway dream.

SUMMARY

This thesis is concerned with the development of finite element techniques for nonlinear dynamic analysis of planar and axisymmetric reinforced concrete structures subjected to blast loading. The main aspects of numerical modelling process to simulate blast loads, structural geometries and material behaviour are addressed. Major attention has been focused on the development of appropriate history and rate dependent constitutive models for concrete and steel where several material nonlinearities are considered in tension and compression as well as the strain rate effects. Computational algorithms and modified solution procedures have been also developed and coded, which are applied to various structural problems under severe dynamic loading conditions.

The basic characteristics of the explosion and blast wave phenomena are presented along with a discussion of the modelling of blast pressures in the free-field due to unconfined and confined explosions. Predictions methods are considered which allow an estimation to be made of the associated internal or external airblast loads on above-ground structures.

The dynamic equilibrium equations for a blast-loaded structure are derived using the principle of virtual work in total Lagrangian approach. The finite element discretization of the equations of motion in space is adopted in accordance with isoparametric formulations. The steel reinforcement is modelled by bar or membrane elements embedded within the basic 8-node isoparametric concrete element. Perfect bond is assumed between steel and surrounding concrete. The integrals, which define the element matrices and vectors are obtained numerically by use of Gaussian quadrature. Hinton's lumping scheme has been employed to generate the lumped mass matrix from the consistent mass matrix for both concrete and steel.

The compressive behaviour of concrete is modelled as a strain rate sensitive elasto-viscoplastic material. The onset of viscoplastic behaviour and the softening regime are defined by rate dependent yield and failure surfaces. Based on Kupfer's results, four different functions are developed for the representation of these surfaces in the principal stress space. In the pre-peak range, a history and rate dependent hardening rule is developed to control the expansion of the loading surfaces with the increase of viscoplastic strain. Strain hardening function is derived to fit quasi-static experimental results and is extended for dynamic problems by including the strain rate effects upon the concrete compressive strength and the corresponding strain. In the post-fracture range, the contraction of the loading surface is controlled by a rate dependent softening rule which is described as a function of the post-failure viscoplastic dissipated energy and strain rate until crushing occurs, according to proposed strain controlled

crushing conditions. The viscoplastic strain rate is calculated by a rate dependent associated flow rule in which the fluidity parameter is derived as a function of the effective strain rate. In tension, concrete is modelled as a linear elastic strain softening material where crack initiation is controlled by a rate dependent strain criterion. The smeared crack approach is employed to simulate cracks, post-cracking behaviour is governed by an objective nonlinear softening rule based on concrete fracture energy and crack characteristic length. Shear transfer across the cracks is considered by a suitable simple model. The strain rate-induced anisotropy is introduced by employing different rate sensitivity functions for tension and compression. Steel is modelled as a uniaxial strain rate dependent elasto-viscoplastic material in tension and compression in which the yield stress and the fluidity parameter are strain rate sensitive. The identification of model parameters of concrete and steel are performed using some standard experimental results.

A modified explicit central difference scheme based on the Newmark-β method is proposed to advance the nodal displacements, velocities and accelerations in time. Numerical stability has been controlled using appropriate time increments and energy balance check. The details of an explicit Euler scheme for time integration of time rate constitutive equations of concrete and steel are described in which a semi-empirical *a priori* stability criterion for the definition of time step length is proposed.

To implement the proposed models and schemes, a versatile and comprehensive computer program, FEABRS, has been developed for the finite element linear and nonlinear dynamic analysis of two-dimensional reinforced concrete structures. Using the program, several reinforced concrete structures are analysed and reported in detail, with the results obtained being compared with those from other numerical and experimental sources. A good agreement is obtained and it is shown that many aspects of the structural behaviour can be well presented by the proposed analysis.

TABLE OF CONTENTS

Page

LIST OF TABLES

LIST OF FIGURES

LIST OF MAIN NOTATIONS

*** Blast loading parameters (Chapter 3)**

A_s	Internal surface area of the structure
A_v	Vent area
A_w	Area of vented wall or roof
A_{vr}	Maximum airblast-induced vertical ground acceleration
A_H	Maximum airblast-induced horizontal ground acceleration
a_v	Peak directly transmitted vertical ground acceleration
a_h	Peak directly transmitted horizontal ground acceleration
a_o	Speed of sound at standard sea level
C_f	Drag coefficient for the front face of structure
C_t	Drag coefficient for the roof of structure
C_r	Coefficient for pressure rise rate of confined deflagrative explosion
C_p	Compression wave seismic velocity of the soil
C_o	Speed of sound in the undisturbed atmosphere
D_v	Maximum airblast-induced vertical ground displacement
D_H	Maximum airblast-induced horizontal ground displacement
d_v	Peak directly transmitted vertical ground displacement
d_h	Peak directly transmitted horizontal ground displacement
g	Acceleration due to earth gravity
H_{TNT}	Heat of detonation of Trinitrotolune, TNT
H_{exp}	Heat of detonation of explosive in question
ΔH_f	Standard heat of combustion of the explosive fuel

i_s	The impulse of blast wave per unit of projected area
$\bar{I}_s$	Energy-scaled impulse of blast wave per unit area
i_r	The impulse of reflected shock wave per unit area
K_g	Ratio of the smallest cross-sectional area of the enclosure in which the explosion occurs to the area of vent
M_s	Mach number corresponding to specific peak overpressure
M_{su}	Reference Mach number of the explosive fuel
P	Total airblast pressures due to external explosion
P_s	Peak overpressure in the incident shock wave
P_r	Peak overpressure in the reflected shock wave
$P_s(t)$	Overpressure-time function
P_o	Ambient pressure
$\bar{P}_s$	Energy-scaled overpressure
P_d	Peak dynamic pressure
$\bar{P}_i$	Scaled initial gas pressure due to confined explosion
P_{qs}	Peak quasi-static gas pressure due to confined explosion
P_m	Maximum internal pressure due to deflagrative confined explosion
P_v	The pressure at which the vent is created
$\dot{P}_c$	Rate of pressure rise due to confined deflagration explosion
$\dot{P}_{ve}$	Rate of pressure relief by venting
P_{abs}	Absolute pressure at given time
P_{ad}	Theoretical limiting adiabatic pressure for fuel
R	Distance from the centre of explosion to a given location

R_o	Characteristic distance of unconfined vapour cloud explosion
$\bar{R}$	Energy-scaled distance of unconfined vapour cloud explosion
r_b	Radius of circular area over which the pressure due to contact blast is applied
r_c	Radius of exploding charge
S	The smaller of the height of structure or one half of the structure width
T_s	Duration of equivalent pulse of initial shock wave loading due to confined explosion
T_r	Duration of equivalent pulse of reflected shock wave loading due to confined explosion
t_a	Arrival time of shock wave at a given location
t_s	Duration of initial shock wave in the free field
t_i	Duration of equivalent pulse of shock wave in the free field
t_i'	Duration of equivalent pulse of dynamic pressure
t_∞	Intercept on time axis of initial decay slope of overpressure-time curve
t_q	Duration of dynamic pressure positive phase
t_{ir}	Duration of equivalent pulse of reflected shock wave
t_c	Clearing time necessary for the decay of the reflected pressure to the side-on overpressure on the front face of the structure
t_{rf}	The rise time of pressure on the front face of structure
t_{rb}	Time needed for the pressure build-up on the near face of structure
t_{rr}	The rise time of pressure on the roof of structure
t_{ds}	Duration of equivalent pulse of the roof loading
t_b	Blow-down time at which the pressure due to confined high explosive returns to ambient

t_v	Rise time to the peak airblast-induced vertical ground velocity
t_{ag}	Arrival time of the direct ground shock to a given location
W	Weight of explosive material
W_f	Weight of explosive fuel released into the atmosphere
W_{TNT}	Equivalent weight of TNT charge
W_{exp}	Weight of the explosive in question
V	(or V_c) Internal volume of the structure
V_v	Maximum airblast-induced vertical ground velocity
V_H	Maximum airblast-induced horizontal ground velocity
V_{vd}	Peak directly transmitted vertical ground velocity
V_h	Peak directly transmitted horizontal ground velocity
U_s	Shock front velocity
u_s	Peak wind velocity behind the shock front
Z	Scaled distance or proximity factor of a given explosion
α	Dimensionless shock wave form parameter
λ	Yield factor of a given explosion
γ_h	The ratio of specific heat of air
ρ_s	Air density behind the shock front
ρ_o	Air density ahead of the shock front
$\bar{\tau}$	Scaled blow-down duration
α_e	Vent area ratio (= A_v/A_w)
ψ	Ratio between vent area to internal volume of structure
ρ_p	Mass density of the soil

	* Finite element and solution techniques parameters (Chapters 4, 6)
a_o, a_1	Time integration constants
B	Element strain displacement matrix of concrete
B^s	Strain displacement matrix of reinforced bar or membrane
b_o, b_1	Rayleigh damping parameters
C, C^e	Global and element damping matrices
C_p	Acoustic wave speed of the structural material
D	Stress-strain matrix
d, $\dot{d}$, $\ddot{d}$	Nodal displacements, velocities and acceleration vectors
d^e	Element nodal displacements vector in the global coordinate system
F	Vector of externally applied airblast nodal loads on the structure
$\ddot{d}_g$	Nodal airblast-induced accleration vector in global coordinate system
J	Jacobian matrix
det J	Determinant of Jacobian matrix
K, K^e	Global and element stiffness matrix
M, M^e	Global and element mass matrix
m_{ii}	Diagonal term of lumped mass matrix for a typical node i
m^s_{ii}	Diagonal term of lumped mass matrix for a typical node i due to steel bar or membrane
N, N^e	Global and element shape functions matrix
n	Integer suffix for time step number
nd	Total number of degrees of freedom in the structure
P	Vector of nodal internal resisting forces
P_s	Reinforcement contribution in the vector of nodal internal resisting forces

Q	Vector of total externally applied forces on structure
S_1, S_2	Steel material parameters of *a priori* stability criterion of time integration
t_1, t_2	Concrete material parameters of *a priori* stability criterion of time integration
Δt	Step-by-step integration time increment
Δt_{cr}, Δt^s_{cr}	Critical time step length for concrete and steel
W	Measure of the total energy of the structural system
W^{kin}, W^{int}, W^{ext}	Kinetic, internal and external energies of the structural system
V, dV	Space domain and elemental volume of concrete
V_s, dv_s	Space domain and elemental volume of reinforcement member
x, y	Cartesian coordinates in the global coordinate system
r, z	Global coordinate system for axisymmetric solids
δ, β	Parameters of Newmark-β time integrator
θ	Control parameter of time integration of 1st order differential equation
μ	Reduction factor for the time step length
ξ	Damping ratio for the highest mesh frequency
ω_{max}	Maximum frequency of the system
λ_{max}	Maximum eigenvalue of the system
ψ	Eigenvalue associated with the highest frequency
ξ, η	Natural coordinate system of isoparametric element
	*** Stresses, strains and invariants (Chapters 2, 5)**
I_1	First invariant of stress tensor
$I_1^{\backslash}$	First invariant of strain tensor

J_2	Second invariant of stress deviator tensor
$J_2^{\backslash}$	Second invariant of strain deviator tensor
σ	Stress component at a point
ε	Strain component at a point
$\boldsymbol{\sigma}$	Stress vector in the global coordinate system
$\boldsymbol{\varepsilon}$	Strain vector in the global coordinate system
$\boldsymbol{\sigma}^*$	Stress vector in local coordinate system (crack directions)
$\boldsymbol{\varepsilon}^*$	Strain vector in local coordinate system (crack directions)
σ_1, σ_2	Principal stresses
ε_1, ε_2	Principal strains
σ_m	Mean normal stress
ε_{oct}	Octahedral normal strain
γ_{oct}	Octahedral shear strain
$\boldsymbol{\varepsilon}_e$, ε_e	Elastic strain vector and elastic strain component at a point
$\boldsymbol{\varepsilon}_{vp}$, ε_{vp}	Viscoplastic strain vector and viscoplastic strain component at a point
$\dot{\boldsymbol{\varepsilon}}_{vp}$, $\dot{\varepsilon}_{vp}$	Viscoplastic strain rate vector and viscoplastic strain rate value at a point
$\dot{\bar{\varepsilon}}_{vp}$	Effective viscoplastic strain rate
$\bar{\varepsilon}_{vp}$	Effective viscoplastic strain
$\dot{\varepsilon}_{eff}$	Effective strain rate at a point
ε_{eff}	Effective strain at a point
ε_{vp}^f	Viscoplastic strain at concrete failure
$\varepsilon_{vp}^{\backslash}$	Post-failure viscoplastic strain of concrete
$\Delta\ \varepsilon_{vp}$	Viscoplastic strain increment
τ	Effective stress of concrete at a point
τ^s	Effective stress of steel at a point
$\sigma_{ref}, \varepsilon_{ref}$	Cracking reference values of stress and strain

* Material parameters (Chapters 2, 5)

A_1, B_1, C_1	Compound material constants of concrete failure or yield criteria
a_1, b_1, c_1	Material constants of concrete failure or yield criteria
B_1, B_2	Material constants of concrete fluidity parameter
$\mathbf{a}$	Flow vector of concrete flow rule
$\mathbf{D}_c$	Elasticity matrix of uncracked concrete
$\mathbf{D}_{cr}$	Elasticity matrix of cracked concrete
E, E_s	Young's modulus of concrete and steel
E_t	Slope of steel stress-strain curve in the viscoplastic range
$F(.)$	Initial yield and subsequent loading surfaces of concrete
$f(.)$	Failure or yield function of concrete
$F^f(.)$	Bounding failure surface of concrete
G	Uncracked shear modulus of concrete
G_c	Cracked shear modulus of concrete
G_f	Concrete fracture energy
$G(.)$	Crushing surface of concrete
$g(.)$	Crushing function of concrete
H	Hardening modulus of steel
K_1, K_2	Material constants of steel fluidity parameter
K_s	Post-failure viscoplastic energy of concrete
L_c	Crack characteristic length
$\mathbf{T}$	Concrete transformations matrix
t_f	Time at which concrete failure surface is reached
W_{vp}	Concrete viscoplastic work in compression
$\sigma^{\backprime}_{cs}$, $\sigma^{\backprime}_{cd}$	Static and dynamic compressive strength of concrete
$\varepsilon^{\backprime}_{cs}$, $\varepsilon^{\backprime}_{cd}$	Static and dynamic peak strain of concrete

$\sigma^{\backslash}_{ts}$, $\sigma^{\backslash}_{td}$	Static and dynamic tensile strength of concrete
$\varepsilon^{\backslash}_{ts}$, $\varepsilon^{\backslash}_{td}$	Static and dynamic concrete cracking strain
σ_{ys}, σ_{yd}	Static and dynamic concrete stress at the elastic limit
ε_{ys}, ε_{yd}	Static and dynamic concrete strain at the elastic limit
σ^{s}_{ys}, ε^{s}_{yd}	Static and dynamic yield stress of steel
ε^{s}_{ys}, σ^{s}_{yd}	Static and dynamic yield strain of steel
$\sigma^{\backslash}_{ch}$	Concrete characteristic cube strength
ε_{cu}	Concrete crushing strain
ε_{m}	Concrete ultimate tensile strain
ϕ_1 to ϕ_4	Concrete strain rate sensitivity functions
ϕ_s	Strain rate sensitivity function of steel yield stress
$\phi(F)$	Concrete flow function
γ, γ_s	Concrete and steel fluidity parameters
$\sigma^{\backslash}_{cb}$	Concrete biaxial strength
ρ, ρ_s	Concrete and steel density
ν	Concrete Poisson's ratio
α	Concrete elastic limit
β	Reduction factor of concrete shear modulus
κ	Concrete constant of the flow function
η_h	Constant of concrete hardening rule
δ	Concrete softening parameter in compression
ψ	Concrete softening parameter in tension
μ	Concrete parameter of shear reduction factor
α_{cr}	The angle of the normal to primary crack direction
α^{*}_{cr}	Concrete crack angle

CHAPTER 1

INTRODUCTION

1.1 GENERAL BACKGROUND

The assessment of the effects of explosives on structural systems was apparently not studied systematically until World War I. Prior to that the information which did exist was through some field observations and little seems to have been published. With the increased need to design structures to resist damage to explosive attack during the 1914-1918 War, the information was initially treated as highly sensitive and many researchers were obliged to keep their results classified. The first published work was that of Hopkinson [1] in which he outlined his theory for using scale models with the statement:

"If two structural systems, identically similar except in size, be subjected to blast loading from two explosive charges whose weights are in proportion to the cube of the ratio of the linear dimensions of the two structures then the behaviour of the two structural systems will be identically similar with distortions scaling as the ratio of the linear dimensions".

Little further information became readily available until that released after World War II. The few published papers [2, 3] were based on research which had been undertaken during the war, on the behaviour of shelter systems under bombing attacks and the development of the first non-spherical charges for attacking hardened structural systems. The explosions were highly localized because of the difficulties related to the delivery of large quantities of explosive.

The advent of nuclear weapons changed the situation completely. Single aeroplanes, each with one nuclear bomb, devastated two major Japanese cities (1945) in just

two raids. As a result, the criteria on which simple shelter structures could be designed, underwent major changes [4, 5]. Since 1945, the number of reported experimental and analytical studies of the effects of blast loading on the behaviour of structures has markedly increased. The objective has been, first, to study the nature of the blast wave and the factors affecting its behaviour in free air and as it encounters a structure. Secondly, the aim has been to examine and develop means of predicting the response of a structure to blast overpressures. Other problems, associated with blast, have also been the focus of concern because of the perceived hazards.

Blast loading is a type of extraordinary dynamic load to which reinforced concrete structures may be subjected in addition to normal loads. Inspite of the fact that the most common blast loading used by most investigators is that resulting from a nuclear weapon, the general term 'blast' refers to both fluctuations of air pressure due to man-made explosions and to vibrations induced in the ground. The former, obviously, includes conventional explosions, which yield blast waves comparable to the atomic burst in the nature of explosion, but not in magnitude. A sonic boom may also be considered as a type of blast load. The airblast loads may act internally or externally depending on the position of the explosion source, relative to the structure. Internally, blast loading may result from the detonation of high explosives, usually placed deliberately, or from detonation of chemical ammunitions, or from the deflagration of low explosives, usually accumulations of flammable gas/air mixtures. Externally, blast excitations may result from one or other of these causes but there is the added possibility of loads acting over the entire structure as a result of distant atomic explosions.

1.2 STATEMENT OF THE PROBLEM

The uncertainty involved in the design of reinforced concrete structures, as a direct result of the nature of the expected blast force system, may require that the structure be designed to provide its full resistance if necessary. Also in some cases, the low probability of incidence of blast loads requires design of the structural elements such that some level of irreversible structural deformation and material damage is acceptable. Any structural member failing to perform as expected under the given loading conditions may reduce the probability of survival of the entire structure. However, the major studies in investigating the behaviour of blast loaded structures in the past have been focused on simplified methods of analysis in which many assumptions were made. The blast forces have been traditionally represented by equivalent static forces, so that the design and analysis of such structures are based on simple equilibrium conditions and empirical formulae according to design codes. Stress analysis of the structure is based on linear elastic theory and the design of reinforced concrete components according to the limit state theory. In most studies, dynamic analysis of the structural component is represented by equivalent single degree of freedom systems with elastic or elasto-plastic material properties. Although this approach has generally resulted in safe designs, it contains inherent inconsistencies and does not reflect the complete structural behaviour. The stresses and deformations resulting from simplified approach are often significantly different from those which may occur under blast loading. Furthermore, the damage mechanisms caused by intense dynamic stresses such as crushing, cracking, shear failure, tensile fracture and yield of steel, as well as the strain rate effect on the behaviour of concrete and steel, are either ignored or treated in an approximate manner. In conclusion, this approach may be only appropriate for preliminary analysis of reinforced concrete structure under blast loading conditions.

The emergence of numerical methods has made possible the solution of complex engineering problems. One of these numerical techniques now widely used is the finite element method. Originally, this method was developed as an extension of earlier established analysis procedures, and was intended for application to the design of advanced aircraft structures. Since early 1960's the method has been developed as a very efficient and powerful tool for the analysis of a wide range of structural and field problems. The first attempt to apply the finite element method to a reinforced concrete structure was reported [6] in 1967. Since then, reinforced concrete structures have been successively analysed as plane stress, plane strain, plate bending, shell, axisymmetric solid, beam, or three-dimensional solid finite element models. The geometric nonlinearities can be modelled with the well-known kinematic formulations of large displacement analyses. The various material nonlinearities of reinforced concrete structures namely, progressive cracking of concrete in tension, inelastic response in compression, crushing, tension stiffening, bond slip, yield of reinforcing steel, dowel action, aggregate interlock and unloading and reloading, can all now be incorporated more realistically into the analysis. However, much of the research work reported to date has been limited to nonlinear static problems and relatively few studies have addressed the nonlinear dynamic transient situations. Furthermore, the limitations of the existing dynamic material models for concrete and steel indicate the need for the development of more comprehensive and reliable models for the nonlinear response of these materials under blast loading environment. This is largely due to the complex behaviour of reinforced concrete under dynamic loading, since strain rate effects in tension and compression, effects of crack opening and closure, postcracking behaviour and history dependence in the pre-failure and post-failure regimes play an important role in the prediction of inelastic response of concrete

structures. It has been recognised that the incompleteness of material models for reinforced concrete is the biggest limiting factor to the capability of a finite element analysis. Additionally, considering the available nonlinear dynamic analysis procedures, the accurate analysis of a nonlinear finite element model can present some major difficulties. First, the cost of analysis is usually high, but a more serious factor is that considerable experience and judgement by the analyst may be required to assure a stable and accurate solution. Therefore, further progress in the understanding and prediction of structural behaviour necessitates the development of a numerical material model in conjunction with solution algorithms with increased accuracy and efficiency, for the nonlinear dynamic analysis of reinforced concrete structures under severe dynamic loading such as blasts.

1.3 SCOPE AND OBJECTIVES OF THE PRESENT RESEARCH

The aim of this thesis is to develop a numerical technique for the nonlinear analysis of plane and axisymmetric reinforced concrete structures subjected to blast loading. To describe the behaviour of the physical structural system, in the numerical model, there are a number of idealizations to be made; the geometry and environment of structure, the material properties and applied loading. Various characteristics of each idealized component are identified according to their physical properties using the laws of mechanics. As far as the idealization of geometry is concerned, the finite element is clearly the most versatile and powerful method available at the present time. The determination of the loading usually receives only marginal attention and in most cases it is assumed that the loading is given. Also, most of the material models adopted at present in engineering analyses still have a very limited range of applicability, especially under severe dynamic loading conditions.

In the present research, attention was mainly paid to the development of appropriate history and rate dependent constitutive models for concrete and steel under high strain rates. However, many problems were encountered in the transient dynamic analysis. In the search for a better understanding of blast-loaded reinforced concrete structures and as a result of the limitations of existing finite element software, a new, efficient computer program has been developed for the nonlinear dynamic analysis, which incorporates the proposed material models and computational algorithms for the concrete cracking process and loading conditions. In developing the computer program, consideration has been given to the discretization in time and solution techniques of the dynamic equilibrium equations and to the time rate dependent inelastic straining equations of concrete and steel, together with aspects of numerical stability.

Thus, the principal aims of the thesis were extensive and can be summarized as follows:

1. To review the several material modelling approaches found in the literature for simulating the behaviour of concrete and steel with discussion of the limitations of the existing models under high rates of loading. This literature review also highlights the characteristics of the observed experimental behaviour that must be considered in the development of sound constitutive equations for concrete and steel.

2. To describe the airblast phenomena and to summarize factual information on blast loads so that structures can be designed to resist the effects of confined or unconfined explosions due to conventional or nuclear sources. The dynamic loads, incident and reflected overpressure, dynamic pressure and ground shock, are presented in simple form suitable for computer implementation.

3. To present the finite element formulations for the spatial discretization of the nonlinear dynamic equilibrium

equations in the search for the most effective procedure. The equations of motion of a body subjected to airblast loading and ground excitation are derived in line with the total Lagrangian approach. The kinetic equations of concrete and steel are taken in accordance with isoparametric formulation and Gaussian quadrature rules.

4. To develop rational and consistent material constitutive models for the nonlinear analysis of two-dimensional reinforced concrete structures under blast loading conditions. For concrete, the model should consider strain rate effects, stress and strain history dependency, cracking, crushing, biaxial compressive failure of concrete and the post-failure residual strength.

5. To establish a sound computational strategy for concrete cracking process under dynamic loads which can take into account the effect of strain rate on the crack initiation limit as well as strain softening and shear transfer effects on the post-cracking behaviour.

6. To examine the time discretization procedures and integration schemes of the equations of motion as well as the time rate dependent constitutive equations of concrete and steel. Particular attention is given to a refined explicit central difference time integrator technique for the semi-discretized dynamic equilibrium equations. A simple *a priori* stability criterion based on theoretical and experimental considerations is derived for the definition of time increment for the Euler explicit scheme of the viscoplastic strain rate governing equation.

7. To develop a versatile and comprehensive computer program for the finite element dynamic analysis which embodies the proposed numerical model and the solution schemes above and possesses sufficient flexibility to add new options to promote further research. The program is restricted to plane and axisymmetric problems at present.

8. To use the computer program developed to study the response characteristics of reinforced concrete structures

under short duration dynamic loads, with special emphasis on blast loads. The validation of the numerical model and program are established by comparing results with those of other numerical or experimental studies.

9. To perform a parametric study in order to examine the effects of strain rate sensitivity and pre and post-fracture concrete modelling parameters on the overall dynamic response of reinforced concrete structures.

1.4 LAYOUT OF THE THESIS

In Chapter 2 the constitutive material modelling approaches for concrete and steel are reviewed. A brief of the observed experimental behaviour of these materials under static and dynamic loading conditions is given. Several modelling techniques are found in the literature for simulating the nonlinear behaviour of uncracked concrete, concrete cracking and reinforcing steel are investigated. The suitability of such approaches to model the material response under high rates of loading is described. Conclusions are drawn for material modelling of blast-loaded reinforced concrete.

Chapter 3 is concerned with the numerical modelling of blast loads on structures as the first component of the mathematical model. The basic characteristics of the explosion and blast wave phenomena are presented in this chapter along with a discussion of the modelling of blast pressures in the free-field due to unconfined and confined explosions. The blast effects considered are those generated as a result of nuclear weapons, conventional high explosives, unconfined vapour cloud explosions and gas and dust deflagrations. Prediction methods are considered which allow an analyst to estimate the associated internal or external airblast on the structure. In addition, the basis of numerical modelling of explosion-induced ground shocks is given. In the final part of this chapter, the main considerations in the modelling of blast loads for

nonlinear dynamic analysis of aboveground reinforced concrete structures are described.

Chapter 4 is devoted to another aspect of mathematical modelling, the spatial discretization. First, the basic dynamic equilibrium equations for a blast-loaded structure are derived using the principle of virtual work in total Langrangian approach. The finite element discretization of the equations of motion in space is adopted in accordance with isoparametric formulations. The chapter also discusses the formulation and Gaussian quadrature rules of the plane 8-noded isoparametric element, the modelling of mass and damping matrices, and the numerical simulation of steel reinforcement as embedded members within the basic concrete elements. The significance of some finite element procedural factors in the calculation of the response of concrete structures is briefly discussed.

Chapter 5 is concerned with the development of material constitutive models of reinforced concrete behaviour under blast loading conditions. A new rate and history dependent elasto-viscoplastic model is proposed for the compressive behaviour of concrete. The onset of viscoplastic response and failure are defined by two rate sensitive limiting surfaces where four different functions are developed on the basis of standard biaxial experimental results for the representation of those surfaces in the principal stress space. Rate and history dependent rules for conrete hardening and softening are developed to control the viscoplastic response in the pre-peak and post-fracture ranges. The viscoplastic strain rate is calculated by associative flow rule in which the fluidity parameter is strain rate dependent. In tension, concrete is modelled as a linear elastic, strain softening material where crack initiation is controlled by a proposed rate dependent cracking criterion. The chapter also discusses the smeared crack approach to simulate concrete cracking, nonlinear

fracture energy-based softening rule as well as simple shear transfer model to account for the post-cracking behaviour. Steel is modelled as a uniaxial rate dependent elasto-viscoplastic material in which the yield and the fluidity parameter are rate sensitive. The material parameters for concrete and steel are identified using appropriate testing data.

Chapter 6 focuses on the time discretization and the solution techniques of the dynamic equilibrium equations as well as governing equations for inelastic straining. After reviewing the existing methods of time integration of equations of motion, a modified explicit central difference integration technique is presented. Then, the details of explicit Euler scheme for time integration of viscoplastic strain rate equations, is described in which a semi-empirical *a priori* stability criterion for the definition of time step length is adopted. The numerical stability regarding the selection of time increment for the time integration of equations of motion is also considered. Some practical considerations relating to explicit integration techniques are given at the end of the chapter.

Chapter 7 deals with the basic structure and analysis capabilities of the computer program, FEABRS, developed within this work. A brief description of the computational algorithms is given, concentrating mainly on the implementation of the material models and solution techniques proposed in the previous chapters.

In Chapter 8, a set of numerical analyses of impulsively and blast-loaded reinforced concrete structures is performed using the numerical models developed in Chapter 5. Three examples are reported in detail and the results obtained are compared with those from other numerical and experimental sources. In order to investigate the influence of the basic material modelling factors, a parametric study is also

presented followed by a discussion of the results and concluding remarks about the model performance.

In chapter 9, conclusions to be drawn from the studies in this thesis are discussed with some suggestions for future research in this area.

CHAPTER 2

REVIEW OF CONSTITUTIVE THEORIES FOR CONCRETE AND REINFORCING STEEL

2.1 INTRODUCTION

Reinforced concrete is a composite material consisting of steel reinforcement and concrete, these two materials having vastly different properties. The mechanical properties of reinforcing steel are generally known within good limits. However, the mechanical properties of concrete are more difficult to define depending upon the particular conditions of mixing, curing, rate of loading and environmental influences. The knowledge of its uniaxial as well as biaxial or triaxial stress-strain behaviour is frequently required. Extensive studies have been undertaken to characterize the response and ultimate strength of plain concrete under multiaxial stress states. A large variety of constitutive models have been proposed to reproduce numerically the observed behaviour. All these models have certain inherent advantages and disadvantages which depend to a large extent on their particular applications.

In modelling reinforced concrete structures not only the constitutive relationships of steel and concrete must be defined, but also the bond slip relation between concrete and steel has to be known. However, perfect bond is usually assumed in global analysis in order to reduce the number of degrees of freedom and to avoid the difficulties in assigning appropriate bond properties which are not yet comprehensively available. Following this approach, the complex bond slip mechanism is not reviewed here and is circumvented by assuming perfect bond.

The purpose of the present chapter is to present mechanical properties of concrete and steel under static and dynamic loading conditions, and to review the previous constitutive theories to model numerically the material behaviour of

concrete and steel.

The basic mechanical properties of concrete on the microscopic and macroscopic levels are given in section 2.2. Then, the previous constitutive models of uncracked concrete are summarized in section 2.3, followed by review of modelling of concrete cracking in section 2.4. In section 2.5, the mechanical characteristics and the previous uniaxial constitutive models of steel are briefly described. The basic considerations to develop material models for concrete and steel under blast loading are included in the final section.

2.2 OBSERVED EXPERIMENTAL CONCRETE BEHAVIOUR

Despite the widespread use of concrete as a structural material and despite the large number of experimental studies that have been carried out over a considerable period of time, our knowledge about its physical and mechanical properties is still rather deficient, especially under dynamic loading. This is not surprising in view of the heterogeneous structure of concrete as well as the difficulties of experimental testing. Most of the experimental investigations are restricted to short term monotonic quasi-static loading conditions with strain rate of 10^{-6} sec $^{-1}$. Although dynamic loading conditions have a significant effect on the response of concrete to stress and strain, the influence of strain rate or loading rate upon the uniaxial compressive and tensile behaviour of concrete has been studied by a few researchers [7-20]. Extensive reviews about the current knowledge of the phenomenological behaviour of concrete are given in [21-24].

The following discussion is confined mainly to the mechanical properties of concrete under uniaxial, biaxial and triaxial states of stress associated with static and dynamic loading in order to provide the necessary background for later description of the constitutive models. However,

before describing these macroscopic aspects of observed concrete behaviour, the microstructure of concrete is briefly summarized to highlight the role of concrete microcracking.

2.2.1 STRUCTURE OF CONCRETE AND MICROCRACKING

Reviews on the microstructure of concrete have been given in [24-28]. The following is a brief summary. Concrete is a composite material mainly consisting of different sized aggregate particles which are embedded in a cement paste matrix. This heterogeneous structure can be considered as a two phase system composed of coarse aggregate and mortar. On a second dimensional level, the mortar matrix can be considered as a two phase system consisting of fine aggregates and cement paste. On a third dimensional level, the cement paste can be seen as a two phase system which is made up of unhydrated cement particles embedded in a matrix of hydrated cement products known as cement gel. It has long been recognized that a large number of micro-cracks exist in concrete at all the dimensional levels. Several techniques such as x-ray and ultrasonic pulse have been employed to study the formation and propagation of micro-cracks. An extensive qualitative review can be found in [24, 28]. According to the experimental observations [25], two types of micro-cracks exist in the concrete system:

1. Bond or interfacial cracks observed at the aggregate-paste interface, and

2. Mortar or paste cracks observed within the mortar or paste matrix.

Interfacial cracks exist in concrete even before any load is applied, and are caused by the settlement of aggregate and due to shrinkage [29].

Relatively recent works [24-26] have indicated how the micro-cracks influence the mechanical behaviour of concrete

subjected to short term loads. It has been demonstrated that under loading the deviation from the elastic behaviour is caused by micro-cracking at the aggregate-paste interface, and also that the disintegration and ultimate failure of plain concrete are caused by the propagation of cracks through the mortar which are mainly associated with deviatoric stress components. Some micro-cracks may be also developed during loading because of the differences in stiffness between aggregates and mortar. These differences can result in the strains in the interface zone several times larger than the average strain [21]. Experimental studies by Hsu et al [30] show that the measured aggregate-mortar tensile bond strength is about 30% to 70% of the tensile strength of mortar. Thus, the primary reason for the low tension strength of concrete is the low strength of the mortar-aggregate interface.

The existing micro-cracks grow under rapidly increasing stress; between some of them a process of bridging takes place and continuous fracture planes are formed. However, it was observed that under impulsive loading conditions [12, 28, 31], much energy is introduced into the specimen in a short time and fracture planes are forced to develop along shorter paths of higher resistance through stronger matrix zones and some aggregate particles. Also, crack branching can occur due to interactions between the rapidly moving crack front and the aggregate particles or other inhomogenieties. These two mechanisms of fracture are considered [31] to be the explanation for higher strength and larger corresponding strains under dynamic loading conditions.

Thus it is possible to explain the macroscopic behaviour of concrete, observed at an engineering level, by the progressive process of microscopic initiation, multiplication and propagation of cracks from before loading up to failure. However, as yet, the theory of micro-cracking can only describe the behaviour in

qualitative terms and give general guidelines towards the type of laws that are applicable.

2.2.2 MECHANICAL PROPERTIES UNDER SHORT TERM STATIC LOADING CONDITIONS

(i) Uniaxial loading

A typical stress-strain curve for plain concrete subjected to uniaxial compression is presented in Figure 2-1. From the origin to a discontinuity point A at about 30% of ultimate compressive stress σ'_{cs}, concrete can be idealized as a linear elastic material [21] and the increase in the number of or size of existing cracks is negligible. Above point A, the nonlinearity commences as a result of the propagation of micro-cracks at interfaces of mortar and aggregate. Up to 75% of the ultimate stress, the crack propagation is stable, because the available internal energy is approximately balanced by the required crack release energy. Unloading exhibits a permanent deformation, even though most of the deformation is still recoverable. Since a finite time is required for the cracks to propagate, the stress-strain curve is dependent on the strain rate (Figure 2-1).

For compressive stress above 0.75 σ'_{cs}, i.e. point B on the curve, cracks are initiated in the mortar, mostly bridging between existing interfacial cracks, causing the stress-strain curve to bend sharply towards the horizontal until it approaches the peak point at C. Since the available internal energy is now larger than the required crack release energy, the crack propagation becomes unstable. In some references [32] point B is called the onset of unstable fracture. Meanwhile, the concrete Poisson's ratio increases, resulting in a volumetric expansion [32, 33]. Since a finite time is required for the bridging cracks to be formed, the magnitude of the ultimate stress and the shape of post-failure stress-strain curve will be strongly affected by the strain rate.

A softening post-failure range follows the ultimate stress point C and finally ends with a complete crushing at point D. The use of continuum mechanics during the softening stage can only be an approximation [34].

The typical stress-strain curve in uniaxial tension is illustrated in Figure 2-2 which shows some similarities with the compression curve. The curve is now linear almost up to the peak stress. Concrete also exhibits considerable post-failure residual strength. The ratio of tensile strength σ'_{ts} to compressive strength is usually about 0.1 [35, 36] although the Young's modulus is almost the same in both loading conditions.

The initial modulus of elasticity is generally taken as a function of the compressive strength [21]. Poisson's ratio ranges from 0.15 to 0.22 with 0.18 being a representative value.

(ii) Biaxial loading

Extensive experimental investigations have been undertaken regarding the strength, deformation and cracking behaviour of concrete under biaxial stress state [37-39]. However, considerable scatter of results has been observed and collaborative studies have been undertaken to identify the principal factors influencing this variation [40]. For example, reported strength values for the equal biaxial compression (σ'_{cb}) are found to vary from 80% to 350% of uniaxial compressive strength [27]. This can be explained by many factors such as shapes of specimen, loading conditions, types of concrete etc. Apart from the inherent variability of concrete, most of these differences are attributed to the difficulties in producing stress fields that are independent of machine and testing effects [27]. Figure 2-3 illustrates typical stress-strain curves of concrete under biaxial compression and tension respectively [37]. Qualitatively, the mechanical behaviour of concrete

in biaxial states is similar to the uniaxial behaviour. As a consequence of micro-crack confinement, the ultimate strength of concrete under biaxial compression is larger than that under unixial compression. A maximum strength of approximately 125% is achieved at a stress ratio of σ_1/σ_2 = 0.5 and is reduced to 116% at an equal biaxial compression state [37-39]. Under biaxial compression-tension, the compressive strength decreases almost linearly as the applied tensile stress is increased (Figure 2-4). The strength under biaxial tension is almost the same as under uniaxial tension [37]. For all stress combinations the failure of concrete occurs by tensile splitting with the fractured surface orthogonal to the direction of the maximum stress or strain.

The ductility of concrete under biaxial stresses also differs depending on whether the stress states are compressive or tensile as shown in Figure 2-3. The maximum compressive strain under uniaxial and biaxial compression is about $2\text{-}3\times10^{-3}$ m/m. The maximum tensile strains for biaxial compression range between 2×10^{-3} m/m to 4×10^{-3} m/m, which is greater than under uniaxial compression. In biaxial tension the maximum principal tensile strain is lower than 10^{-4} m/m and in the confined states of stress both the maximum principal compressive and tensile strains decrease as the tensile stress increases.

The state of stress in many practical structures is a biaxial one. Therefore, biaxial strength envelope, directly based on experimental results, have been frequently used. Figure 2-4 represents a biaxial envelope proposed by Kupfer et al [37] as well as the corresponding experimental results. These results have been used by many researchers as a basis for developing new failure criteria for concrete under multiaxial state of stress. The various failure criteria for biaxial compression available in literature have been compared with selected experimental data in [41, 42]. The conclusions drawn from these studies are as

follows:

1. Classical failure theories such as von Mises, Mohr-Coulomb and Drucker-Prager, are crude approximations of the concrete failure envelope and they can represent only limited regions of total stress space.

2. The biaxial degenerations of some criteria proposed for triaxial compression yield unexpected biaxial failure envelopes which deviate from the experimental observations.

To simulate the biaxial failure envelope of concrete, some criteria have been proposed in [42, 43] as functions of the first two stress invariants (I_1, J_2). The correlation between these criteria and experimental data were found to be quite good.

(iii) Triaxial loading

Several studies on the behaviour of concrete under triaxial stress state have been reported [32, 44-47]. However, test results are less complete and less reliable than uniaxial or even biaxial data. A large dispersion of experimental results has also been observed. Two principal factors are responsible for this scatter [40]. Variation of the materials tested, and variation in the test methods.

Figure 2-5(a) shows typical stress-strain curves from tests by Richard et al [40] which were conducted at a low or moderate confining stress state. Some main conclusions are:

1. The axial strength increases with increasing confining pressure.

2. The high strength is always accompanied by a large deformation. Axial strains over 0.06 were registered at ultimate load (the uniaxial values are usually around 0.002).

3. Inelastic compaction is prominent at high volumetric compression as shown in Figure 2-5(b) [46].

4. The unloading at the beginning is parallel to the initial tangent, later declining from the tangent as a result of the stiffness degradation of concrete under high hydrostatic compression.

Experimental studies [45] have indicated that the three-dimensional strength envelope for concrete can be defined in terms of the three stress invariants. The characteristics of concrete failure surface under triaxial stress have been studied in [21, 24, 28, 45]. Several failure theories have been proposed to capture these features. The most commonly used failure criteria are the five parameter model of William-Warnke [48] and the four parameter criterion proposed in [49].

2.2.3 MECHANICAL PROPERTIES UNDER DYNAMIC LOADING CONDITIONS

It has been mentioned in Section 2.2.1 that the material behaviour of concrete under dynamic loading conditions can be significantly different from that under static conditions. Although numerous experimental works for plain concrete under dynamic loading have been reported, most available data are obtained from uniaxial tests. Extensive reviews of such tests have been given in [7, 8].

The results of some tensile and compressive tests carried out at higher strain rates than the conventional static tests, are summarized in Table 2-1. These experimental studies have covered a wide range of strength, moisture content, age at test and testing techniques. It can be observed from the results in Table 2-1 that increasing the stress or strain rate in tension or compression results in higher concrete strength. The tensile response of concrete is more strain rate sensitive than its compressive strength. The inequality of rate effects in tension and compression has been termed as strain rate induced anisotropy [50]. Some studies [16] have reported that concrete with a lower static strength exhibits a higher strain rate sensitivity

than concrete with a higher static strength. Another conclusion from these tests is that the strain rate has little or no effect [12, 50] on the initial tangent modulus, but results in an increase in the secant modulus. Generally, it has been also observed that the nonlinearity of the stress strain curves decrease with the increase of strain rate. In tension [12, 31] these curves are almost linear and show only curvature in the final phase of loading. As the nonlinearity of the constitutive diagrams has been associated with micro-cracking, it can be surmised that increase in the strain rate results in a decrease in the amount of micro-cracking. In some tests [19] when the strain rate was increased, the value of the concrete strain at maximum compressive stress increased while in some other tests [18] it decreased. On the basis of the least squares curve fitting to the experimental data, it has been found [20] that increasing the strain rate from the static value of 10^{-5} sec^{-1} to values as high as 10^{-1} sec^{-1} results in reduced values of strain at maximum compressive stress. At strain rates higher than 10^{-1} sec^{-1}, however, the compressive peak strain becomes larger than the static value. As contrasted with dynamic compressive tests, the influence of the strain rate upon the tensile cracking strain of concrete has been a lesser subject of research. However, recent experimental studies [12, 31] have indicated that increasing the strain rate results in increased values of the cracking strain in a similar fashion to the observed rate sensitivity of concrete tensile strength.

Biaxial or triaxial testing under dynamic loading is extremely difficult and only Nelissen [51] has conducted biaxial tests at different states of straining. The tests were performed at strain rates of 3.3×10^{-3} to 1.7×10^{-4} sec^{-1}. The influence of strain rate has been found to be different for different stress ratios.

2.3 A REVIEW OF CONSTITUTIVE MODELS OF UNCRACKED CONCRETE

Research test specimens often have dimensions which require microscopic modelling to idealize concrete components as separate units. However, concrete structures have such dimensions that a constitutive modelling on the macroscopic level is necessary. The present research is concerned with macroscopic numerical models. During the last two decades, several approaches, based on experimental data have been developed for simulating the complicated behaviour of concrete under various stress states and loading conditions. A brief review of these models, which are only based on continuum-mechanics approach, is given below. An extensive review on this topic can be found elsewhere [21, 28].

2.3.1 ELASTICITY BASED MODELS

Early constitutive models were based on linear elasticity to represent concrete behaviour where cracking is the most important factor of nonlinearity [6, 52]. The stress-strain relationship is linear almost up to peak load. However, the linear elasticity based model proved to be a good approximation of the concrete behaviour only in the tensile loading environment.

According to the Hookean formulation, the nonlinear elasticity based models can be grouped into two types: finite material characterization in the form of secant formulation (termed as hyperelastic model) and incremental model in the form of tangential stress-strain relation (or hypoelastic model).

(i) Hyperelastic model

This is based on the assumption of the existence of a strain energy density function, W (ε), such that [28]

$$\sigma = \frac{\partial W}{\partial \varepsilon} = S_s(\varepsilon)\ \varepsilon \qquad (2\text{-}1)$$

The term S_s is the stiffness tensor, which is dependent on the current strain. Based on a curve fitting of the

experimental data, the shape of the function W can be determined. However, this class of formulation is not popular for concrete modelling since the material model constants do not usually have physical interpretations. From the results of an extensive biaxial stress testing series, Kupfer et al [53] developed a unique relationship between octahedral stress and strain, and the secant bulk and shear moduli.

The behaviour of the hyperelastic model is reversible and path independent. It can model many of the concrete characteristics such as nonlinearity, dilatation and strain or stress induced anisotropy, but is incapable of describing history dependence, strain softening and rate effects.

(ii) Hypoelastic model

The material behaviour is described in terms of the stress and strain increments as

$$d\sigma = S(\sigma)\ d\varepsilon \qquad (2\text{-}2)$$

where the variable tangent stiffness, S, is a function of the current state of stress (or strain). This constitutive model is history dependent and satisfies the reversibility condition only in the infinitesimal sense. In the form of (2-2) the model exhibits stress-induced anisotropy and the tangent stiffnesses are identical in loading and unloading. For concrete, Coon et al [54] obtained reasonable agreement with uniaxial and biaxial test results by using S as a linear function of σ.

Through the decomposition of the stress and strain into hydrostatic and a deviatoric components, nonlinear elastic models for biaxial [55] and triaxial stress states [56] have been simulated. Based on experimental data, consistent octahedral stress-strain relationships have been established for all states of stress. From these relationships, secant and tangent bulk (K_s, K_t) and shear (G_s, G_t) moduli can be

derived. Following a similar concept, Ottosen [57] proposed a more general form of triaxial constitutive relation based on variable secant moduli where a sophisticated failure surface [49] is used as a limiting surface. Generally, the variable moduli models provide a good fit to the available test data but the accuracy is increasingly lost as failure or softening regime approaches. Another approach to constructing hypoelastic models is based on an orthotropic assumption [58]. These models are based on the equivalent uniaxial stress-strain relation so the elasticity moduli E_1 and E_2 are taken as functions of the state of stress and strain in each of the principal stress directions. These models were extended by Darwin [54] and Elwi [60] to represent concrete under cyclic load. An objection has been made [61] to orthotropic models since the requirement that the principal stress axes coincide with principal strain axes does not hold for concrete under general loading.

The effects of strain rate have been incorporated by Pal [62] in an isotropic hypoelastic model which assumed that the expansion of the failure surfaces depends on the strain rate effect. In general, nonlinear elasticity models are simple to use. However, their applicability is restricted to stress conditions which lie inside the range covered by the material testing data used to determine the material functions.

2.3.2 VISCOELASTICITY BASED MODELS

In the classical form of linear viscoelasticity, the stress at a given instant depends not only on the current strain but also on the previous strain history. Such a constitutive law can be expressed using the hereditary integral as [28]

$$\sigma\ (t) = \sigma^{\circ} + \int_{o}^{t} R\ (t,\ t\grave{}\ )\ \frac{d}{dt}\ \varepsilon\ (t\grave{}\ )\ dt\grave{} \qquad (2\text{-}3)$$

where R denotes the relaxation tensor and σ° is the initial

stress. As the evaluation of this integral requires the record of the previous strain history, it is customary to approximate the relaxation tensor by an exponential series (Dirichlet Series) [50] of the form

$$R\ (t,\ t^{\backprime}) = \sum_{i=1}^{N} R_i\ (t^{\backprime})\ e^{-(t-t^{\backprime})/\tau_i} \qquad (2\text{-}4)$$

where τ_i are discrete relaxation times and N is the number of elements in series. Combining equations (2-3) and (2-4) one can obtain

$$\sigma\ (t) = \sigma^{\circ} + \sum_{i=1}^{N} \sigma_i\ (t) \qquad (2\text{-}5)$$

where σ_i can be obtained from

$$\dot{\sigma}_i\ (t) = R_i\ (t)\ \dot{\varepsilon}(t) - \frac{1}{\tau_i}\ \sigma_i \qquad (2\text{-}6)$$

These equations correspond to a generalized Maxwell chain model with age dependent stiffness R_i and viscosities $\tau_i\ R_i$. In contrast to the heredity integral, only current strain rates and stresses are needed if a forward Euler difference formula is utilized to obtain the stresses [28].

Pozzo [63] has reported the results on a study conducted on the applicability of this theory for predicting the dynamic behaviour of concrete using a 3-parameter model (2 elastic element and a viscous Newtonian damper). However, he pointed out that the dissipative mechanism of concrete is not solely of a viscoelastic nature but was prevalently solid-friction type.

Bazant et al [64] developed a generalization of the nonlinear triaxial relations proposed for concrete compressive behaviour [65] to include strain rate effects. Recently, similar concept has been adopted by Oh [66] for concrete tensile behaviour. In these models, the strain rate effect upon the peak stress and the sharpness of the

peak stress were accounted for by introducing functions for their strain rate dependence. Considering concrete to be linearly viscoelastic they also obtained an expression for the variation of the initial modulus with strain rate. However, most of the results presented in the literature indicate that the initial tangent modulus is strain rate insensitive [12, 50].

The main drawback of linear viscoelasticity is that a rheology based model with a broad relaxation spectrum demands excessive programming, computer storage and material parameters [28, 50].

2.3.3 PLASTICITY BASED MODELS

The classical theory of plasticity is well founded on a physical and mathematical basis with a long history of successful applications involving metals. For compressive loading, concrete initially exhibits almost linear behaviour up to the elastic limit, after which the material is progressively weakened by internal microcracking up to failure. The nonlinear deformations are basically plastic since, upon unloading, only the elastic strain portion can be recovered from the total deformation. This has resulted in using extensively, in recent years, the plasticity approach to describe the nonlinear behaviour of concrete [67]. One criticism of the application of this concept to concrete is that the inelastic behaviour predicted by a plasticity theory is not accompanied by the degradation of elastic moduli, i.e. the decrease of the unloading stiffness. However, this is not significant in the prefailure regime. Besides, the theoretical background of work-hardening plasticity has been quite consolidated.

There are three basic assumptions in the incremental theory of plasticity [21]: an initial yield surface, a hardening rule and a flow rule. An initial yield surface in stress space defines the stress level at which plastic deformation

begins. A hardening rule regulates the evolution of the subsequent loading surfaces during the course of plastic flow. A flow rule defines an incremental plastic stress-strain relationship using a plastic potential function. The application of the theory to concrete requires considerable modifications of the shape of the yield surface, the hardening rule and the flow rule. Most of the research has in the past been made towards defining a suitable failure surface. The initial yield surface is usually assumed to have the same shape as the failure surface but with a reduced size.

The loading surface which is dependent upon the current state of stress σ and a number of hardening parameters H_i can be expressed [28] as

$$F(\sigma, H_i) = 0 \qquad i = 1, 2, \ldots \tag{2-7}$$

Equation (2-7) represents an envelope of stress state in the material which causes the onset of plastic behaviour. Each stress point inside the surface represents an elastic state of stress and each point on it a plastic state. Due to the hardening parameters, H_i, the loading surface can translate and change its shape until the failure surface is reached. The failure surfaces which are widely used in the numerical analyses of concrete structures include classical failure criteria and failure theories based on a biaxial or triaxial testing data. Detailed reviews of the failure theories proposed in the last two decades are given in [21, 28].

A perfectly plastic body is defined by the yield criterion which depends only on the stress tensor, $F(\sigma) = 0$. During plastic deformation this criterion remains unaltered. The simplest hardening rule is isotropic hardening where the yield surface expands uniformly as

$$F(\sigma, \lambda) = 0 \tag{2-8}$$

In this case, the yield surface depends on a scalar

parameter λ that monotonically increases with plastic deformation. To describe anisotropy of hardening, the yield function is expressed [34] as

$$F\ (\sigma - \alpha,\ \lambda) = 0 \qquad (2\text{-}9)$$

The initial yield surface undergoes rigid body translation with varying α representing the centre of the yield surface. Any plastic strain is accompanied by variation of α and λ. In order to define α, different translation rules have been proposed by Prager [68], Ziegler [69], and Dafalias et al [70]. For concrete material, combined isotropic and kinematic hardening has been proposed by Chen [43] and Argyris [71]. Non-uniform hardening rule rather than the usual isotropic hardening rule is developed in [72] to employ a closed initial yield surface.

The flow rule defines [21, 67] that the plastic strain increments are proportional to the stress gradient of the plastic potential $Q\ (\sigma,\ H_i)$. If the yield function coincides with the plastic potential $F = Q$, the associated flow rule is obtained. A stable material, according to Drucker, requires the associated plastic flow to be normal to the yield surface. For concrete, the associative flow rule is often incorporated into the development of a plasticity based model and reasonably good results are obtained [42, 43, 67, 73]. The deviation, however, is observed in the estimation of volumetric strain. Volume expansion near failure tends to be overestimated. Therefore, the application of a non-associative flow rule has been introduced [72, 74]. It has been successful in controlling the volumetric strains and in describing the stress-strain relationship, but much computational effort involving several material constants is usually required.

The extension of the classical plasticity theory has recently been made in the strain space formulation to provide consistent modelling over the entire range of concrete behaviour [75]. The flow theory of plasticity can

exhibit both stress and strain history dependence and stress induced anisotropy. However, this theory is not well adapted to model material softening observed in concrete, and it is difficult to incorporate rate dependence.

2.3.4 VISCOPLASTICITY BASED MODELS

Nonlinear behaviour of real material originates both from plastic and viscous internal dissipation of energy. In the theory proposed for rate dependent behaviour of plastic materials, Perzyna [76] assumed that the viscous properties of the material become manifest only after the passage into the plastic state. In this approach, the strain rate $\dot{\varepsilon}$ was decomposed into a linear elastic strain rate $\dot{\varepsilon}_e$ and viscoplastic strain rate $\dot{\varepsilon}_{vp}$. In analogy with the theory of plasticity, a static loading function is assumed which is expressed as

$$F\ (\sigma,\ H_k) = 0 \qquad k = 1,\ 2,\ \ldots \tag{2-10}$$

The shape of the surface in the stress space depends on a set of hardening (or internal) variables H_k. In contrast to the plasticity theory, stresses outside the loading surface can exist and the magnitude of the viscoplastic strain rate is considered to be a function of the excess stress above the static loading surface. The flow rule is defined such that the viscoplastic strain rate is directed along the gradient to the viscoplastic potential, $G\ (\sigma,\ H_k)$. Thus, the constitutive relation may be written as

$$\dot{\sigma} = D \left[\dot{\varepsilon} - \gamma \langle \phi(F) \rangle \frac{\partial G}{\partial \sigma} \right] \tag{2-11}$$

where D is the linear elastic stiffness tensor, γ denotes the fluidity parameter, and

$$\langle \phi(F) \rangle = \begin{cases} 0 & \text{if} \quad F \leq 0 \\ \phi\ (F) & \text{if} \quad F > 0 \end{cases} \tag{2-12}$$

From the constitutive relation, it can be observed that the

flow theory of plasticity can be obtained as a subclass of viscoplasticity [28]. Thus, many of the modelling techniques familiar in plasticity such as yield criteria and hardening rules can be adopted in the theory of viscoplasticity.

Instead of using a solely elasto-viscoplastic model, Nilsson [28] used a combined elasto-viscoplastic-plastic-brittle theory to model the dynamic behaviour of concrete. The rate effects upon the ductile yield and brittle failure surfaces were introduced in the form of single hardening parameter which was expressed as a function of the effective strain rate and determined by fitting the experimental data of rate effects upon the ultimate compressive strength. To satisfy the ultimate stress constraints with increasing strain rate, the fluidity parameter was assumed to be dependent on the effective strain rate. The introduction of a single rate hardening parameter into the loading surfaces yields isotropic strain rate sensitivity while the experimental results indicate a greater rate dependency in tension as compared to compression. Attempting to modify the rate hardening parameter to accommodate this effect would result in complicating an already very much intractable model. Furthermore, the rate dependent function employed to define the fluidity parameter was based more on heurostic discussions than on experimental results. The ideal elastic brittle response in tension is also a severe drawback of this model.

A rate dependent model for plain concrete under seismic loading condition has been proposed by Bicanic [77]. The model is a modification of the classic viscoplasticity theory, using a rate sensitive fluidity parameter and a damage monitoring failure surface to initiate the degradation of the loading surface once failure has occurred. The original Bicanic model was extended to include tensile cracking in [78, 34]. However, the rate effects upon the yield and failure surfaces were not

included and consequently the strain rate induced anisotropy effect was ignored. The model also did not account for strain hardening observed experimentally in the pre-failure range of concrete behaviour. The strain rate independent crack initiation in tension does not match the recently published test results [15, 31].

The elasto-viscoplastic model is capable of describing age, rate and stress and strain history dependence. Thus, it holds much promise in developing a constitutive theory for the dynamic behaviour of concrete. In contrast to the flow theory of plasticity, no special difficulties arise in the modelling of material softening behaviour. However, the application of classic theory to concrete under dynamic loading conditions is not conceptually straightforward. Introducing the necessary modification to fulfil the constraints observed in the pre-failure and post-failure ranges of dynamic behaviour of concrete, must be performed.

2.3.5 ENDOCHRONIC MODELS

The endochronic theory, originally proposed for metals by Valanis [79], was first applied to concrete by Bazant et al [80]. In this model, inelastic strains are not obtained from a loading surface, but directly from the evaluation of a measure of irreversible damage, referred to as intrinsic time, which is a non-decreasing scalar variable, depending on strain increments. The intrinsic time measure is comparable to that of the effective plastic strain in the plasticity theory. The inelastic strains are related to the intrinsic time through a series of mapping functions which depend on the current state of stress and strain, and are determined from the experimental data. Consequently, the model is incrementally nonlinear. Bazant has shown that many characteristics of concrete such as strain-hardening and softening, hydrostatic pressure sensitivity of inelastic strain, inelastic volume dilatancy, hysteretic behaviour, and rate dependency may be predicted by this theory.

However, the increase of scope is achieved at the expense of greater complexity and increasing number of material parameters. It involves many functions which are computed by a complicated optimal fitting procedure. The incremental nonlinearity is another disadvantage which requires iterations for each increment of loading and may cause some difficulties in the finite element analysis procedure. As a result, the practical application of the model is still limited.

2.3.6 RECENT MODELLING APPROACHES

Apart from the endochronic theory, the other constitutive models described earlier are incapable of exhibiting the progressive loss of unloading stiffness observed in concrete. To model such behaviour, the progressive fracturing and the damage mechanics theories have been recently adopted to develop numerical concrete models which are briefly described here for completeness. It should be mentioned that these models have not yet been fully explored in their applications to concrete structures.

The theory of progressively fracturing solids, developed by Dougill [81], is well suited for modelling the stiffness degredation during loading. During loading and unloading, the stress is obtained from

$$\sigma = D\,\varepsilon \qquad (2\text{-}13)$$

Time differentation yields

$$\dot{\sigma} = D\,\dot{\varepsilon} + \dot{D}\,\varepsilon = \dot{\sigma}_e - \dot{\sigma}_f \qquad (2\text{-}14)$$

where $\dot{\sigma}_e$ is the nonlinear elastic stress rate and $\dot{\sigma}_f$ denotes the rate of fracturing stress. To distinguish between loading and unloading, Dougill employed a fracturing surface which enclosed all possible elastic deformations

$$F\,(\varepsilon,\ H_l) = 0 \qquad l = 1,\ 2\ \ldots \qquad (2\text{-}15)$$

Due to the hardening parameters H_l which are dependent on the dissipated energy due to fracturing, the surface was allowed to translate and change its shape by exhibiting history dependence. Similar to the flow theory of plasticity, it was assumed that the fracturing stress can be obtained from the gradient of the fracturing potential, $G(\varepsilon, H_l) = 0$. Plastic fracturing theory proposed by Bazant et al [65] combines the conventional plasticity and the elastic fracturing theory to account for non-reversible strains. The basic idea is that inelastic strains consist of one part due to plastic deformations connected to the micro-mechanism of slip; and a strain softening part due to micro-cracking in concrete. Good modelling of concrete behaviour has been obtained [65]. However, the matrix of tangential moduli is non-symmetric which is an inconvenience in finite element analysis. It must also be emphasized that very few experiments have been conducted to determine the shape of initial and subsequent fracturing surfaces.

A continuous damage theory was first suggested by Kachanov [82] in an attempt to describe the degradation of materials under creep conditions. Damage was defined as the density of voids in a given cross section. The damage was treated as a kinematic variable, the growth of which resulted in the gradual degradation of the material. Loland [83] and Mazars [84] have adopted a similar scalar damage variable to predict the quasi-static stress-strain relation of concrete as

$$\sigma = E\ (1 - \omega_p)\ \varepsilon \qquad (2\text{-}16)$$

where ω_p is the damage parameter. By treating the damage as an internal state variable which influences the free energy of the material, a generalization of the damage theory has been achieved by Surais [50]. The existence of a free energy function dependent on the damage was postulated and the constitutive equations as well as the damage evolution equations were developed consistently, subject to

thermo-dynamic restrictions. The model has been employed to predict successfully the dynamic behaviour of concrete under uniaxial state of stress [50].

2.4 REVIEW OF CRACKED CONCRETE MODELLING

Cracking is one of the major sources of nonlinearity observed while analysing reinforced concrete structures. During monotonic loading of a structure continued up to failure, cracking occurs at an early stage of loading and introduces distinct geometrical discontinuity within the structure. Previous investigations have shown that treatment of post-cracking behaviour, in terms of strain softening [85] can greatly influence the ultimate load predictions and even paths to failure.

In order to model crack initiation and post-cracking behaviour, four basic areas are usually incorporated in the analytical model: a criterion for crack initiation, a method for crack description, a rule for tension stiffening (or tension softening) and finally a model for crack interface shear transfer.

2.4.1 CRACK INITIATION CRITERIA

The maximum stress and strain theories are frequently used to determine whether tensile cracking has occurred in the concrete [21]. If the maximum principal stress or strain in a point of the structure reaches the uniaxial tensile strength or tensile strain limit, cracking is assumed to form in planes perpendicular to the direction of the maximum tensile stress or strain and in that direction the stress is subsequently reduced to zero.

The uniaxial tensile strength can be obtained from different experimental tests. Direct tension tests conducted by Kupfer et al [37] provide the best available definition of concrete strength. Other test have been used to obtain the tensile strength such as the split cylinder test and the

bending test. From the bending test of plain concrete beams, the modulus of rupture which characterizes the tensile strength in bending seems to give a better prediction of structural behaviour than either the splitting tensile strength or the direct tensile strength [37]. The rupture strength, σ_r can be related to the uniaxial compressive strength [86] by

$$\sigma_r = 0.62 \left(\sigma'_{cs}\right)^{1/2} \qquad (2\text{-}17)$$

where σ_r and σ'_{cs} are expressed in MPa. For concrete structures subjected to dynamic loading, the maximum tensile strain criterion has been successfully employed to represent the tensile cracking of concrete [34, 78]. This criterion has also been adopted for static loading [87].

The main drawback of the existing crack initiation criterion is the strain rate insensitivity whereas recent dynamic tensile tests [15, 31] indicate that both uniaxial tensile strength and the cracking strain are highly strain rate dependent.

2.4.2 CRACK DESCRIPTION METHODS

In the finite element context, two main approaches have been used for crack representation [21]: the discrete crack model and the smeared crack model. The choice between one or the other model depends on the purpose of the finite element analysis. If local behaviour is of main interest, the discrete approach is convenient, since it can account better for bond slip, dowel shear effects and aggregate interlocking across cracks, giving realistic crack patterns. However, in cases where the overall behaviour of a structure is desired or where many cracks have formed, the smeared crack concept is preferable.

(i) Discrete crack model

The discrete cracking technique was first introduced by Ngo

and Scordelis [6] to analyse experimental reinforced concrete beams. In their study, the finite element mesh contained a few predefined crack directions. Elements along each direction were double-noded and upon crack initiation those nodes were separated to simulate a physical crack. This model was later improved by Nilson [52] and by Ngo et al [88] to include flexibility in specifying crack directions and linkage elements along the separated nodes to simulate aggregate interlock and dowel action. When the average stress in two adjacent elements exceeded the concrete tensile strength, corresponding elements were disconnected at their common nodes. As Nilson pointed out, this procedure overestimated the crack length since the crack must be initiated throughout the element boundary. The discrete crack approach was further improved and partially automated by Al Mahaidi [89] who used a predefined crack utilizing two nodes at one point connected by a linkage element. When the stress in the elements exceeded the concrete cracking strength, the linkage was set to have a reduced stiffness to allow the crack to open.

Despite all these improvements the cracks are still forced to follow the mesh lines and hence, lack total generality in propagation direction. This model is suitable for cases in which only a few cracks dominate the behaviour of the structure. As far as the ultimate capacity of most structures is concerned, there is little need to model each crack in great detail. The discrete representation has received limited acceptance as it requires detailed knowledge of kinematic quantities in advance such as location of crack tip, crack length and crack opening displacement for each individual crack. Further numerical complications due to redefinitions of the original finite element mesh and consequently destruction of the bandwidth of the structural stiffness matrix discards this method as being practically unusable.

(ii) Smeared crack model

The smeared crack approach which was proposed by Rashid [90], offers a more practical alternative for crack representation while using the finite element method. Upon crack initiation at a sampling point, representing average behaviour of some tributary area around that point, the constitutive matrix is modified to take into account the damage due to cracking which induces anisotropy. After cracking, concrete is assumed to become orthotropic. The elastic modulus is reduced in the direction perpendicular to the crack plane, and Poisson's effect is usually neglected [21]. This has the effect of smearing the crack over a certain area and imposes discontinuities in the stress field without making the displacement field discontinuous. Using the smeared approach, cracks in different directions can be generated automatically without the need for redefining the initial finite element mesh.

Due to its generality and simplicity, this approach is frequently employed for crack representation. Recently, it has been used by Nilsson et al [91], Bazant et al [92], Olemberg [93] and Rots et al [94] among others. However, some concern has been expressed regarding the ability of the model to represent failure mechanisms with dominant discrete cracks [95]. Although for these cases, the discrete crack model seems more adequate, the smeared approach using fine meshes of low order elements should be able to represent narrow mechanism bands leading to failure. Although Rots et al [94] favour the opinion that the smeared model can successfully represent discrete cracks, their numerical results show that no objectivity is found regarding the orientation of the finite element mesh. The crack is found to prefer to propagate parallel to the element boundaries. This behaviour may be caused by the integration rule employed [78]. It has been suggested [96] that it could be meaningful to test the smeared model with a mesh updating procedure to overcome this undesired effect.

According to the smeared crack treatment, an infinite number of parallel fissures distribute over the element at the instant of cracking. If the element size is sufficiently small, the tensile strains and stresses in the adjacent element just ahead of the crack tip could become sufficiently large, and the crack could propagate under a sufficiently small load. Consequently, the smaller the element size, the lower the predicted structural capacity would be. Such unobjective results known as size effect which was first recognised by Bazant [97] and later also reported by Nilsson et al [91]. In order to solve the subjective treatment of post-cracking behaviour, fracture energy based strain softening curves are substituted for the strength (or no softening) criterion.

2.4.3 TENSION STIFFENING OF CRACKED CONCRETE

Cracking results in the permanent loss of both tensile stiffness and tensile strength, and once it has occurred, the internal stress pattern of concrete changes to accommodate the associated geometric discontinuities. It has been a usual assumption in the early numerical analysis studies that concrete is an inelastic brittle material in tension [6]. When cracking occurs, the stress normal to the crack direction is immediately released and reduced to zero. It was soon discovered that this procedure leads to convergence difficulties, and more importantly, to results that are dependent on the size of the finite elements used in the analysis. Moreover, the experimental evidence [25] on unreinforced concrete shows that cracks in large specimens tend to grow in a stable manner. When reinforcement bars bridge concrete cracks, the strength mechanism becomes much more complex as a result of their highly different behaviour. This lack of material compatibility results in stress redistribution in cracked reinforced concrete as well as bond slip between concrete and steel reinforcement [98]. It has been argued [99] that due to bond forces, the concrete between cracks possesses a

tensile load carrying capacity normal to the direction of the crack which decreases with the increase of crack width. This effect is often known as the tension stiffening effect of cracked concrete.

Tension stiffening, in a number of studies [99-101], is considered by assuming that the loss of tensile strength in concrete after cracking occurs gradually according to a specified descending stress-strain curve. Many different shaped curves, with different limiting tensile strains, have been proposed. Scanlon [99] used a stepped piecewise linear unloading. A similar approach was used by Lin et al [100], but with a smooth unloading curve. Crisfield [101] applied a constant unloading scheme. Another approach to modelling tension stiffening effects based on a modified stress-strain diagram for the tensile steel is suggested in [102]. The concrete is assumed to carry no stress normal to a crack, but an additional stress is added to the reinforcing steel. The relative effects of different tension stiffening representation have been studied in [102].

The inclusion of tension stiffening effects does not only simulate the real behaviour of concrete, but it also improves the stability of the numerical analysis. However, two main problems remain unsolved [78]. The first one is that there is no objective way of measuring how much tension stiffening should be included in the model. It is easy to choose a tension stiffening curve based on experimental results but very difficult to make any a priori prediction. Secondly, the effect, if explained in terms of bond interaction with the reinforcing steel, cannot be applied to plain concrete structures, or to concrete located at a certain distance from the reinforcement.

Considerable experimental research has recently been directed towards the study of the post-peak behaviour of cementitious materials [103]. These studies have shown the efficiency of using some fracture energy concepts in

modelling the observed tension softening of concrete [103]. The implementation of the fracture energy release rate as a material property leads to a local strain-softening law which depends on a characteristic length relating to the size of the finite element mesh. In defining a curve to model the strain softening effect, two aspects have to be considered: the shape of the descending curve and the value of the parameters needed to define it. In most of the cases, either a simple line shape [85], or a bi-linear shape [104] have been used. In [78, 91, 93], nonlinear curves have been proposed which fit adequately the experimental results. These models include several fracture parameters such as the tensile strength $\sigma_{ts}^{\backslash}$, the fracture energy, G_f, softening constant, and the limiting tensile strain.

2.4.4 CRACK INTERFACE SHEAR TRANSFER

Experimental results [105-108] show that a considerable amount of shear stress can be transferred across the surfaces of cracked concrete. Two mechanisms are present in that transference: the aggregate interlock and the dowel action of reinforcing bars.

A considerable amount of shear stress can be transferred across the rough and irregular surfaces of a cracked concrete by aggregate interlock and frictional forces [105-106]. When the crack is subjected to shear forces rising from the redistribution of internal forces, the crack interfaces tend to override each other as a result of the shear slip. This tendency may be constrained either by surrounding a portion of concrete or by the reinforcing bars crossing the cracks. The interface shear capacity depends on the effectiveness of concrete in developing this constraining force normal to the crack plane. It has been shown experimentally that the crack width is the main variable in the aggregate interlock action. Smaller crack widths correspond to greater shear stiffness.

The dowel action mechanism is activated when reinforcing bars, particularly those of larger diameter, cross a crack subjected to shear slip [107, 108]. However, despite experimental analytical studies on dowel action, a comprehensive analytical expression for the dowel effect is not yet available. This is mainly due to the fact that the dowel stiffness depends on many factors such as the bar diameter, dowel embedment length, the presence of stirrups, concrete cover and the state of concrete surrounding the reinforcement.

Shear transmission can be simply accounted for in the smeared crack model by the introduction of a reduced value of concrete shear modulus, βG. Many researchers have used a constant value of β throughout the analysis [21, 34]. However, in an analysis of structures failing in shear, it is necessary that the cracked shear modulus is assumed to be a function of the fictitious tensile strain normal to the crack plane or the current crack width. Several formulations [21, 42, 78, 89] based on experimental results have been proposed for the cracked shear stiffness which are have been compared elsewhere [34].

2.5 REVIEW OF MATERIAL MODELLING OF REINFORCING STEEL

In this study steel reinforcement consists of one-dimensional elements in the form of bars. As a result, it is not necessary to introduce the complexities of multiaxial constitutive relationships for steel. A uniaxial linear or nonlinear stress-strain relation is fully adequate for monotonic as well as cyclic loading. Only a brief review of the uniaxial mechanical properties and the previously proposed constitutive models for steel is given here. More details can be found in reviews published in [7, 28, 109].

2.5.1 MECHANICAL PROPERTIES OF STEEL IN STATIC AND DYNAMIC LOADING CONDITIONS

Typical stress-strain curves for steel reinforcing bars under monotonic static tensile loading are plotted in Figure 2-6. These curves are normally characterized by the following features [109]:

1. An initial elastic region up to the yield strain ε^{s}_{ys} with mean modulus of elasticity of 200000.0 N/mm^2.

2. A yield plateau followed by a strain hardening region from ε_y to the ultimate strain ε_u, to the fracture strain ε_f.

3. The ultimate strength is approximately 1.55 times the yield strength.

4. As the strength of the reinforcement is increased, its capacity to undergo inelastic deformation, or its ductility, is decreased.

Ductility of reinforcement is necessary to ensure ductile behaviour of concrete structures and, hence to prevent brittle failure, especially under severe dynamic loading such as blast. In general, strength may be increased by changing the chemical composition of the steel, cold working, heat treating, or some combination of such techniques. Under monotonic loading, it is generally assumed that the steel behaviour is identical in tension and compression. Unloading and reloading result in a response path approximately parallel to the original elastic shape. When subjected to stress reversal after initial yielding, reinforcing steel exhibits curvilinear response known as the Bauschinger effect [110].

Steel is classified as a crystalline material whose material properties depend mainly on the properties of the crystal grains. The elastic deformation of steel takes place within the crystal lattice, while the non-recoverable deformations are principally associated with slip along crystallographic

planes [28]. The mechanism of the slip can be described as a propagation of dislocations which takes place once the magnitude of stress exceeds the yield stress. The slip also causes a break up of the grain boundaries and thereby decreases the cohesion between the grains resulting in a propagation of microcracks along the direction of the slip bands [111]. This mechanism appears as a decrease in the elastic stiffness. It is generally observed that the propagation of dislocations and microcracks is time-related [111]. Thus, the yield stress and the non-recoverable deformations of steel are strongly affected by the strain rates.

A vast amount of literature is available on the dynamic properties of steel. Mainstone [7], Sauris et al [8] and Nilsson [28] have presented a review of some of the published data. The effect of strain rate upon steel can be illustrated by the uniaxial tension stress-strain curves of Figure 2-7. From the survey of the available experimental results, some principal features of the steel behaviour under dynamic loading conditions on the macroscopic level can be summarized as:

1. The initial modulus of elasticity is unaffected by strain rate.

2. The yield stress and the ultimate strength of steel increase with increased strain rate. The steel with higher static yield strength shows less enhancement of strength under dynamic conditions than steel with lower static strength.

3. The ductility is observed to decrease with increasing strain rate as the ultimate strain is almost constant.

4. In contrast to concrete, the strain rate effects are isotropic, i.e. equal in tension and compression [8, 28].

5. There is no simple consistent effect on the effective stress in the strain hardening range.

2.5.2 CONSTITUTIVE RELATIONSHIPS FOR REINFORCING STEEL

Several constitutive theories have been proposed for steel. Indeed, most of the reviewed constitutive theories of concrete described in section 2.3 were primarily developed for steel or other metals. However, the most common approach found in the literature for the material modelling of reinforcing steel is the elasto-plastic constitutive model. Under transient [27] and dynamic loading conditions [28, 34], the viscoplasticity has been adopted.

For simplicity in the analysis which requires consideration of plastic deformation, it is often necessary to idealize the steel stress-strain curve. Bilinear or trilinear idealization has been commonly used depending on the accuracy required [109]. For each idealization, it is essential to determine experimentally the values of the stress and strain at the onset of yield, strain hardening and the ultimate tensile strength. Bilinear curves are used with simple kinematic and isotropic strain hardening rules. However, the trilinear relation is suitable only for use with isotropic hardening rule [109]. In general, these rules do not fit experimental data accurately. The isotropic hardening is incapable of modelling the Bauschinger effect. On the other hand, the kinematic hardening normally does overestimate the Bauschinger effect. In the investigation of the performance of different hardening rules, Nilsson [28] suggested a general nonlinear hardening function. However, due to the simplicity and the numerical convenience of the isotropic hardening, it is usually found sufficiently accurate for the behaviour of reinforcing steel. In this case, the onset of plastic (or viscoplastic) hardening is governed by [112]

$$\tau^{s} = \sigma^{s}_{ys} + H\,\varepsilon_{p} \qquad (2\text{-}18)$$

in which τ^{s} is the effective stress level controlling the yield condition, H is the strain hardening parameter of steel, and σ^{s}_{ys} is the static yield stress of steel.

The total strain, ε_s, is decomposed into elastic and inelastic components (whether produced by plastic deformation-creep or temperature) and the stress σ_s is expressed [109] as

$$\sigma_s = E_s \left(\varepsilon_s - \varepsilon_p - \varepsilon_t\right) \qquad (2\text{-}19)$$

in which ε_p represents the plastic (or viscoplastic) strain which may be positive or negative, ε_t is the thermal and/or creep strain, and E_s is the modulus of elasticity of steel. For problems where the response is purely elastic, ε_p is set to zero in equation 2-18. Most applications involving calculation of inelastic strain based on the plasticity theory, require step-by-step iterative solution techniques and it is necessary to retain the plastic strain from the previously converged step in order to determine the stress associated with current strain as well as to check the violation of the yield conditions. The details of such computations can be found elsewhere [109, 112]. For viscoplasticity based models, the associative flow rule in conjunction with incremental time stepping procedure has been often employed [27, 112] to determine the incremental viscoplastic strain such that

$$\Delta\varepsilon_p = \gamma_s \left[\sigma_s - \tau^s\right] \Delta t \qquad (2\text{-}19)$$

in which γ_s is the steel fluidity parameter and Δt is the arbitrary time step.

Under dynamic loading conditions, a few models have been proposed which consider the strain rate effect by introducing modifications to the existing constitutive models. Methods employing the dynamic yield stress of steel [28] as a function of the static yield stress and the strain rate, or deriving the fluidity parameter as a function of the strain rate [34] to account for the rate dependence in the viscoplastic range have been reported.

2.6 CONCLUDING CONSIDERATIONS FOR MATERIAL MODELLING OF BLAST RESISTANT REINFORCED CONCRETE

In view of the mechanical properties presented in section 2.2 and from experience that has been gained from the quasi-static and dynamic behaviour of concrete, a comprehensive model for nonlinear analysis of concrete structures subjected to blast loading conditions should embrace essentially the following features of concrete behaviour:

1. Nearly reversible behaviour until combined state of stress reaches initial yielding in compression (30-50% of compressive strength) or tensile cracking in tension.

2. Irreversible behaviour due to micro-cracking process, which is stress and strain history and rate dependent, in the range between initial compressive yield and compressive failure.

3. History and rate dependent strain softening regime to simulate the post-failure behaviour in compression until crushing.

4. Development of tensile macrocracks, the main source of material nonlinearity, according to a rate dependent crack initiation criterion.

5. Strain rate-induced anisotropy resulting from the greater rate sensitivity of concrete in tension than in compression.

6. Strain-induced anisotropy exhibited by loaded concrete due to cracking.

7. Tension softening in the post-cracking behaviour based on concrete fracture energy and the characteristic length of the crack.

8. Crack interface shear transfer to account for aggregate interlock and dowel action mechanisms.

Based on the mechanical properties of steel reviewed in section 2.5.1, some desired characteristics to be exhibited

by the concrete material during a blast can be concluded as follows:

1. Linear elastic rate independent behaviour until initial yielding is reached which is strain rate sensitive.

2. Above yielding, inelastic response in tension and compression which is history and rate dependent.

From the previously mentioned experimental studies of concrete and reinforcing steel and considering the drawbacks of the existing material models found in the literature, it becomes necessary to develop new constitutive models to achieve reasonable simulation of the material behaviour under blast loading. The principal features of appropriate constitutive models would be as described below:

1. The models should be comprehensive enough to capture the above mentioned nonlinear features of materials as well as the rate and history dependence required under blast loading.

2. The models are expected to be based on a solid foundation of constitutive theory for the macroscopic analysis of structures.

3. Total number of parameters used in the models should not be more numerous as compared with existing models.

4. The models should not present numerical difficulty in finite element analysis and should be easy for computer implementation.

5. The characterization of the models by experiments should be relatively easy.

Chapter 5 describes the material models developed in this thesis, for use in finite element analysis of concrete structures subjected to blast loading.

Reference	Type	$\dot{\varepsilon}_s$	$\dot{\varepsilon}_d$	$\sigma_s^{\backslash}$	$\sigma_d^{\backslash}/\sigma_s^{\backslash}$
Takeda et al [9]	T	5×10^{-6}	5×10^{-2}	–	1.7
	C	10^{-5}	1	-	1.4
Cowel [10]	T	5×10^{-6}	2×10^{-1}	3.55	1.75
	T	"	"	3.96	1.72
	T	"	"	4.89	1.70
	T	"	"	5.55	1.50
	C	10^{-5}	5×10^{-1}	31.5	1.43
	C	"	"	38.0	1.35
	C	"	"	57.3	1.40
	C	"	"	62.3	1.24
Birkimer [11]	T	2.5×10^{-7}	20.0	3.21	6.0
Kormeling [12]	T	2.5×10^{-6}	0.75	2.62	2.11
Hughes et al [13]	C	–	30	22	2.13
	C	-	"	53	1.94
	C	-	"	63	1.78
Sparks et al [14]	C	2.5×10^{-5}	2.5×10^{-1}	30	1.32
	C	"	"	30	1.12
	C	"	"	20	1.33
Atchley et al [15]	C	5×10^{-6}	2	17.2	1.58
	C	"	"	25.5	1.55
	C	"	"	34.5	1.62
Watstein [16]	C	10^{-6}	10	17.2	1.85
	C	"	"	44.8	1.85

T : Tension C : Compression

$\dot{\varepsilon}_s$: Static strain rate $\dot{\varepsilon}_d$: Dynamic strain rate

$\sigma_s^{\backslash}$: Static strength $\sigma_d^{\backslash}$: Dynamic strength

Table (2-1) Summary of concrete test data

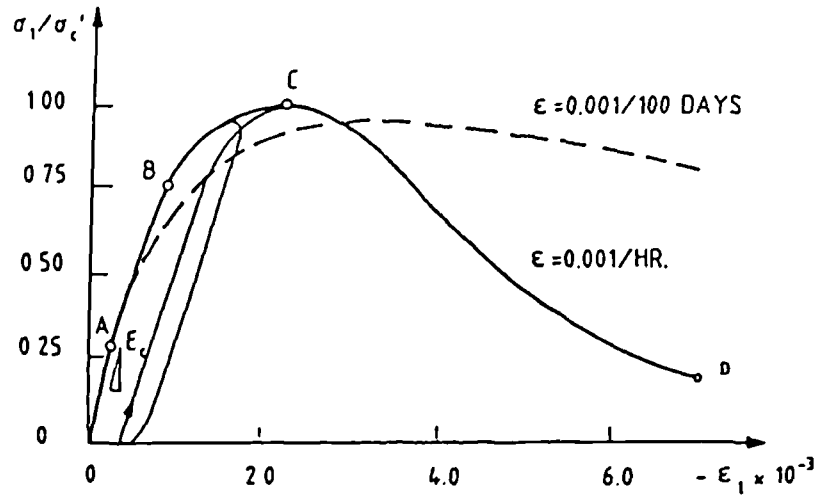

Figure 2.1 Stress-strain curves of concrete under uniaxial compression

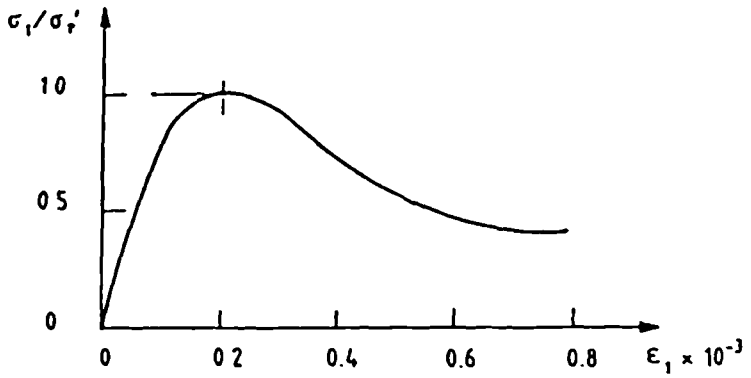

Figure 2.2 Stress-strain curves of concrete under uniaxial tension [21]

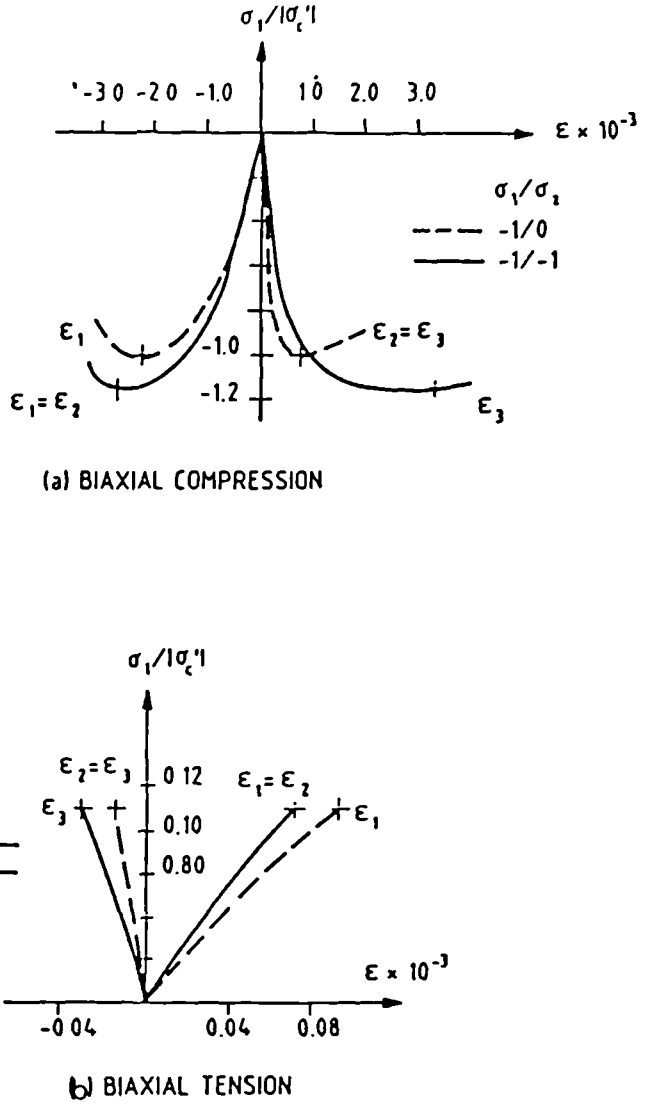

Figure 2.3 Stress-strain curves of concrete under biaxial stress [37]

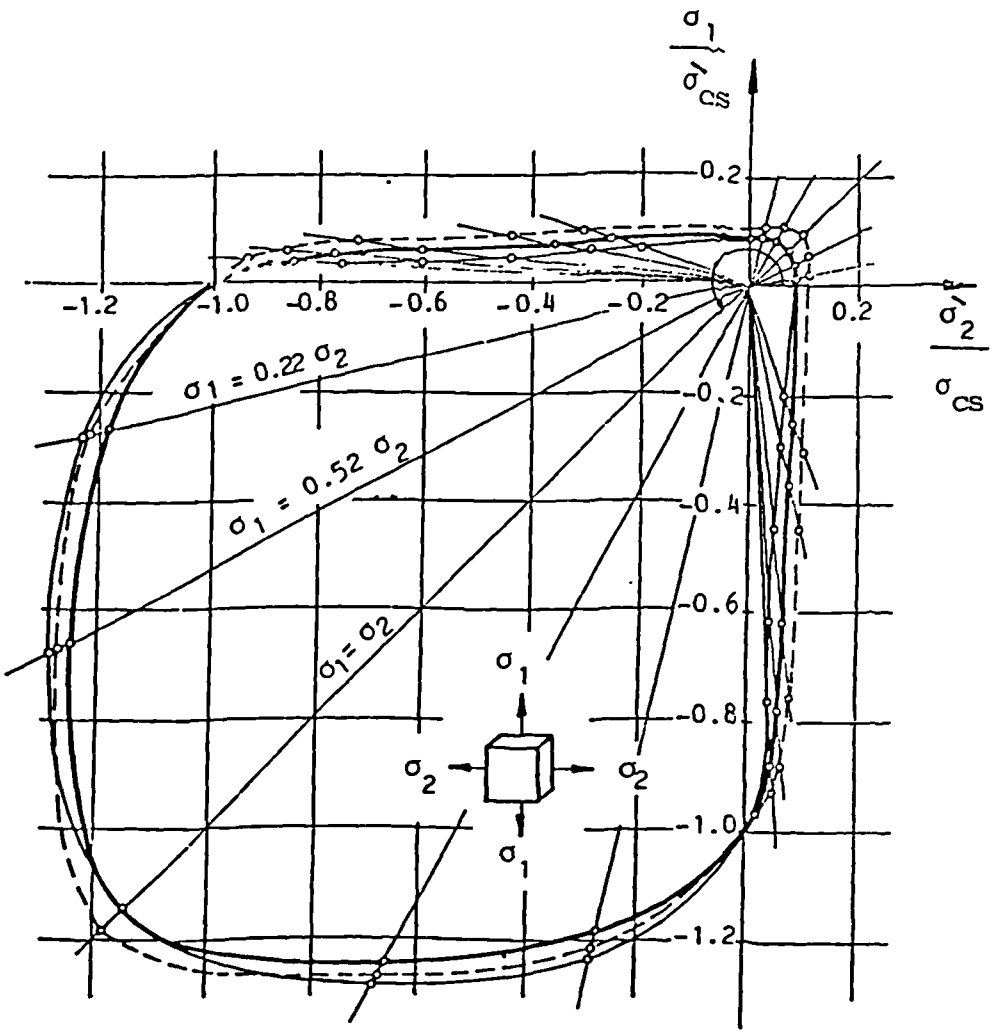

------ σ'_{cs} = -1.86 kN/cm²

——— σ'_{cs} = -3.09 kN/cm²

——— σ'_{cs} = -5.79 kN/cm²

Figure 2.4 Biaxial strength of concrete [37]

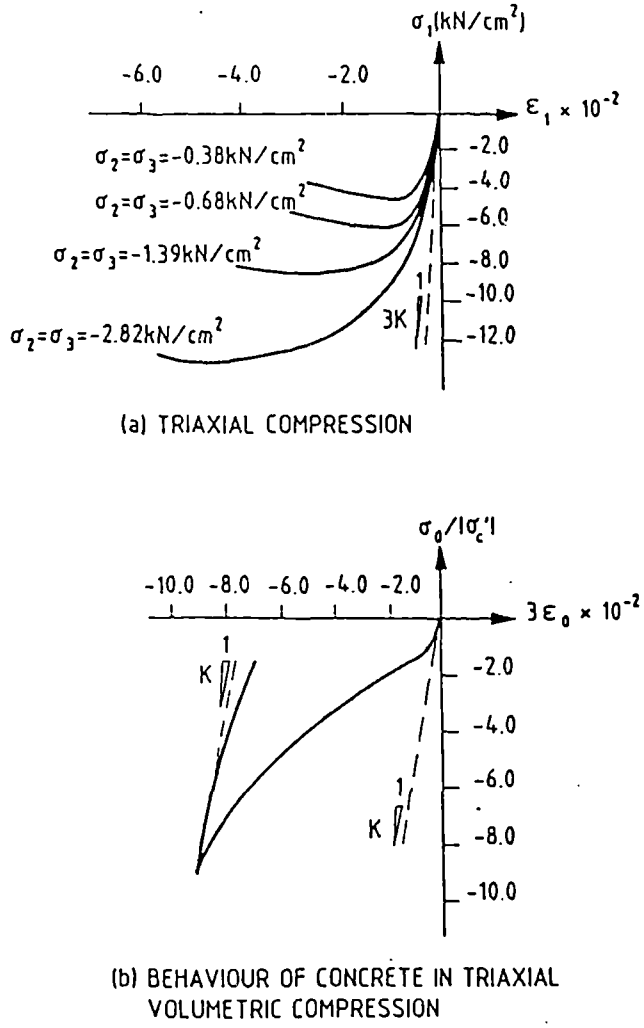

Figure 2.5 Concrete behaviour under triaxial stress [45]

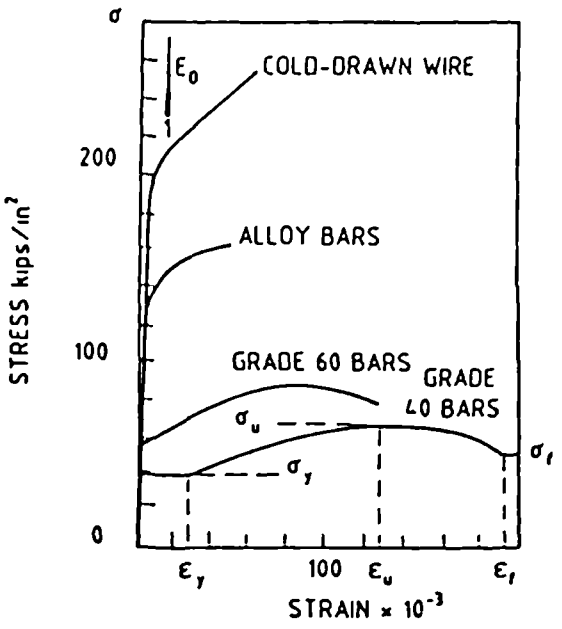

Figure 2.6 Typical stress-strain curves for steel reinforcement [21]

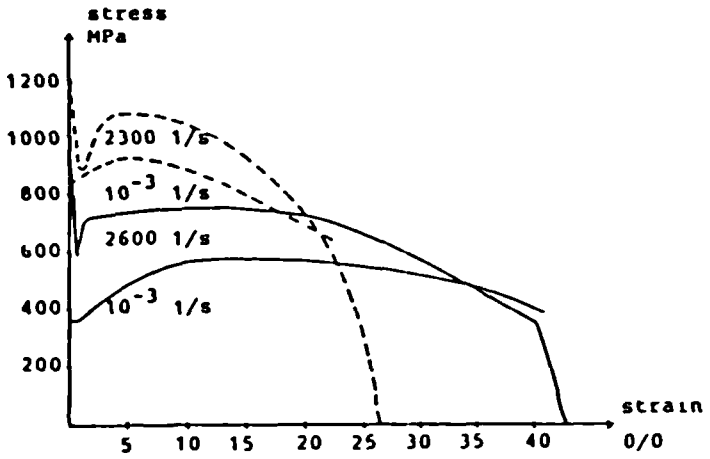

Figure 2.7 Stress-strain diagrams for two steel specimens at different rates of straining [28]

CHAPTER 3

MODELLING OF BLAST LOADING ON CONCRETE STRUCTURES

3.1 INTRODUCTION

A dynamic disturbance that commands much attention in the design or analysis of structures of military and civilian nature is the airblast caused by explosions outside or inside the structures. This requires evaluation of the magnitude of the blast loads which act on the various structural elements. In dynamic analyses, the excitation load is usually defined in one of two forms - either in a spectral form or as a given loading-time history. The former is adopted to characterise the periodic and random types of transient loading. Impact or blast loading is generally idealized through a load pattern, multiplied by some time varying function. For some explosions, the modelling of another excitation, namely blast-induced ground motion, also has to be considered.

It is not intended that this chapter serves as a complete source of information on airblast phenomonology and the induced loads. In view of the wide scope of the field and the fact that much literature in this field is classified for security reasons, only a limited discussion of the subject is made.

The objective of this chapter is to present information on modelling of airblast loading histories on structures due to confined or unconfined explosions in a mathematical form readily adaptable to structural response computations, to include subjects such as the evaluation of explosion-induced ground shock in a simplified form, and to bring together sources of additional information from the unclassified literature. The explosion sources considered are nuclear and conventional weapons as well as accidental explosions due to the ignition of gas and dust clouds.

The basic characteristics of the explosion and blast wave are briefly discussed in section 3.2. Then, the numerical modelling of airblast loading due to external explosions in the free-field as well as on structures are described in section 3.3, followed by the methods of prediction of internal airblast loading caused by confined explosions and contact blast in section 3.4. In section 3.5, the evaluation of explosion-induced ground shocks is given. The main considerations in modelling blast loads in order to perform nonlinear dynamic analysis of above-ground reinforced concrete structures are summarised in the final section.

3.2 EXPLOSION AND BLAST WAVE PHENOMENA

3.2.1 THE EXPLOSION PROCESS

In general, explosion is a phenomenan resulting from a rapid and sudden release of a large amount of energy [113-127]. Conventional explosives, such as trinitrotolune, known as TNT, depend on a rearrangement of their atoms for the energy, whereas nuclear explosions result from the release of energy binding protons and neutrons within the atomic nuclei. For flammable materials, the energy is mainly derived from the chemical reaction. Explosive materials may be classified according to their physical state: solids, liquids and gases. Solid explosives are primarily high explosives for which the blast effects are best known. Other materials, named low explosives, exhibit a variation of their blast pressure output depending on the molecular structure. In many cases, an explosion of these materials is incomplete and only a portion of the total mass of explosive is involved in the detonation process. The remainder of the mass is usually consumed by deflagration resulting in a large amount of the material's chemical energy being dissipated as thermal energy which, in turn, may cause fires.

The shock or blast wave is generated when the atmosphere

surrounding the explosion is forcibly pushed back by the hot gases produced from the explosion source. This wave moves outward from the central part only a fraction of a second after the explosion occurs. The front of the wave, called the shock front, is like a wall of highly compressed air and has an overpressure much greater than that in the region behind it. This peak overpressure decreases rapidly as the shock is propagated outward. After a short time, the pressure behind the front may drop below the ambient pressure, as shown in Figure 3-1. During such a negative phase, a partial vacuum is created and air is sucked in. High winds are also associated with the movement of the pressure wave being directed away from the explosion in the positive phase and towards the explosion in the negative phase.

When the shock wave of an air burst leaves the point of explosion, it travels as an incident wave until it strikes some object of density greater than that of the normal atmosphere. Upon striking such an object, a reflected wave travels back toward the point of explosion. The overpressure in the reflected wave may be much greater than the pressure due to the incident shock alone. Since the velocity of the reflected wave is greater than that of the incident wave, it follows that, at a point some distance from the explosion centre, the reflected wave will catch up with the incident wave, producing a single vertical wave front called a Mach stem [113-122] which moves horizontally along the surface of the ground. The junction point is known as the triple point [113-122]. As the pressure wave advances along the ground, the triple point describes a path as shown in Figure 3-2. Structures below this path will experience a single shock, whereas objects above this path will be subjected to two shocks; the incident and reflected waves. Below the path, as in the case of a surface burst, the shock front moves on the ground surface with an essentially vertical front near the ground.

3.2.2 BLAST WAVE CONFIGURATION

Although the physical properties of the explosion source affect the observed characteristics of airblast waves in many respects, evidence indicates that at a reasonable distance from the centre of the explosion, all blast waves, regardless of the source, share a common configuration. The pressure-time of a typical blast wave as observed at a location removed from the centre of explosion [121-127] is shown in Figure 3-3. At an arrival time of t_a after the explosion, the pressure at this location suddenly jumps to a peak value of overpressure, P_s over the local ambient pressure, P_o. The pressure then decays to ambient in time t_s, to a partical vacuum of very small amplitude, and eventually returns to P_o. The quantity P_s is usually termed the peak side-on overpressure, or merely the peak overpressure [121-127]. The portion of the pressure time history above initial ambient pressure is called the positive phase of the duration t_s. The portion of the overpressure below zero is called the negative or suction phase. In most blast studies, the negative phase of the blast wave is ignored and only blast parameters associated with the positive phase are reported. In order to study the blast effects on a given structure, the characteristics of the blast wave must be known. Such properties include density, wind velocity, shock front velocity, peak overpressure and dynamic pressure.

The decay of the overpressure illustrated in Figure 3-3 is usually described as quasi-exponential in character. Attempts to define the form of the wave decay in mathematical terms have not been easy. Expressions of varying complexity have been suggested to describe the positive phase as reported by Baker [113] The following expression to describe the positive phase is the most commonly used. In terms of a dimensionless wave form parameter α and time t measured from the instant the shock front arrives, the relation is established as

$$P_s(t) = P_s \left(1 - \frac{t}{t_s}\right) e^{-\alpha t/t_s} \qquad (3\text{-}1)$$

For a blast wave, the impulse per unit of projected area is obtained by integration of equation 3-1 such that

$$i_s = \int_0^{t_s} P_s(t)\, dt \qquad (3\text{-}2a)$$

$$= P_s t_s \left[\frac{1}{\alpha} - \frac{1}{\alpha^2}\left(1 - e^{-\alpha}\right)\right] \qquad (3\text{-}2b)$$

It has been suggested [117-127] that the overpressure-time curves can be represented by triangular equivalents as shown in Figure 3-3. These equivalent triangles have the same initial peak overpressure but have different durations depending on the expected time of maximum *structural* response. The durations are determined as follows:

a - If maximum response occurs after the overpressure has decayed to zero, a duration t_i, is selected so that the total impulse of the equivalent triangular curve is equal to that of the actual curve

$$t_i = 2\, i_s/P_s \qquad (3\text{-}3)$$

b - If maximum response occurs early in the pressure-time history, the slope of the equivalent traingular pulse is assumed to be tangent to the actual curve, resulting in the duration t_∞.

3.2.3 TNT EQUIVALENCY

The majority of data on blast effects in practice relates to the blast pressures output of a spherical charge of TNT explosive. This data can be extended to include other mass-detonating materials, even nuclear weapons, by relating the explosive energy of the effective charge weight of those materials to that of an equivalent weight of TNT. The

equivalency of material compared to TNT may be affected by other factors such as the material shape (flat, square), the number of explosive items, explosive confinement, nature of source and the pressure range being considered [115, 128]. The effects of the energy output of explosive material, relative to that of TNT, can be expressed [128] as a function of the heat of detonation as follows:

$$W_{TNT} = \frac{H_{exp}}{H_{TNT}} W_{exp} \qquad (3\text{-}4)$$

where W_{TNT} is the equivalent TNT charge weight, W_{exp} is the weight of the explosive in question, H_{TNT} is heat of detonation of TNT, and H_{exp} is the heat *of detonation of* explosive in question. The heat of detonation of the more commonly used explosives and chemicals are given in [115, 116, 128]. The heat ratio is described in some references as the TNT equivalent factor.

3.2.4 THE BLAST SCALING LAW

Characteristics of the blast wave generated in an explosion depend both on the explosive energy release and on the nature of the medium through which the blast propagates. These properties are measured for controlled explosions in experiments. Such test explosions are termed reference explosions. To find data for other explosions, scaling laws can be employed. A comprehensive description dealing with the blast scaling methods can be found in [113, 115]. The most common form of blast scaling is Hopkinson [1] or 'cube root' scaling law. This law states that when two charges of the same explosive and geometry but of different size are detonated in the same atmosphere, the shock waves produced are similar in nature at the same scaled distances. The scaled distance or the proximity factor Z, is defined as

$$Z = R/W^{1/3} \qquad (3\text{-}5)$$

where R is the distance from the centre of explosion to a given location and W is the weight of explosive. Another parameter which is useful in blast scaling is the explosives

yield factor λ, which is defined as

$$\lambda = \left(\frac{W}{W_r} \right)^{1/3} \tag{3-6}$$

where W_r is the weight of reference explosion, it is easy to deduce from equation 3-6 that similar shock effects occur at the same scaled distance.

$$Z = \frac{R_r}{W_r^{1/3}} = \frac{R}{W^{1/3}} \tag{3-7}$$

where R_r is the distance of reference explosion which is related to R as

$$R = \lambda R_r \tag{3-8}$$

Scaling can also be applied to time parameters. The scaled time τ_{sc} is defined for a time t [1] as

$$\tau_{sc} = \frac{t}{W^{1/3}} \tag{3-9}$$

Thus, the values of the arrival time and duration time for a shock wave are related to the corresponding time reference values (t_{ar}, t_{sr}) as

$$t_a = \lambda t_{ar} \tag{3-10}$$

$$t_s = \lambda t_{sr} \tag{3-11}$$

The decay parameter α and the overpressure P_s are not scaled, but the values used are those which correspond to the scaled distance. It is worth mentioning that the scaling law of the height of burst is similar to that of the

scaled distances. Reference data on blast effects due to standard explosives such as TNT are available in tabular and graphical form. For other charges and different distances, the blast parameters are obtained from the reference data using the scaling laws.

3.3 MODELLING OF AIRBLAST LOADING DUE TO EXTERNAL EXPLOSIONS

External blast loads may arise from the detonation of high explosives including atomic warheads, or from low explosives like flammable gases and vapours. The airblast loading on an exposed surface is a function of the airblast pressure, and the orientation, geometry and size of the surface which the shock wave encounters. Three components of loading are normally considered; overpressure, reflected pressure and dynamic pressure. The overpressure is simply the airblast pressure-time history that occurs in the free field *outside* the structure. Reflected overpressures occur due to momentum change when the propagating shock waves strike a surface in the path of propagation. Dynamic pressures, associated with the airflow behind the shock, cause drag and lift on objects that interfere with the flow of such air. In the literature, semi-empirical relations have been proposed for the prediction of airblast wave characteristics as well as the resulting transient pressure loads applied to the structures.

3.3.1 OVERPRESSURE LOADING PARAMETERS DUE TO ATOMIC WEAPONS

Analytical approximations to the nuclear burst overpressures as a function of time and range have been developed and used extensively for decades [123-125]. A detailed description of nuclear airblast phenomena is available in [113, 114]. In the last thirty years or so, considerable experimental and theoretical studies have been made to obtain the characteristics of blast waves from atomic sources. The detailed experiments conducted in the 1970's [129] have provided a better definition of peak overpressures. At a

given location where the shock wave passes over, the peak overpressure is a function of the energy yield of explosion, the ground range from the point of burst, the height of burst, and the medium in which the weapon is detonated [120, 121]. The peak value which occurs at a given range from a given yield can be predicted with confidence within a factor of 2. The range at which a given overpressure will occur can be predicted with an accuracy of 20%.

The following expression represents a good approximation for the variation of peak overpressure, P_s, with distance and explosion yield for a surface nuclear burst [120].

$$P_s = 15 \left[\frac{1000}{10^{15}} \right] \left[\frac{1000}{R} \right]^3 + 11 \left[\frac{W}{10^{15}} \right]^{1/2} \left[\frac{1000}{R} \right]^{3/2} \quad N/cm^2 \qquad (3\text{-}12)$$

W is the weapon yield in Joules and R denotes the ground range at the point of interest in metres. Pertinent weapon yield is ordinarily presented in units of one megaton (1 MT = 4.184×10^{15} J). Surface bursts are assumed to be twice as effective as air bursts for blast effects. Accordingly, one half of the actual burst yield, W, in equation 3-12 can be used to calculate free air overpresssure due to an air burst. However, the effect of reflection of air overpressures on the ground surface should be included. In Reference [116], the peak overpressure generated in the nominal meteorological standard atmosphere as computed for a spherical charge with energy release equivalent to one kiloton (1-KT) for nuclear air burst, is given as

$$\frac{P_s}{P_o} = 3.2 \left(10^6 \right) Z^{-3} \left[\left(1 + \left(\frac{R}{87} \right)^2 \right]^{1/2} \left[1 + \frac{R}{100} \right] \qquad (3\text{-}13)$$

where $\frac{P_s}{P_o}$ is the ratio of explosion overpressure to ambient pressure P_o, and scaled distance R is the actual distance away from a nuclear explosion with an energy release of 1 KT

of TNT. The overpressures may be scaled to other yields by multiplying by the ratio $\left(\frac{W}{W_r} \right)^{1/3}$, where W_r is the reference yield (= 1 KT).

Since the time of arrival, t_a, and the positive phase duration, t_s, for a given overpressure can be scaled according to the cube root law, it is convenient to relate these parameters to a reference overpressure ratio. In [120, 121], graphical relationships for a surface burst of 1 MT are given for these parameters. For air bursts it is suggested that the cube root of the ratio of one half the air burst yield could be used to utilize surface burst data. In [116], the time required for a shock front to travel to a given location, R, is expressed as

$$t_a = \frac{1}{C_o} \int_{r_c}^{R} \frac{1}{M_s} \, dr \qquad (3\text{-}14)$$

in which r_c is the charge radius, C_o is the speed of sound in the undisturbed atmosphere, and M_s is the Mach number for the corresponding peak overpressure expressed as

$$M_s = \left[1 + \left(\frac{\gamma_h + 1}{2 \gamma_h} \right) \frac{P_s}{P_o} \right]^{1/2} \qquad (3\text{-}15)$$

where γ_h is the ratio of specific heat of air. The corresponding duration of the overpressure positive phase is given [116] as

$$\frac{t_s}{W^{1/3}} = \frac{180 \left[1 + \left(\frac{R}{100} \right)^3 \right]^{1/2}}{\left[1 + \left(\frac{R}{40} \right) \right]^{1/2} \left[1 + \left(\frac{R}{285} \right)^5 \right]^{1/6} \left[1 + \frac{R}{50000} \right]^{1/6}} \qquad (3\text{-}16)$$

where $\frac{t_s}{W^{1/3}}$ is the duration in seconds for 1-KT of TNT

reference explosion and R is the distance in metres when scaled to the reference explosion.

At a specified location, the variation of overpressure with time is a function of peak overpressure with the initial rate of decay being rapid at higher overpressures. As a result, typical nuclear explosion shows a smaller blast impulse per unit area compared with conventional explosion of identical duration and peak overpressure [116]. From the initial peak value, the time history of overpressure for surface bursts can be described as the sum of exponentially decreasing components given in the following equation [120]

$$P_s(t) = P_s \left(1 - \tau_r\right) \left(a\, e^{-\alpha \tau_r} + b\, e^{-\beta \tau_r} + c\, e^{-\gamma \tau_r}\right) \tag{3-17}$$

where $\tau_r = \frac{t}{t_s}$, t is the time measured from the instant of shock wave arrival, and the empirical coefficients a, b, c, α, β and γ are as given in [120]. It is worth mentioning that the simpler exponential form for the analytical expression of the overpressure history described earlier in section 3.2.2 has been employed in many references [115-119, 128] as an empirical adjustment to measured overpressure-time seconds. The wave form parameter, α, has been defined as a constant value of unity in Reference [128] and as a variable dependent on the intensity of the shock front in [116]. The time approximation ordinates t_1, t_∞ needed for triangular representation of overpressure-time curves are graphically described in [120] for 1-MT surface burst.

3.3.2 CHARACTERISTICS OF OVERPRESSURE LOADING DUE TO CONVENTIONAL HIGH EXPLOSIVES

There are a number of data sources for scaled blast parameters for conventional weapons. References [113] and [130] give shock front properties for incident and normally

reflected waves for spherical pentolite charges detonated in free air. Data are given in [131] for incident waves for surface bursts of TNT which are generally accepted as the standard waves for this reflection situation. Detailed compilations for both air and surface bursts of TNT are available in [113, 122]. A comparison of the predictions of blast wave properties can also be found in [132].

When a high explosive detonates at the ground surface, at distances beyond the volume occupied by the explosive itself, the maximum blast overpressure is given, in bars, [126] as

$$P_s = 6784 \frac{W}{R^3} + 93 \left(\frac{W}{R^3} \right)^{1/2} \qquad (3\text{-}18)$$

in which R is the distance in metres on ground surface from centre of detonation to the point of interest and W is the total energy of detonation measured in equivalent weight of metric tons of TNT. In Reference [133, 134], a structure in the remote region of an explosion is considered to be subjected to an overpressure which is related to the proximity factor, Z, as follows

$$P_s = \frac{1772}{Z^3} - \frac{114}{Z^2} + \frac{108}{Z} \quad KN/m^2 \qquad (3\text{-}19)$$

in which W is the equivalent charge weight measured in kilograms of TNT. The overpressure-distance relation for conventional air burst is given [116] by

$$\frac{P_s}{P_o} = \frac{808 \left[1 + \left(\frac{Z}{4.5} \right)^2 \right]}{\left\{ \left[1 + \left(\frac{Z}{0.048} \right)^2 \right] \left[1 + \left(\frac{Z}{0.32} \right)^2 \right] \left[1 + \left(\frac{Z}{1.35} \right)^2 \right] \right\}^{1/2}} \qquad (3\text{-}20)$$

in which the proximity factor, Z, is the actual distance scaled to an energy release of 1-KT of TNT in the standard atmosphere.

For surface burst, the total positive phase duration of blast overpressure, in millisec, is expressed [126] as

$$t_s = 10\ W^{1/3} \qquad (3\text{-}21)$$

The corresponding value for air burst, in millisec, is suggested [116] to be

$$\frac{t_s}{W^{1/3}} = \frac{980\left[1 + \left(\frac{Z}{0.54}\right)^{10}\right]}{\left\{\left[1 + \left(\frac{Z}{0.02}\right)^{3}\right]\left[1 + \left(\frac{Z}{0.74}\right)^{6}\right]\left[1 + \left(\frac{Z}{6.9}\right)^{2}\right]\right\}^{1/2}} \qquad (3\text{-}22)$$

The exponential form of the overpressure-time history expressed by equation 3-1 has been suggested in [116, 128]. As the rate of decay of overpressure with time is much slower for conventional bursts compared with nuclear explosions, the overpressure-time curve can be approximated by the triangular representation in which the intercepts on the time axis are expressed in millisec, [126] as

$$t_\infty = 3.20\ \frac{W^{1/3}}{P_s^{1/3}} \qquad \text{for } P_s < 3.4 \text{ bar} \qquad (3\text{-}23a)$$

$$= 6.21\ W^{1/3} / P_s^{7/8} \qquad \text{for } P_s \geq 3.4 \text{ bar} \qquad (3\text{-}23b)$$

$$t_i = 10.23\ W^{1/3} / P_s^{1/2} \qquad \text{for } P_s < 70 \text{ bar} \qquad (3\text{-}24a)$$

$$= 20.77\ W^{1/3} / P_s^{2/3} \qquad \text{for } P_s \geq 70 \text{ bar} \qquad (3\text{-}24b)$$

The relations for conventional air burst can be used to estimate data for surface burst by using effective charge weight which accounts for ground reflections. A conversion factor of 1.8 has been suggested [128].

3.3.3 OVERPRESSURE PREDICTION DUE TO UNCONFINED VAPOUR CLOUD EXPLOSION

Another type of explosion which is particularly important in

the context of industrial and nuclear plants is the explosion of a cloud of flammable vapour. Such explosions are the result of a massive spill of a combustible hydrocarbon into the open atmosphere, followed by ignition and sufficient acceleration of the flame propagating through the cloud to produce a destructive shock wave. Severe damage can be inflicted to structures located hundreds of metres away from the cloud centre. Depending on the speed of the flame front, there are two different mechanisms in the explosion [135-140]. In the case of deflagration, the combustion velocity is of the order of 10 m/sec. Despite a substantial literature existing on many aspects of the unconfined vapour cloud explosions, there are gaps in the state of knowledge on the subject. A full understanding of such explosions must await the solution of several experimental and theoretical problems outlined in [115, 139].

Some important features of vapour cloud explosions which differentiate them from a TNT explosion may be summarized [135, 136] as

1 - The explosion source can be of very large dimensions depending on the rate of fuel release and the delay before ignition. A vapour cloud is also not hemispherical but more of a pancake shape which makes the spatial dimensions even larger.

2 - The blast energy is only a fraction of the total combustion energy of the cloud since a significant portion remains unburnt.

3 - The overpressure at the explosion centre is much less than that at the point source of TNT explosion. Depending on the combustion mode, the blast effects inside the cloud as well as the airblast decay outside the cloud can be drastically different. It has been suggested [135] that the practical upper limit of overpressure is probably about 1 bar at the centre and about 0.7 bar at the boundary of the

cloud.

4 - The shape of initial blast wave is different from that of concentrated charge explosion, but it is assumed that at a sufficient distance from the source, it becomes indistinguishable in form from the wave of TNT explosion.

5 - The duration is generally considered to be longer than that of the condensed phase explosion. For design of structures with the assumed overpressure 1 bar at the cloud centre, a duration time of 30 ms has been provisionally adopted [135, 136].

Despite these known differences, the existing guidelines for estimating the blast damages from chemical explosions are based on the TNT equivalent yield concept [135-137, 139, 140]. The other alternative models presented in [135] are untried. If W_f kg of a certain fuel is released into the atmosphere and ΔH_f is the standard heat of combustion of this fuel in Joules/kg, then the TNT equivalent yield is obtained by [136]

$$W_{TNT} = \alpha \frac{\Delta H_f \; W_f}{4.198 \times 10^6} \qquad (3\text{-}25)$$

where α is some empirical factor ($0 < \alpha < 1$) and 4.198×10^6 is the explosion energy of TNT in Joules/kg. The empirical factor α is used to account for the differences between the two types of explosions. From the reconstruction of past accidents, it is found [136] that α can vary from an insignificant fraction of a percent to values as high as 30%. As a guide, a value of 0.05 to 0.10 may be used. Once W_{TNT} is found, a characteristic explosion distance R_o can be defined by

$$R_o = \left(\frac{W_{TNT} \times 4.198 \times 10^6}{P_o} \right)^{1/3} \qquad (3\text{-}26)$$

At a given location R from the centre of explosion, the energy scaled distance, $\bar{R}$, is defined as

$$\bar{R} = R / R_o \qquad (3\text{-}27)$$

A systematic study of the effect of normal burning velocity on the blast wave produced by central ignition of a spherical cloud has been performed by Strehlew et al [141]. The normal burning velocity of the fuel under consideration divided by the local velocity of sound was considered to be a reference Mach number M_{su}. The output of the study was standard charts to yield the scaled overpressure $\bar{P}_s$ as a function of the energy-scaled distance. Such charts are shown in Figure 3-4 and 3-5. In Figure 3-4, curves are given for deflagrative explosion with various normal burning velocities. The curve labelled P is for Pentolite, D is for detonation, and S is for open sphere burst. The minimum value of $\bar{R}$, 0.01, is reported as the effective wave width of the idealized spherical cloud. The maximum wave overpressure and impulse are then computed from the scaled values [115] as

$$P_s = \bar{P}_s P_o \qquad (3\text{-}28)$$

$$i_s = \bar{I}_s \left(W_{TNT} \times 4.198 \times 10^6\right)^{1/3} \frac{P_o^{2/3}}{C_o} \qquad (3\text{-}29)$$

Employing the triangular representation for the overpressure-time curve leads to the evaluation of the overpressure duration time as

$$t_s = 2\, i_s / P_s \qquad (3\text{-}30)$$

3.3.4 DYNAMIC PRESSURE PREDICTION

The most destructive effect of a blast wave is generally characterized by the peak overpressure. However, in many cases, depending on the structure geometries, the strong transient winds behind the shock front can be of greater significance. These drag forces are a function of the size and shape of the structure, and the peak value of the dynamic pressure resulted from the wind behind the shock

front. To predict the peak value of dynamic pressure, the shock front velocity, peak wind velocity and the density of the air behind the shock front are needed. The shock front propagates outward from the point of burst with a velocity which is a function of the peak overpressure just behind the shock front and the ambient conditions of the air ahead of the shock wave. The shock front velocity, U_s, at the point of interest is calculated [161] as

$$U_s = C_o M_s \tag{3-31}$$

In terms of shock velocity, the wind speed is given [113, 114, 116] as

$$u_s = \frac{2}{1 + \gamma_h} \left(\frac{U_s^2 - C_o^2}{U_s} \right) \tag{3-32}$$

In terms of overpressure, the peak wind velocity and the air density, ρ_s, behind the shock front are expressed [113, 115] as

$$u_s = \frac{C_o P_s}{\gamma_h P_o} \left[1 + \left(\frac{\gamma_h + 1}{2 \gamma_h} \right) \frac{P_s}{P_o} \right]^{-1/2} \tag{3-33}$$

$$\rho_s = \rho_o \left[\frac{(\gamma_h + 1) P_s + 2 \gamma_h P_o}{(\gamma_h - 1) P_s + 2 \gamma_h P_o} \right] \tag{3-34}$$

The dynamic pressure is proportional to the square of the wind velocity and the density of the air. The peak dynamic pressure, P_d, is defined [113-128] as

$$P_d = \frac{1}{2} \rho_s u_s^2 \tag{3-35}$$

From the above relations, this can be shown to be [113, 115]

$$P_d = \frac{P_s^2}{2 \gamma_h P_o + (\gamma_h - 1) P_s} \tag{3-36}$$

Under ideal gas conditions ($\gamma_h = 1.4$), equation 3-36

reduces to

$$P_d = \frac{5}{2}\left(\frac{P_s^2}{7P_o + P_s}\right) \qquad (3\text{-}37)$$

Equation 3-37 agrees reasonably well with measured data up to an overpressure of about 689 N/m^2 [120]. In general, it is estimated that the predicted range at which a given dynamic overpressure due to a nuclear burst occurs, is predicted reliably within an error of 25%.

The dynamic pressure time arrival is considered [120, 122-127] to be the same as that of the peak overpressure discussed earlier. The dynamic pressure positive phase duration, t_q, is expressed in seconds for 1-MT surface nuclear burst [121] as

$$t_q = \left[\frac{4}{1 + 0.085\,P_s + 0.0075\,P_s^2} + \frac{0.077\,P_s}{1 + 0.00042\,P_s^2} + \frac{0.02662\,P_s}{1 + 0.011\,P_s}\right] W^{1/3} \qquad (3\text{-}38)$$

in which W is the explosion yield in megaton. Values for other nuclear weapon yields can be obtained by the cube-root rule. For conventional explosions the drag pressure duration is defined in millisec [126] as

$$t_q = 20\,W^{1/3} \qquad (3\text{-}39)$$

in which W is the explosion yield in metric tons of equivalent TNT.

The variation of dynamic pressure with time is much like that of the overpressure with a sharper decay but a longer duration. As in the case of overpressure, it is often more convenient to use an equivalent triangular pulse to represent the actual dynamic pressure-time curve. The peak dynamic pressure is used as the initial value of the

equivalent pulse. The duration time and the drag impulse duration are defined graphically in [120, 121] for 1-MT nuclear surface burst. The corresponding value for conventional explosions, $t_i^{\backslash}$ is expressed in millisec [126] as

$$t_i^{\backslash} = 9.04 \left(\frac{W}{P_s} \right)^{1/3} \quad \text{for } P_s < 2 \text{ bar} \qquad (3\text{-}40a)$$

$$t_i^{\backslash} = 14.35 \; W^{1/3} / P_s \quad \text{for } P_s \geq 2 \text{ bar} \qquad (3\text{-}40b)$$

3.3.5 REFLECTED OVERPRESSURE PREDICTIOM

Reflection is caused by a momentum change when the propagating airblast strikes a surface in the path of propagation. The ratio of reflected overpressure to incident overpressure is called the reflection factor [121, 122] which is a function of the peak overpressure in the incident wave and the angle at which the wave strikes the surfaces. When the blast reaches an object at right angles, or nearly so, the resulting reflection produces a peak reflected overpressure, P_r, given [135] by

$$P_r = 2 P_s + (1 + \gamma_h) P_d \qquad (3\text{-}41)$$

Considering ideal gas conditions ($\gamma_h = 1.4$) and substituting for P_d from equation 3-41, the peak reflected overpressure is expressed as

$$\frac{P_r}{P_s} = 2 + \frac{6 P_s}{P_s + 7 P_o} \qquad (3\text{-}42)$$

Equation 3-42 is valid for ideal gas when the overpressure, P_s, is less than 10 bars. The peak reflected overpressure given by equation 3-41, can approach a value of twice the peak incident overpressure for weak shocks in which the peak dynamic pressure is negligible, but to approach a value of eight times the peak overpressure for strong shocks in which the peak dynamic pressure is dominant [113, 135]. This

upper limit is probably considerably in error [113, 135], for it is based on the assumption that the air behaves as a perfect gas even at the high pressures and temperatures existing under strong shock conditions. It has been shown [142] that this ratio can be much greater, perhaps 20, if real gas effects such as dissociation and ionization of the molecules are accounted for. Brode [143] has calculated this ratio for normal reflection of shocks assuming air dissociation ionization. Thus, for P_s greater than 10 bars, he suggested an empirical modification given as

$$\frac{P_r}{P_s} = 4 \log_{10} P_s + 1.5 \qquad (3\text{-}43)$$

In this relation, P_r/P_s should not be taken greater than 14, [126].

Equation 3-42 or equation 3-43 give only peak pressures and, hence, little indication of time histories of reflected pressure. Lacking more accurate prediction methods, it is suggested [115] that one can roughly estimate the reflected impulse, i_r, if the side-on impulse is known, by assuming similarity between the time histories of side-on overpressure and normally reflected overpressure. This assumption gives

$$\frac{i_r}{i_s} = \frac{P_r}{P_s} \qquad (3\text{-}44)$$

The actual reflected overpressure time history is idealized by an equivalent triangular pulse. The actual positive duration is replaced by a ficticious duration expressed as

$$t_{ir} = 2\, i_r / P_r \qquad (3\text{-}45)$$

3.3.6 EXTERNAL BLAST LOADS ON ABOVE-GROUND STRUCTURES

In the examination of airblast loading on structures, it is generally assumed [121, 122] that

1 - The loading is considered to be associated with an ideal shock in which the peak overpressure is reached instantaneously.

2 - The structure is in the Mach reflection region, where the airblast front is propagating parallel to the ground surface. However, a structure located in the regular reflection region can be considered by employing higher shock loads in the Mach reflection region to account for the incident blast wave reflections on the ground surface.

3 - The initial shock loads on solid objects can be decoupled from the response of the objects to the loads.

4 - The structures are treated as rigid bodies which cause processes such as shock reflection, diffraction and alteration of air flow behind the shock front. This is acceptable because of differences in elastic properties as well as in density between the wave transmitting media (air) and concrete structures.

The procedure presented here for the determination of the external blast loads are limited to rectangular structures positioned above the ground surface where the structures will be subjected to a plane wave shock front. However, the procedures can be extended to include structures of other shapes as well as structures positioned at and below the ground surface. Given the many uncertainties involved in the evaluation of blast loads, as well as in the interaction process between the blast wave and the structure, it is recommended [115, 120-127] that the actual blast effects in the incidental and reflected shock waves may be approximated by equivalent triangular pulses of similar impulses. Each pulse has a peak pressure value similar to the actual blast effect and ficticious durations defined earlier as functions of the impulse and the peak pressure.

On the front face of an above-ground structure, the pressures vary with time in the manner shown in Figure 3-6.

There is a very rapid rise time to the peak reflected pressure P_r followed by a rapid decay as the high reflected pressure causes a flow around the structure. The decay of the reflected pressure to the side-on overpressure plus dynamic pressure takes place in a clearing time, t_c, which is a function of the shock velocity U_s and the shortest distance from the point on the structure where the reduction in pressure takes place most slowly. The clearing time is given by the relation [122, 126]

$$t_c = 3 S / U_s \qquad (3\text{-}46)$$

where S is equal to the height of the structure or one-half the structure width, whichever is less. After the clearing time, the pressure decreases to zero with the decay in side-on overpressure and dynamic pressure. During this decay period, the maximum pressure is given [120-127] by

$$P = P_s + C_f P_d \qquad (3\text{-}47)$$

where C_f is the drag coefficient for the front face. It generally ranges in value from 0.8 to 1.5 and may be taken as 1.2, [126]. The values t_i' and t_i shown in Figure 3-6 are evaluated as the ficticious durations of the dynamic pressure and the incident overpressure, respectively. The rise time, t_{rf} to the peak pressure is small and can be generally neglected.

The loading on the rear face of an above-ground rectangular structure is shown in Figure 3-7. No pressure is transmitted to the rear face until the shock front reaches that face. Using the same time reference as for the front face, average pressure begins to build up on the back face at a time equal to the length of the structure (L) in the direction of the shock propagation divided by the velocity of shock propagation. At some time after the rear face has become completely engulfed in the blast, the pressure reaches a maximum value equal to the side-on overpressure

reduced by an amount equal to the drag pressure, which acts as a suction on the rear surface. The time needed for the pressure build up on the rear face is expressed [126] as

$$t_{rb} = \frac{L + 5\ S}{U_s} \qquad (3\text{-}48)$$

The drag coefficient for the rear surface C_r generally decreases from about 0.5 for low pressures to less than 0.3 for high pressures and may be taken as 0.4 for most purposes [126]. The net transverse loading on the structure as a whole is the difference between the front and rear face loadings. Care must be taken to subtract the pressure values at the time ordinates of the loading histories.

As the blast wave passes over the structure, the roof loading at any time is equal to the incident overpressure reduced by a negative drag pressure or suction associated with the flow of air around the structure. The average roof loading is idealized as a triangular load [122, 126] with time rise given by

$$t_{rr} = t_{rf} + \frac{L}{U} \qquad (3\text{-}49)$$

The peak value of the pressure is expressed as [122, 126] as

$$P = P_s - C_t\ P_d \qquad (3\text{-}50)$$

and the duration of the equivalent pulse is equal to

$$t_{ds} = t_{rr} + t_i \qquad (3\text{-}51)$$

The drag coefficient for the roof C_t is assumed to be the same as that of the rear face of the structure.

For situations where the front and rear of a structure are separated by a length sufficiently large so that it represents an appreciable scaled distance, the blast waves at the front and the rear may differ with regard to their basic characteristics. In this case, separate loading-time

histories are computed for the front and rear faces.

3.4 AIRBLAST LOADING DUE TO THE INTERNAL EXPLOSIONS AND CONTACT BLAST

Explosions which occur within structures normally develop a very complex pressure-time history at any position inside the structure. Although this complex loading cannot be predicted exactly, approximations and model relationships have been developed [115, 122] which can be used to define blast loads with a degree of confidence.

3.4.1 EFFECTS OF CONFINEMENT AND VENTING

The loading from an explosive charge detonated within a vented or unvented structure consists of two essentially distinct phases [115, 128], Figure 3-8. The first phase is a dynamic pressure from the initial and reflected shock waves. This consists of an initial high pressure (free-air pressure), short duration reflected wave, plus perhaps several reflected pulses arriving later at times closely approximated by twice the average time of arrival of first pulse at the structure walls. These later pulses are usually attenuated in amplitude because of an irreversible thermo-dynamic process and are very complex in waveforms as a result of the nature of the reflection process within the structure whether vented or unvented. The second loading phase is a quasi-static gas pressure pulse associated with the accumulation of the gaseous products and temperature of the chemical process involved in the explosion. The gas pressure build up will not begin until sometime after the onset of the shock pressures. Furthermore, it takes a finite length of time after the onset of gas pressure to reach its maximum value. However, these rise times are very small and for analysis purposes, the time rise is treated as instantaneous [115, 122, 128]. The amplitude of the quasi-static gas pressure depends on the specific energy and the weight of the high explosive as well as the volume of the confinement. Typically for the confined explosion, the

gas pressure will remain after the dissipation of the reflected shock waves. Depending on the degree of confinement, the confined effects of these pressures may cause severe damage to the structure unless it is designed to sustain the effects of internal pressures. Provisions for explosion venting will reduce the magnitude and duration of the applied pressures. The use of structuures with one or more surfaces either sufficiently fragile or open to the atmosphere will provide some degree of venting depending on the opening size. The fragile elements of structure fail and thus reduce the confinement of the explosive gases and hence the amplification of the shock pressures.

Internal blast can also result from the rapid combustion of fuel dispersed within a confined volume of air. Examples include destruction of grain elevators by grain dust explosions and damage to buildings and plants as a result of leakage of flammable gases and liquids. Pressures generated in confined gas-phase explosions are not high compared with ordinary detonation pressures. However, durations can be comparatively long, perhaps of the order of seconds versus milliseconds for a conventional external blast wave. The mechanism of the propagation of the explosion reaction is considered in most cases to be of the deflagrative type [116, 144-147]. A pressure-time trace for a typical internal explosion is shown in Figure 3-9. This figure shows three distinct pressure regions [116]. First of these, indicated by (a), is an initial pressure rise that occurs at a rate set by the chemical kinetics of the combustion reaction. The high pressure region, marked by (b), occurs at the central portion of the trace where pressures are limited by heat sinks of chemical dissociation. The third region, part (c), is that of pressure decay which results from the cooling effects of confining walls, plus pressure relief effects as gases escape through leaks or vents.

3.4.2 HIGH EXPLOSIVE SOURCE

As a result of the close-in effects of the explosion and the amplification of blast pressures due to reflections within the structure, the distribution of the dynamic loads on any surface will be non-uniform with the structural surface closest to the explosion being subjected to the maximum load. In the literature, semi-empirical methods for the calculation of the previously mentioned two phases of internal loading have been proposed.

(i) Shock wave loading

The air shock loading on the interior surfaces of structure is quite complex for all real structural geometries. However, approximate loading predictions have been made [122, 128] with the aid of simplifying assumptions. First, it is assumed that the initial reflected parameters can be taken as the ideal normally reflected parameters, even for oblique reflections from the structure walls. This assumption is reasonably valid for strong shock waves up to an angle of incidence of about 40 degrees and for weak shock waves up to about 70 degrees, provided that the slant range is used as the distance from charge centre to the point of interest. The second simplifying approximation is that the incident and reflected blast pulses (P_s, P_r) are triangular with abrupt rises, i.e.

$$P_s(t) = P_s\left(1 - \frac{t}{T_s}\right), \quad 0 \le t \le T_s \qquad (3\text{-}52a)$$

$$P_s(t) = 0, \quad t \ge T_s \qquad (3.52b)$$

$$P_r(t) = P_r\left(1 - \frac{t}{T_r}\right), \quad 0 \le t \le T_r \qquad (3.53a)$$

$$P_r(t) = 0, \quad t \ge T_r \qquad (3\text{-}53b)$$

The duration of these pulses (T_s, T_r), are not the same as the actual blast wave durations, but instead are adjusted to preserve the magnitude of impulses, i.e.

$$T_s = 2\, i_s / P_s \qquad (3\text{-}54)$$

$$T_r = 2\, i_r / P_r \qquad (3\text{-}55)$$

As a third assumption, the re-reflected pressure waves after shocks are ignored in estimating blast loading because the pressures and impulses are then much lower than in the initial pulse. For more exact predictions, it is suggested [115] that the combined loads from all the successive reflected shocks could be assumed to be 1.75 times those from the initial pulse. Thus, the duration T_r calculated by equation 3-53 is to be multiplied by 1.75.

Following the above assumptions, the maxima for the initial phase of internal blast loads on a structure can be estimated from the analytical relations of the parameters relevant to normal blast wave reflection from a rigid wall for a free air burst of spherical TNT, presented earlier in section 3.3.2. The actual time history is idealized to the triangle pulse (P_r - T_r) as depicted in Figure 3-8.

(ii) Quasi-static gas pressure

When an explosion from a high explosive occurs within a confined area, gaseous products will accumulate and the temperature within the strcuture will rise, thereby forming a blast pressure whose magnitude is generally less than that of the shock pressure but whose duration is significantly longer. The magnitude of the gas pressure which eventually settles to a slowly decaying level, is a function of the volume and vent area of the structure. The smaller the venting area, the longer the duration of the pressure.

Concurrent with experimental work which preceded applications to blast resistant structures, Baker et al [128] have suggested a simplified quasi-static gas pressure form shown in Figure 3-8 in which the gas venting pressure

is assumed to follow a linear curve with zero time rise. The two parameters of interest for the construction of the quasi-static portion of the idealized loading function are, the peak quasi-static pressure, P_{qs}, and the time, t_b, at which the pressure returns to ambient. Such time is often referred to as the blow-down time [122, 128]. The maximum value for the overpressure, P_{qs}, in the gas venting phase is the pressure rise which would occur in an unvented enclosure before heat transfer effects attenuate it. From data and analyses in several references, the curve of Figure 3-10 has been shown [115, 128] to yield good predictions of P_{qs} if the quantity of explosive W and the internal volume of the structure V are known. To evaluate the duration t_b of the gas pressure, Baker et al [128] defined the following scaled quantities; the scaled initial gas pressure $\bar{P}_1$ and the scaled blow-down time, $\bar{\tau}$. These quantities are given by

$$\bar{P}_1 = \frac{P_{qs} + P_o}{P_o} \tag{3-56}$$

$$\bar{\tau} = \left(\frac{\alpha_e A_s}{V^{2/3}} \right) \left(\frac{a_o}{V^{1/3}} \right) t_b \tag{3-57}$$

in which a_o is the speed of sound at standard sea level, A_s is the internal surface area of the structure, α_e is the vent area ratio and V is the internal volume of the structure. The vent area ratio for a vented roof or wall of structure is given as

$$\alpha_e = A_v / A_w \tag{3-58}$$

where A_v and A_w are the vent area and the wall area respectively. Figure 3-11 gives the scaled duration of gas overpressure as function of scaled maximum pressure. Thus, equation 3-57 leads to the corresponding dimensional quantity as

$$t_b = \bar{\tau} \left(\frac{V}{\alpha_e A_s a_o} \right) \tag{3-59}$$

In Reference [122], the terms partially vented and fully vented are defined according to values of the scaled vent area ratio $A_v/V^{2/3}$. If this parameter is greater than 0.60, gas venting times should be less than initial shock load durations, and the structure is fully vented, i.e. gas pressure parameters can be ignored. But, if it is less than or equal to 0.60, the structure is partially vented, and gas pressure parameters must be considered. Figures 3-10 and 3-11 give upper limit predictions compared with the data represented in several graphs of Reference [122].

3.4.3 COMBUSTIBLE GAS OR DUST MIXTURES WITH AIR

Accidental explosions within structures are much more likely to occur with combustible gases or dust suspended in air. As a result, there is a large volume of literature dealing with internal gaseous [144-153] and dust explosions [135, 154-157] and the effects of venting on pressures generated. Parameters assumed to be important in these studies are geometric ones such as shape and volume of the enclosure, the vent area, heat of combustion of the dust or gaseous fuel and the ratio of the actual fuel supply to that of idealized combustion. These parameters determine the maximum pressure P_m, maximum rate of pressure rise $\dot{P}_c$ and the rate of pressure relief by venting, $\dot{P}_{ve}$, which in turn are employed to establish the pressure-time curve according to the explosion mechanism described earlier in section 3.4.1.

A variety of relationships have been derived [144, 148] to predict maximum internal pressure rise P_m that can be generated by the ignition of a gas-air mixture in a vented enclosure. Rasbash [149, 150] has correlated the results of various workers and from studies conducted on small enclosures [149], derived the empirical equation

$$P_m = A_{gas} P_v + B_{gas} K_g \qquad (3\text{-}60)$$

where P_v is the pressure at which the vent is created, K_g is the ratio of the smallest cross-sectional area of the enclosure in which the explosion occurs to the area of vent, A_{gas} and B_{gas} are constants given as 1.2 kN/m^2 and 2.8 kN/m^2 for natural gas and about 3 times these values for town gas [144]. The limitations of equation 3-60 are listed as

1 - The ratio of maximum and minimum dimensions of the enclosure is less than 3.

2 - The vent area factor K_g is between 1 - 5.

3 - The weight of the covering on the vent does not exceed 24 kg/m^2.

4 - The pressure P_v does not exceed 7 kN/m^2.

On the basis of tests carried out by the Dutch Institute, TNO, Dragosavic [152] has derived the maximum internal pressure as the greater of the following two values

$$P_m = A_{gas} P_V + \frac{B_{gas}}{\psi^2} + C_{gas} \qquad (3\text{-}61a)$$

$$P_m = P_v + C_{gas} \qquad (3\text{-}61b)$$

where

$$\psi = A_v/V \qquad (3\text{-}61c)$$

The suggested values of the constants A_{gas}, B_{gas}, C_{gas} for natural gas are 0.5, 0.4 kN/m^2 and 3.0 kN/m^2 respectively.

For dust explosions, the following semi-empirical relationship has been given [154] for calculating the maximum pressure as

$$P_m = P_o + \frac{C_{dust}}{P_{ad}^3} \left[\frac{V_c}{A_v} \left(\frac{dP}{dt} \right)_{max} \right] \qquad (3\text{-}62)$$

where $\left(\frac{dP}{dt}\right)_{max}$ is the maximum rate of pressure rise, P_{ad} is

the theoretical limiting adiabatic pressure, and V_c is the volume of enclosure. The constant C_{dust} is an empirical constant which depends on the ratio of specific heat of dust and the density of unburnt dust suspension at ambient condition. The maximum rate of pressure rise can be evaluated [156] from

$$\left(\frac{dP}{dt}\right)_{max} V_c^{1/3} = K_g \qquad (3\text{-}63)$$

The flame front travels a considerable distance from the point of ignition before most of the fuel or dust is burnt out. The rate at which the combustible material becomes engulfed is proportional to the internal surface area of the confining volume. Furthermore, pressure increase is inversely proportional to this volume. These considerations provide the following expression for the rate of pressure rise, $\dot{P}_c$, in a confined explosion [116] as

$$\dot{P}_c = C_p \left(\frac{S_c}{V_c} \right) \left(P - P_{ind} \right) \left(P_{ad} - P_{abs} \right) \qquad (3\text{-}64)$$

where C_p is a coefficient, S_c is the total internal surface area of confining volume V_c, and P_{ind} is the induction pressure ($\cong$ 0.92 the initial pressure). The coefficient of pressure rise rate has been defined [116] in terms of flame front laminar burning velocity U_f (m/sec)

$$C_r = 30\ U_f \qquad (3\text{-}65)$$

By considering the second law of thermodynamics, the rate of pressure relief due to vents of gases retained within a volume V_c, is suggested [116] as

$$\dot{P}_{ve} = -375 \left(\frac{A_v}{V_c} \right) P_{abs} \quad \text{for } P > 1.75 \text{ bars} \qquad (3\text{-}66a)$$

$$\dot{P}_{ve} = -875 \left(\frac{A_v}{V_c} \right) \left(P_{abs} - P_o \right) \quad \text{for } P < 1.75 \text{ bars} \tag{3-66b}$$

in which P_{abs} is the absolute pressure at a given time.

There is still a considerable amount of research to be done to enable a reasonable prediction of the loading function for gas and dust cloud explosions. For gaseous deflagrations, it has been suggested [144, 145] that the pressure-time history can be represented by a triangular pulse of time rise of 0.1 - 0.15 seconds, a duration of 0.3 second and a peak pressure of 25 - 50 $kN/m9^2$. For design purposes, a value of 34 kN/m^2 uniformly applied pressure has been recommended [158]. A more realistic estimate for the maximum pressure, based on the volume of closure, vent area, and relief pressure P_v, has been given in Reference [135].

3.4.4 CONTACT BLAST

A contact blast is the loading that arises from the explosion of a conventional weapon either directly on or in the near vicinity of a structure. In free air, the region of contact blast corresponds to a proximity factor of less than 0.4 $m/kg^{1/3}$. The blast loading, P_s, on a concrete slab is defined [134] as a function of the concrete cube strength as

$$P_s = 8000 \, \sigma'_{ch} \quad kN/m^2 \tag{3-67}$$

where σ'_{ch} is the characteristic cube strength of concrete in N/mm^2. This loading is assumed to apply over a circular area of radius r_b given [134] in metres by

$$r_b = 1.08 \left(W/\sigma'_{ch} \right)^{1/3} \tag{3-68}$$

in which W is the equivalent charge weight measured in kilograms of TNT.

In addition to considering the loading of a contact explosion, local effects need to be considered. The thickness of the structural member will be generally determined by consideration of blast local effects. A weapon striking or exploding against the external face of a concrete slab results in compressive stresses on the external face sufficiently large to cause plastic flow and cratering of the surface. The resulting compressive shock wave in concrete travels to the interior face of the slab where it is reflected with a change of sign. This means that the compressive stresses are converted to tensile stresses. As the tensile strength of concrete is much less than its compressive strength, tensile fracturing on the interior face of the slab occurs with the result that spalling of concrete occurs at the interior of the structure with concrete particles being projected at considerable velocities.

The compressive plastic deformation of the slab under blast loading may be sufficiently large and rapid to cause lumps of concrete to ditch from the interior slab face in a similar way to spalling. This effect is termed [122, 134] as scabbing. To ensure that spalling is either limited or prevented, Reference [134] makes recommendations for the minimum thickness of concrete slab as follows:

a) thickness to resist spalling $0.32\ W^{1/3}$ metres

b) thickness at which slight spalling occurs $0.27\ W^{1/3}$ metres

c) thickness at which heavy damage occurs $0.23\ W^{1/3}$ metres

Frequently, metal spall plates are attached to the interior face of a concrete slab to prevent spall being projected into the interior. In this case the slab thickness used may be in the range of thickness from slight spalling to heavy damage.

3.5 MODELLING OF GROUND SHOCK LOADS

When an explosion occurs at or near the ground surface, ground shock results from the energy imparted to the ground by the explosion and transmitted through the air and the ground [120-122] to the point of interest. Air-induced ground shock results when the airblast shock wave compresses the ground surface and sends a stress pulse into the underlying media. The magnitude and duration of the stress pulse in the ground depends on the character of the airblast pulse and the ground media. Generally, the air-induced ground motions are maximum at the ground surface and attenuate with depth [120, 121]. Direct ground shock results from the explosive energy being transmitted directly through the ground. This motion includes both the true explosion-induced motion and cratering-induced motion. The resulting motions have a longer duration than the air-induced ground shock and the waveform tends to be sinusoidal.

The prediction methods found in the literature combine nuclear and high explosive test data with relationships from theoretical studies. The main assumption cited in these methods is the free-field ground shock phenomenon [120-122]. The complicated interaction of ground stress curves with the structure is not included.

3.5.1 AIRBLAST-INDUCED GROUND SHOCK

The prediction of actual ground motion is quite complicated. However, conservative results to estimate airblast-induced ground shock from nuclear explosion were presented by Newmark [124] based on one-dimensional wave propagation theory and experimental data. The same approach has been adopted [122] for conventional high explosives. The peak displacements, velocity and acceleration are found in terms of overpressure, charge yield, rise time and the density and seismic velocity of the soil. Since the range of seismic velocities of soils is so large it is recommended that the

lower bound value of the velocity be used to produce a conservative estimate of the induced motion.

For a surface structure located on ground media having uniform properties, the maximum vertical velocity at the ground surface, V_v, can be expressed [122, 124] in terms of the peak overpressure at the point of interest as

$$V_v = \frac{P_s}{\rho_p C_p} \tag{3-69}$$

where ρ_p and C_p are, respectively, mass density of the soil and the compression wave seismic velocity of the soil. The impedance ($\rho_p C_p$) in equation 3-69 is approximately 6.67×10^5 kg/m^2 sec. The following relationship applies for the mean value [121]

$$V_v = 1.5 P_s \text{ m/sec} \tag{3-70}$$

in which P_s is given in MegaPascals.

The maximum airblast-induced vertical displacement near the earth's surface is obtained by integrating equation 3-70 with respect to time [122, 124]. The time integral of the overpressure is simply the total positive phase impulse per unit area so that

$$D_v = \frac{i_s}{\rho_p C_p} \tag{3-71a}$$

$$\text{or} \quad D_v = \frac{0.5 P_s t_i}{\rho_p C_p} \tag{3-71b}$$

To consider the effect of soil layering, an empirical relation [121] is established to calculate D_v in metres as

$$D_v = 0.09 \ W^{1/6} \ (H/50)^{0.6} \ P_s^{2/3} \tag{3-72}$$

in which W is the explosion yield in Megaton and H is the

depth of the reflecting soil layer in metres.

The peak vertical acceleration is a function of the shape and duration of the rise curve to the peak velocity. Based on the assumption of a linear rise of surface pressure and particle velocity [122, 124], the maximum vertical acceleration A_{vr}, can be expressed as

$$A_{vr} = V_v / t_v \qquad (3\text{-}73)$$

where t_v is the rise time to the peak velocity. At the surface this is equal to the rise time of the airblast. It is suggested [122] that an airblast rise time of 0.001 sec can be used and the results are increased by about 20% to account for nonlinearity of the rise. In terms of peak overpressure, the mean value of the peak vertical acceleration induced by airblast [121] is

$$A_{vr} = 150\ P_s\ g \qquad (3\text{-}74)$$

in which P_s is in MegaPascals and g is acceleration due to gravity.

The maximum horizontal ground motins are expressed in terms of the maximum vertical motions, the seismic velocity of soil and the shock wave velocity [122, 124], so that

$$D_H = D_v \tan \left[\sin^{-1} \left(C_p / U_s \right) \right] \qquad (3\text{-}75)$$

$$V_H = V_v \tan \left[\sin^{-1} \left(C_p / U_s \right) \right] \qquad (3\text{-}76)$$

$$A_H = A_{vr} \tan \left[\sin^{-1} \left(C_p / U_s \right) \right] \qquad (3\text{-}77)$$

For (C_p / U_s) greater than unity, it is recommended [121, 122, 124] that the horizontal motion be set equal to the calculated vertical motion. The mean value of the horizontal velocity [121] is expressed in terms of the peak

overpressure (in MegaPascals) as

$$V_H = 10 \sqrt{\frac{P_s}{\rho_s}} \qquad (3\text{-}78)$$

3.5.2 DIRECTLY TRANSMITTED GROUND MOTION

Present knowledge of directly transmitted earth shock is substantially less extensive than that of induced effects. Empirical equations have been developed to predict the resulting ground motion [121, 122, 124]. The equations apply for TNT detonations at or near ground surface where the ground shock parameters are expressed in terms of the charge weight, the ground range and the scaled distance from the explosion. The maximum vertical displacment, d_v, and the horizontal components, d_h, of the ground surface are given as

$$d_v = \frac{0.025\ R^{1/3}\ W^{1/3}}{Z^{1.3}} \quad \text{for rock} \qquad (3\text{-}79a)$$

$$d_v = \frac{0.17\ R^{1/3}\ W^{1/3}}{Z^{2.3}} \quad \text{for soil} \qquad (3\text{-}79b)$$

$$d_h = 0.5\ d_v \quad \text{for rock} \qquad (3\text{-}80a)$$

$$d_h = d_v \quad \text{for soil} \qquad (3.80b)$$

For all ground media, the maximum vertical velocity, V_{vd}, and the maximum horizontal component, V_h, are expressed as

$$V_{vd} = \frac{150}{Z^{1.5}} \qquad (3\text{-}81)$$

$$V_h = V_{vd} \qquad (3\text{-}82)$$

Finally, the maximum acceleration components are given by

$$a_v = \frac{10000}{W^{1/8}\ Z^2} \qquad (3\text{-}82)$$

$$a_h = 0.5\, a_v \quad \text{for dry soil} \tag{3-83a}$$

$$a_h = a_v \quad \text{for rock and wet soil} \tag{3-83b}$$

3.5.3 NET GROUND SHOCK LOADS ON STRUCTURES

The net ground shock associated with an explosion is a combination of the air-induced and direct ground shock. Since the methods of analysis described in this thesis are applicable to rigid concrete structures located at some distance from an explosion, the structural motions are taken equal to ground motions in the vicinity of the structure. Similar assumptions have been made elsewhere [120, 122, 124]. The time at which the shock is felt at adjacent structures and the magnitude and duration of the motion is a function of the quantity of explosive detonating, the ground range and the soil media. As the air-induced ground shock is a function of the airblast, the arrival time and duration of the ground shock may be taken equal to the arrival time t_a and duration t_s of the airblast described in section 3.3. The arrival time of the direct ground shock, t_{ag}, is derived as a function of the seismic velocity of soil and the distance from the explosion [122] such that

$$t_{ag} = \frac{12000\ R}{C_p} \tag{3-84}$$

The actual duration of the direct shock load is not readily available. However, it is sufficient to realise that the duration is long, that is, many times longer than the duration of the air-induced ground shock [122].

The net ground shock is obtained from consideration of the arrival time and duration of each type of induced shock. If $(t_a + t_s)$ is less than t_{ag}, the structure is subjected to superseismic ground shock [122, 124] where the air-induced shock arrives at the structure first and is dissipated by the time the direct shock arrives. If t_a is greater than

t_{ag}, the structure is subjected to an overtaking ground shock. The direct induced ground shock arrives at the structure first, and since its duration is long, the air-induced ground shock will arrive at the structure while the directly transmitted shock is still acting. The structure receives the combined effects of the induced shock. If t_a is slightly less than t_{ag} and $(t_a + t_s)$ is greater than t_{ag}, the combined induced ground shocks have to be considered. In practice, the effect due to directly transmitted ground motion is negligible compared to air-induced earth motion due to the fact that soil is not able to transmit high frequency motion [159].

3.6 MODELLING CONSIDERATIONS OF BLAST LOADS FOR NONLINEAR DYNAMIC ANALYSIS

The procedure presented in this chapter for the numerical modelling of blast loads caused by different sources of explosions, is applicable to above-ground structures. The shock loads and the resulting structural motions apply to rigid concrete structures positioned in the near and remote regions of the explosion source. At distances corresponding to the pressure ranges resulting from these conditions, the shock loads are uniform across the structure. The response of structures located at comparatively close distances to an explosion that is, contact blast, as well as the motion of non-rigid structures may be determined. However, the local effects associated with these conditions such as motions due to cratering and fragment impact must be accounted for in the determination of structural response. For the purpose of this thesis, the blast effects are most conveniently represented as a loading-time history that is applied to the elements of a structure as transient loading. The way a blast load affects the structure depends not only upon its duration but upon its rise time and general shape as well. The load can be classified as impulsive, dynamic or quasi-static relative to a specific structural component. If the period of the fundamental vibration of the component

is very short compared with the load duration, the load may be quasi-static. If the period of vibration is long, then the load may be impulsive for that component. The intermediate region between impulsive and quasi-static, where the periods are about the same as loading time, is considered as dynamic. For most concrete structures, blast effects are idealized as impulsive or dynamic loading.

From reviewing the available unclassified literature, it is concluded that precise loading information is hard to obtain and may not be justified because of the many uncertainties involved in the interaction process between the blast wave and the structure, the soil-structure interaction, the ideal gas assumption in the derivation of governing relations, and the venting process in case of internal explosions. Idealized representations of time history of shock loads are based on a linear approximation.

For nonlinear dynamic analysis of blast-loaded structures, two distinct types of shock loads, air shock and ground shock, have to be considered. $P_{as}(t)$ is the blast load due to air shock which acts on the structural system. $U_g(t)$, $\dot{U}_g(t)$ and $\ddot{U}_g(t)$ are the displacements, velocities and accelerations induced by the ground shock at the base of the corresponding values of the structure. Thus, the total displacements, velocities and accelerations of the structure with respect to a stationary point $\{U_t(t), \dot{U}_t(t), \ddot{U}_t(t)\}$ are expressed in terms of the structure relative to the ground $\{U(t), \dot{U}(t), \ddot{U}(t)\}$, and the explosion-induced ground components as

$$\begin{aligned} U_t(t) &= U(t) + U_g(t) \\ \dot{U}_t(t) &= \dot{U}(t) + \dot{U}_g(t) \\ \ddot{U}_t(t) &= \ddot{U}(t) + \ddot{U}_g(t) \end{aligned} \tag{3-85}$$

Also, if $P_{tot}(t)$ is the total applied load, then

$$P_{tot}(t) = P_{as}(t) - m \ddot{U}_g(t) \qquad (3\text{-}86)$$

in which m is the mass of the structure and $m \ddot{U}_g(t)$ is the inertial force due to the ground shock. All of these loads may act independently or they may occur in combination, depending upon the nature of the exploding material and the position of the structure relative to the explosion. For predicting the maximum structural response, the following features have to be considered in the modelling of these loads on above-ground reinforced concrete structures:

1 - The types of loads that can be produced on a structure by an external explosion are

* Side-on overpressure produced by incident shock wave.
* Reflected overpressure on surfaces located normal to the direction of wave propagation.
* Dynamic pressure caused by the wind behind the wave front.
* Direct and airblast-induced ground shocks.

The procedures for the calculation and distribution of these loads are explained in section 3.3 and section 3.5.

2 - The internal loads that can be caused by a confined explosion are

* Shock wave loading (for high explosives).
* Quasi-static gas venting pressure.

The numerical modelling of such loads is explained in section 3.4 which also discusses briefly the loading due to contact blast.

3 - For external explosions caused by nuclear weapons and high explosives, the most severe loading case is due to the combined effects of air shock and airblast-induced ground

shock. Being caused by the same source, namely airblast, these dynamic excitations are treated to be in phase.

4 - Since the vertical motion of a concrete structure is restricted by the ground which is already compressed due to the dead load of the structure and its contents, explosion induced vertical ground motion must necessarily be small and can be safely neglected.

5 - Given the expected difference in the time arrival of the various shocks to the structures, the direct ground shock can usually be ignored.

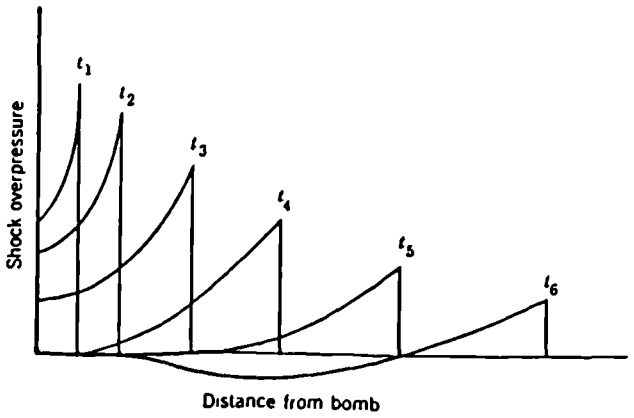

Figure 3.1 Variation of overpressure with distance from centre of explosion at various times [119]

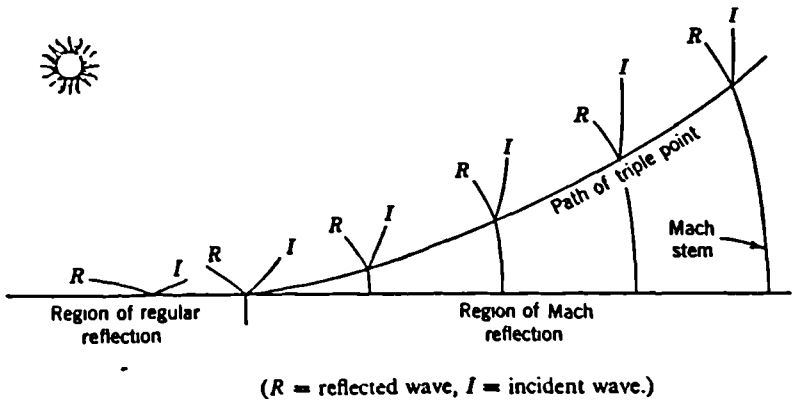

Figure 3.2 Shock wave reflection phenomena [119]

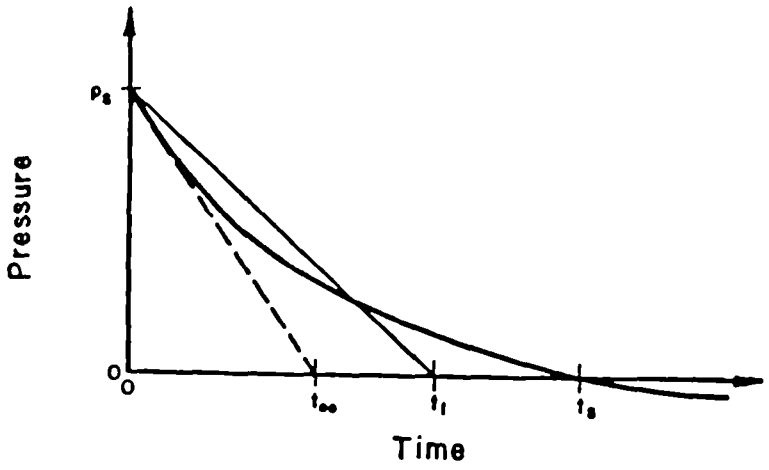

Figure 3.3 Blast wave load-time curve representations [126]

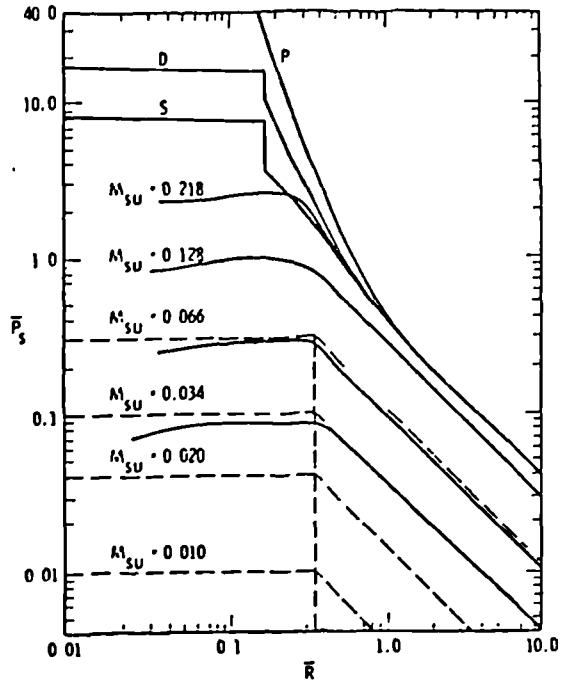

Figure 3.4 Maximum wave overpressure versus energy - scaled distance for deflagrative explosions [115]

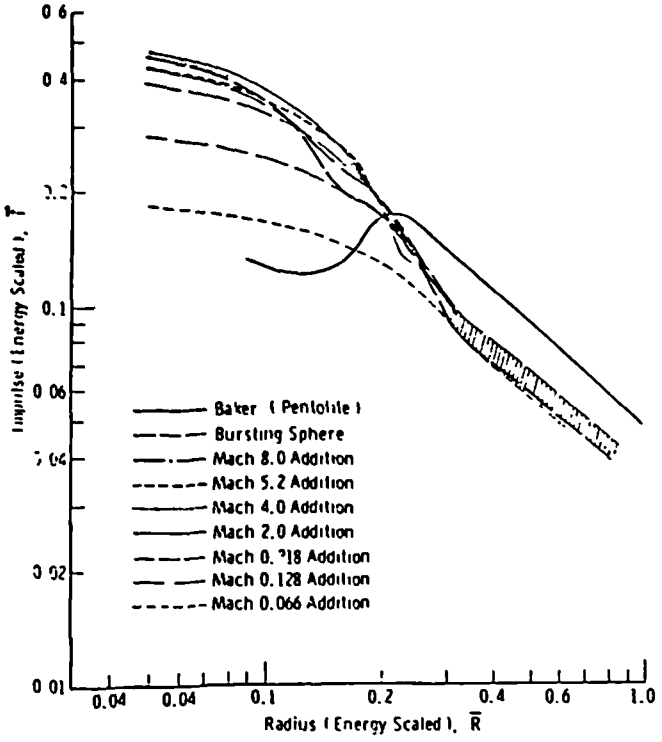

Figure 3.5 Energy-scaled impulse versus energy-scaled radius for deflagration explosions [115]

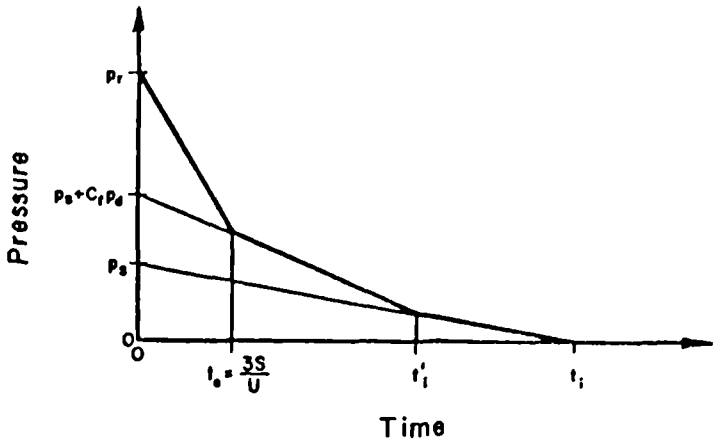

Figure 3.6 Pressure on front face of structure [126]

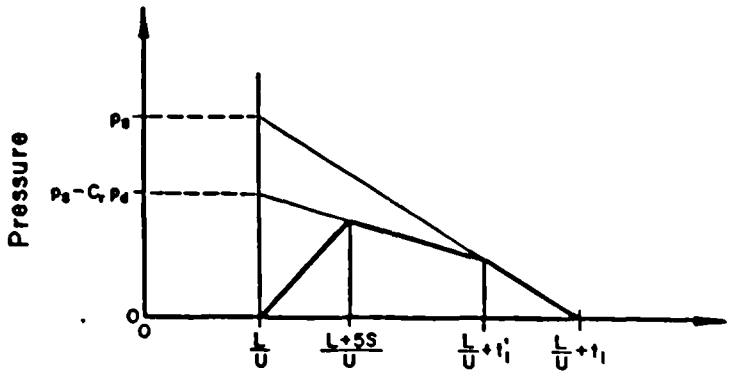

Figure 3.7 Pressure on rear face of structure [126]

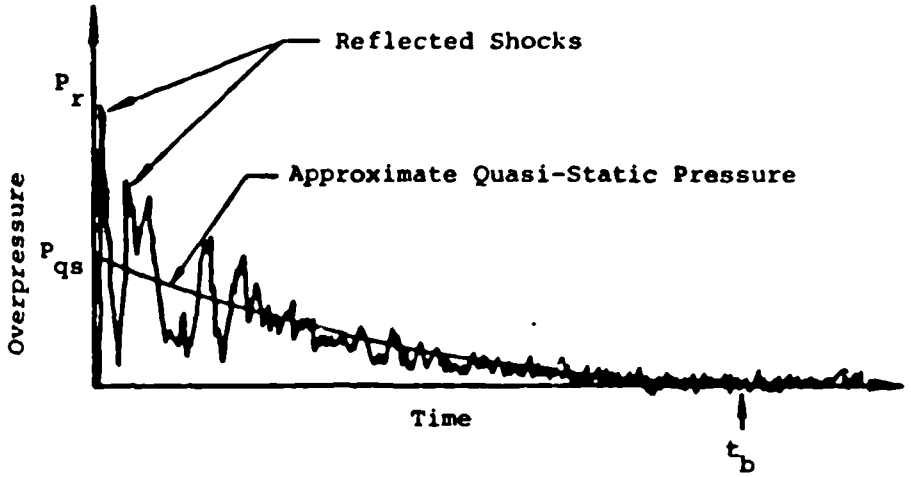

a. Typical Actual Pressure-Time History (Electronically Filtered)

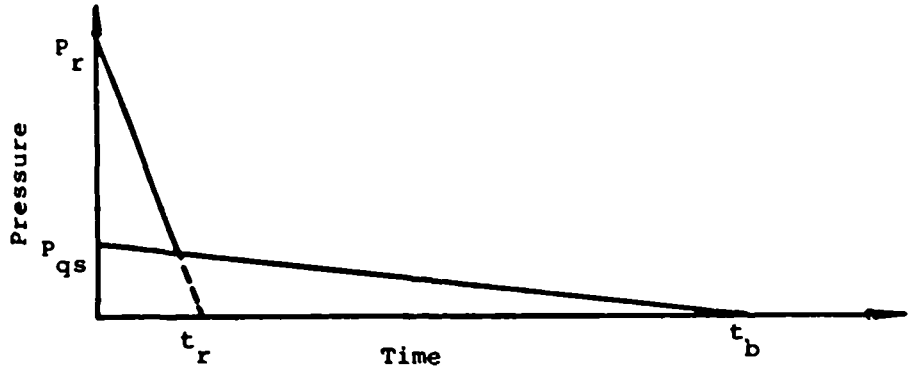

b. Idealized Pressure-Time History

Figure 3.8 Internal pressure loading at inner surface of a structure [128]

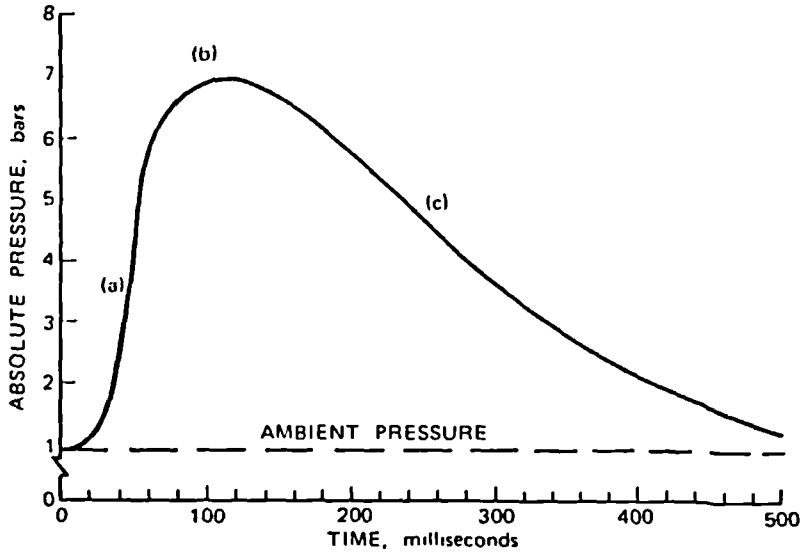

Figure 3.9 Pressure-time trace for a typical internal deflagrative explosion [116]

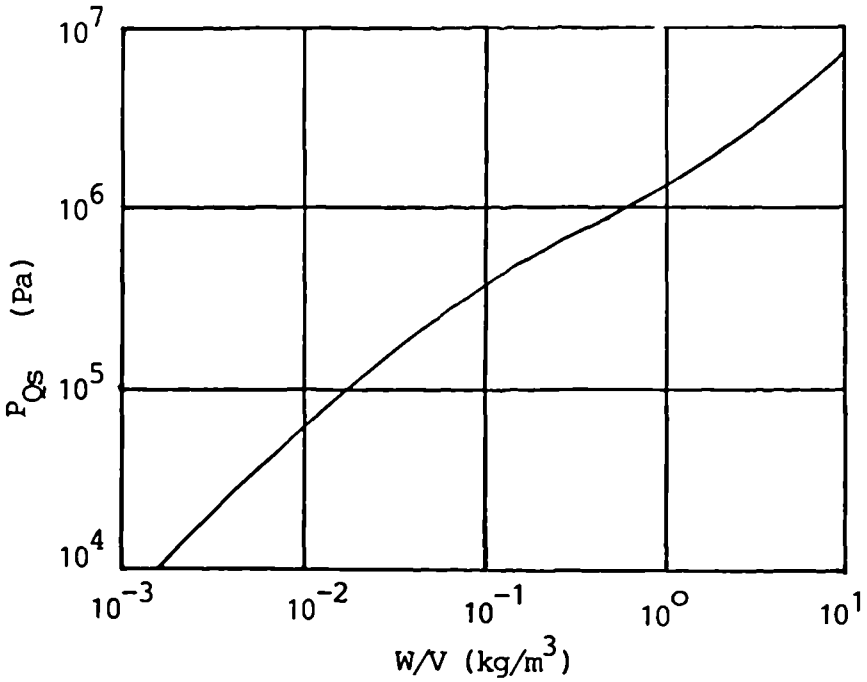

Figure 3.10 Peak quasi-static pressure for TNT explosion in a structure [115]

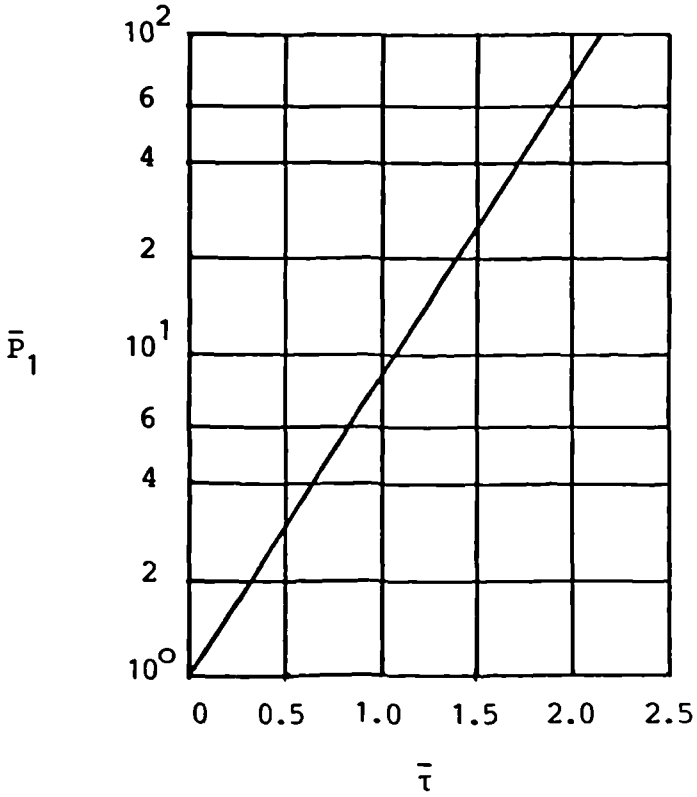

Figure 3.11 Scaled blowdown duration versus scaled maximum pressure for TNT explosion in structure [115]

CHAPTER 4

FINITE ELEMENT FORMULATION OF REINFORCED CONCRETE STRUCTURES SUBJECTED TO BLAST LOADING

4.1 INTRODUCTION

The finite element method, FEM, which was developed during the mid-fifties, is certainly the most widespread numerical method and is very well established in research and engineering applications. The method is extensively studied and described in many textbooks [112, 160-163] and numerous publications. Application of the method to reinforced concrete beams was first reported in 1967 by Ngo and Scordelis [6]. Since then, the FEM has been recognised as a most powerful and widely used approach for linear or nonlinear static and dynamic analysis of reinforced concrete structures, which may possess arbitrary geometry, loading and support conditions, irregular stiffening and many other aspects of practical design. Comprehensive state of the art reviews can be found in [98, 109, 164, 165].

The complexity of blast loading as a transient and impulsive loading and its combination to the various material nonlinearities of concrete and steel necessitate the use of finite element in the analysis of blast resistant and protective structures. This approach enables the response of various reinforced concrete structures to be more accurately modelled and the internal structural action to be more clearly understood.

The objective of this chapter is to introduce the finite element formulations necessary for the spatial discretization of the transient dynamic equilibrium equations of plane and axisymmetric reinforced concrete structures subjected to blast loading.

The basic finite element discretization process in dynamic analysis is summarized in Section 4.2. The formulation of

isoparametric element characteristics and the associated numerical integrations are discussed in Section 4.3. The computational modelling of the mass and damping matrices are studied in Sections 4.4 and 4.5 respectively. In Section 4.6, the modelling of steel reinforcements is described. In the final section of this chapter, the significance of some FE procedural factors in the prediction of concrete structural behaviour is given.

4.2 FINITE ELEMENT DISCRETIZATION OF DYNAMIC EQUILIBRIUM EQUATIONS

4.2.1 VIRTUAL WORK ANALYSIS

Consider the motion of a body V subjected to simultaneous airblast loading and airblast induced ground excitations $\ddot{U}_g$ for which the internal stresses σ are in equilibrium with the surface tractions t acting on the portion Γ_t of the boundary Γ and volumetric forces Z that include body, inertial and damping contributions.

According to the principle of virtual work, if the body in equilibrium is subjected to any virtual consistent displacements δu, then the virtual work done by internal forces must equal that done by the external forces irrespective of material behaviour. Noting that

$$Z = b - C\,\dot{u} - \rho\,(\dot{u}^{\cdot} + \dot{u}_g^{\cdot}) \qquad (4\text{-}1)$$

where b, $\rho\,(\dot{u}^{\cdot} + \dot{u}_g^{\cdot})$, $C\,\dot{u}$ are the body, inertial and damping forces, respectively, with ρ the mass density, C the damping parameter and dots denoting the time differentation, we may therefore write

$$\int_v (\delta\varepsilon)^T \sigma\, dv = \int_v (\delta u)^T [b - \rho(\dot{u}^{\cdot} + \dot{u}_g^{\cdot}) - c\dot{u}]\, dv + \int_{\Gamma_t} (\delta u)^T t\, d\Gamma \qquad (4\text{-}2)$$

where $\delta\varepsilon$ is the virtual strain vector associated with δu.

4.2.2 FINITE ELEMENT SPATIAL DISCRETIZATION

In order to obtain a solution of the differential equation (4-2), discretization has to be performed. The spatial discretization of continuum problems by the finite element method is employed here for representation of concrete structures. A brief outline only is given, noting that the discrete equations are presented in matrix and vector form as this is the more suitable form of notation for the finite element discretization.

Following the standard finite element procedure [160], the spatial domain V is divided into a finite number of m arbitrary sub-domains, V_e, finite elements which are connected at n nodal points. The isoparametric elements [112, 160-162, 166-168] which have been applied to many practical problems, are used throughout this work. A single set of functions is employed to interpolate the geometry and the field variables inside each element from the respective set of nodal values. These shape functions are defined in a normalized coordinate system onto which the real or distorted element is mapped. Thus, the displacements, velocities and accelerations u, $\dot{u}$, $\dot{u}^*$, $\dot{u}^*_g$ can be expressed in terms of their nodal values d, $\dot{d}$, $\ddot{d}$, $\ddot{d}_g$ by

$$u = \sum_{i=1}^{n} N_i(\xi,\eta)\, d_i = N\, d \qquad (4\text{-}3a)$$

$$\dot{u} = \sum_{i=1}^{n} N_i(\xi,\eta)\, \dot{d}_i = N\, \dot{d} \qquad (4\text{-}3b)$$

$$\dot{u}^* = \sum_{i=1}^{n} N_i(\xi,\eta)\, \ddot{d}_i = N\, \ddot{d} \qquad (4\text{-}3c)$$

$$\dot{u}^*_g = \sum_{i=1}^{n} N_i(\xi,\eta)\, (\ddot{d}_g)_i = N\, \ddot{d}_g \qquad (4\text{-}4c)$$

in which N_i (ξ,η) is the global shape functions matrix composed of submatrices N_i^e $(\xi, \eta) = N_i$ I, with I being a r×r identity matrix and r, the number of variables per node, is 2 for plane and axisymmetric problems. With the element strain displacement matrix B, we may relate the virtual strain vector to the nodal variables as,

$$\delta\varepsilon = \sum_{i=1}^{n} B_i \delta d_i = B\ \delta d \qquad (4\text{-}4)$$

4.2.3 DYNAMIC EQUILIBRIUM EQUATIONS IN SEMI-DISCRETE FORM

Substituting equations 4-3 and 4-4 into equation 4-2 and rearranging, we obtain

$$\delta d^T [M \ddot{d} + C \dot{d} + P(d)] = \delta d^T [F - M \ddot{d}_g] \qquad (4\text{-}5)$$

in which M is the global mass matrix, C denotes the global damping matrix, P(d) is the global internal resisting force vector and F is the externally applied airblast load vector. The terms in equation 4-5 are separately evaluated from each element. Summing the contributions from all elements, the characteristic matrices and vectors of equation 4-5 can be expressed as

$$M = \sum_{e=1}^{m} M^e = \int_{V_e} (N^e)^T \rho\ N^e\ dv \qquad (4\text{-}6a)$$

$$C = \sum_{e=1}^{m} C^e = \int_{V_c} (N^e)^T\ C\ N^e\ dv \qquad (4\text{-}6b)$$

$$P = \sum_{e=1}^{m} P^e = \int_{V_e} B^T \sigma\ dv \qquad (4\text{-}6c)$$

$$F = \sum_{e=1}^{m} F^e = \int_{\Gamma_e} (N^e)^T\ t\ d\Gamma + \int_{V_e} (N^e)^T\ b\ dv \qquad (4\text{-}6d)$$

where Γ_e and V_e denote the surface and volume of the element under consideration. By invoking the arbitrariness of the virtual displacements δd, a resulting system of governing

equations for dynamic problems is established as

$$M \ddot{d} + C \dot{d} + P(d) = F - M \ddot{d}_g \qquad (4\text{-}7)$$

For linear elastic situations, the stresses σ are related to the strains ε by

$$\sigma = D \varepsilon = D B d$$

with the stress-strain matrix D, the dynamic equilbrium equations can be rewritten as

$$M \ddot{d} + C \dot{d} + K d = F - M \ddot{d}_g \qquad (4\text{-}8)$$

where

$$K = \sum_{e=1}^{n} K_e = \sum_{e=1}^{n} \int_{V_e} B^T D B \, dv \qquad (4\text{-}9)$$

is the global stiffness and K_e is the element constribution in this matrix. The form of equation (4-7) has been used throughout this thesis as it is especially convenient for temporal discretization using explicit stepping procedure (Chapter 6), where the global stiffness matrix K need not be assembled.

4.3 ISOPARAMETRIC ELEMENTS: FORMULATION AND NUMERICAL INTEGRATION

Two isoparametric element families have been extensively used - Lagrangian and Serendipidity families [160]. The difference between them is based on the choice of shape function. In this thesis, the 8-node biquadratic Serendipity element has been adopted for plane problems. It is the commonly used element for static and dynamic analysis of two dimensional concrete structures. Providing that the blast loading and boundary conditions in an axisymmetric solid do not vary in circumferential direction, the solution is independent of the circumferential coordinates, θ. Under these conditions, this three dimensional configuration reduces to a two dimensional problem justifying the use of the biquadratic element for the spatial discretization of

axisymmetric solids. The radial and axial coordinates designated as r and z respectively correspond to the cartesian coordinates (x, y) of plane problems.

4.3.1 FORMULATION OF ISOPARAMETRIC ELEMENT CHARACTERISTIC MATRICES AND VECTORS

For the evaluation of the integrals in equation 4-6, it is necessary to know the element geometry, element strain field, and the elemental volume. To define the geometry, typical 8-node isoparametric element shape functions are shown and listed in Figure 4-1.

To evaluate the B-matrix in equation 4-4 the relationship between the natural coordinate system (ξ, η) and the cartesian coordinates system (x, y) is defined first through the Jacobian.

$$J = \begin{bmatrix} \frac{\partial x}{\partial \xi} & \frac{\partial y}{\partial \xi} \\ \frac{\partial x}{\partial \eta} & \frac{\partial y}{\partial \eta} \end{bmatrix} = \sum_i \begin{bmatrix} \frac{\partial N_i^e}{\partial \xi} x_i & \frac{\partial N_i^e}{\partial \xi} y_i \\ \frac{\partial N_i^e}{\partial \eta} x_i & \frac{\partial N_i^e}{\partial \eta} y_i \end{bmatrix} \qquad (4\text{-}10)$$

The cartesian shape function derivatives used in the B-matrix in Table (4-1) may be obtained using the chain rule of differentation [112, 160].

The discretized elemental volume is given as

$$dV_e = t \quad \det J \quad d\xi \quad d\eta \qquad (4\text{-}11)$$

in which detJ is the determinant of the Jacobian matrix and t is the element thickness which is problem dependent as given in Table 4-1.

Finally, the integration of equation (4-6) is performed in natural coordinate system where the elements of the matrices and load vectors are evaluated numerically.

4.3.2 NUMERICAL INTEGRATION

The evaluation of isoparametric element characteristic matrices and vectors is carried out numerically [169] on the element level by the use of Gauss quadrature formulae with n×n sampling points leading to

$$\int_{v_e} F_{ij}\,(x,\ y)\ dv = \int_{-1}^{+1}\int_{-1}^{+1} F_{ij}\,(\xi,\ \eta)\quad t\quad Det J\ d\xi d\eta$$

$$= \sum_{p=1}^{n}\sum_{q=1}^{n} F_{ij}\,(\xi_p,\ \eta_q)\quad t\ Det\ J\ W_p\ W_q \qquad (4\text{-}12)$$

in which F_{ij} is the appropriate integral and, ξ_p, η_q are the natural coordinates of the sampling points and W_p, W_q are the corresponding weighting functions.

Numerical integration provides accurate results if the integration order is adequate to evaluate exactly the element volume. An n^{th} order quadrature permits the exact integration of a polynomial of degree (2n-1) or less [160, 151, 169]. The optimum choice of the integration order is very important, not only because of the cost of analysis is increased when a higher order integration is employed, but also because the results can differ significantly depending on the order of integration rule adopted [170, 171]. For two dimensional parallelogram biquadratic elements, a 3×3 integration rule ensures exact integration.

In the literature, three commonly used integration schemes are found namely full, selective and reduced schemes. The name full stands for the exact integration order. The selective integration scheme is based on a different integration order for different strain components [172, 173]. The reduced integration scheme [174, 175] uses an integration order which is one order lower than that required for full integration for all strain terms. The corresponding reduced quadrature order for biquadratic

elements is 2×2. As already known, there are basically two reasons for reducing the integration order: firstly, a lower integration order softens the element, i.e. improving its performance, and secondly, it reduces the cost of analysis. However, the use of reduced quadrature scheme may result in a certain stressless deformation mode which - if excited - can completely destroy the solution. These modes are called Kinematic or zero energy modes [175].

The conclusion of the excellent study in [175] which is based on the examination of the stiffness, mass and natural frequency modelling characteristics of the isoparametric family is that the reduced integration can safely be applied for the evaluation of the stiffness matrix of the biquadratic Serendipity element while the full inetgration scheme is recommended for the mass matrix to improve the mass modelling properties of that element. Following this conclusion for the nonlinear dynamic analysis of concrete structures reported in the literature, e.g. [77, 93, 176], resulted in an excellent result and more economic analysis. Thus, for the present analysis, the 3×3 integration rule is adopted for the evaluation of the element mass matrix while the load vectors are numerically integrated by 2×2 integration scheme.

4.4 MODELLING OF MASS MATRIX

In the context of finite element, the mass matrices are either consistent or lumped matrices according to the time integration scheme chosen for temporal discretization of the dynamic equilibrium equations (Chapter 6).

4.4.1 CONSISTENT MASS MATRIX

The term $\mathbf{M}^e$ in equation 4-6 represents an element consistent mass matrix, when the shape functions $\mathbf{N}^e$ are chosen to be the same as the ones used in the evaluation of element stiffness matrix. In general, applying the full integration to calculate the consistent mass matrix gives the correct

system of frequency [161]. This is because the actual mass distribution of the system with the consistent mass formulation is preserved and maintains consistency of the momentum energy with the strain energy in the element. However, it is a full matrix in which the off-diagonal terms yield a cross coupling between the element nodal inertia forces and lead to disadvantages in computation. Noting that the term $\mathbf{M}^e$ uses the shape functions $\mathbf{N}^e$ while the stiffness computation involves their derivatives B, it is therefore evident that the consistent mass matrix provides a more accurate approximation for the structural inertia forces than is obtained for the internal resisting forces [177].

For these reasons, the inertial properties of the mesh are often approximated by a lumped mass matrix.

4.4.2 LUMPED MASS MATRIX

In the solution of the dynamic equilibrium equations, it is generally beneficial to make the mass matrix a diagonal matrix which is crucial for explicit time stepping schemes [176]. Lumping of mass by physical reasoning is fairly straightforward for simple elements, but it is not obvious for higher order elements.

In the literature review, several lumping procedures can be found which can be divided into two main categories:

(i) Employ a set of different, lower order shape functions to form the lumped mass matrix. Clough [178] has defined physical lumping in terms of separate shape functions $\mathbf{N}_i^e$, i.e.

$$\mathbf{M}_{ij}^e = \int_{v_e} \mathbf{N}_i^e \, \rho \, \mathbf{N}_j^e \, dv \qquad (4\text{-}13)$$

where $\mathbf{N}_i^e$ are piecewise constant and non-overlapping functions, which equal to unity in the vicinity of a node and are zero elsewhere. For linear vibration problems this

mass representation ensures convergence [179]. Hinton et al [180] proposed a special mass lumping scheme where the diagonal terms of the consistent mass matrix are scaled to preserve the total mass of the element. The method has been successfully used in the context of plane elements [176, 181], Mindlin plate [182] and shell elements [34].

(ii) Using numerical integration to obtain lumping. The sampling points for numerical integration are chosen to coincide with the element nodes, thereby yielding a diagonal matrix as all except one shape function are zero at each node. Fried [183] claims no loss of convergence rate if the appropriate order of integration is selected. However, some of the mass matrix terms may be negative and this can lead to the computation of imaginary vibration frequencies [184].

Here lumped mass matrices for the 8-node isoparametric element are presented in accordnace with the special lumping scheme [180]. The diagonal mass matrix for such element can be obtained by distributing the element mass in proportion to the diagonal terms of the consistent matrix. Thus, for a typical node i, the diagonal term m_{ii} of the lumped mass matrix can be evaluated by

$$m_{ii} = \frac{M_{ii}}{\sum_{k=1}^{n} M_{kk}} M_e \qquad (4\text{-}14)$$

where M_e is the total element mass and n is the number of element nodes. Using the right substitutions, equation 4-14 can be rewritten as

$$m_{ii} = \frac{\int_{V_e} N_i^e \rho N_i^e \, dv}{\sum_{k=1}^{n} \int_{V_e} N_K^e \rho N_K^e \, dv} \int_{V_e} \rho \, dv \qquad (4\text{-}15)$$

where ρ is the mass density of concrete. This technique has

proved to be successful in the linear and nonlinear dynamic analysis of concrete structures [34, 77, 93, 176].

4.5 MODELLING OF DAMPING MATRIX

In practice it is difficult, if not impossible, to determine for general finite element assemblages the element damping parameters in particular because the damping properties are frequency dependent. For this reason, the damping matrix C is usually not constructed from the element damping matrices like the mass and stiffness of the element assemblage. In order to approximate the overall energy dissipation during a system response, a concept of modal damping [161] is used to evaluate the damping matrix, since the total damping in the structure is often assumed to be a sum of individual modal damping, which can be estimated from the known physical properties of the structure. However, the modal damping concept is not considered here as it is limited to linear dynamic analysis and the resulting damping matrix is a full matrix which is computationally inefficient for explicit time integration scheme.

Very limited information is available on damping properties of concrete structures in linear problems and there is even less data available for damping in the nonlinear situations. As a result it is assumed here that the damping matrix is proportional to the mass and stiffness matrices. This is known as Rayleigh damping [112, 161] given as

$$C = b_o M + b_1 K \tag{4-16}$$

where b_o and b_1 are damping parameters. Since the global stiffness matrix is not formed in explicit time stepping procedure, the second damping parameter must be set to zero so that

$$C = b_o M \tag{4-17}$$

where,

$$b_o = 2 \xi_r \omega_r \tag{4-18}$$

in which ξ_r and ω_r are the damping factor and the circular frequency, respectively, for the r^{th} mode. A disadvantage of Rayleigh damping is that the higher modes will be less damped than the lower ones whereas the opposite would be more desirable. However, in the analysis of structures with widely varying material properties such as concrete, the assumption of Rayleigh damping is found to be adequate. Overall energy dissipation during a system response is governed here by the proposed rate dependent viscoplasticity based material models of concrete and steel (Chapter 5).

4.6 FINITE ELEMENT MODELLING OF STEEL REINFORCEMENT

4.6.1 REINFORCEMENT REPRESENTATION

In developing a finite element model of reinforced concrete member, three alternative modelling techniques have been employed [109], namely: smeared model, embedded model and discrete model.

In the smeared model, the reinforcement is assumed to be distributed uniformly over the element [185]. Assuming perfect bond between concrete and steel, a composite concrete-reinforcement constitutive relation is used in this case [185].

The embedded model has been usually used in connection with higher order isoparametric elements [168]. The reinforcing bar is considered to be an axial member embedded in the basic concrete element such that its displacements are consistent with those of the element. Again perfect bond must be assumed.

In the discrete model, a one-dimensional bar element or beam element is superimposed on the two-dimensional concrete elements [89]. The advantage of this representation is that it can account for bond slip. However, since the element mesh patterns has to follow the location of the reinforcement, the total number of nodal points becomes

larger. Numerically it is less efficient than other models.

A major advantage of isoparametric elements is that fewer and larger elements are required to adequately simulate a particular structure than lower order elements. In order to retain this efficiency, yet incorporate reinforcement details, the embedded model has been adopted in the present work. Steel has been simulated by axial bars for plane problems, Figure 4-2a. For axisymmetry, the reinforcement in the radial direction has been idealized by a membrane with no hoop stiffness while in the hoop direction, the reinforcement has been modelled as a membrane of no stiffness in radial planes Figure 4-2b.

The geometry of such a bar lying anywhere within an element along constant local coordinate lines, Figure 4-2a is defined by using the same shape functions as the basic concrete element.

4.6.2 FORMULATION OF THE EMBEDDED REPRESENTATION OF STEEL

The global coordinates of any point p(x, y) on the embedded member as indicated in Figure 4-2a are given by

$$\mathbf{x}_p = \begin{Bmatrix} x \\ y \end{Bmatrix} = \sum_{i=1}^{8} N_i^e \left(\xi, \eta_c\right) \begin{Bmatrix} x_i \\ y_i \end{Bmatrix} = \mathbf{N}^e \mathbf{x}^e \qquad (4\text{-}19)$$

where $\mathbf{x}^e$ are the basic element nodal coordinates. As full displacement compatibility between the bar and the basic element is assumed, the displacements of the bar are obtained from the displacement field of the basic element by

$$\mathbf{d} = \sum_{i=1}^{8} N_i^e \left(\xi, \eta_c\right) \mathbf{d}_i = \mathbf{N}^e \mathbf{d}^e \qquad (4\text{-}20)$$

At point p, the strain of the bar given in the local x'-y' coordinate system is defined by only one strain component as

$$\varepsilon_p^{\backslash} = \frac{\partial u^{\backslash}}{\partial x^{\backslash}} \tag{4-21}$$

where $u^{\backslash}$, $v^{\backslash}$ are the corresponding displacements as shown in Figure 4-2a. Using appropriate transformation and observing that $x^{\backslash}$ and ξ coincide and differ only in magnitude, the local strain component can be established [168] in the following form

$$\varepsilon_p^{\backslash} = \sum_{i=1}^{8} B_i^{*} \; d_i^{e} \tag{4-22}$$

where B_i^{*} is the strain matrix of the bar element and d_i^{e} represents the vector of nodal displacements in the global coordinate system. The explicit form of the strain matrix is

$$B_i^{*} = \frac{1}{h^2} \; [A, \; B] \tag{4-23}$$

where

$$A = \left\{ c_1 \frac{\partial N_i^{e}}{\partial x} + c_2 \frac{\partial N_i^{e}}{\partial y} \right\} \tag{4-24}$$

$$B = \left\{ c_2 \frac{\partial N_i^{e}}{\partial x} + c_3 \frac{\partial N_i^{e}}{\partial y} \right\} \tag{4-25}$$

$$h = \left[\left(\frac{\partial x}{\partial \xi} \right)^2 + \left(\frac{\partial y}{\partial \xi} \right)^2 \right]^{1/2} \tag{4-26}$$

and

$$c_1 = \left(\frac{\partial x}{\partial \xi} \right)^2 , \; c_2 = \left(\frac{\partial x}{\partial \xi} \frac{\partial y}{\partial \xi} \right) , \; c_3 = \left(\frac{\partial y}{\partial \xi} \right)^2 \tag{4-27}$$

The strain defined by equation 4-22 is applicable in both plane and axisymmetric (x and y are replaced by r and z) problems. However, in the latter case there is a further strain in the circumferential direction defined by

$$\varepsilon_\theta = \frac{u}{r_p} = \frac{N^{e} \; u^{e}}{N^{e} \; r^{e}} \tag{4-28}$$

where r_p is the radius at point p. In this case, the

strain matrix can be explicitly expressed [27] as

$$B_i^s = \left[\left(N_i^e \Big/ \sum_{j=1}^{8} N_j^e \, r_j \right) , \; 0 \right] \qquad (4\text{-}29)$$

Using the stresses and the strain matrix of the bar (or membrane) element, the internal resisting force vector of the membrane is then derived in the standard way according to

$$P_s = \int_{v_s} \left(B^s \right)^T \sigma \, dv_s \qquad (4\text{-}30)$$

where dv_s is the element volume given for plane situations as

$$dv_s = A_s \; h \, d\xi \qquad (4\text{-}31)$$

and for axisymmetry

$$dv_s = 2 \, \pi \, r \, t \, h \, d\xi \qquad (4\text{-}32)$$

where A_s is the bar area and t is the thickness of a circumferential membrane.

The contribution of the reinforcement members to the lumped mass matrix of the basic concrete element is taken into consideration by employing Hinton's special lumping scheme [180]. Thus, for a typical node i, the diagonal term m_{ii}^s of the lumped mass matrix due to a bar or membrane is evaluated by

$$m_{ii}^s = \frac{\int_{v_s} N_i^e \, \rho_s \, N_i^e \, dv_s}{\sum_{k=1}^{8} \int_{V_s} N_k^e \, \rho_s \, N_k^e \, dv_s} \int_{V_s} \rho_s \, dv_s \qquad (4\text{-}33)$$

where ρ_s is the mass density of steel.

Naturally, numerical integration must be used again for

evaluating equations 4-30 and 4-33 but the integration orders are applied only in one direction.

Finally, the composite internal resisting force vector and the total lumped mass matrix are obtained from adding the reinforcement member contributions to those basic concrete elements containing it.

4.7 THE SIGNIFICANCE OF SOME FE PROCEDURAL FACTORS IN THE PREDICTION OF CONCRETE STRUCTURAL BEHAVIOUR

4.7.1 FE MESH CONFIGURATION

In finite element analysis, no mathematical rules exist which can determine in advance the size of FE mesh required to achieve a given level of accuracy. The only existing criterion is that the finer the mesh, the more accurate the numerical results. It is usually recommended to adopt a fine mesh where localized effects take place.

In analysis of reinforced concrete structures using finite elements, it has been found that the overall stiffness and predicted ultimate load decrease with the size of the element mesh. When the size of the elements decrease, the crack initiation is accelerated and the modelling exhibits greater softening in the postcracking range [78]. Furthermore, refining the mesh locally can induce size dependent influences since this intensifies the local stress field. Nonlinear effects such as corrections due to constitutive relationship and cracking can also cause deceptive effects [186] in the modelling of such localized zones. For example a localized fine mesh in the vicinity of a point load will exhibit higher compressive stresses in the direction of the loading but also a significant tensile stress orthogonal to that direction, with the possibility of inducing cracks at very early loading stages. The stress corrections due to concrete constitutive relationship in the high compressive stress zone can also manifest this mesh size dependency.

For the present analysis, the conclusions of the only comprehensive study [187] found in the literature on the significance of FE mesh configuration have been considered. These conclusions can be summarized as

(1) The element size should be the largest possible size that describes adequately the structural configuration. The lower bound limit to the size of concrete finite elements is the length of the strain gauge used to record deformations on concrete specimens i.e. 2 to 3 times the maximum aggregate size used in the concrete mix [187].

(2) The mesh-size dependency rising from the localized fine meshes can be minimized by adopting a FE mesh configuration, which is as regular as possible over the whole structure.

In the postcracking range, the mesh-size dependency has been treated by employing an objective nonlinear softening model for concrete, to be described in Chapter 5.

4.7.2 THE INTEGRATION RULE RELATED TO CONCRETE CRACKING PROCESS

Cracks create discontinuities in the displacement field of the element and that cannot be reproduced without introducing internal boundaries in the structure. To overcome this difficulty in the context of finite element analysis of concrete structures, the smeared crack approach described in Chapter 5 has been commonly used where cracked concrete is assumed to remain a continuum and the material properties are modified to account for the damage due to cracking. However, the method cannot be applied to any finite element type without considering the consequences of the continuity in displacements imposed by the shape functions.

The 8-node isoparametric element gives a linear continuity in strains which will lead to a critical condition if more

than 2×2 integration rule is used [93]. In the case of a 3×3 integration scheme, a typical situation may occur if the stress or strain is large enough to initiate crack at one sampling point which means that an additional increase in strain in this cracked point results in a stress release. However, this will also result in an increasing strain in the uncracked neighbouring point giving stress increase at this point. This possibility is undesirable as the stress is locked-in (spurious stiffening). Another consequence is that a crack in any intermediate sampling point may be followed by a crack at another point. Thus two cracks may open while it should be only one. This phenomenon is also undesirable as it discourages localizations (spurious cracking). These phenomena do not disappear on mesh refinement, since refinement does not remove the fundamental assumption of displacement continuity. This situation is avoided if only the 2×2 rule is employed. Thus, employing the 2×2 integration rule was necessary in the present work to release partially the continuity requirements imposed by the shape function of 8-node isoparametric element. However, the calculated crack patterns are not to be accepted without considering their relevance.

VARIABLES	PLANE STRESS	PLANE STRAIN	AXISYMMETRIC
Coordinates, x_i Displacements, d_i Strain vector, ε Stress vector, σ	$[\,x_i,\ y_i\,]^T$ $[\,u_i,\ v_i\,]^T$ $[\,\varepsilon_x,\ \varepsilon_{yy},\ \gamma_{xy}\,]^T$ $[\,\sigma_{xx},\ \sigma_{yy},\ \sigma_{xy}\,]^T$		$[\,r_i,\ z_i\,]^T$ $[\,u_i,\ w_i\,]^T$ $[\,\varepsilon_{rr},\ \varepsilon_{zz},\ \gamma_{rz},\ \varepsilon_{\theta\theta}\,]^T$ $[\,\sigma_{rr},\ \sigma_{zz},\ \sigma_{rz},\ \sigma_{\theta\theta}\,]^T$
Strain Matrix B_i^e	$\begin{bmatrix} \frac{\partial N_i^e}{\partial x} & 0 \\ 0 & \frac{\partial N_i^e}{\partial y} \\ \frac{\partial N_i^e}{\partial y} & \frac{\partial N_i^e}{\partial x} \end{bmatrix}$		$\begin{bmatrix} \frac{\partial N_i^e}{\partial r} & 0 \\ 0 & \frac{\partial N_i^e}{\partial z} \\ \frac{\partial N_i^e}{\partial z} & \frac{\partial N_i^e}{\partial r} \\ \frac{\partial N_i^e}{\partial r} & 0 \end{bmatrix}$
Elastic stress-strain matrix, D	$\frac{E}{(1-\nu^2)}\begin{bmatrix} 1 & \nu & 0 \\ \nu & 1 & 0 \\ 0 & 0 & \frac{1-\nu}{2} \end{bmatrix}$	$\frac{E}{(1+\upsilon)(1-2\upsilon)}\begin{bmatrix} (1-\upsilon) & \upsilon & 0 \\ \nu & (1-\upsilon) & 0 \\ 0 & 0 & \frac{1-2\upsilon}{2} \end{bmatrix}$	$\frac{E}{(1+\upsilon)(1-2\upsilon)}\begin{bmatrix} (1-\upsilon) & \upsilon & 0 & \upsilon \\ \upsilon & (1-\upsilon) & 0 & \upsilon \\ 0 & 0 & \frac{(1-2\upsilon)}{2} & 0 \\ \upsilon & \upsilon & 0 & (1-\upsilon) \end{bmatrix}$
Element volume, dV^e	$t\,dx\,dy = t \det J\, d\xi\, d\eta$	$dx\,dy = \det J\, d\xi\, d\eta$	$2\pi r\ dr\,dz = 2\pi r \det J\, d\xi\, d\eta$
Element surface, dA^e	$t\,ds = t \det J'\, d\xi$	$ds = \det J'\, d\xi$	$2\pi r\ ds = 2\pi r \det J'\, d\xi$
Notation:	E - Elasticity modulus,	υ - Poisson's ratio	t = thickness

Table (4-1) Some characteristic vectors and matrices for two-dimensional solid mechanics applications

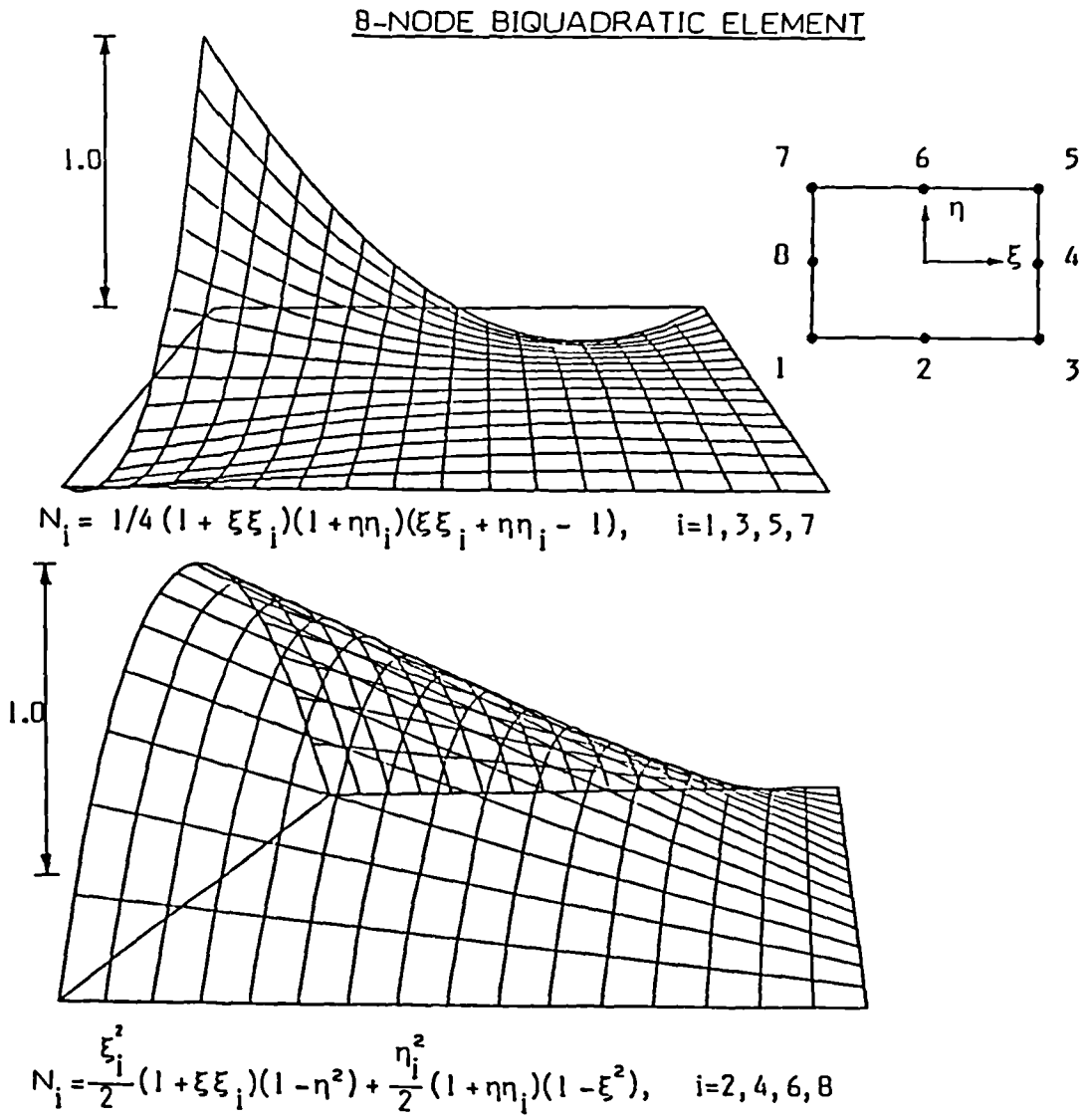

Figure 4.1 Typical shape functions of 8-node isoparametric element [27]

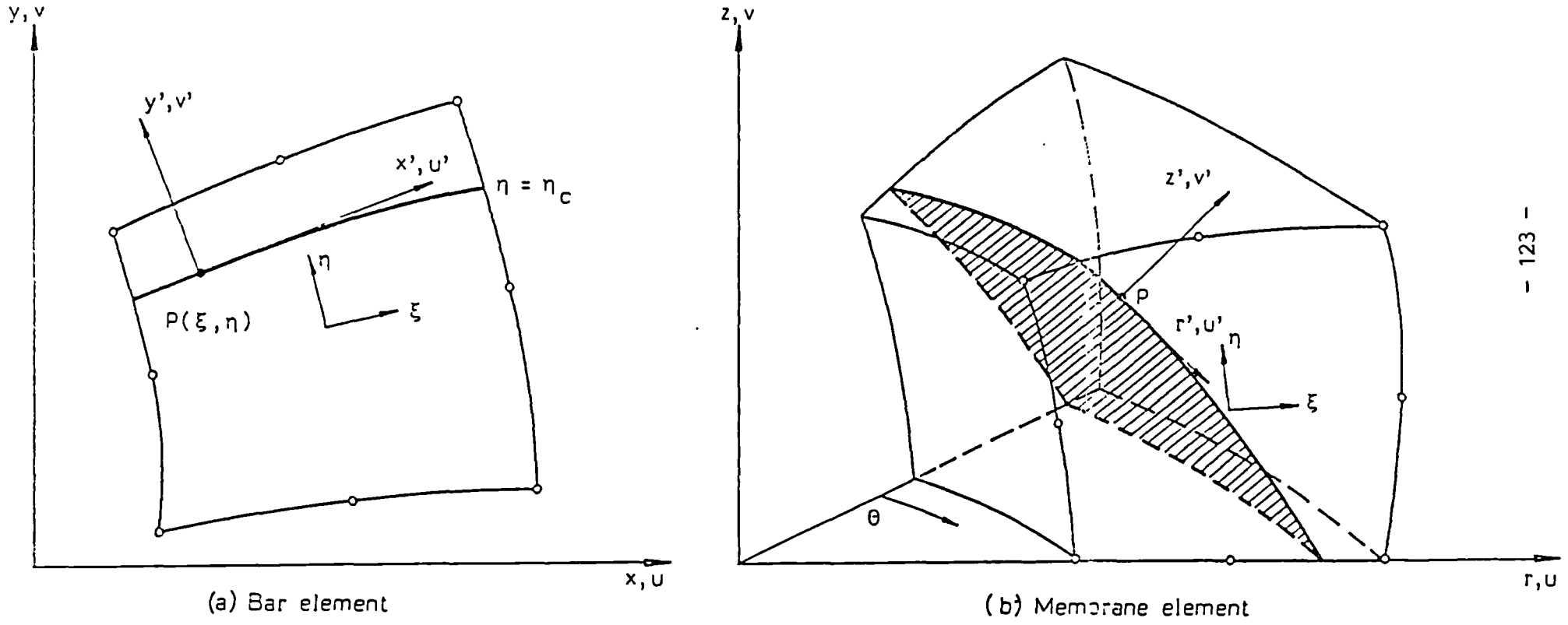

Figure 4.2 Bar and membrane elements within concrete elements [27]

CHAPTER 5

MATERIAL MODELLING OF BLAST RESISTANT REINFORCED CONCRETE STRUCTURES

5.1 INTRODUCTION

The ability of reinforced concrete to absorb energy under dynamic loading conditions has led to its utilization for structures which may be subject to blast loads. The low probability of occurence of these loads necessitates design of such structures according to the limit state concept, ultimate load theories or plastic methods in which irrecoverable structural deformation and material damage are acceptable, provided that overall structural integrity is maintained. Therefore, the numerical simulation of such structural response requires a realistic modelling of material nonlinearities in reinforced concrete structures such as the inelastic response in compression, the progressive cracking of concrete in tension zones, and the inelastic deformation of reinforcing steel.

Another main characteristic of material behaviour which the structure is to expect during a blast loading is high strain rates. For high and conventional explosives, the range of strain rate may be of the order of 10^{-2} to 100 sec^{-1}. For gas explosions, typical values are between 10^{-4} to 10^{-2} sec^{-1}. In general, the mechanical response of any structural material is dependent on the srain rate. The rate sensitivity of concrete plays a considerable role in its dynamic load capacity. By increasing the strain rates, the strength of concrete is significantly increased in both tension and compression [16, 17, 31, 50]. The same conclusion is obtained for reinforcing steel [188-190]. However, in previous analytical models for concrete material models, these rate effects have been neglected with the exception of Refs. [28, 34, 76], which employ a modified viscoplasticity theory in which only the fluidity parameter is rate dependent. As a result of introducing some

simplified assumptions to account for the complex features of concrete behaviour, these models suffer some drawbacks which were discussed in Chapter 2. Therefore, there is a need to provide a more realistic constitutive model for both concrete and steel by including rate effects as well as material nonlinearities.

The aim of the present chapter is to develop rate and history dependent constitutive models for concrete and steel under blast loading conditions. Furthermore, the progressive concrete cracking in a smeared fashion and the concrete material nonlinearities in the pre-failure and post-failure regimes in compression as well as in tension are simulated using suitable proposed rate dependent rules. A perfect bond at the interface between reinforcement and concrete is assumed.

The basic characteristics of the proposed concrete model are summarized in section 5.2. Then, the details of the numerical modelling of concrete compressive behaviour as a strain rate dependent elasto-viscoplastic material are given in section 5.3. A strain rate sensitive linear elastic strain softening model is proposed in section 5.4 for the numerical modelling of concrete in tension. Based on the proposed material modelling of concrete, the constitutive relationships are provided in section 5.5. In section 5.6, the identification of concrete strain rate sensitivity functions is considered. The constitutive modelling of reinforcing steel as a strain rate dependent uniaxial elasto-viscoplastic material in tension and compression is presented in section 5.7 followed by the experimental characterisation of the material parameters for the concrete and steel models in the final section of this chapter.

5.2 MAIN CHARACTERISTICS OF THE PROPOSED CONCRETE MODEL

It is clear from the conclusions drawn from the static and dynamic tests of concrete, reviewed in Chapter 2, that any

numerical model for concrete intended for blast resistance analysis should be rate and history dependent. Within the framework of constitutive theories, only the viscoplastic and endochronic theories are suitable for a realistic modelling of observed concrete behaviour. In practice, the endochronic model is rather complex and requires much computer effort and definition of several material parameters.

For the compressive behaviour of concrete a strain rate sensitive hardening-softening elasto-viscoplastic model with two rate dependent surfaces is developed as a modification of Perzyna's theory [76]. The proposed model has the following main differences compared with the classical model:

1. The initial yield surface which defines the initiation of the viscoplastic range is strain rate dependent.

2. During inelastic deformation history, the expansion of subsequent loading surfaces in the pre-fracture range, as well as the shrinkage of these surfaces in the post-fracture regime, are governed by rate and history-dependent rules.

3. A variable rate dependent failure surface is introduced as a damage monitoring device defining the initiation of the loading surface degradation.

4. The magnitude of the viscoplastic strain rate is not only dependent on the position of the loading surface but also the total strain rate. The fluidity parameter in the flow rate is developed as a function of the effective strain rate.

In the tensile region, concrete is modelled as a linear elastic strain softening material in which the smeared crack initiation is determined by a proposed strain rate criterion. The post-cracking behaviour is accounted for through an objective fracture energy based strain softening rule and a simple model for the shear transfer across the

crack.

An important consideration is the strain rate induced anisotropy effect which is introduced by employing strain rate sensitivity functions for tension and compression. Figure (5-1) illustrates the two-dimensionsl representation in the principal stress space of the proposed concrete model.

5.3 NUMERICAL MODELLING OF CONCRETE BEHAVIOUR IN COMPRESSION

Experimental evidence indicates that the nonlinear deformation of concrete is basically inelastic and therefore the stress-strain relations may be separated into recoverable and irrecoverable components. In the present model, linear elasticity is used for the recoverable part of the strain, and a strain rate sensitive strain hardening-softening viscoplasticity approach is employed to model the irrecoverable part of the deformation in compression. The viscoplastic behaviour is controlled by two strain rate dependent surfaces in the stress space, the initial yield surface F and a bounding or failure surface F^f.

To establish the nonlinear stress-strain relations in compression, the proposed viscoplasticity model requires the full description of the following items

(i) the failure surface,
(ii) the initial yield and subsequent loading surfaces,
(iii) strain rate sensitive hardening rule,
(iv) strain rate sensitive flow rule,
(v) strain rate sensitive strain softening rule, and
(vi) the crushing condition.

In the following sections these items are fully explained in a form suitable for numerical computation.

5.3.1 THE FAILURE SURFACE

It is proposed that the rate sensitive failure surface connects the stress states of ultimate compressive strength of concrete. Furthermore, it is a damage monitoring device which defines the initiation of concrete degradation in compression, i.e. strain softening range. The strain rate dependency is included through altering the concrete ultimate compressive strength. On the other hand, the formulations of failure criteria are proposed to capture the features of the experimentally predicted shape of the failure surface in the biaxial stress space.

(i) Proposed failure criteria

The rate dependent failure surface predicts failure if the state of stress satisfies the following condition

$$F^f\ (I_1,\ J_2,\ \sigma^{\backslash}_{cd}) = f^f_i\ (I_1,\ J_2) - \sigma^{\backslash}_{cd} = 0 \qquad (5\text{-}1)$$

where $f^f_i\ (I_1,\ J_2)$ is the failure function which is assumed to be a function of the first stress invariant I_1 and the second deviatoric stress invariant J_2 expressed (for (for axisymmetry, x, y, z are replaced by r, z, θ) as

$$I_1 = \sigma_x + \sigma_y + \sigma_z \qquad (5\text{-}2)$$

$$J_2 = \frac{1}{6}\left[\left(\sigma_x - \sigma_y\right)^2 + \left(\sigma_y - \sigma_z\right)^2 + \left(\sigma_z - \sigma_x\right)^2\right] + \tau^2_{xy} + \tau^2_{xz} + \tau^2_{yz} \qquad (5\text{-}3)$$

$\sigma^{\backslash}_{cd}$ is the dynamic ultimate compressive strength of concrete. To include strain rate dependency, $\sigma^{\backslash}_{cd}$ is assumed to be a function of the static ultimate compressive strength of concrete, $\sigma^{\backslash}_{cs}$ and the effective strain rate, $\dot{\varepsilon}_{eff}$ such that

$$\sigma^{\backslash}_{cd} = \sigma^{\backslash}_{cs}\ \ \phi_1\ (\dot{\varepsilon}_{eff}) \qquad (5\text{-}4)$$

in which $\phi_1\ (\dot{\varepsilon}_{eff})$ is the rate sensitivity function of the compressive strength. As shown in Figure (5-2), the dynamic failure surface changes its position in stress space,

compared to the fixed static failure surface, in accordance with the value of the effective strain rate.

In the present study, four different failure functions are developed to fit the quasi-static concrete test results in biaxial stress space at failure. These functions are proposed as

$$f_1^f (I_1, J_2) = a_1 I_1 + \sqrt{b_1 I_1^2 + 3c_1 J_2} \qquad (5\text{-}5)$$

$$f_2^f (I_1, J_2) = a_2 I_1 + \sqrt{b_2 \sigma_{cd}^{\backprime} I_1 + 3c_2 J_2} \qquad (5\text{-}6)$$

$$f_3^f (I_1, J_2) = \sqrt{b_3 I_1^2 + 3c_3 J_2} \qquad (5\text{-}7)$$

$$f_4^f (I_1, J_2) = a_4 I_1 + \left[b_4 I_1^2 + 2a_4^{\backprime} \sigma_{cd}^{\backprime} I_1 + 3c_4 J_2\right]^{1/2} \qquad (5\text{-}8)$$

in which a_1 , b_1 and c_1 are material constants. To simplify the determination of the material constants in the second and fourth failure functions, it has been assumed that $b_2 = a_2$ and $a_4^{\backprime} = a_4$ respectively. Each failure criterion has been developed independent of the third deviatoric stress invariant, J_3, which may be expressed as [21],

$$J_3 = \begin{vmatrix} \sigma_x - \sigma_m & \tau_{xy} & \tau_{xz} \\ \tau_{yx} & \sigma_y - \sigma_m & \tau_{yz} \\ \tau_{zx} & \tau_{zy} & \sigma_z - \sigma_m \end{vmatrix} \qquad (5\text{-}9)$$

in which σ_m is the mean normal stress defined as

$$\sigma_m = \frac{1}{3} J_1 \qquad (5\text{-}10)$$

The special choice of the failure criterion as a function of I_1, and J_2 with no dependence on J_3, has proved to be adequate for most practical situations, especially under biaxial loading conditions [21] and also resulted in simple mathematical forms which are easier to implement. Furthermore, every function needs only a few stress points from experiments (2 or 3 points only) to define the material

constants. It should be mentioned that the classic von Mises failure criterion can be recovered from the above proposed criteria by setting $a_i = b_i = 0$ and $c_i = 1.0$.

(ii) Evaluation of material constants

The constants a_i , b_i are evaluated from two stress tests; uniaxial compression test ($\sigma_1 = 0$, $\sigma_2 = -\sigma'_{cs}$), and biaxial compression test ($\sigma_1 = \sigma_2 = \sigma'_{cb}$). To define constant c_i, another biaxial test ($\sigma_2 = 0.5\ \sigma_1$, $\sigma_1 = \sigma_{cb2}$) is employed. Using Kupfer's results [37], the values of the constants were evaluated and listed in Table (5-1). The present criteria are plotted in biaxial stress space in Figure (5-3) and correlate well with Kupfer's results [37].

5.3.2 THE INITIAL YIELD AND SUBSEQUENT LOADING SURFACES

The initial yield surface defines the onset of viscoplastic behaviour. When the stress state lies within this surface, concrete is assumed to be linear elastic. Once concrete is stressed beyond the elastic limit, a subsequent new yield surface is developed. If the material is unloaded and reloaded within this subsequent loading surface, no additional irrecoverable deformation will occur until this new surface is reached.

Due to strain hardening in the prefracture range, the loading surface expands with increasing viscoplastic strain. In the softening range, this surface shrinks with the increase in viscoplastic strain. Here, the loading surfaces are assumed to have the same shape in stress space as that of the failure surface to satisfy the compatibility conditions at failure point. Thus, the general form of loading surface is proposed as

$$F(I_1, J_2, \tau) = f_1(I_1, J_2) - \tau = 0 \qquad (5\text{-}11)$$

where $f_1(I_1, J_2)$ is the loading function which takes the same forms proposed for the failure function with the same material constants, and τ is the effective stress.

To include strain rate dependency, τ is assumed to be a function not only of the effective viscoplastic strain, $\bar{\varepsilon}_{vp}$, but also of the effective strain rate, $\dot{\varepsilon}_{eff}$

$$\tau = h\ (\bar{\varepsilon}_{vp},\ \dot{\varepsilon}_{eff}) \qquad (5\text{-}12)$$

This function governs the growth and the shrinkage of the loading surface according to the hardening and softening rules, respectively. $\bar{\varepsilon}_{vp}$ is defined as

$$\bar{\varepsilon}_{vp} = \int_0^t \sqrt{\frac{2}{3}\ \dot{\varepsilon}_{vp}\ \ \dot{\varepsilon}_{vp}^T}\ dt \qquad (5\text{-}13)$$

in which $\dot{\varepsilon}_{vp}$ is the viscoplastic strain rate vector.

The initial yield surface can be obtained from (5-11) by setting $\bar{\varepsilon}_{vp}$ to zero which results in the following strain rate dependent initial yield surface

$$F(I_1,\ J_2,\ \sigma_{yd}) = f_1\ (I_1,\ J_2) - \sigma_{yd} = 0 \qquad (5\text{-}14)$$

in which σ_{yd} is the dynamic elastic limit stress of concrete in compression and which is given by

$$\sigma_{yd} = \sigma_{ys}\ \ \phi_1\ (\dot{\varepsilon}_{eff}) \qquad (5\text{-}15)$$

when σ_{ys} is the static elastic limit stress of concrete which is expressed as

$$\sigma_{ys} = \alpha\ \sigma_{cs}^{\backslash} \qquad (5\text{-}16)$$

where α is the static elastic limit which ranges between 0.2 to 0.4. As shown in Figure (5-2), the dynamic yield surface changes its position to the static yield surface, which is fixed in stress space, according to the level of strain rate. It should also be pointed out that if $\dot{\varepsilon}_{eff}$ was replaced by the effective viscoplastic strain rate, $\dot{\bar{\varepsilon}}_{vp}$, in (5-12), then the explicit dependency of the initial yield surface on the strain rate would not have existed since $\dot{\bar{\varepsilon}}_{vp}$

= 0 at that stress level.

5.3.3 STRAIN RATE SENSITIVE HARDENING RULE

To obtain the movement of the subsequent loading, surfaces during inelastic stress history of the prefracture range, a strain rate sensitive isotropic nonlinear hardening rule is developed which assumes a uniform expansion of the loading surface. According to (5-12), the amount of expansion is history and rate dependent. First, for static monotonic loading, a relationship between the accumulated viscoplastic strain and the effective stress τ is developed. In this way the concepts of effective viscoplastic strain $\bar{\varepsilon}_{vp}$ and effective stress allow for extrapolation of results from uniaxial tests to multiaxial situation. The dynamic hardening curve is then developed as a modification to the proposed static one.

(i) Strain hardening function for static monotonic loading

To develop this function, the following assumptions are made:

1. The stress-strain relation is linear up to the elastic limit stress $\alpha\sigma'_{cs}$ and then the relation is parabolic up to the ultimate strength.

2. The strain ε'_{cs} corresponding to ultimate strength σ'_{cs} is given by

$$\varepsilon'_{cs} = 2\,\sigma'_{cs} / E \qquad (5\text{-}17)$$

in which E is the initial Young's modulus of concrete.

From the parabolic curve a b in Figure 5-4, the excess stress at point c, σ_p, above the initial yield point a is expressed as

$$\sigma_p = y_o - \frac{y_o}{x_o^2}(x_o - \varepsilon_p)^2 \qquad (5\text{-}18)$$

The values of x_o, y_o and ε_p can be found from Figure 5-4 as

$$x_o = \varepsilon'_{cs} - \varepsilon_{ys} \tag{5-19}$$

$$\varepsilon_{ys} = \text{initial static yield strain} = \frac{\alpha\, \sigma'_{cs}}{E} \tag{5-20}$$

$$y_o = (1 - \alpha)\, \sigma'_{cs} \tag{5-21}$$

$$\varepsilon_p = \varepsilon - \varepsilon_{ys} \tag{5-22}$$

Substituting equations (5-17) and (5-19) to (5-22) into equation (5-18) and rearranging, the stress σ_p can be rewritten as

$$\sigma_p = (1 - \alpha)\, \sigma'_{cs} - \frac{E^2(1-\alpha)}{\sigma'_{cs}(2-\alpha)^2}\, (\varepsilon'_{cs} - \varepsilon)^2 \tag{5-23}$$

The stress level at point c as a function of the effective strain, ε, may be obtained by adding the elastic limit stress σ_{ys} to both sides of (5-23) taking into consideration that $\sigma = \sigma_p + \sigma_{ys}$

$$\frac{\sigma}{\sigma'_{cs}} = 1 - \eta_h \left(1 - \frac{\varepsilon}{\varepsilon'_{cs}}\right)^2 \tag{5-24}$$

in which η_h is a constant defined as

$$\eta_h = \frac{4(1-\alpha)}{(2-\alpha)^2} \tag{5-25}$$

To develop the effective stress-effective viscoplastic strain relations, the effective strain in (5-24) is decomposed into the elastic and viscoplastic parts

$$\varepsilon = \varepsilon_e + \varepsilon_{vp} \tag{5-26}$$

Substituting (5-26) into (5-24) and rearranging results in the following biquadratic equation

$$\sigma^2 + b'\sigma + C' = 0 \tag{5-27}$$

where $$b^{\backslash} = \frac{2\,\sigma^{\backslash}_{cs}}{\eta_h}\left[1 - \eta_h + \frac{\eta_h}{\varepsilon^{\backslash}_{cs}}\,\varepsilon_{vp}\right] \qquad (5\text{-}28)$$

$$C^{\backslash} = 4\,\sigma^{\backslash 2}_{cs}\left[1 - \frac{2}{\varepsilon^{\backslash}_{cs}}\,\varepsilon_{vp} + \frac{1}{\varepsilon^{\backslash 2}_{cs}}\,\varepsilon^2_{vp} - \frac{1}{\eta_h}\right] \qquad (5\text{-}29)$$

Solving (5-27) and rearranging gives the static hardening rule as

$$\frac{\sigma}{\sigma^{\backslash}_{cs}} = \frac{2}{\eta_h}\left[1 - \eta_h + \frac{2\eta_h}{\varepsilon^{\backslash}_{cs}}\,\varepsilon_{vp}\right]^{1/2} - \frac{2}{\eta_h}\left[1 - \eta_h + \frac{\eta_h}{\varepsilon^{\backslash}_{cs}}\,\varepsilon_{vp}\right] \qquad (5\text{-}30)$$

As can be seen in Figure (5-5), very good agreement is obtained with Kupfer's results [37] where α is taken as 0.3.

(ii) Strain hardening function for dynamic loading

To include the strain rate effect for dynamic problems, the governing parameters $\sigma^{\backslash}_{cs}$ and $\varepsilon^{\backslash}_{cs}$ in (5-30) are replaced by the corresponding dynamic conjugates $\sigma^{\backslash}_{cd}$, $\varepsilon^{\backslash}_{cd}$

$$\sigma^{\backslash}_{cd} = \sigma^{\backslash}_{cs}\;\phi_1\,(\dot{\varepsilon}_{eff}) \qquad (5\text{-}31)$$

$$\varepsilon^{\backslash}_{cd} = \varepsilon^{\backslash}_{cs}\;\phi_2\,(\dot{\varepsilon}_{eff}) \qquad (5\text{-}32)$$

in which $\varepsilon^{\backslash}_{cd}$ is the strain corresponding to the ultimate dynamic compressive strength. The variation of the effective stress level with the accumulated viscoplastic strain and the strain rate is shown in Figure (5-6).

The advantages of the proposed hardening rule can be summarized as follows

1. The effective stress τ is defined as a unique normalized parameter using one expression.

2. Only three material parameters ($\sigma^{\backslash}_{cs}$, $\varepsilon^{\backslash}_{cs}$, α) are needed to define the rule.

3. It is easy to include the strain rate effect not only for the compressive strength but also for the corresponding strain $\varepsilon_{cd}^{\backslash}$.

5.3.4 STRAIN RATE SENSITIVE FLOW RULE

(i) Viscoplastic strain rate vector

To construct the stress-strain relationship in the viscoplastic range the flow rule is defined such that the increments of the viscoplastic strain can be evaluated from a given stress state. An associative flow rule is employed here in which the viscoplastic strain rate vector is assumed to be normal to the current loading surface. Although there is limited supportive experimental evidence available [38], the associative flow rule has been successfully adopted for concrete in the context of quasi-static [21] and dynamic problems [28, 34, 77].

Assuming that the viscoplastic strain rate depends on current stresses only, the associated flow rule may be given [76] as

$$\dot{\varepsilon}_{vp} = \gamma < \phi(F) > a \qquad (5\text{-}33)$$

in which γ is a fluidity parameter controlling the plastic flow rate, ϕ (F) is a positive monotonically increasing flow function governing the amount of viscoplastic straining and a is the flow vector which defines the direction of the viscoplastic flow as follows:

$$a = \left[\frac{\partial f}{\partial \sigma} \right]^T \qquad (5\text{-}34)$$

The expression $< \phi(F) >$ is equal to $\phi(F)$ for positive values of F and zero otherwise.

In short-term static and dynamic loading conditions, the primary nonlinearities of concrete are caused by micro-crack growth and pore collapses. These nonrecoverable effects which occur once the stress rate exceeds the initial yield

conditions, are measured by the accumulated viscoplastic strain. However, the results of dynamic tests emphasize the fact that the strain rate effects observed for concrete can be, to a large extent, attributed to the rate sensitivity of the micro-cracking process [50]. Therefore, a relationship must exist between the velocity of the growth of micro-cracks and the viscoplastic strain rate in the present model. To include this rate dependence, the rate of viscoplastic flow computed by (5-33) is modified to be dependent not only on the position of the loading surface but also on the strain rate which is expressed as

$$\dot{\varepsilon}_{vp} = \gamma(\dot{\varepsilon}_{eff}) < \phi(F) > a \qquad (5\text{-}35)$$

The fluidity parameter is assumed to be a function of the effective strain rate, in order to fit stress and strain terms at failure to specified values. By assuming a constant strain rate it is possible to obtain the relationship between the fluidity parameter and the effective strain rate based on the uniaxial elasto-viscoplastic stress-strain relation of the present model and the results of the dynamic tests.

(ii) Uniaxial elasto-viscoplastic stress-strain relation

The total strain rate $\dot{\varepsilon}$ is decomposed into a linear elastic strain rate, $\dot{\varepsilon}_e$, and a viscoplastic strain rate, $\dot{\varepsilon}_{vp}$

$$\dot{\varepsilon} = \dot{\varepsilon}_e + \dot{\varepsilon}_{vp} \qquad (5\text{-}36)$$

Using the uniaxial form of Hooke's law, the elastic strain rate is expressed as

$$\dot{\varepsilon}_e = \dot{\sigma} / E \qquad (5\text{-}37)$$

The viscoplastic strain rate can be obtained from the uniaxial expression equivalent to (5-35) which may be written as:

$$\dot{\varepsilon}_{vp} = \gamma(\dot{\varepsilon}) \ (\sigma - \tau) \qquad (5\text{-}38)$$

Using (5-37) and (5-38), equation (5-36) can be rearranged and rewritten as

$$\dot{\sigma} + E\,\gamma(\dot{\varepsilon})\,(\sigma - \tau) = 0 \qquad (5\text{-}39)$$

Considering a loading history for which the strain rate is constant specified as $\dot{\varepsilon} = C_c$, (also $\gamma(\dot{\varepsilon}) = \gamma$) and taking the time derivative of (5-39) leads to the following second order differential equation

$$\ddot{\sigma} + E\,\gamma\,(\dot{\sigma} - \dot{\tau}) = 0 \qquad (5\text{-}40)$$

From the proposed hardening rule, the effective stress, τ, is described as

$$\tau = \sigma_{cd}^{\backslash} - \eta\,(\varepsilon_{cd}^{\backslash} - \varepsilon)^2 \qquad (5\text{-}41)$$

in which $\eta = \eta_h \dfrac{\sigma_{cd}^{\backslash}}{\varepsilon_{cd}^{\backslash 2}}$ and η_h is as defined in equation (5-25). Differentiating (5-41) with time and using $\varepsilon = C_c t$ in which t is the time, the effective stress rate $\dot{\tau}$ is expressed as

$$\dot{\tau} = -2\,\eta\,C_c\,(\varepsilon_{cd}^{\backslash} - C_c\,t) \qquad (5\text{-}42)$$

Using (5-42) and rearranging, equation (5-40) can be rewritten as

$$\ddot{\sigma} + E\,\gamma\,\dot{\sigma} = 2\,\eta\,C_c\,E\,\gamma\,(\varepsilon_{cd}^{\backslash} - C_c\,t) \qquad (5\text{-}43)$$

Adopting the standard procedure, the general solution of the second order differential equation (5-43) is obtained as

$$\sigma = C_1 + C_2\,e^{-\gamma E t} - C_c^2\,\eta\,t^2 + K\,t \qquad (5\text{-}44)$$

in which C_1 and C_2 denote inetgration constants, and K is a constant given by

$$K = 2\,\eta\,C_c\,(C_c + E\,\gamma\,\varepsilon_{cd}^{\backslash}) \,/\, E\gamma \qquad (5\text{-}45)$$

With the initial conditions

$$\sigma\ (t_o) = \sigma_{yd}\ ,\ \dot{\sigma}\ (t_o) = C_c\ E \qquad (5\text{-}46)$$

and the time-strain definitions

$$t_o = \varepsilon_{yd} / C_c\ ,\ t = \varepsilon / C_c \qquad (5\text{-}47)$$

in which ε_{yd} is the dynamic elastic limit strain and t_o is the corresponding time, equation (5-44) is rewritten

$$\sigma = \sigma_{yd} - \frac{1}{\gamma E}\ (K - 2\dot{\varepsilon}\eta\ \varepsilon_{yd} - E\dot{\varepsilon})\ [1 - e^{\frac{-\gamma E}{\dot{\varepsilon}}\ (\varepsilon - \varepsilon_{yd})}]$$

$$- \eta\ (\varepsilon^2 - \varepsilon_{yd}^2) + \frac{K}{\dot{\varepsilon}}\ (\varepsilon - \varepsilon_{yd}) \qquad (5\text{-}48)$$

The above equation (5-48) represents the general uniaxial form of the proposed elasto-vicoplastic model. At failure ($\sigma = \sigma'_{cd}$, $\varepsilon = \varepsilon'_{cd}$), equation (5-48) can be written as

$$\sigma'_{cd} = \sigma_{yd} - \frac{1}{\gamma E}\ (K - 2\dot{\varepsilon}\eta\ \varepsilon_{yd} - E\dot{\varepsilon})\ [1 - e^{\frac{-\gamma E}{\dot{\varepsilon}}\ (\varepsilon'_{cd} - \varepsilon_{yd})}]$$

$$- \eta\ (\varepsilon'^2_{cd} - \varepsilon_{yd}^2) + \frac{K}{\dot{\varepsilon}}\ (\varepsilon'_{cd} - \varepsilon_{yd}) \qquad (5\text{-}49)$$

(iii) Identification of strain rate dependent fluidity parameter

As already mentioned only uniaxial test data are available for plain concrete under dynamic loading conditions similar to those which occur during a blast loading. From published results, Watstein's [16] and Hatano's [17] experiments may be considered as the most complete tests for dynamic compression behaviour of concrete which cover the whole range of concrete properties and strain rates that may be used in the blast resistant construction. Typical test results are shown in Figure (5-7). The following assumptions were made:

a - All tests were conducted under constant strain rate conditions.

b - The stress and strain values at elastic limit and

failure are strain rate dependent.

The following procedure was adopted for evaluating the fluidity parameter:

1. Based on the average concrete compressive strength, the tests have been classified into 4 grades: 18.27 N/mm^2 (Watstein), 27.02 N/mm^2 (Hatano), 44.2 N/mm^2 (Hatano & Watstein), 59.4 N/mm^2 (Hatano).

2. The stress and strain values at failure and initial yield, the Young's modulus and the average strain rate are evaluated from the given stress-strain curve and other results for every test in each grade.

3. For these specified concrete parameters at failure, the value of the fluidity parameter valid for a particular constant strain rate test can be evaluated from (5-49). A computer program was written where gradually increasing values of fluidity parameter were assumed and the corresponding failure stress σ_f^1 was calculated using equation (5-49). This analysis was repeated until the final calculated failure stress σ_f^1 was close to the target failure stress σ_f of the experiment

$$| \sigma_f^1 - \sigma_f | / \sigma_f \leq 0.01 \qquad (5\text{-}50)$$

4. Since different strain rate tests give different failure stress, different values of fluidity parameter have been found appropriate. For each concrete grade, the least squares curve fitting has been used to obtain the relationship between the fluidity parameter and the strain rate. A linear regression between log γ and log $\dot{\varepsilon}$ seemed reasonable and resulted in the following relation

$$\log \gamma = B_1 + B_2 \log \dot{\varepsilon} \qquad (5\text{-}51)$$

$$\gamma = 10^{B_1} \dot{\varepsilon}^{B_2} \qquad (5\text{-}52)$$

where the parameters B_1 and B_2 depend on the concrete cylinder compressive strength Figure 5-8 and can be obtained

by interpolation from Table (5-2). Expression (5-52) is assumed to be valid for strain rate range $10^{-5} \leq \dot{\varepsilon} \leq 10$. To extend the expression (5-52) to multiaxial state of stress, the strain rate $\dot{\varepsilon}$ can be replaced by the effective strain rate, $\dot{\varepsilon}_{eff}$, which is computed as

$$\dot{\varepsilon}_{eff} = \left[\dot{\varepsilon}_{oct}^{2} + \frac{1}{4} \dot{\gamma}_{oct}^{2} \right]^{1/2} \qquad (5\text{-}53)$$

in which $\dot{\varepsilon}_{oct}$ and $\dot{\gamma}_{oct}$ are the octahedral normal strain and octahedral shear strain rate respectively.

(iv) <u>The flow vector</u>

For numerical computation, it is convenient to rewrite the four different loading functions proposed earlier in section 5.3.2 in a unique general form as

$$f_i (I_1, J_2) = A_i I_1 + \sqrt{B_i I_1^2 + 3 C_i J_2} \qquad (5\text{-}54)$$

in which A_i , B_i, C_i are new material constants dependent on the loading function i and to be computed from the original material constants previously defined. These new sets of material constants are listed in Table 5-3 for each loading function.

The main advantage of this formulation is that it permits the computer coding of the loading function and the flow vector in a general form and necessitates specification of only three constants for any individual criterion.

In terms of stresses, the general form (5-54) can be written for biaxial applications as

$$f_i (\sigma) = A_i \left(\sigma_x + \sigma_y + \sigma_z \right) + \left[\left(B_i + C_i \right) \left(\sigma_x^2 + \sigma_y^2 + \sigma_z^2 \right) \right.$$

$$\left. + \left(2 B_i - C_i \right) \left(\sigma_x \sigma_y + \sigma_x \sigma_z + \sigma_y \sigma_z \right) + 3 C_i \tau_{xy}^2 \right]^{1/2} \qquad (5\text{-}55)$$

The loading functions derivatives which define the flow vector a take the following explicit expressions

$$a = \left[\frac{\partial f_i}{\partial \sigma_x}, \frac{\partial f_i}{\partial \sigma_y}, \frac{\partial f_i}{\partial \sigma_z}, \frac{\partial f_i}{\partial \tau_{xy}} \right]^T \qquad (5\text{-}56)$$

$$\frac{\partial f_i}{\partial \sigma_x} = A_i + \frac{1}{\Delta} \left[2 \left(B_i + C_i \right) \sigma_x + \left(2 B_i - C_i \right) \left(\sigma_y + \sigma_z \right) \right] \qquad (5\text{-}57)$$

$$\frac{\partial f_i}{\partial \sigma_y} = A_i + \frac{1}{\Delta} \left[2 \left(B_i + C_i \right) \sigma_y + \left(2 B_i - C_i \right) \left(\sigma_z + \sigma_x \right) \right] \qquad (5\text{-}58)$$

$$\frac{\partial f_i}{\partial \sigma_z} = A_i + \frac{1}{\Delta} \left[2 \left(B_i + C_i \right) \sigma_z + \left(2 B_i - C_i \right) \left(\sigma_x + \sigma_y \right) \right] \qquad (5\text{-}59)$$

$$\frac{\partial f_i}{\partial \tau_{xy}} = \frac{1}{\Delta} \left[6 C_i \tau_{xy} \right] \qquad (5\text{-}60)$$

where

$$\Delta = 2 \left[\left(B_i + C_i \right) \left(\sigma_x^2 + \sigma_y^2 + \sigma_z^2 \right) + \left(2 B_i - C_i \right) \left(\sigma_x \sigma_y + \sigma_y \sigma_z + \sigma_x \sigma_z \right) + 3 C_i \tau_{xy}^2 \right]^{1/2} \qquad (5\text{-}61)$$

(v) The flow function

Several proposals of the flow function have been given by Perzyna [76], which are derived from curve fitting of experimental data. The following function has been adopted here

$$\phi (F) = \left(\frac{F}{\tau} \right)^{\kappa} = \left(\frac{f - \tau}{\tau} \right)^{\kappa} \qquad (5\text{-}62)$$

The excess stress above the current loading surface is normalized against the current effective stress in order to give non-dimensional values of the flow function. The parameter κ of equation (5-62) determines the rate of growth of ϕ. It has been taken as 1.0 in this study.

5.3.5 STRAIN SOFTENING IN COMPRESSION

In order to perform a progressive failure analysis of a concrete structure, i.e. to trace the overall response up to the ultimate state, complete constitutive relations must be known not only including the pre-peak viscoplastic behaviour but also the post-failure response. The reasons are that the local failure of some components of a concrete structure subjected to blast loading does not imply the collapse of the whole structure. Also the blast resistant design based on neglecting the strength degradation can be very uneconomical. The importance of dealing with the post-failure response has been increasingly recognised in recent years which has mainly focused more on the post-cracking modelling, than strain softening in compression.

For the present analysis, once the stress point reaches the failure surface, the softening regime is initiated and the subsequent loading surfaces degrade according to a strain rate sensitive softening rule based on the post failure viscoplastic dissipated energy. This means that the concept of a failure surface is no longer meaningful.

Following Bicanic's work [77], the loading surface defined by equation (5-9) is modified in the post-failure range to the following form

$$F\left(I_1, J_2, \tau\right) = f\left(I_1, J_2\right) - \tau\left(W_{vp}, K_s\right) \qquad (5\text{-}63)$$

in which the effective stress, τ, is a function of viscoplastic work, W_{vp}. This function is defined as the strain softening rule

$$\tau\left(W_{vp}, K_s\right) = \sigma_{cs}^{\backslash} \; e^{-\delta K_s} \qquad (5\text{-}64)$$

where δ is a concrete softening property in compression. The viscoplastic work, W_{vp} is defined as

$$W_{vp} \approx \int_{o}^{t} \sigma^{T} \dot{\varepsilon}_{vp} \, d\, t \qquad (5\text{-}65)$$

In equation (5-64), K_s is the postfailure viscoplastic energy which is defined as

$$K_s = W_{vp} - W_{vp}^{f} \qquad (5\text{-}66)$$

$$K_s = \int_{t_f}^{t} \sigma^{T} \dot{\varepsilon}_{vp} \, d\, t \qquad (5\text{-}67)$$

where t_f and W_{vp}^{f} are the time and the viscoplastic work when the failure surface has been reached. As can be seen in Figure (5-9), good agreement is obtained with the experimental results given in [37] by taking $\delta = 0.004$ and $\varepsilon_{vp}^{\backslash}$, the post failure viscoplastic strain, as

$$\varepsilon_{vp}^{\backslash} = \varepsilon_{vp} - \varepsilon_{vp}^{f} \qquad (5\text{-}68)$$

in which ε_{vp}^{f} is the viscoplastic strain when the ultimate strength has been reached.

For dynamic applications, the above function is modified to include the strain rate effect by replacing $\sigma_{cs}^{\backslash}$ in (5-64) and using $\sigma_{cd}^{\backslash}$ instead which resulted in

$$\tau \left(W_{vp}, K_s \right) = \sigma_{cd}^{\backslash} \; e^{-\delta K_s} \qquad (5\text{-}69)$$

The strain rate effect on $\varepsilon_{cs}^{\backslash}$ is included indirectly through W_{vp}^{f} which varies with the change of $\varepsilon_{cd}^{\backslash}$ and $\sigma_{cd}^{\backslash}$. The variation of the postfailure effective stress with the strain rate and the postfailure viscoplastic strain or the postfailure viscoplastic energy is shown in Figure (5-10).

5.3.6 CRUSHING OF CONCRETE

The rate dependent hardening-softening viscoplastic model described previously governs the increase of the inelastic

deformations of concrete in compression. Inelastic deformation continues until crushing occurs. The crushing type of fracture is generally accepted as a strain controlled phenomenon. The lack of available experimental data on concrete ultimate deformation under biaxial and multiaxial stress states has resulted in the need to develop the following appropriate strain criterion by converting the failure functions described in terms of stresses to that in terms of strains. The size of the resulting crushing surface is related to a maximum equivalent strain extrapolated from uniaxial tests. Thus, the general form of the crushing surface is developed as

$$G\left(I_1^{\backslash}, J_2^{\backslash}, \varepsilon_{cu}\right) = g_1\left(I_1^{\backslash}, J_2^{\backslash}\right) - \varepsilon_{cu} = 0 \qquad (5\text{-}70)$$

where $g_1\ (I_1^{\backslash}, J_2^{\backslash})$ is the concrete crushing function which is assumed to be a function of the first strain invariant $I_1^{\backslash}$ and the second deviatoric strain invariant $J_2^{\backslash}$ which are expressed (for axisymmetry x, y, z are replaced by r, z, θ) as

$$I_1^{\backslash} = \varepsilon_x + \varepsilon_y + \varepsilon_z \qquad (5\text{-}71)$$

$$J_2^{\backslash} = \frac{1}{6}\left[\left(\varepsilon_x - \varepsilon_y\right)^2 + \left(\varepsilon_y - \varepsilon_z\right)^2 + \left(\varepsilon_z - \varepsilon_x\right)^2\right] + \frac{1}{4}\gamma_{xy}^2 \qquad (5\text{-}72)$$

ε_{cu} is concrete ultimate total strain obtained from uniaxial test results (0.003 - 0.005). From the previously developed failure functions, the strain invariants based crushing functions have been proposed as

$$g_1\left(I_1^{\backslash}, J_2^{\backslash}\right) = a_1 I_1^{\backslash} + \sqrt{b_1 I_1^{\backslash 2} + 3 c_1 J_2^{\backslash}} \qquad (5\text{-}73)$$

$$g_2\left(I_1^{\backslash}, J_2^{\backslash}\right) = a_2 I_1^{\backslash} + \sqrt{a_2 \varepsilon_{cu} I_1^{\backslash} + c_2 J_2^{\backslash}} \qquad (5\text{-}74)$$

$$g_3\left(I_1^{\backslash}, J_2^{\backslash}\right) = \sqrt{b_3 I_1^{\backslash 2} + 3 c_3 J_2^{\backslash}} \qquad (5\text{-}75)$$

$$g_4\left(I_1^{\backslash}, J_2^{\backslash}\right) \approx a_4 I_1^{\backslash} + \left[b_4 I_1^{\backslash 2} + 2a_4 \varepsilon_{cu} I_1^{\backslash} + 3 c_4 J_2^{\backslash}\right]^{1/2} \quad (5\text{-}76)$$

in which a_1, b_1, c_1 are the material constants defined before in Table (5-1). When concrete reaches the crushing surface it is assumed to release all stresses and lose its stiffness.

5.4 NUMERICAL MODELLING OF CONCRETE TENSILE BEHAVIOUR

The main characteristics of plain concrete behaviour is its low tensile strength. As a result tensile cracking is considered as the major factor contributing to the nonlinear behaviour of reinforced concrete structures, influencing the collapse load and the structure response history.

In the present analysis, concrete in tension is modelled as a strain rate sensitive linear elastic softening material, i.e. concrete behaves elastically until cracks initiate according to a strain rate dependent cracking criterion and then the crack forming process is governed by a fracture energy based softening rule in which concrete tensile strength in the direction normal to the crack is gradually released in uniformity with the crack width.

To fully describe the proposed model requires the following information

(i) crack modelling,
(ii) cracking criterion,
(iii) strain softening rule, and
(iv) shear transfer model.

Finally for completion, the possible configuration of cracks as well as compressive behaviour of cracked concrete are discussed.

5.4.1 FINITE ELEMENT REPRESENTATION OF CRACKS

Ever since cracking has been modelled, the discrete concept and the smeared concept have been the subject of much controversy. The discrete concept fits our material conception of fracture since cracking is identified as a geometrical discontinuity. Conversely, it has been stated that a smeared representation might be realistic considering the bands of micro-cracks that blunt fracture in matrix-aggregate composites like concrete. The width of such bands, which occur at the tip of the visible crack, has even been claimed to be a material property [92]. At present, however, it is difficult to judge these arguments since experimental detection of crack tip related micro-mechanical process in matrix-aggregate composites are scarce and contradictory as the question is concerned whether these processes occur in a discrete manner or not [191].

Following the most common approach, a smeared crack model has been adopted here where cracked concrete is assumed to remain a continuum and the material properties are modified to account for the damage due to cracking. It has been chosen for the following reasons:

1. For blast loading conditions where the cracking patterns are difficult to predict, and also for situations where the scale of the representative continuum, e.g. shear walls or beams, is large compared to the crack spacing, the smeared concept provides a realistic approach for distributed fracture representation compared with the discrete model which seems adequate for simple problems involving a few dominant cracks.

2. The isoparametric elements employed in the present analysis do not blend well with the edge cracking associated with the discrete crack concept [192].

3. The proposed constitutive model is suitable for the description of concrete behaviour at the engineering level but not at the microscopic level which will necessitate the

discrete approach.

4. The simplicity and the computational advantages of the smeared crack approach such as automatic generation of cracks without predefining or redefining the finite element mesh, and also complete generality in allowing crack initiation in any direction.

5.4.2 STRAIN RATE SENSITIVE CRACKING CRITERION

(i) The proposed cracking criterion

Sophisticated theoretical models have been developed to describe the cracking response of concrete [106, 193]. However, the usefulness of these models may be questioned in the light of uncertainties commonly associated with the properties of reinforced concrete members [78]. The value of concrete tensile strength is difficult to measure, and considerable scatter is obtained even in laboratory tests. In situ, uncontrolled environmental and loading conditions cause higher statistical scatter. In the presence of reinforcing steel, the prediction of crack initiation and direction is even more difficult. Simple criteria are therefore commonly employed by most analysts to predict tensile fracture. The maximum tensile stress or strain criterion is frequently adopted for this purpose.

For the present analysis, the tensile crack initiation is based on rate sensitive strain criterion to distinguish the elastic behaviour from tensile fracture. This assumption is realistic as it accounts for concrete brittleness noticed in dynamic tensile tests. The strain rate effect is included in the limiting cracking strain as follows

$$\varepsilon^{\backslash}_{td} = \phi_3 \left(\dot{\varepsilon}_{eff}\right) \varepsilon^{\backslash}_{ts} \qquad (5\text{-}77)$$

in which $\varepsilon^{\backslash}_{td}$ is the dynamic cracking strain, $\varepsilon^{\backslash}_{ts}$ is the static one, and $\phi_3(\dot{\varepsilon}_{eff})$ is the strain rate sensitivity function for cracking strain, and which is assumed to be a function of the effective strain rate.

(ii) Introduction of the cracking process for plane problems

For a previously uncracked sampling point, cracks are assumed to form in planes perpendicular to the direction of maximum tensile strain as soon as this strain reaches the specified concrete dynamic cracking strain, ε'_{td}. Thus, for cracking

$$\varepsilon_1 \geq \varepsilon'_{td} \quad \text{and/or} \quad \varepsilon_2 \geq \varepsilon'_{td} \tag{5-78}$$

where the subscripts 1 and 2 relate to the two principal directions in the plane of a structure. Two orthogonal cracks may form if both principal strains exceed the limiting value at the same time. Thereafter, the behaviour of concrete is no longer isotropic. It becomes orthotropic and the local material axes coincide with the principal strain directions. Following the fixed crack approach [78], the crack directions are assumed to be fixed in the directions corresponding to the principal strain directions when the primary cracks occurred (Figure 5-11) irrespective of the possible rotation of the stresses and strains. It is also assumed that the material parallel to the crack is still capable of carrying stress where the state of stress changes from biaxial to uniaxial condition by reducing the elasticity modulus and Poisson's ratio to zero in the direction perpendicular to the cracked plane.

Under further loading, a secondary crack may occur at a sampling point that was originally cracked in one direction if the strain parallel to the existing crack, ε^*_t, satisfies the cracking condition

$$\varepsilon^*_t \geq \varepsilon'_{td} \tag{5-79}$$

Thus, for plane problems, a set of two cracks are allowed at each sampling point in mutually orthogonal directions.

(iii) Cracking process in axisymmetric analysis

In axisymmetry, the hoop stresses and strains are always

principal quantities, and therefore cracks always lie in radial planes if the hoop strain satisfies the cracking condition

$$\varepsilon_{\theta} \geq \varepsilon'_{td} \qquad (5\text{-}80)$$

No angle is associated with the radical cracks since any hoop differential displacement is, by definition, impossible. The other type of cracks, called the circumferential cracks, can occur in the radial-axial (r-z) plane which are similar to those in planar conditions. The state of stress changes from axisymmetric to biaxial after the first crack and from biaxial to uniaxial after the second crack at the same integration point. Figure (5-12) illustrates the two distinct types of cracking. Thus, taking into account that this third direction, θ, is always a principal direction and is out of plane, the cracking prediction follows the same procedure of plane problems for circumferential cracks.

(iv) Determination of concrete crack angle

The direction of the first principal strain, ε_1, perpendicular to an initiated crack, with respect to the x-axis is given by (Figure 5-11)

$$\alpha_{cr} = \frac{1}{2} \tan^{-1} \left[\gamma_{xy} / \left(\varepsilon_x - \varepsilon_y \right) \right] \qquad (5\text{-}81)$$

However, for $\varepsilon_x - \varepsilon_y = 0$

$$\alpha_{cr} = \pi / 4 \quad \text{for} \quad \gamma_{xy} > 0.0 \qquad (5\text{-}82)$$

$$\alpha_{cr} = -\pi / 4 \quad \text{for} \quad \gamma_{xy} < 0.0 \qquad (5\text{-}83)$$

and for $\gamma_{xy} = 0$

$$\alpha_{cr} = 0.0 \quad \text{for} \quad \varepsilon_x - \varepsilon_y > 0.0 \qquad (5\text{-}84)$$

$$\alpha_{cr} = \pi / 2 \quad \text{for} \quad \varepsilon_x - \varepsilon_y < 0.0 \qquad (5\text{-}85)$$

The crack angle is then given by the angle α^*_{cr} as

$$\alpha^{*}_{cr} = \alpha_{cr} + \pi / 2 \qquad (5\text{-}86)$$

For axisymmetric (r, z,θ) geometry, x and y are replaced by r and z respectively and then the above expressions become directly applicable for the circumferential cracks.

An accurate evaluation of crack directions is essential for a correct overall post-cracking response of concrete structures. However, cracks are not detected in the nonlinear analysis until strains calculated at the end of the solution increment (time step) exceed the limiting cracking value. Naturally the resulting angle of crack will be different from that if sufficient incremental quantities had been used. It is obvious that longer increments increase this discrepancy. In order to minimize the effect of increment size, the modified approach for the calculation of corrected crack angles [168] may be employed. Fortunately, the time increment size necessary for the stability limit of explicit time scheme employed in the present study for the numerical integration the dynamic equations of motion are so small that the errors found in the calculated angles by (5-81) can be ignored.

5.4.3 STRAIN SOFTENING RULE

Fracture and crack propagation in concrete depend on the properties of material in tension and its post-cracking behaviour. Recent experimental studies [103, 194] indicate that the behaviour after cracking is not completely brittle and there is some ductility in the post-cracking region. Also due to bond effects, concrete between the cracks carries a certain amount of tensile force normal to the cracked plane which is known as tension softening. In order to account for these phenomena in the present computational model, it is assumed that the loss of tensile strength in concrete occurs gradually after cracking. This is equivalent to considering concrete as an elastic-strain softening material in tension. An important consideration in selection of crack propagation criterion for the smeared

cracking concept is the objectivity with respect to mesh elements size. The fracture energy release rate, G_f, defined as a material property, is used with a local strain softening rule and a characteristic length, L_c, depending on the finite element mesh for the subjective treatment of the post-cracking behaviour. As a result the fracture energy concept leads to a non-local format of the equivalent softening relation.

(i) Energy criterion and characteristic crack length

In the present study, the element size effect is treated by an approach proposed by Nilsson et al [91], in which the abrupt stress drop is replaced with a gradual process to follow a fracture energy based nonlinear softening curve as shown in Figure (5-13). Thereafter, in addition to the rate dependent strain criterion, which defines the initiation of the cracks, energy criterion is also used to define the crack propagation process. The model has been previously employed by Glemberg [93] and Cervera et al [78] for dynamic analysis.

In the vicinity of a crack tip, see Figure 5-13a, there is a region where micro-cracking starts to form the crack but stresses still can be transformed between the two crack surfaces. The stress, σ, across an opening crack is assumed to be a function of the crack width, w, [91, 93] such that

$$G_f = \int_0^\infty \sigma\,(w)\; dw \qquad (5\text{-}87)$$

G_f represents the energy consumed in the formation and opening of the smeared crack per unit area of the cracked plane of the post-cracking behaviour. Typical values of the fracture energy for normal concretes are in the range of 50 to 200 Nm/m^2.

The smeared approach does not represent individual cracks, so the crack width, w, must be smeared into an equivalent crack strain, ε_c, related to the physical crack opening by a

characteristic length. Following Nilsson [91], the derivation of this relation can be obtained by introducing a control volume, v, containing a crack with surface area A Figure (5-14). It is assumed that all inelastic deformations inside this volume take place in the crack, so the rest of the control volume remains elastic.

The rate of energy dissipation in the crack is

$$\dot{\pi}_A = \int_A \sigma \, \dot{w} \, d \, A \qquad (5\text{-}88)$$

In order to replace the discontinuous crack with an equivalent strain, ε_c, it is assumed that the control volume is subjected to the same state of stress as the crack, but strained by the equivalent strain. The rate of energy dissipation in this continuous volume is

$$\dot{\pi}_v = \int_v \sigma \, \dot{\varepsilon}_c \, dv \qquad (5\text{-}89)$$

If the stress, strain and crack width are assumed to be constant inside the considered volume, then equating the rate of energy dissipation in the crack, (5-88), to that in the control volume, (5-89), gives the relationship between the crack width and the fictitious crack strain as

$$\frac{dw}{d \, \varepsilon_c} = \frac{V}{A} \qquad (5\text{-}90)$$

From Figure (5-14), the characteristic length is defined as the ratio between the control volume and the crack surface. Thus, equation (5-90) can be rewritten as

$$\frac{dw}{d \, \varepsilon_c} = L_c \qquad (5\text{-}91)$$

$$\text{or } w = L_c \, \varepsilon_c \qquad (5\text{-}92)$$

Using equation (5-92), the fracture energy in equation (5-87) is defined as

$$G_f = L_c \int_o^\infty \sigma \, d \, \varepsilon_c \qquad (5\text{-}93)$$

(ii) Nonlinear strain softening model

Based on various experimental evidence, an experimental function is used to simulate strain softening effect [78, 93], so that

$$\sigma = \sigma'_{ts} \; e^{-\frac{\varepsilon - \varepsilon'_{ts}}{\psi}} \tag{5-94}$$

where σ'_{ts} is the tensile strength of concrete, ε'_{ts}, is the cracking strain, ψ is tension softening parameter, and ε is the normal tensile strain in the cracked zone. From Figure (5-13), the stress in the linear elastic part can be defined as

$$\sigma = \varepsilon \frac{\sigma'_{ts}}{\varepsilon'_{ts}} \tag{5-95}$$

Substituting (5-94) and (5-95) into (5-93), we obtain

$$G_f = L_c \frac{\sigma'_{ts}}{\varepsilon'_{ts}} \int_0^{\varepsilon'_{ts}} \varepsilon \, d\varepsilon + L_c \, \sigma'_{ts} \int_{\varepsilon'_{ts}}^{\infty} e^{-\frac{\varepsilon - \varepsilon'_{ts}}{\psi}} \, d\varepsilon \tag{5-96}$$

or

$$G_f = \sigma'_{ts} \, L_c \left[\tfrac{1}{2} \varepsilon'_{ts} + \psi \right] \tag{5-97}$$

Rearranging (5-97) yields the tension softening parameter as

$$\psi = \left(G_f - \tfrac{1}{2} \sigma'_{ts} \, \varepsilon'_{ts} \, L_c \right) / \sigma'_{ts} \, L_c \; > 0 \tag{5-98}$$

In the context of finite element computations, the control volume for a crack is the volume associated with a sampling point in a given element. The characteristic crack length is computed here for each sampling point as [78]

$$L_c = (dv)^{1/3} \tag{5-99}$$

where dv denotes the volume of concrete represented by the sampling point. This definition does not account for the directionality of the crack or distortion of the element but

it can be used as a first order approximation of the actual control length.

It should be mentioned that this approach does not account for the effect of the presence of the reinforcement which may be included by adopting a higher fracture energy for reinforced concrete than for plain concrete. The lack of experimental results on the effect of strain rate on the post-cracking behaviour of concrete has resulted in using the available static concrete properties in the softening range.

5.4.4 SHEAR TRANSFER ACROSS THE CRACKS

At the onset of cracking, the ability of concrete to transfer shear stresses across the crack is greatly reduced. However, phenomena such as aggregate interlock and dowel action due to reinforcing bars must be taken into consideration. Both mechanisms are controlled by the width of the crack, the shear transfer capacity being reduced as the width increases.

To account for the shear capacity of cracked concrete in the smeared crack approach, a simplified procedure is generally employed which consists of assigning to the uncracked shear modulus, G, a reduced value, G_c, defined as

$$G_c = \beta\, G \qquad (5\text{-}100)$$

where β is a reduction factor in the range of zero to one. In the present work, the reduction factor is related, by a monotonically decreasing function, to the tensile strain normal to the crack plane, a smeared measure of the crack width, by the expression

$$\beta = 1 - \left(\varepsilon_t \,/\, \varepsilon_m \right)^{\mu},\ \beta = 0 \text{ if } \varepsilon_t \geq \varepsilon_m \qquad (5\text{-}101)$$

where ε_t is the current tensile strain normal to the crack plane, ε_m is the maximum limiting tensile strain, and μ is a

parameter in the range 0.3 to 1.0 [195]. The value of the maximum limiting strain is in a the range 0.004 - 0.005 for structural analysis [195].

5.4.5 CLOSING AND OPENING OF EXISTING CRACKS

The redistribution of stresses due to cracking in other sampling points, or further loading or unloading may force some of the previously open cracks to close partially or fully. Closing and opening of the existing cracks are admissible in the present concrete model. Various possible crack configurations for plane and axisymmetric problems are shown in Figure (5-15).

The current strain normal to the crack direction is used to assess the state of the cracks in already cracked concrete. Thus, a crack is assumed to be fully closed if the strain becomes negative, as

$$\varepsilon_n^* \leq 0 \quad \text{and/or} \quad \varepsilon_t^* \leq 0 \tag{5-102}$$

and/or additionally for axisymmetric problems

$$\varepsilon_\theta \leq 0 \tag{5-103}$$

The compressive stresses can then again be transmitted across the cracks. If the current strain normal to the crack direction decreases, but is still positive, partial closing of the crack is assumed. This situation may occur when the current strain, ε, is smaller than the reference strain, ε_{ref}, recorded as the maximum tensile strain reached across the crack under consideration at the previous time steps. In this case, the stress normal to the crack is calculated from

$$\sigma = \frac{\sigma_{ref}}{\varepsilon_{ref}} \varepsilon \tag{5-104}$$

in which σ_{ref} is the interpolated stress corresponding to the strain ε_{ref}. This secant unloading path is shown in Figure (5-13).

Re-opening of fully closed crack is also monitored by the tensile strain normal to the crack direction, i.e.

$$\varepsilon_n^* > 0 \quad \text{and/or} \quad \varepsilon_t^* > 0 \qquad (5\text{-}105)$$

and/or for axisymmetric problems

$$\varepsilon_n^* > 0 \text{ and/or } \varepsilon_t^* \text{ and/or } \varepsilon_\theta > 0 \qquad (5\text{-}106)$$

In this case, the crack follows the same secant path (see Figure (5-13) until ε_{ref} is exceeded and then the stress is interpolated from the strain softening governing equation (5-94).

It should be mentioned that from the moment of first cracking, for each integration point, a record of the crack angle, the crack state, and the cracking reference values (ε_{ref}, σ_{ref}) is kept and constantly updated at each time step.

5.4.6 COMPRESSIVE BEHAVIOUR OF CRACKED CONCRETE

The cracking of concrete is considered to be only a partial fracture, since the strength characteristics in the directions parallel to the crack planes are not affected. In such directions, a second cracking plane can be formed according to the strain sensitive cracking criterion described earlier, or if compressive stresses are present, then viscoplastic yielding can occur as well as the crushing type of fracture. The elasto-viscoplastic analysis of a point where the concrete is cracked in one direction or two directions (only for axisymmetry) is performed as previously described for uncracked points.

It is worth mentioning that the discontinuity of the yield or failure surfaces, due to the intersection of tension cut-off planes, does not cause numerical difficulties in defining a unique stress transfer path at the corners. This is because in the computer implementation of the present concrete model, the cracking fracture process in the primary

and secondary directions is verified in advance, then with the modified stress state, the viscoplastic behaviour and crushing are checked and the material state variables are updated accordingly. Thus, the discontinuous description furnishes additional information on the type of fracture and its direction.

The application of the crushing criteria to concrete with one crack plane (or two planes in the case of axisymmetric situations) at a sampling point is not very straightforward. The fictitious strain components used in the smeared crack approach, the strain component normal to the cracking plane and the shear strain component on this plane, must be taken equal to zero when any of the crushing conditions is employed. For concrete cracked in two directions for plane problems (or in three directions for axisymmetry) at the integration point, viscoplastic yielding and crushing of concrete are assumed not to occur if the cracks are open in these directions.

5.5 CONSTITUTIVE RELATIONSHIP FOR CONCRETE

5.5.1 UNCRACKED CONCRETE

Following conventional engineering approach, uncracked concrete is assumed to be an isotropic material in which the principal axes of stress and strain coincide.

In the elastic range, the stress-strain relation is linear and given by

$$\sigma = D_c \varepsilon \qquad (5\text{-}107)$$

where σ, ε are the stress and total strain vectors respectively, and D_c is the elasticity matrix which is dependent upon the type of problem being plane stress, plane strain or axisymmetric (Table 4.1).

For stress points outside the loading surface in compression, the elasto-viscoplastic response is assumed.

The total strain is decomposed into elastic and viscoplastic parts

$$\varepsilon = \varepsilon_e + \varepsilon_{vp} \qquad (5\text{-}108)$$

The elasto-viscoplastic stress-strain relation is obtained from

$$\sigma = D_c \varepsilon_e \qquad (5\text{-}109)$$

$$\sigma = D_c \left(\varepsilon - \varepsilon_{vp} \right) \qquad (5\text{-}110)$$

The viscoplastic strain vector at time t is computed as

$$\varepsilon_{vp} = \int_o^t \dot{\varepsilon}_{vp} \, dt \qquad (5\text{-}111)$$

in which the viscoplastic strain rate is to be equated by the flow rule explained earlier. The temporal discretization and the solution procedure to obtain a numerical solution (5-111) is discussed in Chapter 6.

When the crushing condition is satisfied, concrete is assumed to lose all its characteristics of strength and rigidity, i.e. the constitution matrix is null

$$D_{crush} = [\ 0\ ] \qquad (5\text{-}112)$$

5.5.2 CRACKED CONCRETE

The onset of cracking introduces orthotropic conditions and new constitutive relations are then established with respect to the local coordinate system which has axes parallel and perpendicular to the crack. In general, the stress-strain relationship is given as

$$\sigma^* = D_{cr} \varepsilon^* \qquad (5\text{-}113)$$

where D_{cr} is the elasticity matrix of cracked concrete and σ^*, ε^* are the stress and strain vectors with respect to local system

$$\sigma^* = \left[\sigma_n^*,\ \sigma_t^*,\ \tau^*,\ \sigma_\theta^* \right]^T \qquad (5\text{-}114)$$

$$\varepsilon^* = \left[\varepsilon_n^*,\ \varepsilon_t^*,\ \gamma^*,\ \varepsilon_\theta^* \right]^T \qquad (5\text{-}115)$$

To eliminate the tensile stress normal to the crack, σ_n^*, the individual terms in the corresponding row and the columns in the D_{cr} matrix are set to zero. Effectively, the stress component normal to the crack is gradually reduced to zero according to the assumed tension softening descending curve shown in Figure (5-13). The shear stress τ^* along the crack is a linear function of the shear strain γ^* such that

$$\tau^* = G_c\ \gamma^* \qquad (5\text{-}116)$$

where the reduced shear modulus is evaluated by (5-101). The particular forms of the constitutive relationships D_{cr} are dependent on the problem type and cracking state.

(i) Plane problems

At a given sampling point, there are two different possible configurations of cracks which can be expressed as

- Case 1: crack in the y* direction

$$D_c = \begin{bmatrix} 0 & 0 & 0 \\ 0 & E_r & 0 \\ 0 & 0 & G_c \end{bmatrix} \qquad (5\text{-}117)$$

- Case 2: cracks in the y* and x* directions

$$D_c = \begin{bmatrix} 0 & 0 & 0 \\ 0 & 0 & 0 \\ 0 & 0 & G_c \end{bmatrix} \qquad (5\text{-}118)$$

where E_r = E for plane stress,

= E/1 - ν^2 for plane strain cases.

(ii) Axisymmetric problems

Five different combinations of radial and circumferential cracks at the same integration point are possible, each involving a specific form of cracked D-matrix. The possible combinations are

- Case 1: one circumferential crack

$$D_{cr} = \begin{bmatrix} 0 & 0 & 0 & 0 \\ 0 & E_r & 0 & \nu E_r \\ 0 & 0 & G_c & 0 \\ 0 & \nu E_r & 0 & E_r \end{bmatrix} \qquad (5\text{-}119)$$

- Case 2: one radial crack

$$D_{cr} = \begin{bmatrix} E_r & \nu E_r & 0 & 0 \\ \nu E_r & E_r & 0 & 0 \\ 0 & 0 & G_c & 0 \\ 0 & 0 & 0 & 0 \end{bmatrix} \qquad (5\text{-}120)$$

- Case 3: one radial crack + one circumferential crack

$$D_{cr} = \begin{bmatrix} 0 & 0 & 0 & 0 \\ 0 & E & 0 & 0 \\ 0 & 0 & G_c & 0 \\ 0 & 0 & 0 & 0 \end{bmatrix} \qquad (5\text{-}121)$$

- Case 4: two circumferential cracks

$$D_{cr} = \begin{bmatrix} 0 & 0 & 0 & 0 \\ 0 & 0 & 0 & 0 \\ 0 & 0 & G_c & 0 \\ 0 & 0 & 0 & E \end{bmatrix} \qquad (5\text{-}122)$$

- Case 5: one radial crack + two circumferential cracks

$$D_{cr} = \begin{bmatrix} 0 & 0 & 0 & 0 \\ 0 & 0 & 0 & 0 \\ 0 & 0 & G_c & 0 \\ 0 & 0 & 0 & 0 \end{bmatrix} \qquad (5\text{-}123)$$

where

$$E_r = E/1-\nu^2 \qquad (5\text{-}124)$$

5.5.3 TRANSFORMATION RULE

Constitutive relations for cracked concrete are formulated in the local coordinate system which coincides with the crack directions as shown in Figure (5-11). Since in the solution procedure reference is made to the global set of coordinates, the stress vector σ^* is transformed into the global coordinates as follows

$$\sigma = [T]^T \sigma^* \qquad (5\text{-}125)$$

in which the transformation matrix, T, is given by

$$T = \left[\begin{array}{ccc|c} \cos^2 \alpha_{cr} & \sin^2 \alpha_{cr} & \sin \alpha \cos \alpha_{cr} & 0 \\ \sin^2 \alpha_{cr} & \cos^2 \alpha_{cr} & -\sin \alpha \cos \alpha_{cr} & 0 \\ -2 \sin \alpha_{cr} \cos \alpha_{cr} & 2 \sin \alpha_{cr} \cos \alpha_{cr} & \cos^2\alpha_{cr} - \sin^2\alpha_{cr} & 0 \\ \hline 0 & 0 & 0 & 1 \end{array}\right] \qquad (5\text{-}126)$$

where α_{cr} is the angle between the global and local coordinate system which is evaluated by (5-81). For planar structures, only the upper 3 x 3 partition is employed while the complete matrix (4 x 4) is utilized for axisymmetric problems.

5.6 STRAIN RATE SENSITIVITY FUNCTIONS OF CONCRETE

The identification of rate sensitivity functions is based on the uniaxial experimental results reported in the literature. To extend these functions to multiaxial states of stress, the strain rate, $\dot{\varepsilon}$, in the uniaxial form was replaced by the effective strain rate, $\dot{\varepsilon}_{eff}$ which is calculated by (5-53). These functions are valid only for the strain rate range 10^{-5} sec^{-1} $\leq \dot{\varepsilon}_{eff} \leq$ 10 sec^{-1}.

5.6.1 RATE SENSITIVITY FUNCTIONS IN COMPRESSION

Based on the study reported in [20], the strain rate sensitivity for concrete compressive strength, ϕ_1 ($\dot{\varepsilon}_{eff}$), and the corresponding strain, ϕ_2 (ε_{eff}), were obtained from the least squares curve fitting to the test results reported by different investigators as

$$\phi_1 (\dot{\varepsilon}_{eff}) = 1.48 + 0.160 \log \dot{\varepsilon}_{eff} + 0.0127 (\log \dot{\varepsilon}_{eff})^2 \quad (5\text{-}127)$$

$$\phi_2 (\dot{\varepsilon}_{eff}) = 1.08 + 0.112 \log \dot{\varepsilon}_{eff} + 0.0193 (\log \dot{\varepsilon}_{eff})^2 \quad (5\text{-}128)$$

According to the second function, increasing the strain rate from static value of 10^{-5} sec^{-1} to values as high as 10^{-1} sec^{-1} results in reduced values of strain at maximum stress. At strain rate higher than 10^{-1} sec^{-1}, however, the concrete strain at maximum stress becomes larger than the static value.

5.6.2 RATE SENSITIVITY FUNCTIONS IN TENSION

The effect of strain rate upon concrete tensile strength has been dealt with in a small number of publications (Fig 5-16). Recently, Sauris [50] has reported well controlled tests to study the strain rate sensitivity of fracture strength in compression, tension and flexure. The tensile strength rate sensitivity function, ϕ_4 ($\dot{\varepsilon}_{eff}$) was obtained here from the least squares curve fitting of a second order polynominal to the test results found in the literature [197] as (Figure 5-17)

$$\phi_4 (\dot{\varepsilon}_{eff}) = 2.23 + 0.404 \log \dot{\varepsilon}_{eff} + 0.0351 (\log \dot{\varepsilon}_{eff})^2 \quad (5\text{-}129)$$

Concerning the rate effect upon the cracking strain, until recently there was a lack of agreement between the results of the small number of studies reported. However, the

conclusion of recent research [197, 66] is that the strain rate effect upon the cracking strain is similar to that upon the tensile strength and also the normalized σ - ε diagrams obtained from tensile tests with different strain rates are similar in shape. Based on these findings, the cracking strain rate sensitivity function, $\phi_3(\dot{\varepsilon}_{eff})$ is assumed here to be the same as $\phi_4(\dot{\varepsilon}_{eff})$, the function applicable to tensile strength.

5.6.3 STRAIN RATE INDUCED ANISOTROPY

For the purpose of highlighting the strain rate anisotropy, the four rate sensitivity functions are plotted in Figure (5-18). It can be seen that the tensile response is the most strain rate sensitive and the compressive response the least. The difference in strain rate sensitivity for the different response modes means that with an increase in strain rate, the extent of internal micro-cracking decreases and, as a result, the stress-strain curves become less nonlinear at higher strain rates [50, 197]. Based on this evidence, any constitutive law for concrete under blast loading conditions which assumes isotropic strain rate sensitivity may not be sufficiently accurate.

5.7 MATERIAL MODELLING OF STEEL REINFORCEMENT

In reinforced concrete structures, the steel bars are comparatively thin and are considered to be capable of transmitting axial compressive or tensile forces only. A uniaxial stress-strain relationship in the direction of the bars is usually sufficient for general use.

5.7.1 MAIN CHARACTERISTICS OF THE PROPOSED STEEL MODEL

The mechanical properties of steel, in contrast to concrete, are well-known, especially in terms of its uniaxial response. Most of dynamic experimental results strongly

indicate the influence of the strain rate upon the stress-strain diagram. Thus, the use of the static stress-strain curve for the description of dynamic behaviour in blast loading environment is likely to lead to erroneous results. The yield stress and the ultimate stress increase with increasing strain rates while the modulus of elasticity is relatively rate independent. In contrast to concrete, the rate effects are approximately equal in tension and compression. To model such behaviour, viscoplasticity theory has been employed in this study, mainly because of its simplicity and well documented performance.

Steel is modelled as a strain rate sensitive uniaxial elasto-viscoplastic material to account for strain rate sensitivity as well as stress strain history dependence. The stress-strain curve is idealized as a bilinear curve, representing elasto-viscoplastic behaviour with linear isotropic hardening. The curve is assumed to be identical in tension and compression (Figure 5-19). Unloading is assumed to occur elastically.

In the elastic range, the material behaviour is rate independent and linear until the yield stress, which is strain rate dependent, is reached. Above the dynamic yield level, the viscoplastic strain is activated which is governed by rate sensitive flow rule in which the fluidity parameter is developed as a function of the strain rate to account for the rate dependence of the nonrecoverable deformations.

5.7.2 DYNAMIC YIELD STRESS AND HARDENING RULE

The initial dynamic stress is assumed to be a function of the static yield stress, σ^s_{ys} and the strain rate, $\dot{\varepsilon}$, as follows

$$\sigma^s_{yd} = \sigma^s_{ys} \; \phi_s \; (\dot{\varepsilon}) \qquad (5\text{-}130)$$

where ϕ_s $(\dot{\varepsilon})$ is the strain rate sensitivity function for

steel yield stress and which is given by Symmond's equation [196] as

$$\phi_s(\varepsilon) = 1 + \left(\frac{\dot{\varepsilon}}{40}\right)^{1/n} \qquad (5\text{-}131)$$

in which n is a coefficient dependent on the grade of steel. A value of 5 for n has been adopted for the commonly used hot-rolled reinforcing steel. The rate sensitivity function is plotted in Figure (5-20).

An isotropic linear hardening rule was employed whereby the current effective stress level, τ^s, above the initial dynamic yield stress is defined as a linear function of the current viscoplastic strain, ε_{vp}

$$\tau^s = \sigma^s_{yd} + H\,\varepsilon_{vp} \qquad (5\text{-}132)$$

where H is the slope of the stress-viscoplastic strain curve, known as the hardening modulus, which is expressed as

$$H = 0 \quad \text{for no hardening} \qquad (5\text{-}133)$$

$$H = E_t / (1 - E_t / E) \quad \text{for linear hardening} \qquad (5\text{-}134)$$

in which E_t is the slope of the stress-strain curve in the viscoplastic range and E is the initial modulus of elasticity of steel.

5.7.3 STRAIN RATE SENSITIVE FLOW RULE

(i) Viscoplastic strain rate

Following Perzyna's associative flow rule [76], the rate of viscoplastic straining in the direction of reinforcement is assumed to be

$$\dot{\varepsilon}_{vp} = \gamma_s\,(\sigma - \tau^s) \qquad |\sigma| > |\tau^s| \qquad (5\text{-}135)$$

$$\dot{\varepsilon}_{vp} = 0 \qquad |\sigma| \le |\tau^s| \qquad (5\text{-}136)$$

in which σ denotes the stress level in the steel. It is

generally observed from dynamic experiments [111, 189, 190] that the behaviour beyond yield is strongly affected by the strain rates.

To include this rate dependence, the associated flow rule is modified by assuming that the fluidity parameter, a measure of the rate of yielding, is a function of the strain rate as for concrete.

$$\dot{\varepsilon}_{vp} = \gamma_s (\dot{\varepsilon}) (\sigma - \tau^s) \qquad | \sigma | > | \tau | \qquad (5\text{-}137)$$

$$\dot{\varepsilon}_{vp} = 0 \qquad | \sigma | \leq | \tau | \qquad (5\text{-}138)$$

By assuming constant strain rate conditions similar to concrete, the relationship between the fluidity parameter and the strain rate is obtained using the uniaxial elasto-viscoplastic stress-strain relation of the proposed steel model and the results of the dynamic tests.

(ii) Elasto-viscoplastic stress-strain relation

The total strain rate, $\dot{\varepsilon}$, is resolved into elastic and viscoplastic parts

$$\dot{\varepsilon} = \dot{\varepsilon}_e + \dot{\varepsilon}_{vp} \qquad (5\text{-}139)$$

where the elastic strain rate, $\dot{\varepsilon}_e$, is expressed as

$$\dot{\varepsilon}_c = \dot{\sigma} / E \qquad (5\text{-}140)$$

Using (5-137) and (5-140) and considering a loading history for which the total strain rate, $\dot{\varepsilon}$, is constant specified as C_s, ($\gamma_s(\dot{\varepsilon}) = \gamma_s$), equation (5-139) can be rearranged and rewritten in the form

$$\dot{\sigma} + E \gamma_s (\sigma - \tau^s) - C_s = 0 \qquad (5\text{-}141)$$

Taking the time derivative of (5-141) results in the following second order differential equation

$$\dot{\sigma}^{\cdot} + E \gamma_s (\dot{\sigma} - \dot{\tau}^s) = 0 \qquad (5\text{-}142)$$

Differentiating (5-132) with time and using (5-139) and (5-140), the effective stress derivative, $\dot{t}^s$ is expressed as

$$\dot{t}^s = H \left(C_s - \frac{\dot{\sigma}}{E} \right) \qquad (5\text{-}143)$$

Substituting (5-143) into (5-142) and rearranging, can be rewritten as

$$\dot{\sigma} + \gamma_s (E + H) \sigma = E \gamma_s H C_s \qquad (5\text{-}144)$$

The general solution of the differential equation (5-144) is found as

$$\sigma = C_1 + C_2 e^{-\gamma_s (E + H) t} + \frac{E H}{E + H} C_s \qquad (5\text{-}145)$$

in which C_1 and C_2 are integration constants. With the initial conditions at yield point

$$\sigma \left(t_o\right) = \sigma^s_{yd} \quad , \quad \dot{\sigma} \left(t_o\right) = C_s E \qquad (5\text{-}146)$$

and the time-strain relations

$$t_o = \varepsilon^s_{yd} / C_s \quad , \quad t = \varepsilon / C_s \qquad (5\text{-}147)$$

in which ε^s_{yd} is the dynamic initial yield strain of steel, then equation (5-145) is rewritten as

$$\sigma = \sigma^s_{yd} + \frac{E^2 \dot{\varepsilon}}{\gamma_s (E + H)^2} \left[1 - e^{-\frac{\gamma_s (E + H)}{\dot{\varepsilon}} (\varepsilon - \varepsilon^s_{yd})} \right]$$

$$+ \frac{E H}{E + H} \left(\varepsilon - \varepsilon^s_{yd} \right) \qquad (5\text{-}148)$$

For perfectly viscoplastic material, H = 0, and the equation (5-148) reduces to

$$\sigma = \sigma^s_{yd} + \frac{\dot{\varepsilon}}{\gamma_s} \left[1 - e^{-\frac{\gamma_s E}{\dot{\varepsilon}} \left(\varepsilon - \varepsilon^s_{yd} \right)} \right] \qquad (5\text{-}149)$$

(iii) Identification of the rate dependent steel fluidity parameter

Using servo-hydraulic testing equipment, Ammann et al [188] and Limberger et al [189] have conducted numerous uniaxial tests on reinforcing steel to determine the influence of increasing strain rates on yield stress, tensile strength and corresponding strains. Based on the results, complete stress-strain curves for different strain rates were established. These are shown in Figure (5-21).

For the determination of steel fluidity parameter, the following comments are made:

a - All tests were conducted under constant strain rate conditions.

b - Based on the experimental results, the elasticity modulus is strain rate insensitive and its value is 200 kN/mm^2.

c - Linear hardening representation was applied to fit the experimental results in the inelastic part of the stress-strain curve.

Similar procedure to that of concrete fluidity parameter identification was followed to define the fluidity parameter of steel which is valid for a particular constant strain rate test in conjunction with expression (5-149). Different strain rate tests give different values of the fluidity parameter. Similar to concrete, the linear fitting between log γ_s and log $\dot{\varepsilon}$ seemed reasonable and the following relation is established

$$\log \gamma_s = K_1 + K_2 \log \dot{\varepsilon} \qquad (5\text{-}150)$$

$$\gamma_s = 10^{k_1} \dot{\varepsilon}^{k_2} \qquad (5\text{-}151)$$

where the parameter K_1 and K_2 are found to be -0.909 and 0.954, respectively (Fig 5-22). Equation (5-151) is valid for the strain rate range 10^{-5} $sec^{-1} \leq \dot{\varepsilon} \leq 10$ sec^{-1}.

5.7.4 STRESS-STRAIN RELATIONSHIP OF STEEL

In the elastic range, the stress-strain relation is governed by uniaxial Hooke's law as

$$\sigma = E\,\varepsilon \tag{5-152}$$

For stress points above the dynamic yield stress, the constitutive relation is given as

$$\sigma = E\,\varepsilon_c \tag{5-153}$$

or

$$\sigma = E\,(\varepsilon - \varepsilon_{vp}) \tag{5-154}$$

At time t, the viscoplastic strain ε_{vp} is computed as

$$\varepsilon_{vp} = \int_o^t \dot{\varepsilon}_{vp}\, dt \tag{5-155}$$

where the viscoplastic strain rate is to be determined by the rate dependent flow rule described earlier. The time integration of equation (5-155) is numerically performed and explained later in Chapter 6.

5.8 EXPERIMENTAL CHARACTERISATION

A rate and history dependent constitutive model is developed for concrete in which the compressive behaviour is modelled as elesto-viscoplastic material and in tension as a linear elastic strain softening material. Ideally two tests, uniaxial compressive and uniaxial tensile loading tests, are required to obtain all the information necessary to define the constitutive law in the computer input data. Whereas usually in practical situations, only the uniaxial compressive strength is available, it is necessary to estimate the values of remaining properties. The necessary material parameters are listed with their approximate values as follows:

1. Young's modulus, E, given [198] in N/mm^2 as

$$E = K_o + 0.2\ \sigma'_{ch} \qquad (5\text{-}156)$$

in which K_o is a constant closely related to the modulus of elasticity of the aggregate, taken as 20 kN/mm^2 for normal weight concrete σ'_{ch} is the characteristic cube strength of concrete is N/mm^2.

2. Poisson's ratio υ = 0.15 - 0.2

3. Elastic limit factor, 0.3 - 0.4.

4. Uniaxial compressive strength, σ'_{cs}.

5. Peak compressive strain, ε'_{cs} = 0.002 - 0.0025.

6. Uniaxial tensile strength, $\sigma'_{ts} \cong 0.1\ \sigma'_{cs}$.

7. Cracking strain $\varepsilon'_{ts} = \sigma'_{ts}/E$

8. Crushing strain, ε_{cu} = 0.0035.

9. Maximum limiting tensile strain, ε_m = 0.004 - 0.005.

10. Concrete fracture energy, G_f, given in Nm/m^2 [199] as

$$G_f = a_f \left(\sigma'_{ch}\right)^{0.7}$$

The coefficient a_f depends on the maximum aggregate size with 6 as an average value.

11. Fluidity parameters, B_1 and B_2, to be determined from Table 5-2 according to the value of σ'_{cs}.

Steel is modelled as rate dependent uniaxial elasto-viscoplastic material with linear hardening in which the following material parameters are needed for characterisation.

1. Young's modulus (= 200 kN/mm^2).

2. Steel yeild stress (= 250 N/mm^2 for mild steel, 460 N/mm^2 for high yield steel).

3. Hardening moduls, H.

4. Fluidity parameters, K_1 and K_2, (-0.909, 0.954 respectively).

Finally, the validation of the proposed models is established in Chapter 8 through the analysis of several applications and a parametric study is also presented to highlight the significance of strain rate effect and main material nonlinearities on the response of reinforced concrete structures.

Table (5-1) Material constants of the proposed failure criteria

Function i	1	2	3	4
$\sigma'_{cb} / \sigma'_{cs}$	1.18	1.16	1.18	1.16
$\sigma'_{cb2} / \sigma'_{cs}$	1.30	-	-	1.280
a_i	0.154	0.104	-	0.046
b_i	0.001	-	-0.094	-0.039
c_i	1.331	1.323	1.094	1.225

Table (5-2) Material constants of the concrete fluidity parameter

σ'_{cs} N/mm^2	18.3	27.0	44.2	59.4
B_1	0.437	-0.143	-0.384	-1.01
B_2	0.437	-0.143	-0.384	-1.01

Table (5-3) Compound material constants of the proposed failure criteria

Function i	A_i	B_i	C_i
1	a_1	b_1	c_1
2	$1.5\ a_2$	$1.25\ a_2^2$	c_2
3	0.0	b_3	c_3
4	2	$3a_4^2 + b_4$	c_4

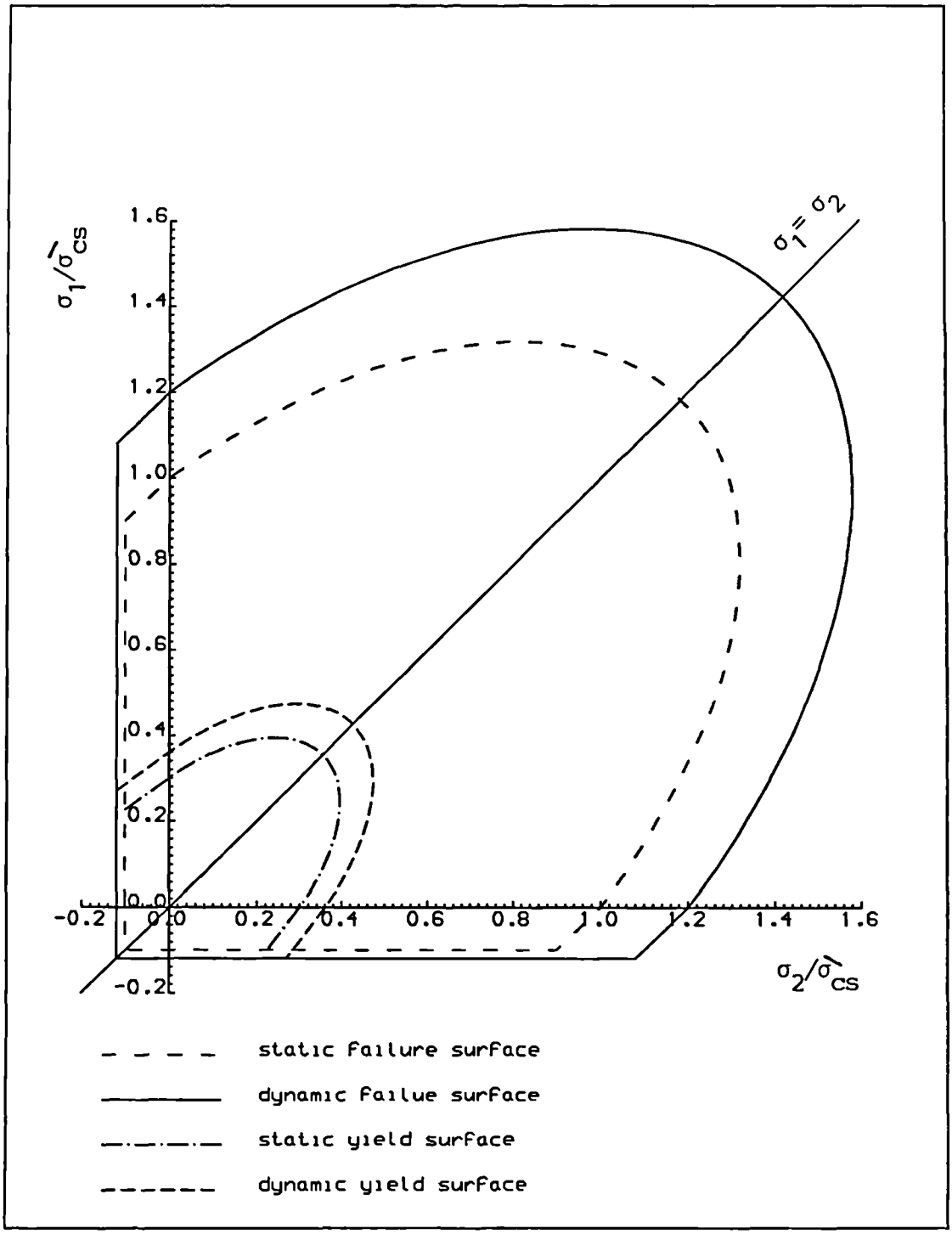

Figure 5.1 2D Stress space representation of the concrete constitutive model

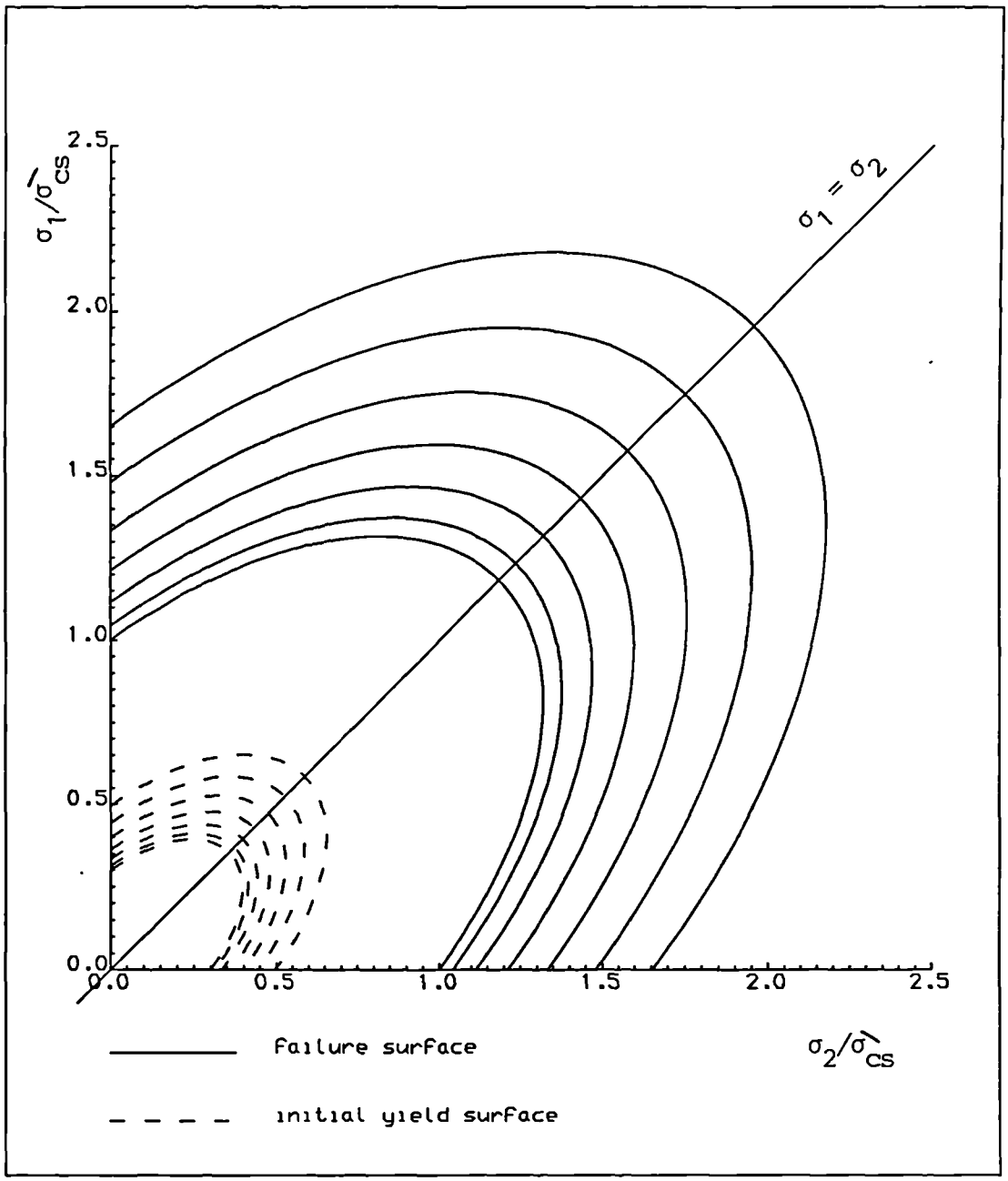

Figure 5.2 Effect of strain rate on the failure and initial yield surfaces

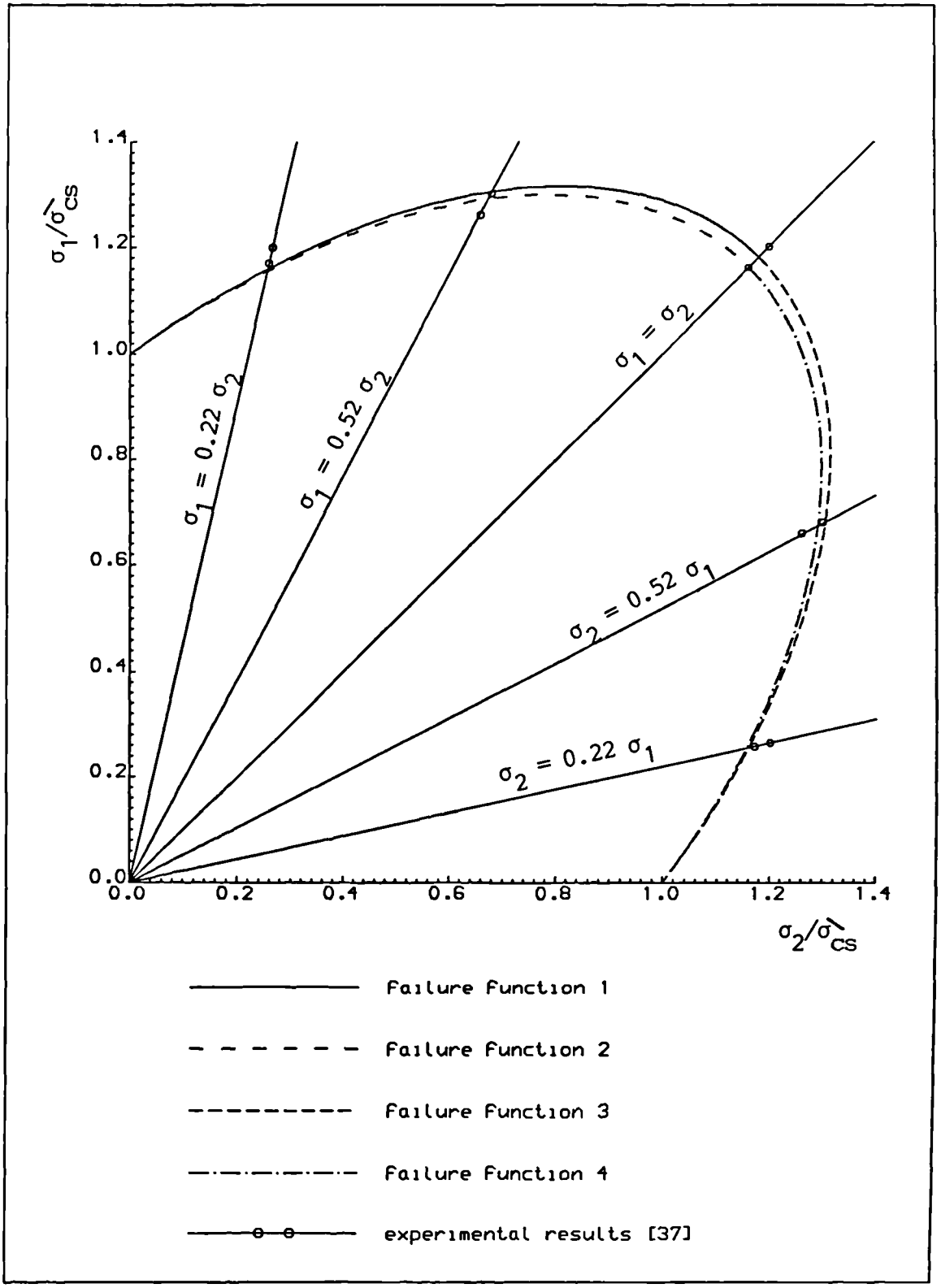

Figure 5.3 Comparison of the proposed failure functions with Kupfer's results

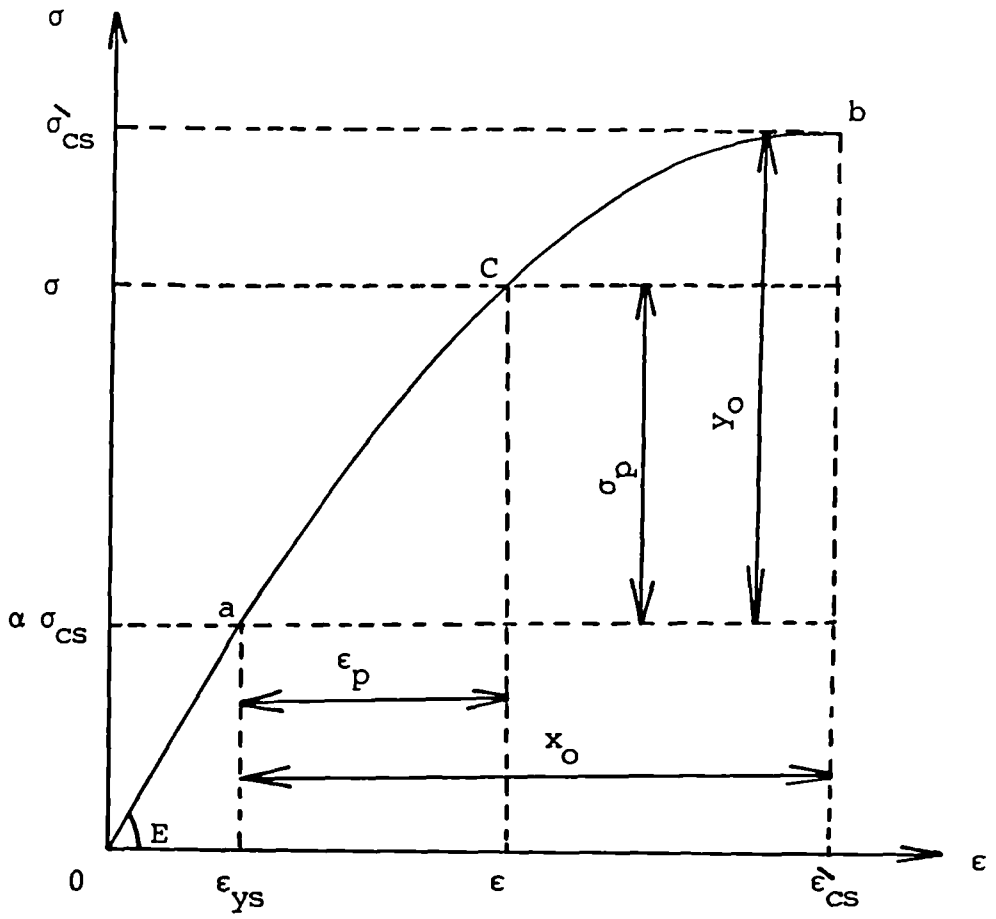

Figure 5.4 Uniaxial stress-strain diagram in the pre-fracture range

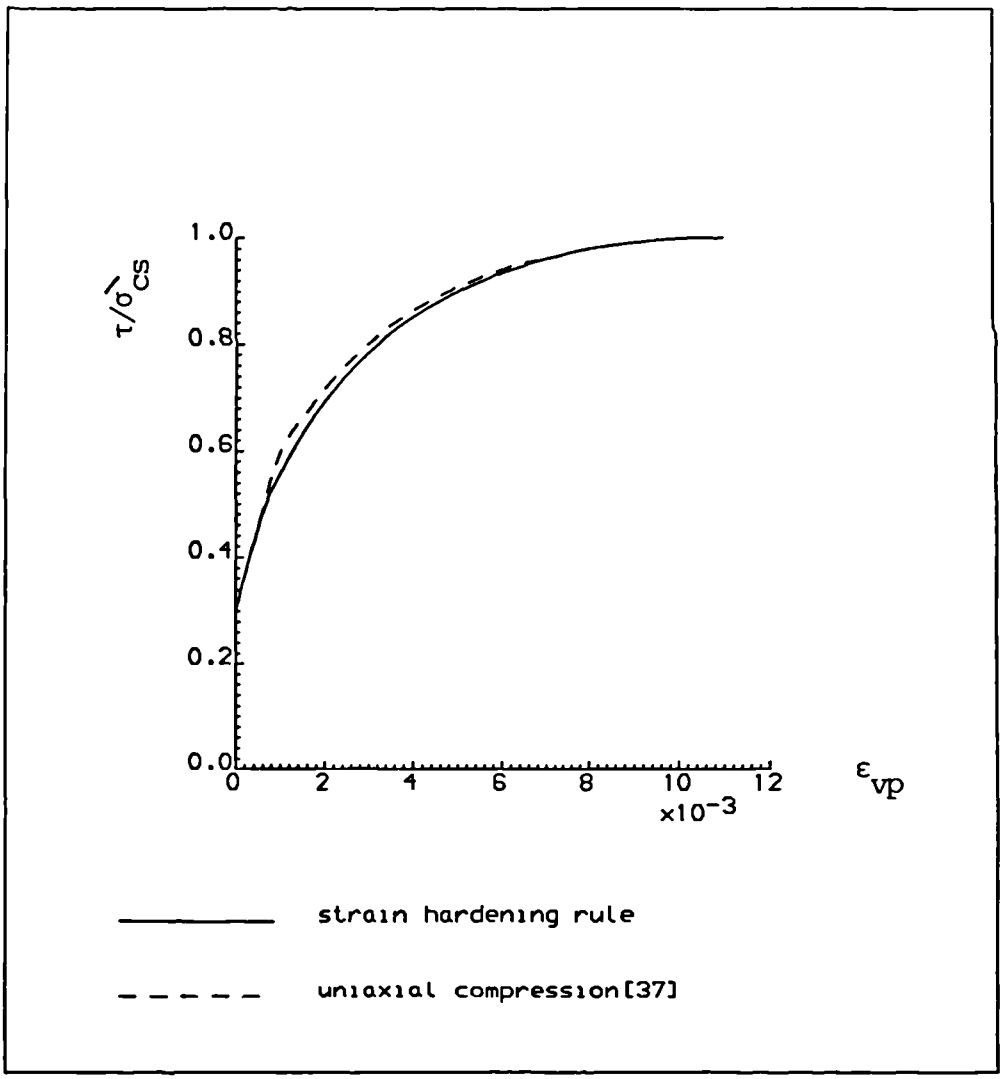

Figure 5.5 Comparison of static hardening function with Kupfer's uniaxial results

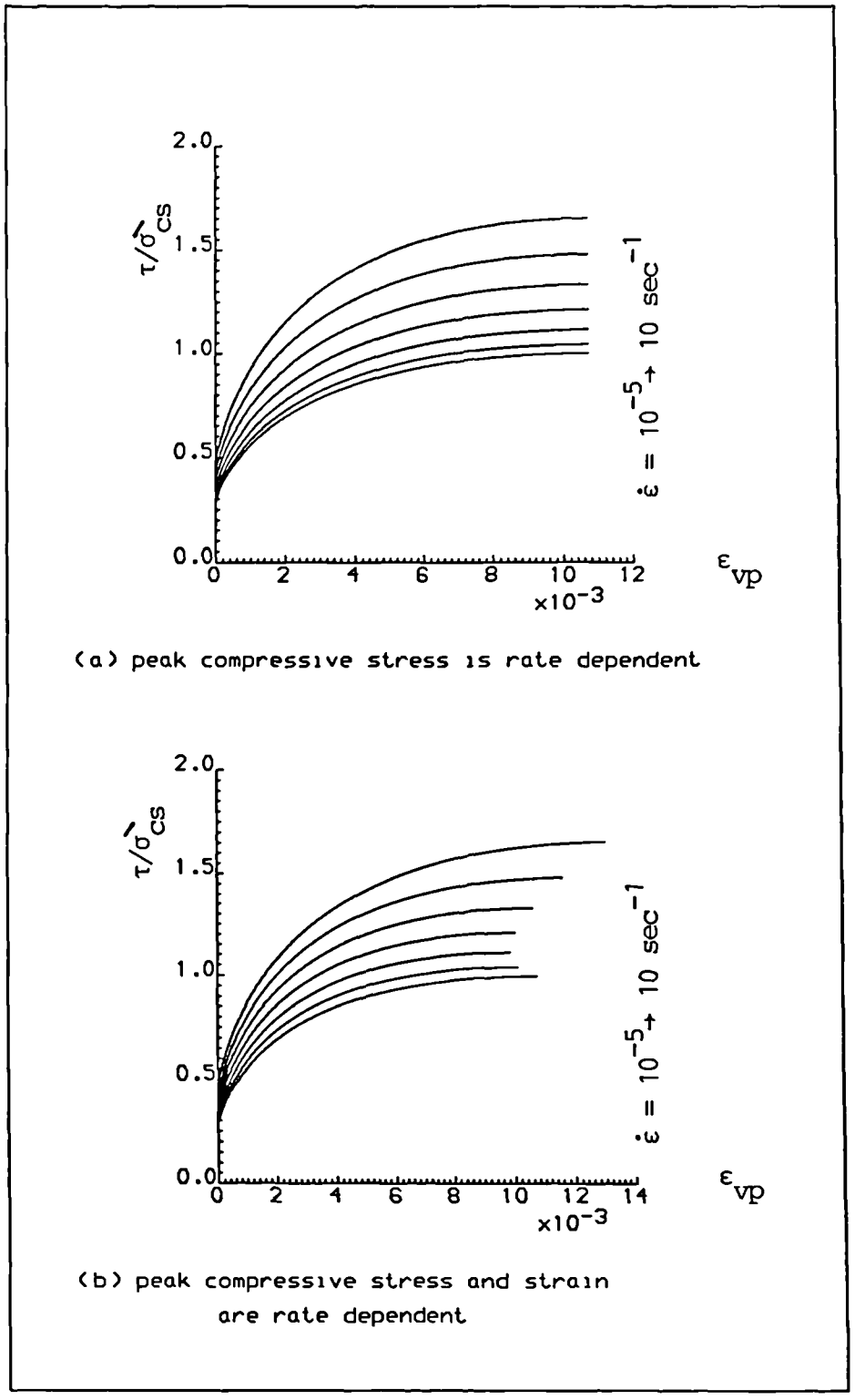

Figure 5.6 Dynamic hardening rule as influenced by strain rate

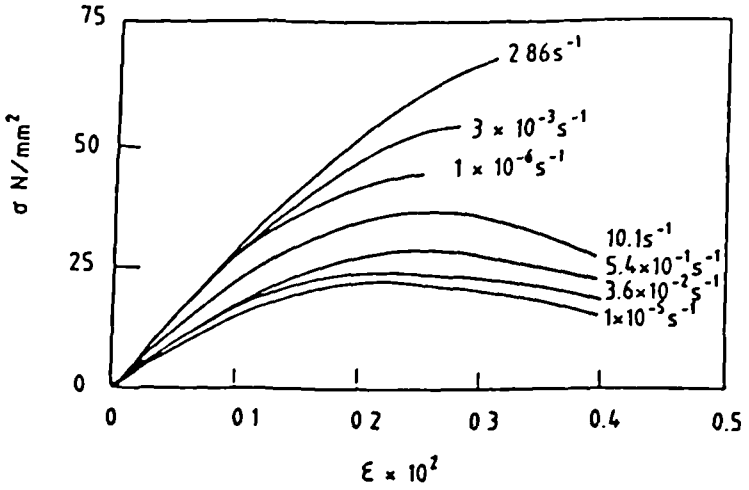

a) Watstein test results [16]

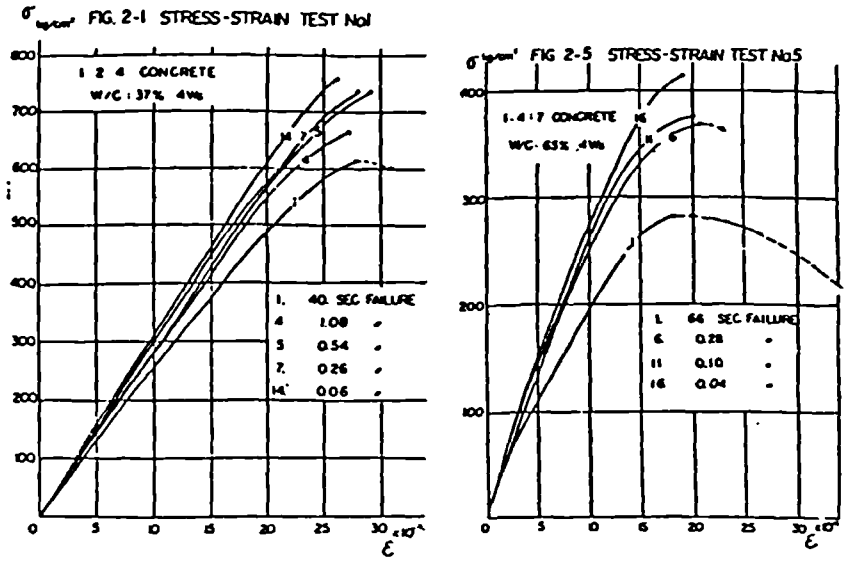

b) Hatano test results [17]

Figure 5.7 Effect of strain rate on compression curves of concrete

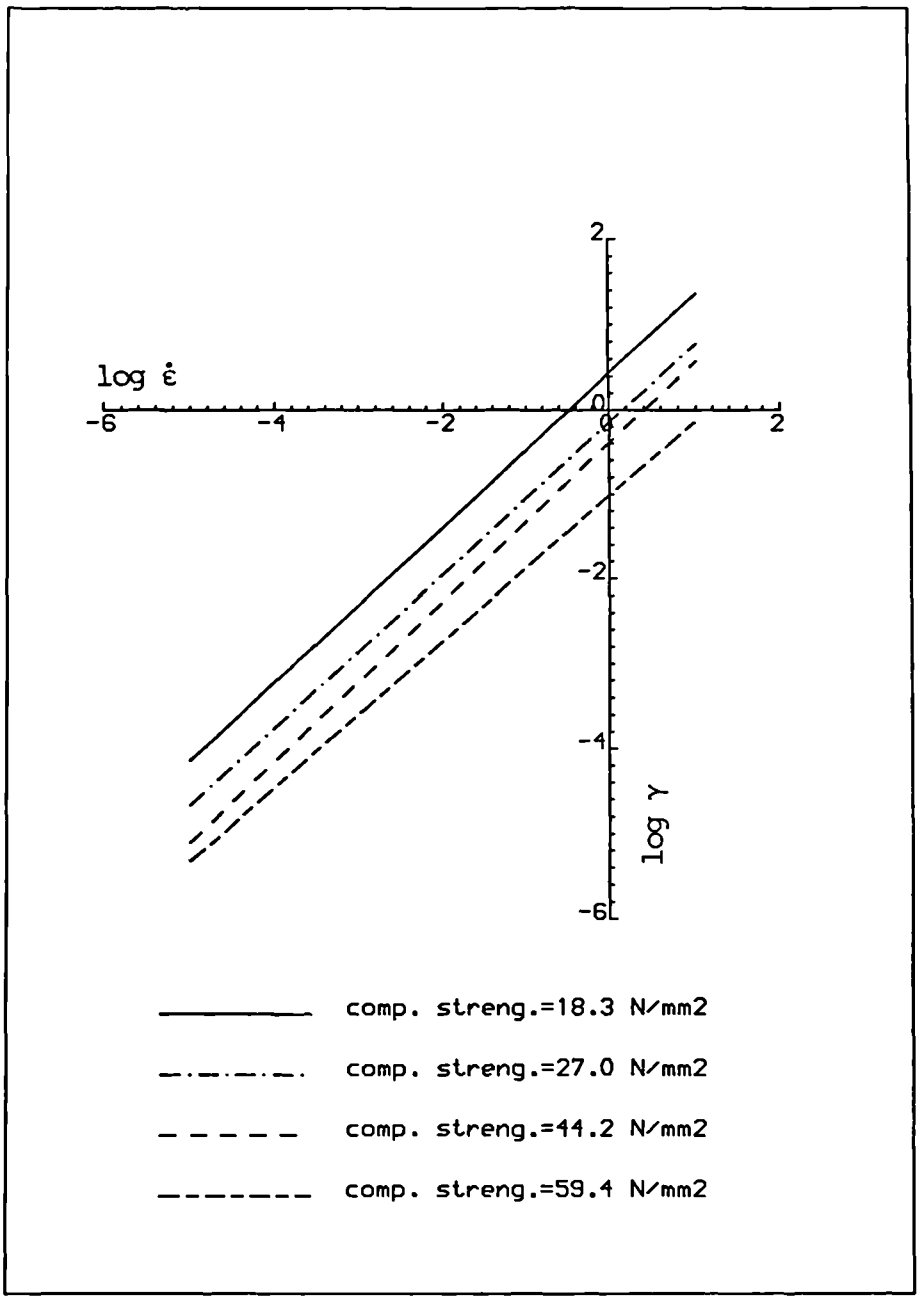

Figure 5.8 Fluidity parameter versus strain rate for different grades of concrete

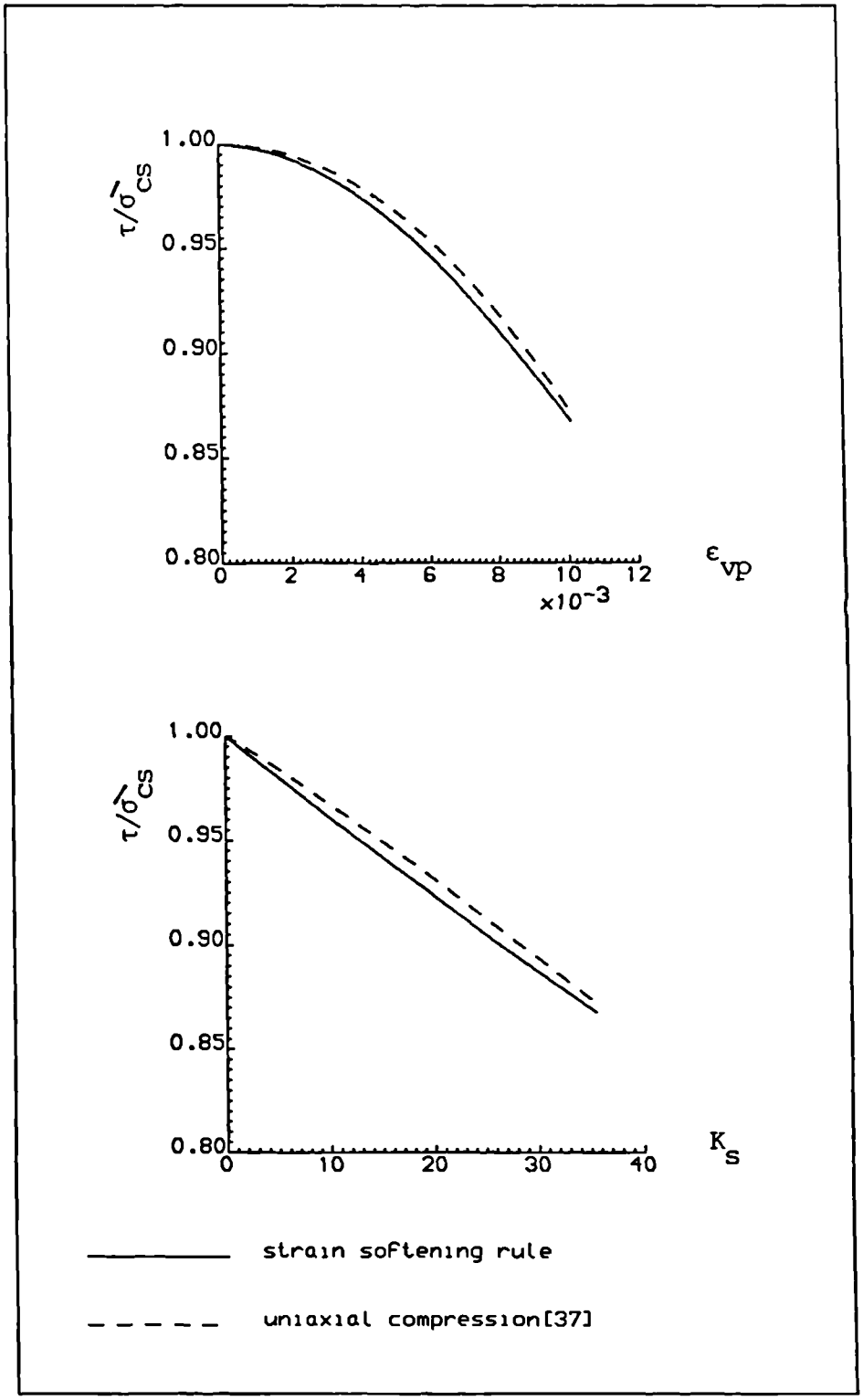

Figure 5.9 Comparison of softening rule in compression with Kupfer's uniaxial results

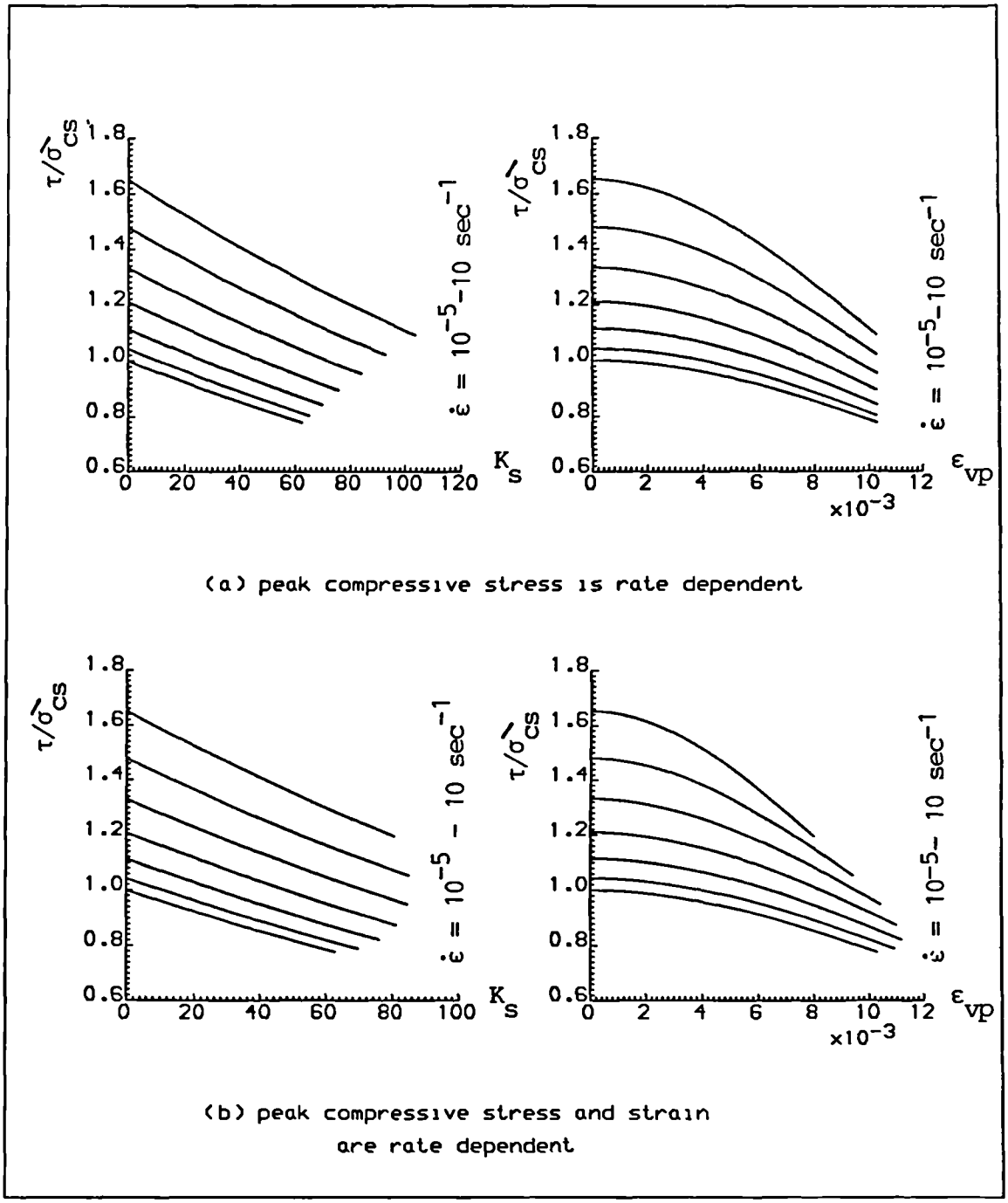

Figure 5.10 Effect of strain rate on dynamic softening rule

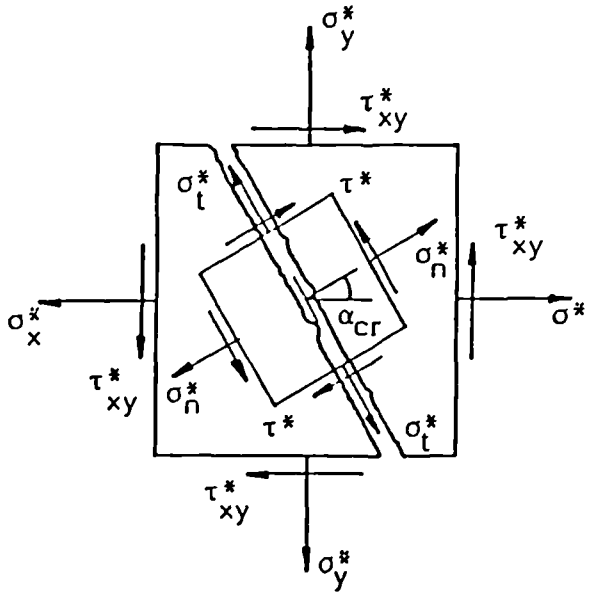

Figure 5.11 Stresses after crack initiation [27]

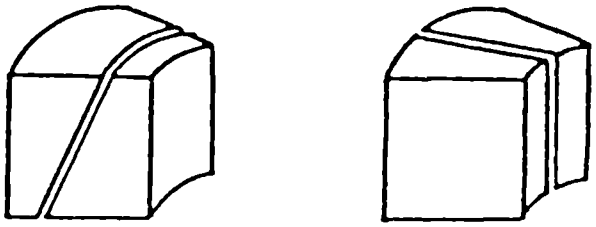

a) Circumferential crack b) Radial crack

Figure 5.12 Cracking types for axisymmetry

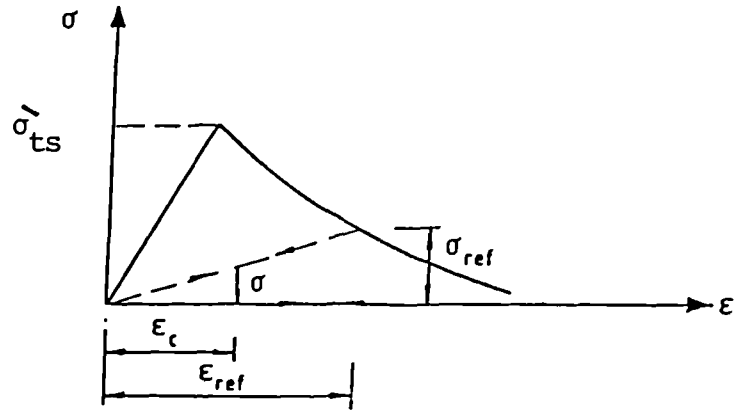

Figure 5.13 Strain-softening curve with secant unloading and reloading [78]

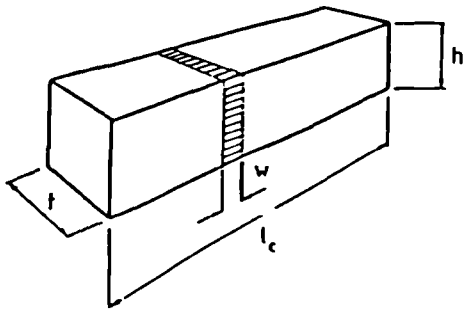

Figure 5.14 Illustration of characteristic length for a prismatic control volume [78]

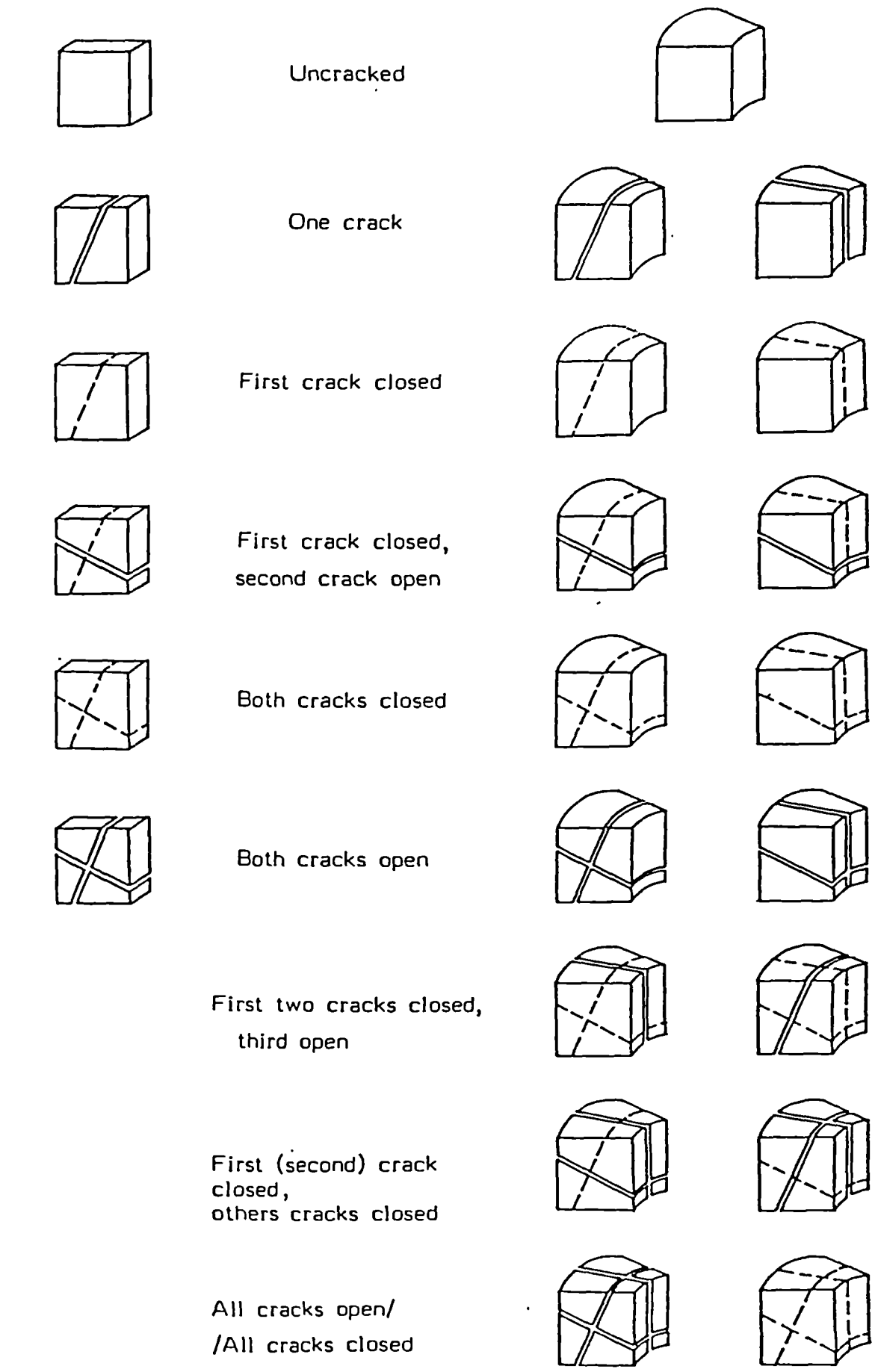

Figure 5.15 Possible crack configurations [27]

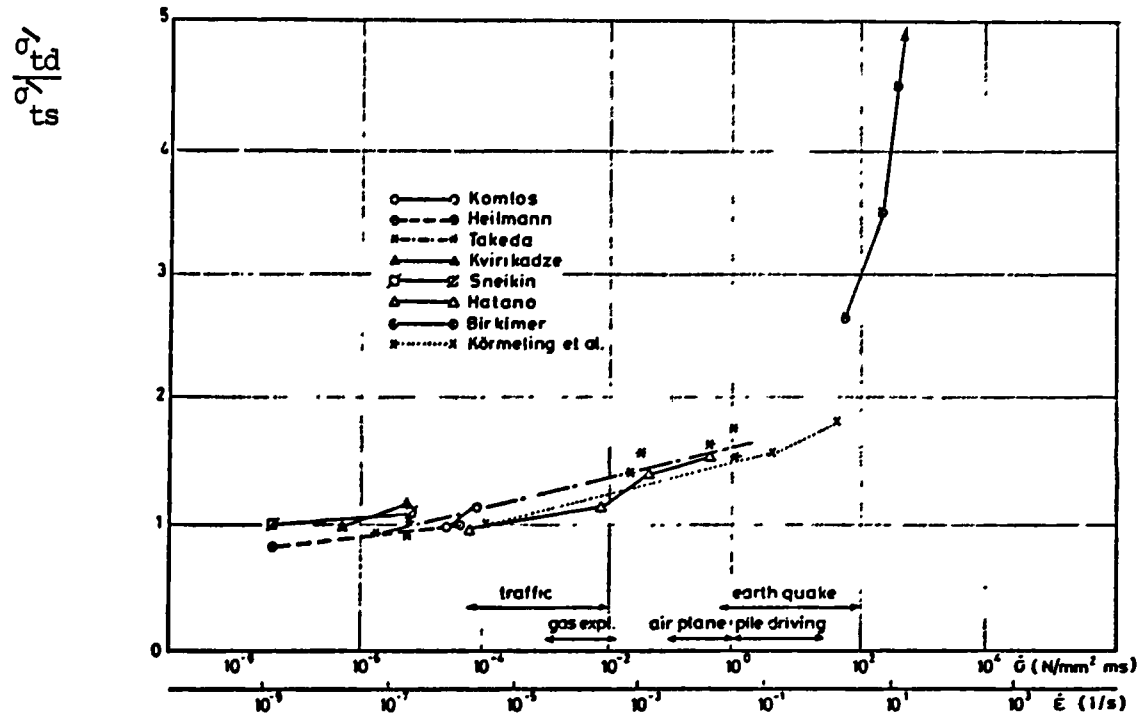

Figure 5.16 Dynamic tensile testing results reported in the literature [197]

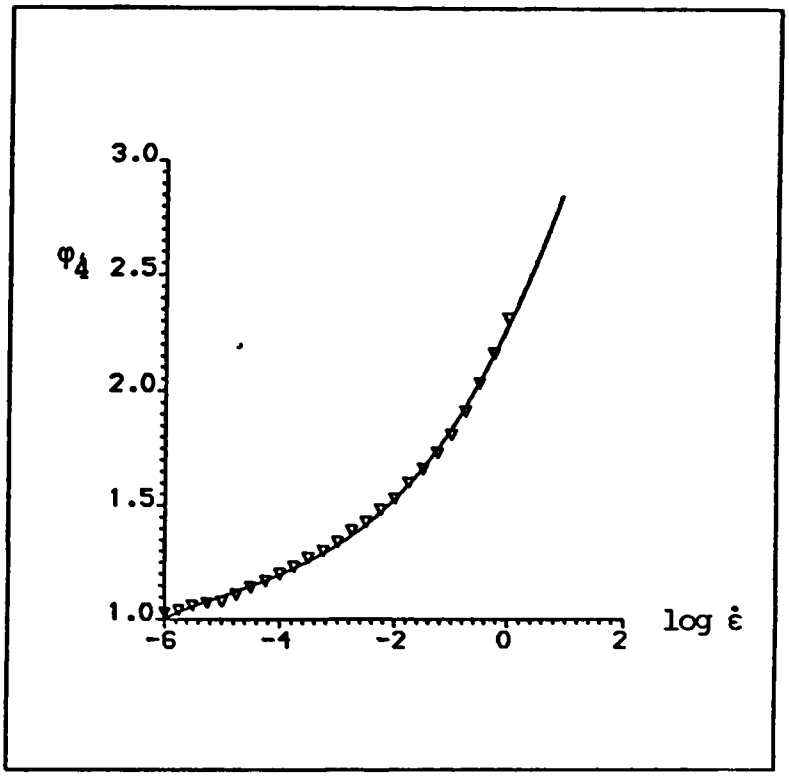

Figure 5.17 Proposed tensile strength rate sensitivity function

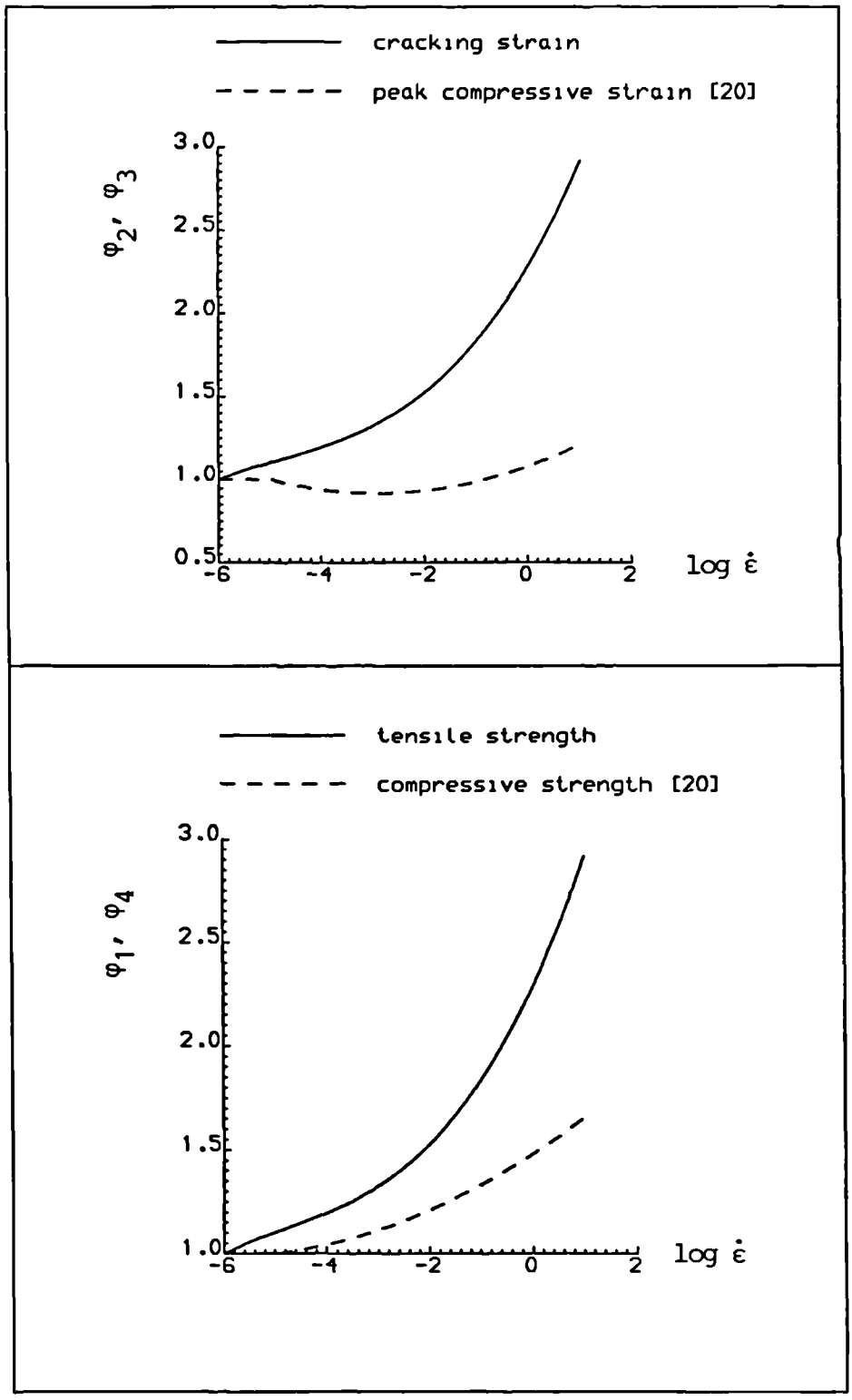

Figure 5.18 Strain rate sensitivity functions of concrete in tension and compression

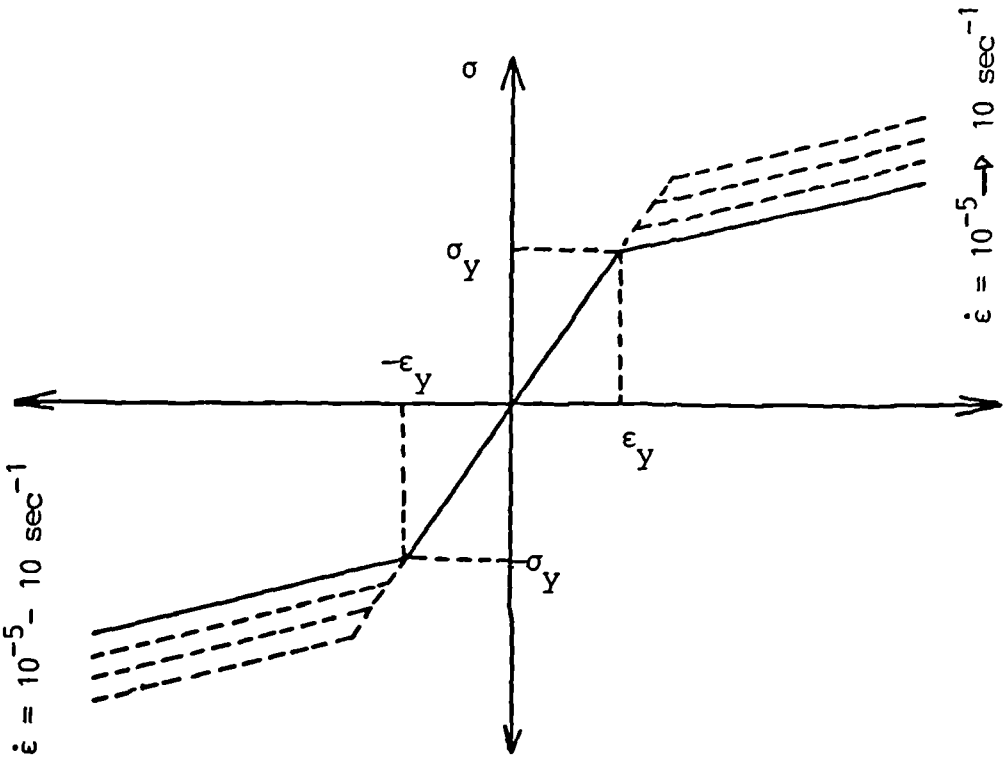

Figure 5.19 Uniaxial stress-strain diagram of steel

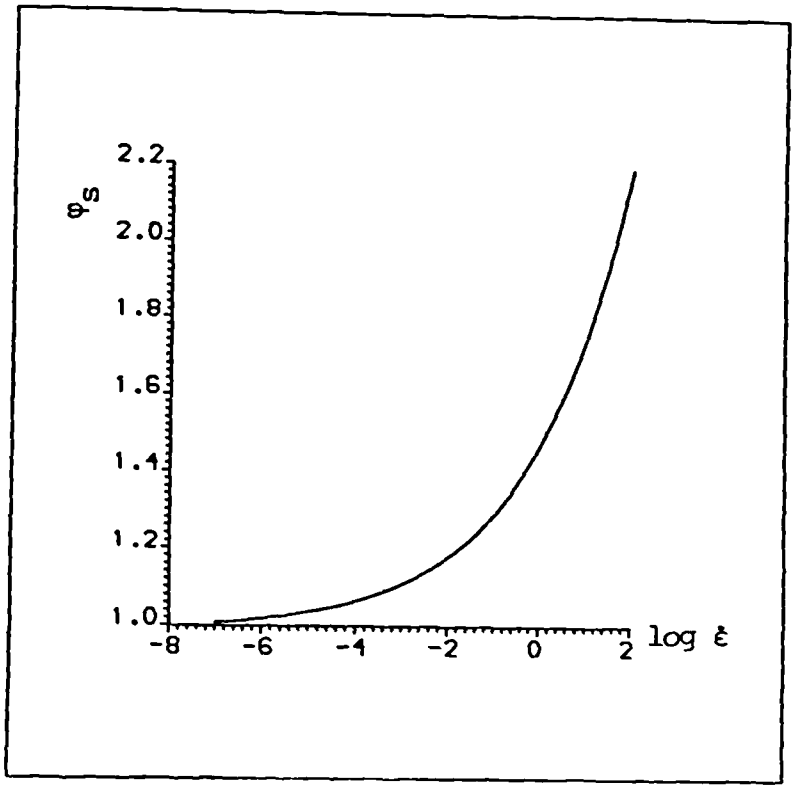

Figure 5.20 Strain rate sensitivity function of steel yield stress [196]

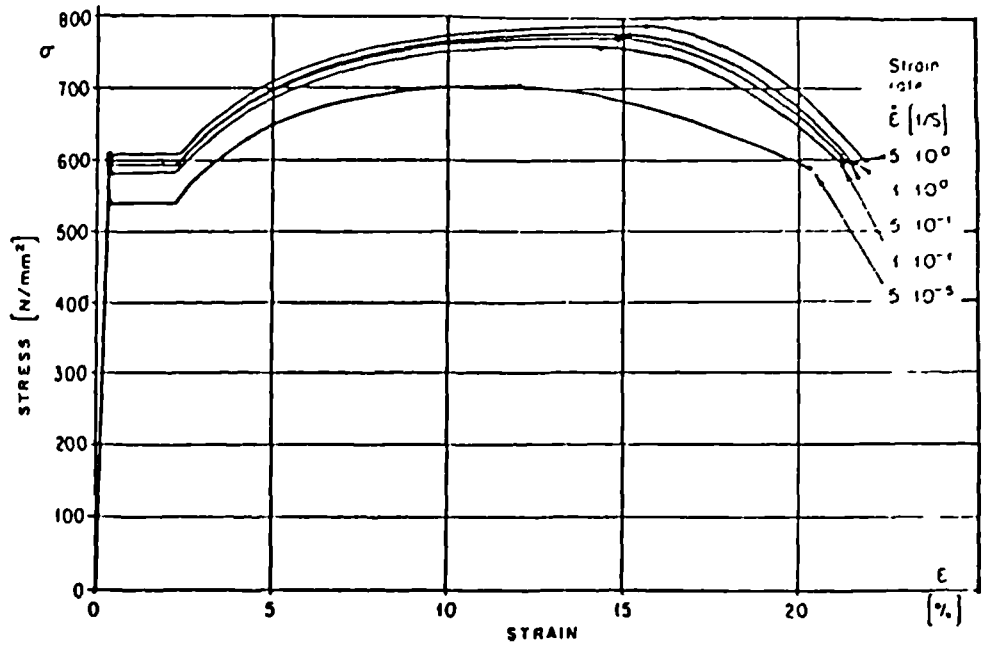

a) Ammann et al test results [188]

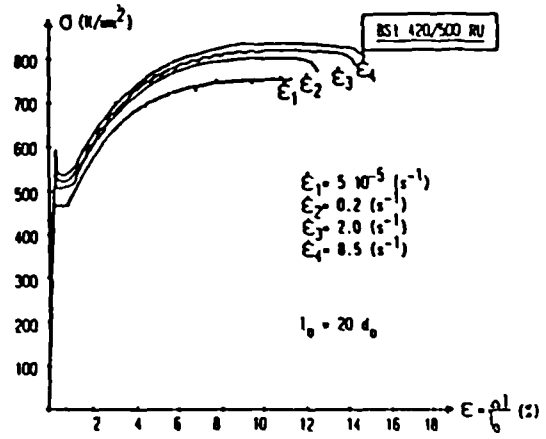

b) Limberger et al test results [189]

Figure 5.21 Dynamic stress-strain curves of steel [188, 189]

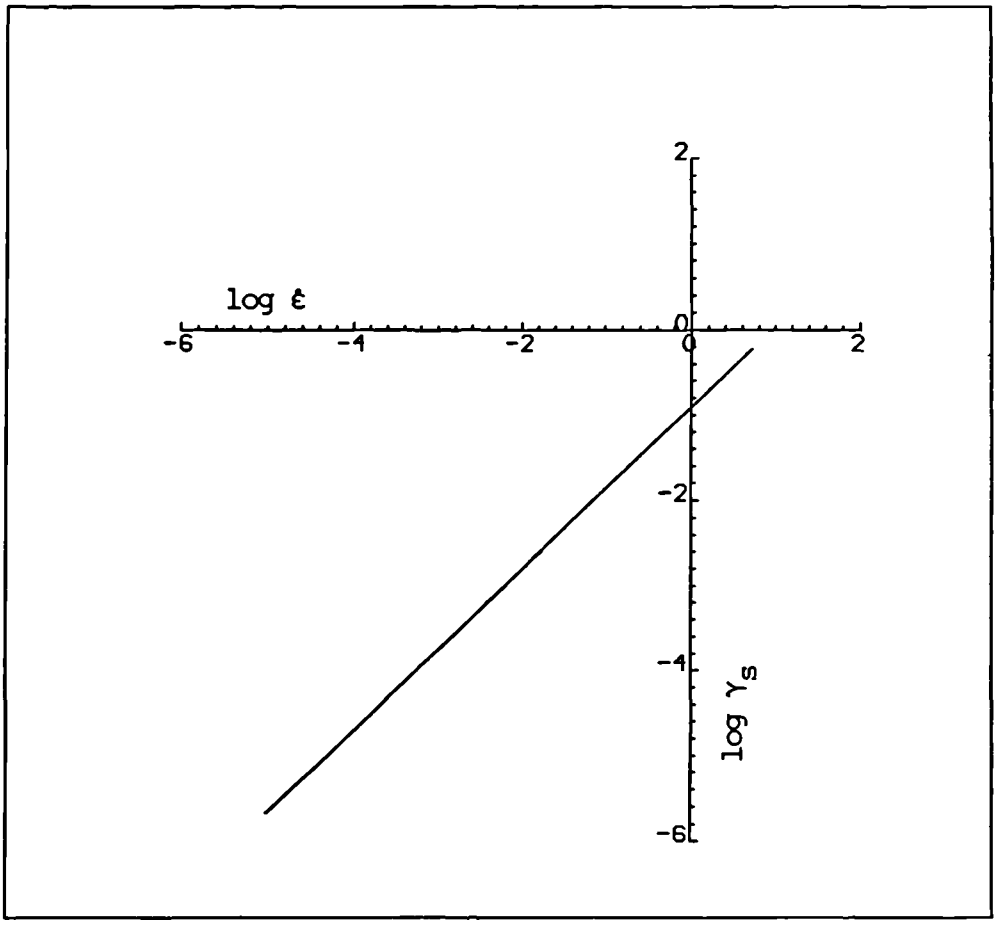

Figure 5.22 Fluidity parameter plotted against strain rate for steel

CHAPTER 6

DISCRETIZATION IN TIME AND THE SOLUTION TECHNIQUES

6.1 INTRODUCTION

In the last ten years, significant advances have been made in the development and application of numerical methods to the solutions of transient engineering problems. A primary factor in this progress has been the parallel development of large high speed digital computers providing the faster execution times required to make the solution of complex engineering problems a feasible proposition.

In previous chapters, the finite element spatial discretization of the dynamic equilibrium equations (Chapter 4) and the strain rate dependent constitutive material relations for concrete and steel (Chapter 5) were considered. In both cases time dependent sets of differential equations were obtained. The discretization in space transforms the original systems of hyperbolic differential equations to a system of second order ordinary differential equations. The equations of motion have the general form

$$M \ddot{d} + C \dot{d} + P(d) = Q \qquad (6\text{-}1)$$

The elasto-viscoplastic constitutive relationship of concrete is given as

$$\dot{\varepsilon} = \dot{\varepsilon}_e + \dot{\varepsilon}_{vp} \qquad (6\text{-}2)$$

$$\dot{\varepsilon} = D^{-1} \dot{\sigma} + \gamma (\dot{\varepsilon}_{eff}) < \phi (F) > \frac{\partial f}{\partial \sigma} \qquad (6\text{-}3)$$

For reinforcing steel a similar constitutive relationship is adopted but in uniaxial form.

The coupling of these two sets of equations can be indicated if the internal force vector, P(d) is written as

$$P(d) = \int_v B^T \sigma \, dv \qquad (6\text{-}4)$$

or
$$P(d) = \int_v B^T D (\varepsilon - \varepsilon_{vp}) \, dv \qquad (6\text{-}5)$$

Substituting (6-5) in equation (6-1) and rearranging results in

$$M \ddot{d} + C \dot{d} + \int_v B^T D \varepsilon \, dv = Q + Q_{vp} \qquad (6\text{-}6)$$

in which Q_{vp} denotes the equivalent force vector associated with the viscoplastic strain.

$$Q_{vp} = \int_v B^T D\varepsilon_{vp} \, dv \qquad (6\text{-}7)$$

The equations which govern viscoplastic strain run parallel in time. The viscoplastic strain is obtained by integrating the viscoplastic strain rate:

$$\varepsilon_{vp} = \int_o^t \dot{\varepsilon}_{vp} \, dt \qquad (6\text{-}8)$$

The complexity of these governing equations excludes the possibility of finding a general closed form solution in the time domain. Consequently, both equations (6-6) and (6-8) must be discretized in time to obtain a numerical solution.

The subject of this chapter is the temporal discretization and solution techniques of the time dependent governing differential equations. A refined explicit central difference time integration scheme is developed for the semi-discretized equations of motion. A simple *a priori* stability criterion based on theoretical and experiemntal considerations is derived for the definition of time increment for Euler explicit scheme adopted for the viscoplastic strain rate governing equations.

The dynamic equilibrium equations are considered in section

6.2 and the time rate constitutive equations in section 6.3, the selection of time increment for nonlinear analysis in section 6.4 and the final section discusses some practical considerations in explicit integration employed.

6.2 TIME DISCRETIZATION OF NONLINEAR DYNAMIC EQUILIBRIUM EQUATIONS

6.2.1 REVIEW OF TIME INTEGRATION METHODS

A brief review of time integration methods is now given to select the most suitable numerical scheme for blast loading conditions. A comprehensive review can be found elsewhere [161, 200-207]. *In practical finite element analysis*, the procedures for numerical solution of the dynamic equilibrium equations given by (6-1) can be divided into two groups: modal superposition technique and direct integration methods.

(i) Modal superposition technique

The dynamic response is obtained by solving separately for each mode of vibration of the structure. The modes are then weighted by the respective modal amplitude and superposed. Practical applications are usually limited to linear problems [161, 203, 204]. The use of modal superposition in nonlinear dynamics can be effective only if a relatively few modes need to be considered in the analysis and if the system is only locally nonlinear [93, 161, 203, 204].

(ii) Direct integration methods

The ease of implementation of these methods along with their ready usability in nonlinear studies has tended to enhance rapidly the popularity of these techniques. In these methods, the dynamic equilibrium equations (6-1) are integrated by a numerical step by step procedure and no transformation of the equations is needed. The method is based on two assumptions [161, 203, 204]:

(1) The equations (6-1) are only satisfied for certain discrete time stations which are assumed to be Δt apart along the time axis.

(2) The variation of accelerations, velocities and displacements within Δt are approximated, giving rise to several direct integration schemes with different respective accuracy, cost and numerical stability.

The approximations in time domain may be based either on finite elements or finite differences. For dynamic problems, the finite element spatial discretization is most often complemented by a finite difference time solution. However, consistent space-time finite elements have been proposed [160], but this approach is not considered here. Assuming that the nodal values at time t_n are known, the requirement is to advance the solution to obtain the corresponding nodal values at time $t_{n+1} = t_n + \Delta t$. Basically, there are two groups of time stepping schemes: explicit and implicit methods. Each approach employs difference equivalents to develop recurrence relations which can be used in a step by step computation of the response.

Explicit methods

In these methods, the solution at time t_{n+1} is obtained by considering the equilibrium conditions at time t_n

$$M\ddot{d}_n + C\dot{d}_n + Kd_n = Q_n \qquad (6\text{-}9)$$

Using the difference formulas that relate the accelerations, velocities and displacements, the displacement vector at time t_{n+1} is determined which is not a function of either of the mechanical loads or the structural stiffness of the system at time t_{n+1}. This eliminates the need for iterative calculations and thereby simplifies the computations. There are several publications on accuracy and efficiency studies of different explicit schemes [161, 202-206, 208-211] which

include the central difference, the Runge-Kutta and the Taylor expansion methods. Among these schemes, the central difference was found to be the most efficient due to its simplicity and relatively large critical time step. For practical solutions, the second order accuracy of the central difference method is sufficient and the higher accuracy achieved by the higher order methods such as Runge-Kutta, does not compensate for the extra computational effort [206, 212]. In central difference scheme, the acceleration and velocity at time t_n are approximated through

$$\ddot{d}_n = \frac{1}{\Delta t^2} (d_{n+1} - 2\, d_n + d_{n-1}) \qquad (6\text{-}10)$$

$$\dot{d}_n = \frac{1}{2\Delta t} (d_{n+1} - d_{n-1}) \qquad (6\text{-}11)$$

Substituting the equations (6-10) and (6-11) into (6-9), the algorithm to define the solution at time t_{n+1} becomes

$$d_{n+1} = \left(\frac{1}{\Delta t^2} M + \frac{1}{2\Delta t} C \right)^{-1} Q_n^* \qquad (6\text{-}12)$$

where Q_n^* is the vector known at time t_n

$$Q_n^* = Q_n - \left(K - \frac{2}{\Delta t^2} M \right) d_n - \left(\frac{1}{\Delta t^2} M - \frac{1}{2\Delta t} C \right) d_{n-1} \qquad (6\text{-}13)$$

Diagonalised matrices are usually employed for M and C so that the global system matrices need not be assembled. Also the computer implementation of this method is very simple and complex material models can be easily accommodated. This approach has been successfully applied to a large number of nonlinear dynamic problems of concrete structures [77, 176, 213-215]. However, explicit schemes are conditionally stable and generally require small time steps to be employed to ensure numerical stability. The conditional stability requires the time step size employed to be inversely

proportional to the highest frequency of the discrete system [202].

Implicit methods

For implicitly integrated equations, the solution at time t_{n+1} is given as

$$M \ddot{d}_{n+1} + C \dot{d}_{n+1} + K d_{n+1} = Q_{n+1} \qquad (6\text{-}14)$$

The most popular implicit schemes are those due to Newmark [216], Wilson et al [217], Houbolt [218] and Park [219]. The Wilson scheme is not suited for impulsive types of problems as it shows erroneous over-shoot behaviour [28]. Both the Houbolt and Park schemes are multi-step schemes, i.e. the integration of one time step requires data from several previous steps. The Newmark method is the most widely used in this group, and is based on the following assumptions

$$\dot{d}_{n+1} = \dot{d}_n + \Delta t \left[(1-\delta) \ddot{d}_n + \delta \ddot{d}_{n+1}\right] \qquad (6\text{-}15)$$

$$d_{n+1} = d_n + \Delta t \dot{d}_n + \frac{\Delta t^2}{2} \left[(1-2\beta) \ddot{d}_n + 2\beta \ddot{d}_{n+1}\right] \qquad (6\text{-}16)$$

where the parameters δ and β control the stability and accuracy characteristics of the method. The Newmark family includes as particular cases many well known methods such as the average acceleration method ($\beta = 0.25$, $\delta = 0.5$) and central difference scheme ($\beta = 0$, $\delta = 0.5$).

Substituting $\ddot{d}_{n+1}$ and $\dot{d}_{n+1}$ from equations (6-15) and (6-16) into (6-14), the solution for d_{n+1} can be obtained. However, as d_{n+1} is associated with all matrices in (6-14), at every time step a new set of equations must be solved and the computed displacements are iteratively corrected. Therefore, considerable computational effort is involved for every time

step depending on the complexity of the material model and the nonlinearity which occurs during the interval Δt. Most implicit schemes are unconditionally stable and the selection of the time step is governed by accuracy conditions.

To combine the features of implicit and explicit schemes, the nodal partition techniques [220] and element partition methods [221] have been developed recently by employing different time integrators on different parts of the system. Explicit -explicit subcycling techniques [222] have been used in dynamic problems when the element size varies over the mesh by assigning different time step size to each group of nodes or elements. The above mixed partition schemes are not considered in this thesis.

6.2.2 SELECTING SOLUTION PROCEDURE FOR THE PRESENT ANALYSIS

Generally, linear or nonlinear dynamics problems are classified as wave propagation problems and inertial problems, depending on the effect of the spectral characteristics of the excitation on the overall response [200-202]. The former problems are those in which the behaviour at the wave front is of engineering importance, and in such cases it is the intermediate and high-frequency structural modes that dominate the response throughout the time span of interest. Problems that fall into this category are shock response explosions or impact loading. Other dynamic problems such as seismic response can be considered as inertial and here the response is governed by a relatively small number of low frequency modes. In practice, wave propagation problems are usually best solved by explicit integration techniques whereas implicit methods are more effective for inertial problems. However, the relative economy and applicability of both approaches is also influenced by the topology of the mesh, the material models and the type of computer to be employed. To justify the preference for a specific problem, the pros and cons of

both methods have to be estimated.

In the present work, the explicit central difference scheme has been employed for the integration of equations of motion. Although the scheme is conditionally stable and stringent limits must be imposed on the time step size, it was chosen for the following reasons:

1. Explicit methods are far easier to program and easier for taking into to account the complex material models of concrete and steel suggested in Chapter 5.

2. No iterative solution is needed, which results in considerably less computational effort per time step compared with implicit methods.

3. The utilization of a lumped mass matrix affords significant computational advantages and improved accuracy of the explicit schemes [209] as the errors introduced by the lumped masses and the explicit operator tend to be compensatory.

4. For some forms of the explicit schemes the factorization of the structural matrices are not required and the nodal internal forces and displacements are computed directly without forming the stiffness matrix resulting in reduced core storage requirements. In these cases, the computational cost per time step is independent of the node numbering, and hence the bandwidth of the mesh, enabling much larger problems to be solved.

5. For path- and rate-dependent material models developed here, the time step required, to follow the material's stress history, strain rate dependent parameters and the progressive concrete crack propagation through the structure, is often not much larger than the stability limit of the explicit scheme. Thus the time step limitations are not a particular disadvantage [200, 206].

6. In shock response problems, the high frequency components of the solution contribute significantly to the response so the time steps of the order necessary for

stability of explicit methods are required simply to capture high frequencies with sufficient accuracy [206, 28].

7. The time step size required for sufficient accuracy with rapidly varying blast excitations, and for accurately monitoring the behaviour of the shock wave front, is already very small [176, 202].

8. The amount of user interaction and the level of user experience needed is much less compared with other schemes. Default and experience dependent values for necessary input quantities of implicit methods such as convergence criterion, amplification factors and iterative technique are not required to be specified.

6.2.3 FORMULATION OF A MODIFIED FORM OF EXPLICIT CENTRAL DIFFERENCE SCHEME

The existing explicit central difference schemes are based on two approaches: the explicit form of the Newmark-β method [216] and central difference scheme which involves the displacements at two previous time stations [200-206]. The drawback of the former one is that to calculate the velocity and acceleration at time t_{n+1}, the damping forces can only be implicitly included through the internal resisting forces. The disadvantage of the other scheme is that at time t_{n+1}, only the velocity $\dot{d}_n$ and the acceleration $\ddot{d}_n$ can be computed. For the present analysis a modified form of explicit central difference scheme based on the Newmark-β method is developed to advance the nodal displacements, velocities and accelerations in time including damping forces defined in general explicit terms.

Setting β=0 in the Newmark -β method [216], the displacement and velocity at time t_{n+1} are given, respectively by

$$d_{n+1} = d_n + \Delta t\, \dot{d}_n + \frac{1}{2}\Delta t^2 \ddot{d}_n \qquad (6\text{-}17)$$

$$\dot{d}_{n+1} = \dot{d}_n + \frac{1}{2}\,\Delta t\,(\ddot{d}_n + \ddot{d}_{n+1}) \qquad (6\text{-}18)$$

To calculate the acceleration d_{n+1}, the equilibrium equation (6-1) is rewritten for time t_{n+1} as

$$M\,\ddot{d}_{n+1} + C\,\dot{d}_{n+1} + P_{n+1} = Q_{n+1} \qquad (6\text{-}19)$$

Substituting equations (6-17) and (6-18) into (6-19) and rearranging, we obtain

$$\ddot{d}_{n+1} = 2\,(2M + \Delta tC)^{-1}\,(Q_{n+1} - P_{n+1}) - 2C\,(2M + \Delta tC)^{-1}\,(\ddot{d}_n + \frac{\Delta t}{2}\,\dot{d}_n) \qquad (6\text{-}20)$$

The acceleration and velocity at time t_n can be expressed in terms of displacements through central difference approximations as

$$\ddot{d}_n = \frac{1}{\Delta t^2}\,(d_{n+1} - 2\,d_n + d_{n+1}) \qquad (6\text{-}21)$$

$$\dot{d}_n = \frac{1}{2\Delta t}\,(d_{n+1} - d_{n-1}) \qquad (6\text{-}22)$$

Substituting equations (6-21) and (6-22) into (6-20) and rearranging, we obtain

$$\ddot{d}_{n+1} = 2\,(2M + \Delta tC)^{-1}\,(Q_{n+1} - P_{n+1}) - \frac{2C}{\Delta t}\,(2M + \Delta tC)^{-1}\,(d_{n+1} - d_n) \qquad (6\text{-}23)$$

For explicit schemes the Rayleigh damping is customarily approximated as

$$C = b_o\,M \qquad (6\text{-}24)$$

If this approximation is used in 6-23, then we can write the expression as

$$\ddot{d}_{n+1} = a_o\,M^{-1}\,(Q_{n+1} - P_{n+1}) - a_1\,(d_{n+1} - d_n) \qquad (6\text{-}25)$$

in which a_o and a_1 are integration constants expressed as

$$a_o = \frac{2}{2 + b_o \Delta t} \tag{6-26}$$

$$a_1 = \frac{b_o}{\Delta t} \; a_o \tag{6-27}$$

For blast loading conditions, the externally applied load vector Q_{n+1} is the resultant of the externally applied air blast load on the structure, F_{n+1}, and the external seismic load on the supports of the structure, $M \ddot{d}_g^{n+1}$

$$Q_{n+1} = F_{n+1} - M \ddot{d}_g^{n+1} \tag{6-28}$$

Using equation (6-28), equation (6-25) is rewritten as

$$\ddot{d}_{n+1} = a_o M^{-1} (F_{n+1} - P_{n+1}) - a_o \ddot{d}_g^{n+1} - a_1 (d_{n+1} - d_n) \tag{6-29}$$

As the mass matrix M, is diagonal, the factorization in the system (6-28) becomes trivial. In that case, the solution for the displacement, acceleration and velocity can be obtained for every degree of freedom in the structure, i, separately leading to

$$d^i_{n+1} = d^i_n + \Delta t \, \dot{d}^i_n + \frac{1}{2} \Delta t^2 \, \ddot{d}^i_n \tag{6-30}$$

$$\ddot{d}^i_{n+1} = a_o M^{-1}_{ii} (F^i_{n+1} - P^i_{n+1}) - a_o \left(\ddot{d}_g^{n+1} \right)^i - a_1 (d^i_{n+1} - d^i_n) \tag{6-31}$$

$$\dot{d}^i_{n+1} = \dot{d}^i_n + \frac{1}{2} \Delta t \, (\ddot{d}^i_n + \ddot{d}^i_{n+1}) \tag{6-32}$$

To start the solution procedure, the value of initial displacements d_o and velocities $\dot{d}_o$ are given as initial conditions. Initial acceleration can be obtained by solving equation (6-29) at time t = 0

$$\ddot{d}_o = a_o M^{-1} [Q_o - P_o] - b_o \dot{d}_o + a_o \ddot{d}_g^o \qquad (6\text{-}33)$$

where p_o is the restoring force vector caused by initial stress in the structure.

6.2.4 COMPUTATIONAL STRATEGY ASPECTS

The architecture of a program for the explicit integration of a finite element system differs markedly from that of static programs and implicit integration programs. Although many analysts have used the traditional finite element approach, with nodal forces computed by multiplication of the tangential stiffness matrix and incremental displacements, that approach is computationally inefficient. In fact, it appears that the use of stiffness matrices in explicit nonlinear transient problems looks to be principally of historical motivation. As described by Heifitz et al [223], such an approach corresponds to first finding the derivatives of the nodal forces with respect to the nodal displacements, and then multiplying these two to compute the nodal forces. This method obviously involves unnecessary computations, and is moreover quite expensive when the response is highly nonlinear. In addition, it implies the use of additional core to store stiffness matrix, and consequently the size of the problem is significantly reduced.

As it can be seen from the formulations of the modified explicit central difference scheme developed in section 6.2.3, the nodal internal forces are computed directly without recourse to a stiffness matrix.

This approach was first used in finite element programming by Belytschko et al [224]. The computational algorithm of the modified explicit scheme is given in Table (6-1). In this table, for purposes of clarity, only the equations for a structural system are presented. The implementation

procedure for the finite element equations and constitutive relationships of concrete and steel are given in detail in Chapter 7. As can be seen from Table (6-1), at any time in the procedure, the displacements are known, and the element relations in conjunction with the constitutive relationships are used to compute the nodal internal forces for that time. Then, these forces are employed in the equation of motion to compute the accelerations which are integrated subsequently to find the new displacements.

In estimating the computational costs of the procedure shown in Table (6-1) it is found that most of the cost lies in the evaluation of nodal internal forces which involves material laws and the element relations, such as the numerical quadrature for the element nodal forces. Thus, the cost of any computation per time step depends on the number of elements, the complexity of elements, and the intricacy of the material laws. In any case, the number of computations varies linearly with the number of elements regardless of node numbering. The only disadvantage of the scheme is that the time step must be small enough to be consistent with the numerical stability limits of both dynamic analysis and viscoplastic strain solution. Finally, the energy balance check mentioned in the table is used to monitor solution stability, and is fully explained in subsection 6.5.1.

6.3 TIME DISCRETIZATION OF THE VISCOPLASTIC STRAIN GOVERNING EQUATION

As described before, time dependent deformations of viscoplastic solids are governed by the flow rule given as

$$\dot{\varepsilon}_{vp} = \gamma \ (\bar{\varepsilon}_{eff}) \ < \phi \ (F) \ > \frac{\partial f}{\partial \sigma} \qquad (6\text{-}34)$$

The above rule holds for every time t_n. To obtain complete solution to a viscoplastic problem, equation (6-34) must be integrated in time throughout the period of interest starting from known conditions at time 0. The viscoplastic strain change in the time interval dt is defined by

$$d\,\varepsilon_{vp} = \int_{t_n}^{t_n + dt} \dot{\varepsilon}_{vp}\, dt \qquad (6\text{-}35)$$

6.3.1 THE VISCOPLASTIC STRAIN INCREMENTS

Assuming that the expression (6-34) is known only for discrete time stations, $\Delta t_n = t_{n+1} - t_n$, the relation (6-35) can be approximated in the traditional manner of initial value problems [160] as

$$\Delta\,\varepsilon_{vp}^{n} = \left[(1 - \theta)\,\dot{\varepsilon}_{vp}^{n} + \theta\,\dot{\varepsilon}_{vp}^{n+1} \right] \Delta\, t_n \qquad (6\text{-}36)$$

in which $\Delta\varepsilon_{vp}^{n}$ represents the vector of viscoplastic strain increments and the parameter θ ($0 \le \theta \le 1$) defines the time integration scheme. For example, $\theta = 0$ gives the Euler or fully explicit scheme, $\theta = 0.5$ defines the implicit trapezoidal rule and $\theta = 1$ results in a fully implicit scheme.

In the present work, the Euler explicit integration scheme has been chosen. Thus, the viscoplastic strain vector at the time step t_{n+1} is given as

$$\varepsilon_{vp}^{n+1} = \varepsilon_{vp}^{n} + \dot{\varepsilon}_{vp}^{n}\,\Delta t \qquad (6\text{-}37)$$

This scheme has been found to be computationally efficient in the context of quasi-static analysis [225] and dynamic problems [34, 77, 176] despite the numerical stability limitations on the time step length which is discussed in the following subsection.

6.3.2 TIME INCREMENT DEFINITION

The time integration scheme represented by (6-36) is conditionally stable for $\theta < 0.5$ [160]. To date several

stability analyses relating to viscoplastic solution procedures have been undertaken to establish rules for choosing the time step length. According to the form of the viscoplastic potential used in the flow rule and referring to the fully explicit integration scheme, Cormeau [226] derived theoretical stability limits for some classic yield criteria such as von Mises and Mohr-Coulomb. It should be mentioned that these stability limits were obtained for quasi-static elasto-viscoplacity with the flow rule a linear function of stress only. As the flow rule adopted in this work involves both stresses and strain rates, these limits are not strictly applicable. Semi-emperical relationships have been proposed in [112] to control the time step length as

$$\Delta t_n \leq \psi \left(\bar{\varepsilon}^n / \dot{\bar{\varepsilon}}^n_{vp} \right) \qquad (6\text{-}38)$$

in which $\bar{\varepsilon}^n$ is the total effective strain, $\dot{\bar{\varepsilon}}^n_{vp}$ is the effective viscoplastic strain rate and ψ is a control parameter which varies between 0.01-0.015 for explicit schemes [112]. Recently Damjanic [27] has developed a method to calculate the critical time step length on the basis of an eigenvalue analysis of one of the matrices involved in the viscoplastic behaviour. This procedure is computationally expensive since the value of Δt changes throughout the transient process, i.e. the eigenvalue analysis should be recalculated at every integration point in which viscoplastic flow occurs, for every time step.

In the present work, an estimate of the allowable time step for concrete viscoplastic behaviour, has been obtained by substituting some representative values from Watstein, [16] and Hatano's [17] tests into one of the criteria given in [226]. The stability limit for the von Mises yield criterion (a particular case of the compression loading functions proposed for concrete) is employed in the form

$$\Delta t \leq \frac{4\ (1 + \nu)\ \tau}{3\ \gamma\ E} \qquad (6\text{-}39)$$

Taking τ, the effective stress, as the initial dynamic yield stress ($\tau = 0.4\ \sigma'_{cd}$) and the strain rates varying from 10^{-6} to 10 sec^{-1} (the range in which the present material model is assumed to be valid) to calculate the concrete fluidity parameters, the critical time steps Δt_{cr}, obtained for different concrete grades are shown in Figure (6-1). Using the linear curve fitting, a unique relation between Δt_{cr} and the strain rate for concrete is established as

$$\text{Log}\ (\Delta t_{cr}) = c_1 + c_2\ \text{Log}\ (\dot{\varepsilon}) \qquad (6\text{-}40)$$

or

$$\Delta t_{cr} = 10^{c_1}\ (\dot{\varepsilon})^{c_2} \qquad (6\text{-}41)$$

where the parameters c_1 and c_2 depend on the concrete cylinder compressive strength and can be obtained by interpolation from Table (6-2). As can be seen, the smallest critical time increment for the same grade of concrete is the one corresponding to the strain rate 10 sec^{-1}. Taking these allowable time steps and the corresponding concrete cylinder compressive strength and employing the linear curve fitting, it is possible to establish a unique relation between Δt_{cr} (in sec) and σ'_{cs} (in N/mm^2) as

$$\Delta t_{cr} = 10^{t1}\ (\sigma'_{cs})^{t2} \qquad (6\text{-}42)$$

where the parameters t_1 and t_2 are found to be - 8.49 and 3.12 respectively. Typical values of critical time steps for some concrete grades are given in Table (6-3).

For steel, the stability limit for viscoplastic solution of the uniaxial case using the Euler time marching scheme [112] has been adopted.

$$\Delta t \leq \frac{\sigma^{s}_{yd}}{E_s \gamma_s} \qquad (6\text{-}43)$$

in which σ^{s}_{yd} is the steel dynamic yield stress. Substituting the representative values from the experimental results for different strain rates given in [188, 189] and applying the linear curve fitting in a similar fashion to that of conrete, the critical time increment for steel is found as a function of the strain rate in the form (Figure 6-2)

$$\Delta t^{s}_{cr} = 10^{s_1} (\dot{\varepsilon})^{s_2} \qquad (6\text{-}44)$$

in which s_1 and s_2 were found to be - 1.55 and - 0.92 respectively. Noticing that the strain rate 10 sec $^{-1}$ gives the smallest allowable time increment and computing the corresponding fluidity parameter and the dynamic magnification factor of steel yield stress, the following relation to define the critical time increment as a function of steel static properties is established as

$$\Delta t^{s}_{cr} = 2.781 \frac{\sigma^{s}_{ys}}{E_s} \qquad (6\text{-}45)$$

The semi-empirical *a priori* stability limits of Euler explicit scheme proposed in equations (6-42) and (6-45) represent an upper bound limit for time step size and have great merit for monitoring the process of elasto-viscoplastic response of dynamically loaded reinforced concrete structures in a simple and stable manner. In dynamic analysis, however, if an explicit integration scheme is used, the stability limit for the step by step integration of the equations of motion will normally govern the choice of the time step length [176, 202]. In particular, when cracking is involved, the time step must be selected so that cracks spread progressively throughout the

structure. If a large number of cracks are formed in the same interval, considerable error and numerical difficulties may be encountered.

6.4 SELECTION OF THE TIME INCREMENT FOR NONLINEAR DYNAMIC ANALYSIS

From the previous discussion, it can be stated that the selection of time increment for numerical integration of the coupled equations (6-6) and (6-8) is usually governed by the stability limit of the central difference scheme [202], i.e.

$$\Delta t \leq \Delta t_{cr}; \quad \Delta t_{cr} = \frac{2}{\omega_{max}} \left[(1 + \xi)^{1/2} - \xi \right] \qquad (6\text{-}46)$$

where ξ is the damping ratio for the highest mesh frequency.

The maximum frequency, ω_{max}, is given as

$$\omega_{max} = \sqrt{\lambda_{max}} \qquad (6\text{-}47)$$

where λ_{max} is the maximum eigenvalue of the system. For undamped system ($\xi = 0$), the stability limit of time increment can be written as

$$\Delta t \leq \frac{2}{\omega_{max}} = \frac{2}{\sqrt{\lambda_{max}}} \qquad (6\text{-}48)$$

It is generally quite inconvenient to determine a stable time step by finding the maximum system eigenvalue. This is particularly true for nonlinear problems, where the eigenvalues change as the solution evolves. Various estimates for the highest mesh eigenvalue have been suggested [202, 224]. The basis for these estimates is provided by the bounding theorem for extreme eigenvalues derived from Rayleigh's principle [230]

$$\lambda_{min}^{element} \leq \lambda_{min}^{mesh} \leq \lambda_{max}^{mesh} \leq \lambda_{max}^{element} \qquad (6\text{-}49)$$

Hence, the highest mesh frequency is less than the highest frequency of its smallest element. Thus, the stability

condition (6-48) can be rewritten as

$$\Delta t \leq \frac{2}{\omega_{max}^{element}} = \frac{2}{\sqrt{\lambda_{max}^{element}}} \qquad (6\text{-}50)$$

From Rayleigh's quotient, the maximum element eigenvalue is defined [202] as

$$\lambda_{max}^{element} = \frac{\psi^T K^e \psi}{\psi^T M^e \psi} \qquad (6\text{-}51)$$

in which K^e is the element stiffness matrix, M^e denotes the element mass matrix and ψ defines the eigenvalue associated with the highest frequency which is often referred to as the noisiest eigenvector [230].

In fact it is not practical to compute even the maximum eigenvalue of the smallest element of the mesh. The reasons for this can be summarized as

1. The considerable increase of computation cost to determine the highest element eigenvalue and then the time increment at every time step.

2. This method is generally valid for regular meshes [77, 202].

3. In nonlinear problems, an accurate maximum eigenvalue to define time step limit does not guarantee stability of solution [224].

Instead, formulas which give the maximum element eigenvalue are used for simple elements [202, 227, 228]. Based on (6-51), the maximum element eigenvalue was found for one dimensional element [202] as

$$\lambda_{max}^{element} = \frac{4\,E}{\rho L^2} = \frac{4\,C_p^2}{L^2} \qquad (6\text{-}52)$$

in which $C_p = \sqrt{\frac{E}{\rho}}$ is the acoustic wave speed and L is the element length. Substituting this estimate into (6-50), the stability condition for 1D elements is rewritten as

$$\Delta t \leq \frac{L}{C_p} \tag{6-53}$$

Due to the convenience of the expression (6-53), it is customary to express also in a similar manner the stability limits for higher order elements. The typical forms used is then

$$\Delta t \leq \mu \frac{L}{C_p} \tag{6-54}$$

where μ is a reduction factor for which different values are suggested [77, 224]

For the 8-node isoparametric elements used here, the length, L, is defined as the smallest length between any two nodes in the mesh. From many computations carried out in the present work a reduction factor varying between 0.2 and 0.4 was found to be necessary to account for the discretizing effects of round off errors and rapidly varying concrete and steel properties. Finally, for 2D applications, the acoustic wave speed is related [214] to the elastic material constants in the form

$$C_p = \sqrt{\frac{E}{\rho\,(1-\nu^2)}}, \text{ for plane stress elements;} \tag{6-55}$$

$$C_p = \sqrt{\frac{E\,(1-\nu)}{\rho(1+\nu)(1-2\nu)}}, \text{ for plane strain and axisymmetric elements} \tag{6-56}$$

6.5 SOME PRACTICAL CONSIDERATIONS IN EXPLICIT INTEGRATIONS

The numerical solution of the discretized system deviates from the exact solution of the continuous system as a result of spatial and temporal discretization effects. Some of the

temporal discretization errors of explicitly integrated equations are discussed and the methods to limit their effects are given.

6.5.1 ENERGY BALANCE CHECK

It is widely accepted that for linear explicit computations, numerical instabilities may easily be detected after a solution is completed by exponential oscillatory growth in nodal displacements. However, in nonlinear calculations, the numerical instability is not always as dramatic and in fact may avoid detection even if the eigenvalues are computed within the time integration loop to determine the stable time increment. The reason for this is that nonlinear processes such as inelastic deformations are capable of dissipating a large amount of energy and hence a decrease in the stiffness and the maximum eigenvalues of the system, so the calculation may regain stability. This process is known as an arrested instability [224].

According to the proposed nonlinear material models in this thesis, concrete and steel are dissipative materials. The spurious energy generated by an instability may rapidly be absorbed as an excessive plastic work as a consequence of viscoplastic response of concrete or steel, or concrete cracking. In these situations simply checking for large unrealistic results may not always provide assurance that no instability has occurred, since an instability may be confined to a small region of the mesh and the problem may even recover stability at a later time. If this happens, the results obtained for the problem may seem quite reasonable, but the earlier instability will render the final results totally inaccurate.

In order to guard against these errors, energy balance check as an alternative method for checking the stability of explicit finite element calculations, is employed. If W^{kin}_{n+1}, W^{int}_{n+1}, W^{ext}_{n+1} denote the kinetic, internal and

external energies of the system at time step n+1, respectively, the energy balance check is given as [202]

$$| W_{n+1}^{kin} + W_{n+1}^{int} - W_{n+1}^{ext} | \leq \delta || W || \qquad (6\text{-}57)$$

where δ is a specified tolerance and $|| W ||$ is some measure of the total energy of the system. The use of any one of the terms of the left hand side of equation (6-57) alone would not provide a useful measure of this energy. For impulsively loaded problems when an initial velocity is prescribed, there would be no external work. For vibration problems, the value of the kinetic and internal energies would oscillate and become very small at some point in the problem. Therefore, a measure of the total energy of the system should include all three terms.

$$|| W || = | W_{n+1}^{ext} | + | W_{n+1}^{int} | + | W_{n+1}^{kin} | \qquad (6\text{-}58)$$

The use of absolute value sign in the left hand side of equation (6-57) is not really necessary since an instability is usually characterized by growth in kinetic and internal energies which are non-negative. Therefore, this left hand side would always be positive in case of an instability.

In time integration, equation (6-57) is checked at each time step to ensure that the work done on the system and the energy of the system are nearly equal (usually $\delta \leq 0.02$). Using the trapezoidal integration, the internal and external energies are calculated as

$$W_{n+1}^{int} = W_{n}^{int} + \frac{1}{2} \sum_{i=1}^{nd} (d_{n+1}^{i} - d_{n}^{i}) \ (P_{n+1} + P_{n}) \qquad (6\text{-}59)$$

$$W_{n+1}^{ext} = W_{n}^{ext} + \frac{1}{2} \sum_{i=1}^{nd} (d_{n+1}^{i} - d_{n}^{i}) \ (Q_{n+1} + Q_{n}) \qquad (6\text{-}60)$$

where nd is the total number of degrees of freedom in the structure. The kinetic energy is given by

$$W_{n+1}^{kin} = \frac{1}{2} \sum_{i=1}^{nd} \left(\dot{d}_{n+1}^{i}\right)^{T} M \dot{d}_{n+1}^{i} \qquad (6\text{-}61)$$

6.5.2 CONTROL OF SPURIOUS OSCILLATIONS

The phenomenon of spurious numerical oscillations is the second troubling consequence of applying explicit temporal integration to spatially discretized equation of motion. The response of a discrete system to excitation with frequency components above the maximum frequency of the system (the cut-off frequency) produces spurious oscillations which dominate the true solution in such a way that the interpretation of results is difficult. Their presence is a result of several possible factors, discussed in [28, 227-229].

It has been indicated [28, 227] that pronounced spurious oscillation is obtained when the excitation consists of a discontinuity such as step type loading. In this case, the spurious oscillation is caused by the fact that the numerical solution describes the discontinuity with a finite slope as a result of the reduced number of eigenmodes of discretized system. Subsequent oscillations about the analytic solution occur with a decreasing amplitude at a constant frequency. The predominant frequency of these oscillations is the cut-off frequency of the system. This is generally referred to as Gibb's phenomenon [227].

While the mesh refinement in regions of interest has few drawbacks in static elasticity problems, the situation is not as simple in transient dynamic problems. From the study of wave propagation in one-dimensional mesh, it was concluded [227] that the refinement of the mesh in the regions of interest results in the following spurious effects: the coarse part eliminates any frequency content beyond its resolution in waves which propagate through it to the area of interest, and the coarse mesh reflects back a

significant part of the high frequency waves generated in the fine mesh which leads to over-estimation of higher frequency characteristics of the mesh. The frequency at a point depends not only on the element size where the response is recorded, but also on the reflected wave frequencies associated with larger elements through which the wave will pass. These spurious reflections result from the fact that the finite element behaves like filters having definite passing bands and cut-off frequencies [28].

Several methods are available to eliminate these oscillations: the use of integration operators with damping such as the Newmark-β operator [216]; the use of artificial viscosities in the elements [229]; the post-processing of solution by digital filters [227, 229]. Generally these techniques have a tendency to increase the dispersion property elements as well as artificial viscosities diminish the amplitude of the solution.

In the present work, when this phenomenon appears, a post-processing of solution by a five point non-recursive filter is applied. This filter consists of the transformation [227]

$$d^{filter}(t) = \sum_{k=-2}^{2} \frac{1}{5} d\left(t + \frac{\pi k}{5 w_s}\right) \qquad (6\text{-}62)$$

where w_s is the frequency to be filtered which is usually the cut-off frequency of the system.

Table (6-1) Step-by-step solution procedure of explicit central difference

---

a. Initial calculations

1. Initialize d_o and $\dot{d}_o$
2. Select time increment Δt, $\Delta t \leq \Delta t_{cr}$
3. Select damping coefficient b_o and then calculate the integration constants, a_o and a_1, using equations (6-26) and (6-27)
4. Form structure lumped mass matrix M
5. Calculate the initial load vectors Q_o and P_o
6. Evaluate initial acceleration vector, $\ddot{d}_o$, using (6-33)

b. For each time step

7. Calculate the displacement at time t_{n+1} using equation (6-17)
8. Update the strains using the element relations and the stresses using the material laws
9. Find internal nodal forces, P_{n+1}, using equation (6-5)
10. Calculate the external applied load vector, Q_{n+1}
11. Solve for acceleration and velocity vectors at time t_{n+1} using equations (6-25) and (6-18) respectively
12. Calculate the external work done and the internal and kinetic energies of the system and then check the energy balance.
13. For next time step, set n = n+1 and go to 7

Table (6-2) Critical time step parameters identified from Watstein's [16] and Hatano's [17] tests

σ'_{cs} N/mm^2	18.3	27.0	421.2	59.11
C_1	- 3.69	- 3.02	- 2.67	- 1.98
C_2	- 0.878	- 0.867	- 0.906	- 0.825

Table (6-3) Critical time step of some concrete grades (Assuming von Mises yield criterion $\dot{\varepsilon}$ = 10 sec^{-1})

σ'_{cs} N/mm^2	18.3	27.0	44.2	59.21
Δt sec	2.7 e-05	1.28 e-04	2.60 e-04	1.54 e-03

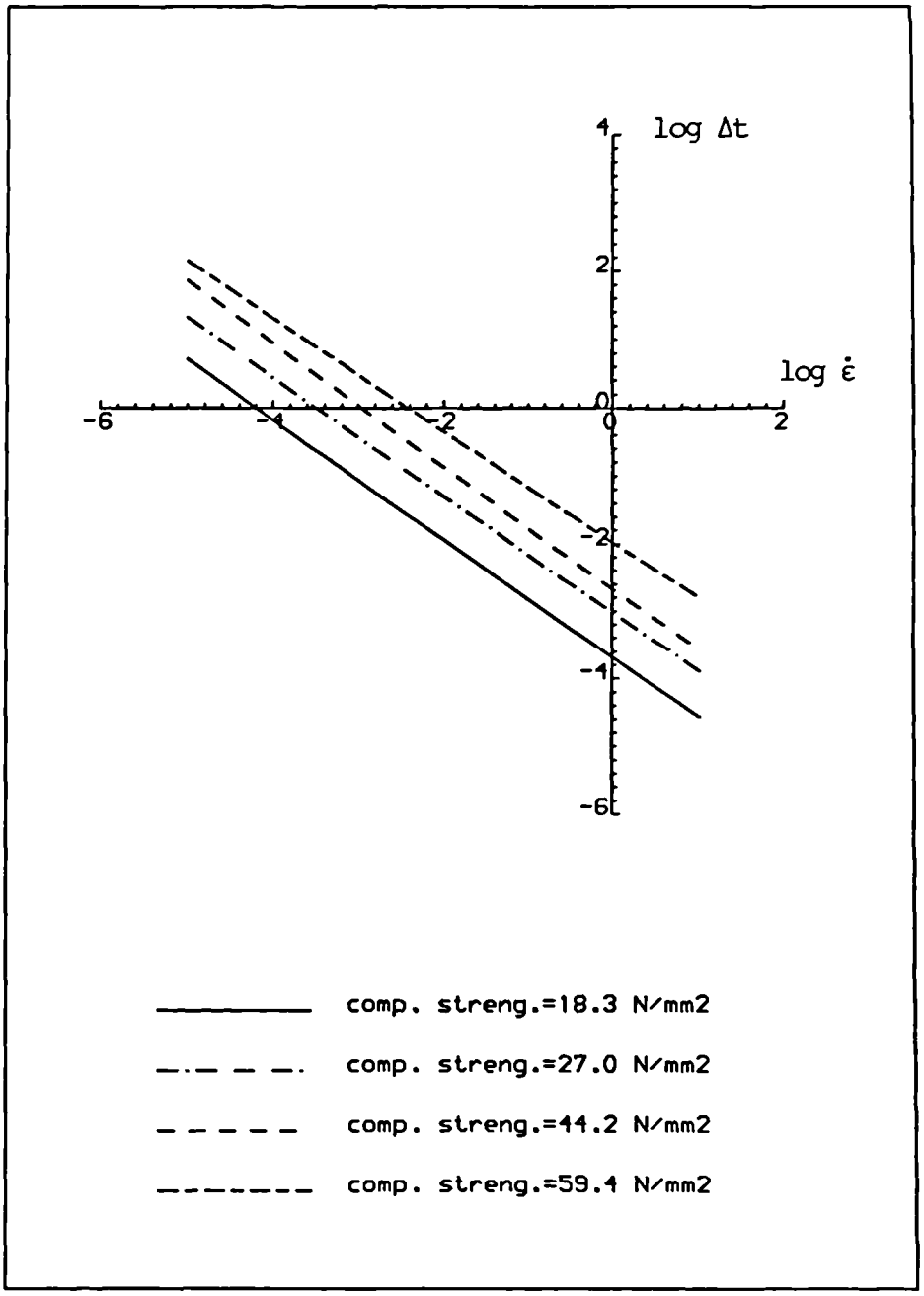

Figure 6.1 Critical time versus strain rate for different grades of concrete

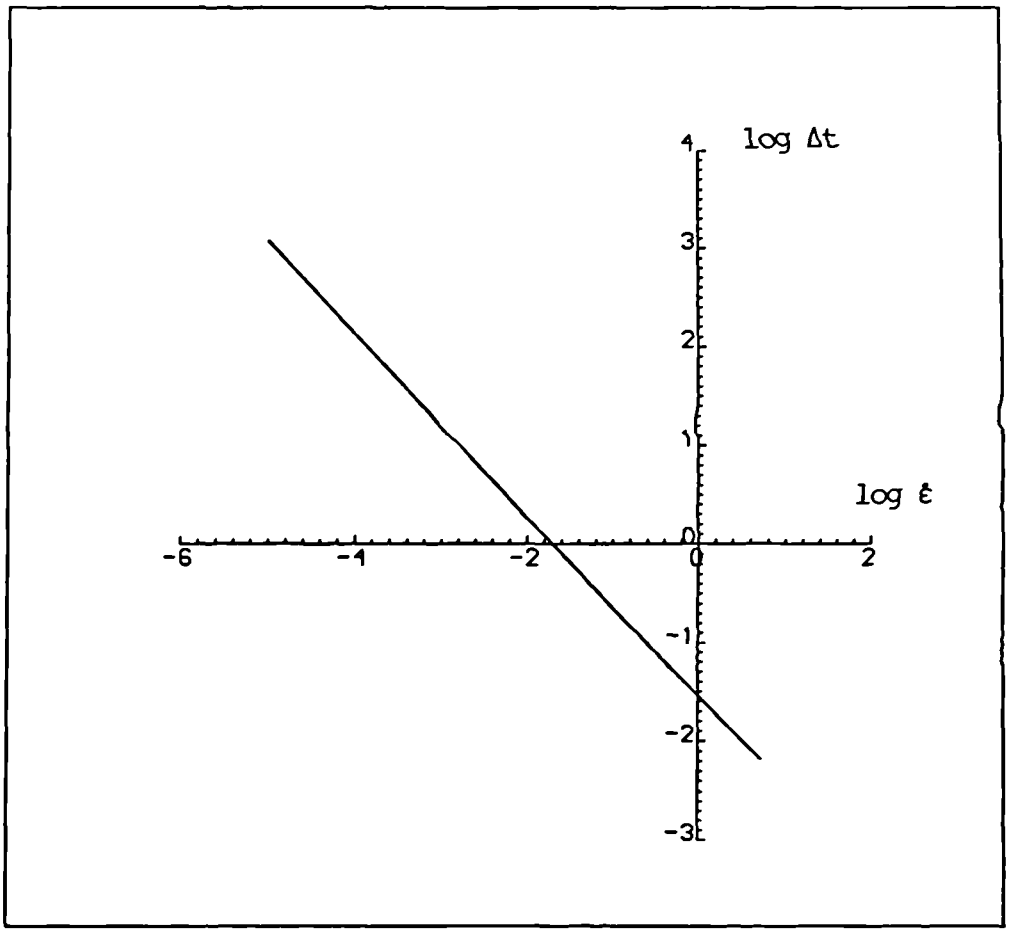

Figure 6.2 Critical time increment versus strain rate for steel

CHAPTER 7

COMPUTER IMPLEMENTATIONS AND BRIEF PROGRAMS DESCRIPTION

7.1 INTRODUCTION

The success of the Finite Element method as a practical design aid depends on the availability of an efficient means of solving the resulting system of linear or non-linear simultaneous equations. The aim of this chapter is to describe briefly the main features of the computer programs developed during the course of this work for the finite element analysis of two-dimensional structures subjected to blast loading or any other impulsive or transient dynamic load, discussed in the previous chapters. Section 7.2 summerizes the software features, the structural analysis capabilities and the structure of the 2D finite element dynamic analysis program, the main computer program developed. The computer implementation of the solution technique (Chapter 6) and the material models (Chapter 5) proposed in this thesis are presented in section 7.3. Finally, section 7.4 discusses briefly the other relevant programs developed for the pre- and post-processing of data to support the main program.

7.2 2D FINITE ELEMENT DYNAMIC ANALYSIS PROGRAM

A versatile and comprehensive computer program for the finite element analysis of blast resistant structures, named FEABRS, has been developed. This program can perform the linear and non-linear explicit step-by-step dynamic analysis for two-dimensional structures under a wide range of dynamic loads. The program embodies the rate dependent constitutive material models proposed for reinforced concrete in Chapter 5. However, the facilities to handle other structural materials such as metals and geomaterials (rock and soils) are available. The basic features, capabilities and the structure of the program are described in the following subsections.

7.2.1 CHARACTERISTIC FEATURES OF FEABRS

In keeping with contemporary programming practice and considering the software design aspects of the finite element method, FEABRS has been written with the following software engineering features:

1. Programming language

The standardization, availability and persistent use of FORTRAN in engineering, despite some technical drawbacks, makes it the only logical choice for currently developed finite element software. FEABRS has been written in FORTRAN-77.

2. Modularity

The clearly defined steps of finite element analysis and the corresponding distinct entities reveal a modularity that should be fully used in software design [231]. A modular approach has been adopted in FEABRS which comprises seven modules, each with a distinct operational function. Each module in turn, as shown in Figure 7-1, is composed of one or more primary subroutines relevant only to its own needs to perform the basic finite element analysis steps. The 15 primary subroutines rely on 43 auxiliary subroutines to carry out secondary operations. An auxiliary subroutine may be required by more than one primary subroutine. Control of the modules is held by the master segment, denoted MAIN, which organises the calling of the primary routines as well as controls the termination of the solutions according to the number of time steps specified in input data.

3. Dynamic dimensioning

Dimensions are fixed in the master routine and all necessary information is transmitted between the routines by the use of arguments. This approach has the advantages that maximum dimensions can be updated in a very simple and straightforward manner. Only the dimensions statement in the main segment and some statements in a control subroutine, called DIMENS which sets the maximum dimensions

sizes, need modification. More sophisticated versions of this approach can be implemented as illustrated by Irons and Ahmed [232]. Such approaches undoubtedly save core storage but they do require careful housekeeping and checking procedures.

4. Portability

The generality of the finite element method and the large investment required to produce good software dictates that such software must be transportable between different computer models and installations. Using parametric data structure dimensions and data transfer block sizes allows the tuning of FEABRS software to fit different machine configurations. The program has been successfully compiled and run under different FORTRAN-77 compilers running under different operating systems. This includes both UNIX and COS.UNIX used on GOULD minicomputers (PN 9005 and PN 6040) and SUN and WHITECHAPEL Workstations. The COS operating system was used on a CRAY X-MP super computer.

5. Reliability

The reliability of FEABRS results from clear definition of the modules with a minimum of interface information, and ease of structured programming within the modules, which allow the verification of modules independently of their use in the overall programming system. Thus, the software errors can be separated from the errors associated with incorrect formulation, misapplication, or data preparation. FEABRS reliability also implies that modules will detect and report any errors in their data that make completion of their task impossible and will return control to the higher-level calling subroutine or controlling program.

6. Expandability

The main control parameters and the modular programming system of FEABRS allow an important facility in that introduction of new capabilities implies only the creation of additional subroutines and data entities without upsetting the organisation of the entire program.

7. Input data flexibility

The data input has been designed to be self-explanatory and in free format. Free format input has the advantage that it reduces the human effort in the preparation of data, obviates the need for special coding forms, minimises input error and is convenient for input from terminals. The program is unitless and assumes that a consistent set of input data are given.

Automatic data generation facilities are not incorporated within FEABRS. However, at any stage during the preparation of input data, the computer system can be instructed to receive data from external files generated by separate data generation programs. This minimises the effort needed to prepare data and also reduces the possibility of making an error. Although the elements and nodes are usually numbered for the convenience of data generation, they may be numbered in any arbitrary manner or gaps in the numbers.

8. Data checking and error diagnostics

The principal of including in a finite element program ample diagnostics which tell the user what is wrong with input data and why the machine has stopped, is now almost universely accepted. FEABRS contains four error diagnostic subroutines which automatically check for wrong or improbable input data. If any errors are detected, another subroutine called ECHO, is called to echo the remainder of the problem data via the line printer [233] before the job is terminated.

9. Output flexibility and presentation of results

The output of results has been designed to be compact-clear and self-explanatory. The user can suppress or call certain areas of the output from an analysis.

The results include displacements of nodal points, internal stresses within the various finite elements and material state variables. All are expressed in the global coordinate

system and presented in a tabular form. For time history analysis, the displacements at selected nodal points and the stress components at specified sampling points are post-processed separately to facilitate interpretation of results.

7.2.2 BASIC STRUCTURAL ANALYSIS FACILITIES

FEABRS has been developed to suit the possibility of performing several dynamic analysis problems of transient and impulsive nature such as blast, impact or earthquakes. To achieve this, the program has been provided with the following facilities:

1. Loads definition flexibility

A structural analysis of a system subjected to different forms of loads and/or time varying forced boundary conditions can be performed. Loads applied to structure can be defined in a number of ways:

- as concentrated loads applied to nodal points.
- as normal and tangential loads per unit length applied to element edges.
- as gravity load
- as prescribed displacements, velocities and accelerations applied to nodal points.

Complex loadings due to blast can be synthesized by combination of multiple load vectors and load-time functions. These functions can include Heavside, step, harmonic, expontential decaying or arbitrary functions. Airblast-induced earth shock or earthquake excitations can be considered by defining the acceleration history for each constrained degree of freedom in the structure from the accelerogram data.

2. Finite element modelling flexibility

The current version of FEABRS features a limited library of

finite elements, which permits the modelling of plane and axisymmetric complex geometries. Based on the isoparametric formulation, three different element types [112] are included:

- The 4-node isoparametric quadrilateral element with linear displacement variation.
- The 8-node Serendipity quadrilateral element with curved sides and a quadratic variation of the displacement field within the element.
- The 9-node Lagrangian quadrilateral element which additionally has a central node.

The use of these higher order elements leads to particularly efficient solution for large applications.

To simulate reinforcement in concrete structures, the bar and membrane elements, as discussed in Chapter 4, have been incorporated as embedded members in the basic isoparametric concrete element. All elements in FEABRS are numerically integrated, and 3×3 or 2×2 integration rules can be specified. Numerical integration enables the software to include facilities such as the computation of nodal forces equivalent to initial stresses, body forces, surface pressures or mass and damping matrices.

3. Material modelling flexibility

The following material models can be selected:

- Isotropic and linear
- Elasto-viscoplastic with flexibility in the choice of the yield criteria and hardening or softening functions.
- User-supplied material, dependent on history, temperature, time etc.

Within the frame of viscoplasticity, the yield criteria can be specified as

- Any of the four failure criteria proposed for concrete in this thesis.
- Von-Mises for metals.
- Mohr-Coulomb and Drucker-Prager for geomechanics.

The hardening regime can be modelled as a linear, expotential or parabolic function of the effective viscoplastic strain. The option to ignore material hardening or softening has been provided. For cementitious materials, a crack monitoring algorithm to control the cracking process, and a crushing control routine have been included to cover the brittle nature of these materials. It is also optional to account for the post-cracking behaviour which is represented by four different models to idealize the tension softening and shear transfer across the cracks. The facility to account for the rate sensitivity of the cracking process as well as the viscoplastic regime is also optional.

4. Analysis capability

FEABRS provides analysis capabilities for the solution of engineering problems which include linear and nonlinear transient dynamic analysis of plane stress, plane strain and axisymmetric problems. The solution technique of the governing equations is based on the explicit time integration scheme, discussed in Chapter 6, which provides a good tool for the solution of very large models and analysis in an accurate, economic and efficient manner.

7.2.3 GENERAL STRUCTURE

The modules, schematically shown in Figure 7-1 are described in relation to their functions as follows:

1. Control and initialization module

This is the first module entered and is controlled by subroutines DIMENS and ZEROAR. The purpose of subroutine DIMENS is to set the values of variables for the dynamic

dimensions which are used elsewhere in the program. If any change in the DIMENSION statement in the master routine is made, then a corresponding change in this subroutine should also be made. The job parameters such as number of elements, number of nodal points, number of materials, type of elements, Gauss integration rule and number of load history functions, are also read and a check is made on the maximum available dimensions. The role of subroutine ZEROAR is to set to zero all arrays required during the analysis.

2. Input module

This is the second module entered and is controlled by four subroutines GMDATA, TMINTP, FTINTP and PSTATE as shown in Figure 7-1.

Subroutine GMDATA handles the input data defining the geometry, boundary conditions and material properties of both isoparametric elements and the various steel embedded elements. It also names the rate sensitivity parameters of the materials. Some data is processed into a form compatible with later program requirements and other constant data, such as Gaussian integration constants, are set up. This routine calls three different data error diagnostic subroutines to check the main control parameters and input data.

Subroutine TMINTP reads input data defining time-stepping procedure, Rayleigh damping and the selective nodal points and integration points for displacement and stress histories output. It also reads the initial displacement velocities. This routine also calls an important subroutine to check the length of time step of the analysis against the critical time increment (Chapter 6).

Subroutine FTINTP deals with the input data which define the type of load history function for each degree of freedom and then the characteristic parameters and ordinates of each function. It also reads the horizontal and vertical

acceleration ordinates if they exist.

Finally, subroutine PSTATE reads the initial forces, stresses and strains.

3. Loading module

The flow of operations through this module is governed by the subroutine LOADAT. The role of this module is to evaluate the consistent nodal forces for each element due to externally applied forces. The types of loading to be considered are controlled by IPLOD, IGRAV and IEDGE. Non-zero values of these respective items indicate that discrete point loads, gravity loading or distributed edge loading per unit element length (or per unit area for axisymmetric problems) are to be considered. The consistent nodal loads are evaluated from each element separately and stored in the array RLOAD. These element force vectors are then assembled into the global external force vector FORCE.

4. Presolution module

This module comprises four subroutines LUMASS, FIXITY, AENBLO and RESIDO. Generally, it organises the initial calculations necessary to start the time stepping procedure in the solution and post-solution modules.

Subroutine LUMASS generates the lumped mass vector by scaling the consistent mass matrix to preserve the total mass. Then the contributions of the reinforcement embedded elements are evaluated, as explained in Chapter 4, and added to the global lumped mass vector. This routine also reads concentrated masses and assembles them into the global diagonal mass vector.

Subroutine FIXITY deals with restrained degrees of freedom in similar manner to that proposed in Reference [112]. The diagonal mass vector is modified for restrained degrees of freedom such that the corresponding components of the global mass vector are set to a large value which artificially

makes the displacement zero.

Subroutine RESIDO is called if the indicator of the previous state equals 1 in order to evaluate the initial resisting force vector due to initial stresses and strains. Finally, subroutine AENBLO calculates the initial accelerations necessary to start the explicit time integration scheme described in Chapter 6. The initial values of kinetic and internal energies as well as the external work done of the system at time zero are also evaluated in this routine.

5. Solution module

This module consists of the subroutine EXPSOL. The general purpose of this module is to perform the direct time integration using the modified explicit central scheme proposed in Chapter 6 to evaluate the nodal displacements at every time step. In this module, the externally applied forces are determined at the current time step by evaluating the value of the time varying function of the airblast load as well as the horizontal and vertical acceleration ordinates due to the earth shock, at this particular time step. The seismic force is only applied for specific degrees of freedom. For IFIXD = 1 only vertical, IFIXD = 2 only horizontal or radial and IFIXD = 0 both components of the acceleration are considered. Appropriate values of the displacements are assigned for restrained nodes.

This module is controlled by the master MAIN because the flow of operations is dependent on the number of time steps of the analysis, NSTEP (See Figure 7-1).

6. Post-solution module

This module is controlled by the subroutines RESIDU and VAENBL. Figure 7-1 shows the subroutines associated with this module which are immediately entered in every time step after the solution module.

Subroutine RESIDU organises first the calculation of the

total and elastic strains as well as rate sensitivity functions. Thus, total stresses, cracking state, post-cracking conditions and viscoplasticity states which include yielding, hardening, failure and softening, in each isoparametric element are updated according to a prescribed material law. These laws of concrete have been described in detail in Chapter 5. This subroutine also controls the evaluation of strain, rate effect, stress and current yield stress in bar and membrane steel elements. A linear elastic solution, if required, is also under the control of subroutine RESIDU. Finally, it organises the determination of the internal nodal forces due to the total stresses. All values of stress, strains, cracking etc., are stored for later use in output module and updating the material state in the next time step.

The general purpose of subroutine VAENBL is to calculate the nodal velocities and accelerations at every time step according to the explicit central difference integrator described in Chpater 6. In order to guard against the arrested instability errors in the dynamic response of dissipative materials, energy balance check, explained in the previous chapter, is also implemented in routine VAENBL.

7. Output module

This module is controlled by subroutine OUTPUT which is entered in every time step after the post-solution module. This routine writes out most of the output on the line printer and on various tapes for plotting purposes. It outputs the nodal displacement, stress components and effective viscoplastic strain every NOUTP steps for isoparametric elements. The principal stresses and their directions are also calculated and output. For steel reinforcement, the routine also writes out the strain and stress of each embedded element every NOUTP steps. The displacement and stress histories of specified nodal and integration points every NOUTD steps are written to tapes 10

and 21 respectively. The complete state of displacements is also written on tape 13 for use in plotting deformed structural shape every NOUTS steps. The routine outputs the complete state of stresses as well as the principal stresses every NOUTS on tape 26 for stress contour plots. The full material state variables every NOUTS are also written on tape 27 for crack patterns. Finally, the strain and stress histories of specified reinforcement sampling points every NOUTD steps are recorded on tape 30.

7.3 COMPUTER IMPLEMENTATION OF SOLUTION TECHNIQUE AND MATERIAL MODELS

The implementation of the strain rate sensitive model of concrete (Chapter 5) combined with a crack monitoring algorithm as well as the strain rate dependent viscoplastic model of steel (Chapter 5) in the computer program FEABRS shown in Figure 7-2, in which the governing dynamic equilibrium equations are solved using the explicit central difference time integration scheme described in Chapter 6. For convenience, the crack monitoring and concrete and steel viscoplasticity algorithms are separately described in Tables (7-1), (7-2) and (7-3) respectively.

The crack monitoring algorithm is activated after strain evaluation in each time step and for each cracked integration point. The function of this algorithm can be summarized as

1. Check of initiation of new cracks for plane and axisymmetric problems based on the strain rate dependent cracking criterion described earlier in section 5.4.2.

2. Monitoring the state of existing cracks (closing or opening) as explained before in section 5.4.5.

3. Evaluation of concrete stresses for cracked state which accounts for post-cracking softening (Section 5.4.3) and shear transfer across the cracks (Section 5.4.4).

4. Updating the concrete material state variables and the

crack reference values.

The role of the concrete viscoplasticity controlling algorithm is briefly explained as:

1. Check the concrete material state in the viscoplastic range; crushing (Section 5.3.6), softening (Section 5.3.5), failing (Section 5.3.1), flowing (Section 5.3.4) or yielding (Section 5.3.2).

2. Evaluation of the effective stress using the rate sensitive hardening rule in the pre-failure range or rate dependent softening rule in the post-failure range and then determination of the viscoplastic rate vector by the rate dependent flow rule.

3. Updating the viscoplastic strain vector and the viscoplastic work.

4. Evaluation of internal resisting force vector on the concrete element level.

The function of steel viscoplasticity controlling algorithm is to check yielding, update steel viscoplastic strain and finally to evaluate the steel members internal force vector which is added to that of concrete elements.

7.4 PRE AND POST-PROCESSING AUXILIARY PROGRAMS

A number of auxiliary programs have been developed to support the main program FEABRS and to demonstrate the features of the material models developed within this work.

In the pre-processing stage, some programs have been created for the determination of material parameters as well as the input data generation. The programs FLUDCO and FLUDST have been developed for the identification of the concrete and steel fluidity parameters as functions of the strain rate based on the experimental results mentioned in Chapter 5. A program named TENRAT has been developed to define the strain rate sensitivity function of concrete strength in tension,

based on curve fitting of test results found in literature. Separate programs called MESHGEN, LOADGEN and FTIMGEN have been written for generating the input data of FEABRS. When the geometry of a problem allows the use of regular grid, MESHGEN can be used to generate the necessary geometry input data. LOADGEN is an edge pressure loading generation program which enables a direct specification of uniformly distributed loads input data. The program FTIMGEN has been developed to generate the type and features of the history functions of externally applied forces.

In the post-processing stage, special attention has been given to graphic representation of results. Programs MESHPLOT, DEFPLOT, PATTERN have been created to plot the undeformed finite element mesh, the deformed structural shape at selected time steps and the crack patterns respectively. Another program, namely HISTPLOT (history plot) is used to plot the displacement, stress or strain histories. All the post-processing programs use the GINO graphic library [234].

Finally, two computer programs, CONDIAG and STEDIAG have been written for the graphical representation of constitutive elements featuring the concrete and steel material models developed within this thesis. These features have been presented in the figures shown in Chapter 5.

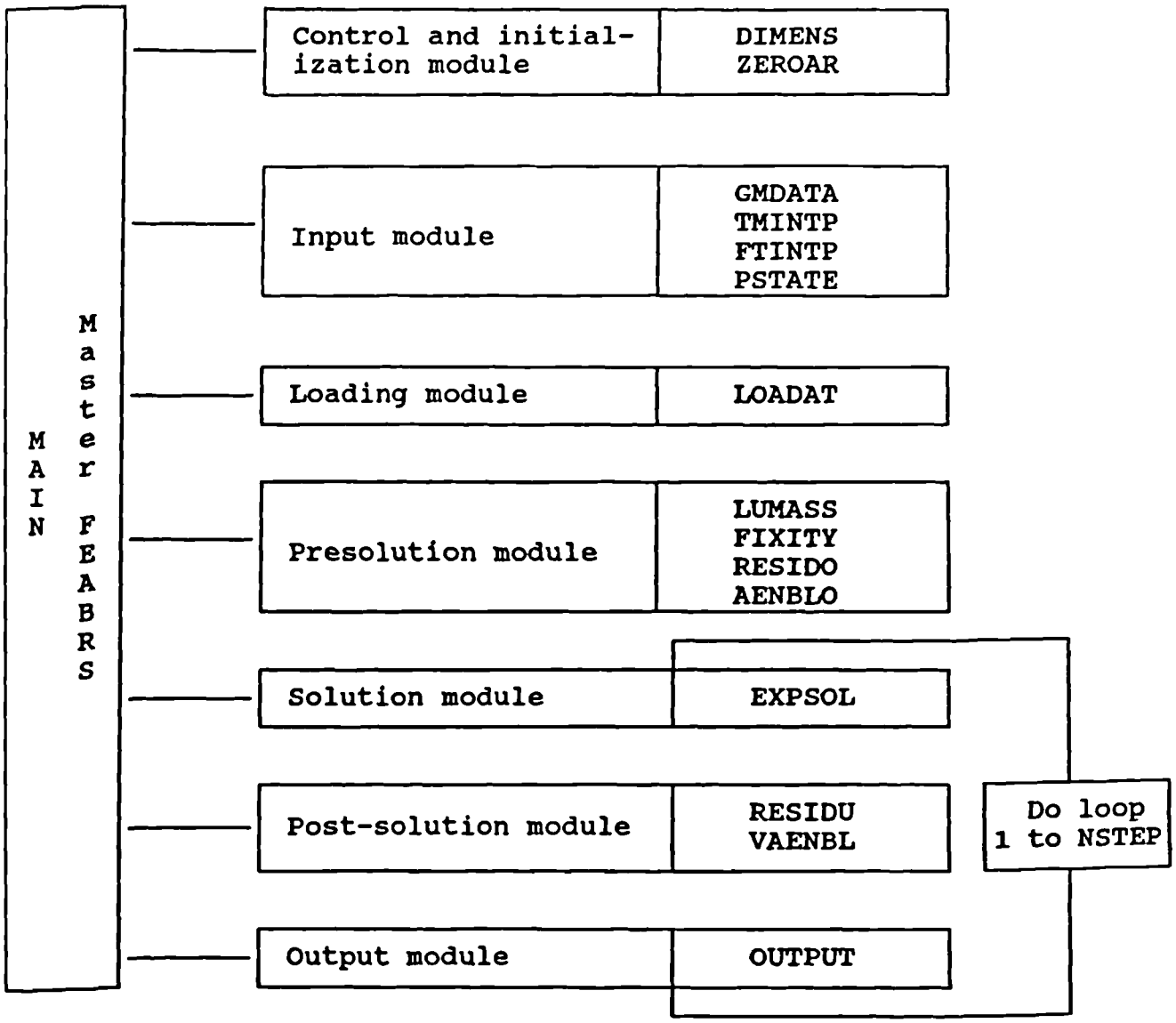

Figure (7-1) Flow diagram of FEABRS

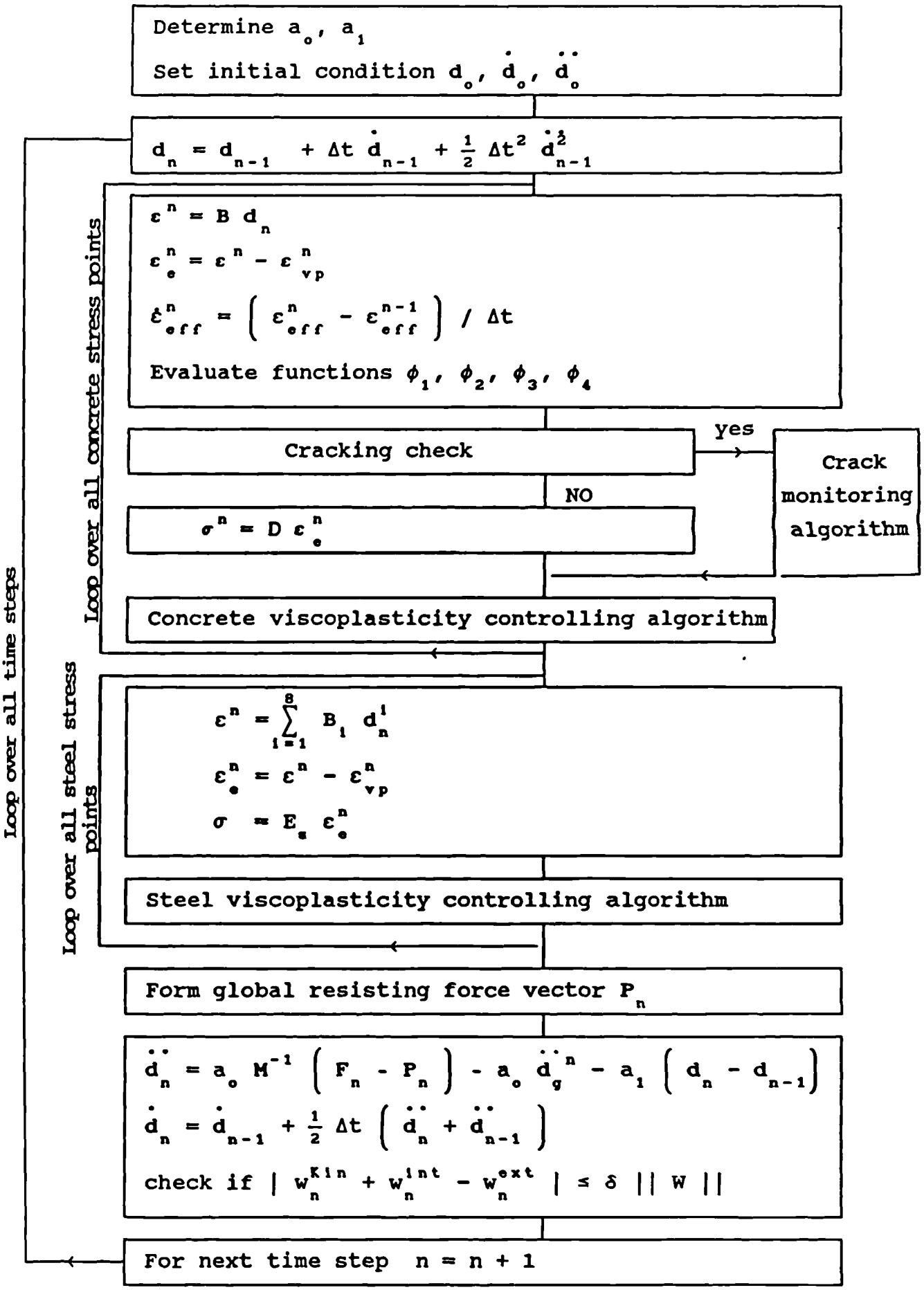

Figure (7-2) Implementation flow chart of solution technique and rate dependent material models in FEABRS

A - Check is the sampling point (GP) previously cracked

B - if not previously cracked (crack has just initiated):

1. - Compute and store crack angle
2. - Set appropriate flags for material state (MSTAT)
3. - Stress evaluation for cracked state, go to D

C - if previously cracked:

1. - Compute strains in local coordinate system.
2. - Check whether each of the old cracks is opened by checking the dilation across each existing crack.
3. - For plane problems, if GP is previously cracked in one direction, check whether a new crack has just opened orthagonal to the direction of first one by checking the strain parallel to the first crack.
4. - For axisymmetric problems, if GP is previously cracked in one direction or two directions check whether another new crack (two for the first case and one for the second) just initiated from the following three possibilities of cracks:

i. radial crack by checking the strain in the hoop direction.

ii. main circumferential crack by checking the strain in the radial direction.

iii. secondary circumferential crack orthogonal to the main one by checking the strain parallel to the main circumferential crack.

5. - Store angle of each new crack
6. - Update appropriate flags for MSTAT
7. - Stress evaluation of cracked state

D - stress evaluation procedure for cracked state:

1. - Evaluate stresses in crack directions using suitable D_{cr} matrix.
2. - Update the normal stresses across the cracks using tension softening rule.
3. - Update shear stresses across the cracks using shear transfer model.
4. - Update the crack reference values.
5. - Transform stresses back to global directions.

Table (7-1) The crack monitoring algorithm in FEABRS

A - Check for crushing

If $g(I_1^{\backslash}, J_2^{\backslash}) \geq \varepsilon_{cu}$ then

set stresses to zero $\sigma = 0$

Go to I

B - Determine the value of fluidity parameter

$\gamma^n = 10^{B_1} (\dot{\varepsilon}^n_{eff})^{B_2}$

C - Determine the current value of the yield function

$f(I_1, J_2)$

D - Check for softening

If $(w^f_{vp}) = 0$ then go to E

else $K_s = w^n_{vp} - w^f_{vp}$

$\tau^n = \sigma^{\backslash}_{cd} e^{-\delta K_s}$

Go to G

E - Check for failing

If $F^f (I_1, J_2 \sigma^{\backslash}_{cd}) \geq 0$ then

$w^f_{vp} = w^n_{vp}$

Go to G

else $w^f_{vp} = 0$

F - Determine the strain hardening function

$$\frac{\tau^n}{\sigma^{\backslash}_{cd}} = \frac{2}{\eta_h}\left[1 - \eta_h + \eta^{\backslash}_h \varepsilon^n_{vp}\right]^{1/2} - \frac{2}{\eta_h}\left[1 - \eta_h + 0.5\, \eta^{\backslash}_h \varepsilon^n_{vp}\right]$$

where $\eta^{\backslash}_h = 2\, \eta_h / \varepsilon^{\backslash}_{cd}$

G - Check for viscoplastic yielding

If $F(I_1, J_2, \tau^n) \geq 0$ then

$\dot{\varepsilon}^n_{vp} = \gamma^n < \phi^n (F) > a$

else $\dot{\varepsilon}^n_{vp} = 0$

H - Update viscoplastic strain vector and viscoplastic work

$\varepsilon^{n+1}_{vp} = \varepsilon^n_{vp} + \dot{\varepsilon}^n_{vp} \Delta t$

$w^{n+1}_{vp} = w^n_{vp} + \sigma \dot{\varepsilon}^n_{vp} \Delta t$

I - Calculate internal resisting force of concrete

$P_n = \int_v B^T \sigma^n \, dv$

Table (7-2) Concrete viscoplasticity controlling algorithm in FEABRS

A - Calculate steel fluidity parameter

$$\gamma_s^n = 10^{K_1} (\dot{\varepsilon}^n)^{K_2}$$

B - Determine the effective stress

$$\tau^s = \sigma_{yd}^s + H\, \varepsilon_{vp}^n$$

C - Check for viscoplastic yielding

if $\sigma^s > \tau^s$ then

$$\dot{\varepsilon}_{vp}^n = \gamma_s^n (\sigma^s - \tau^s)$$

else $\dot{\varepsilon}_{vp}^n = 0$

D - Update viscoplastic stress

$$\varepsilon_{vp}^{n+1} = \varepsilon_{vp}^n + \dot{\varepsilon}_{vp}^n \Delta t$$

E - Calculate internal resisting force of steel

$$P_s = \int_{V_s} B^T \sigma \, dv_s$$

Table (7-3) Steel viscoplasticity controlling algorithm in FEABRS

CHAPTER 8

NUMERICAL APPLICATIONS

8.1 INTRODUCTION

In this chapter, the finite element solution of some planar and axisymmetric reinforced concrete structures under impulsive loading conditions are described in detail. The solutions have been obtained using FEABRS, described in the previous chapter. The main objectives of these analyses are as follows:

1 - To analyse the validity and accuracy of the proposed material models and to justify the associated parameters used in the models.

2 - To demonstrate the capabilities and efficiency of the explicit central difference solution technique.

3 - To demonstrate the generality and versatility of the associated computer code developed.

4 - To study the structural response and respective failure mechanism in high rate of loading conditions such as those associated with blast and impact.

5 - To conduct parametric study on the strain rate sensitivity and the pre- and post-failure behaviour of concrete.

Three examples of impulsively loaded concrete members were selected. The first one which is discussed in section 8.2, is a single span beam under impulsive concentrated loads. In section 8.3, the analysis details of a clamped circular reinforced concrete slab subjected to uniformly distributed jet force are given. The third example, in section 8.4 is a simply supported beam subjected to uniformly distributed blast loading. Numerical solutions obtained for each sample problem are compared either with available experimental results or with existing analytical solutions found in the literature. The main objective in each case is to discuss

the deflection history, cracking patterns, deformations, stresses and effective strain rate distribution in concrete, and stresses in reinforcing steel. A parametric study is given in section 8.5 on the effect of the rate sensitivity and pre- and post-fracture concrete modelling parameters on the behaviour of the structures. Finally, in section 8.6, discussion of results obtained and some concluding remarks are presented.

8.2 SIMPLY SUPPORTED REINFORCED CONCRETE BEAMS UNDER IMPULSIVE CONCENTRATED LOADS

8.2.1 GENERAL BACKGROUND

A simply supported reinforced concrete beam, shown in Figure 8-1, subjected to two symmetrically applied concentrated loads of impulsive nature is considered here. The solution of the problem has also been reported in [78, 235].

8.2.2 GEOMETRY, MATERIAL PROPERTIES AND LOADING

The geometry and the loading of the reinforced concrete beams under analysis are illustrated in Figure 8-1. The beam is reinforced in the lower position by 1290 mm^2 steel area. The material properties of concrete and steel, as seen in Table 8-1, are assumed to be the same as those specified in [78, 235]. Concrete material constants describing the strain rate dependence of the fluidity parameter are obtained from the empirical relation developed in chapter 5, according to the concrete compressive strength. The concentrated loads are applied as step loads at time zero, each with magnitude of P = 30 kN.

8.2.3 NUMERICAL MODEL

Due to symmetry conditions, only one half of the beam needs to be considered in the study. Half span is spatially discretized by ten 8-noded isoparametric elements with embedded axial bars to simulate the steel reinforcement. The plane stress finite element mesh is shown in Figure 8-1.

The loading and boundary conditions assumed are also given in the same figure. Reduced integration is used for the evaluation of internal resisting forces. Structural mass is modelled using Hinton's lumping scheme [180], with full integration order.

The dynamic response is evaluated using the rate dependent material models proposed in Chapter 5 in conjunction with the explicit central difference time integration scheme. The time step is selected to be 0.000002 sec to meet the numerical stability considerations discussed in Chapter 6. No viscous damping has been considered.

8.2.4 RESULTS

a) Mid-span deflection history

As a check, an elastic analysis was first performed and the results found to be in excellent agreement with those given in [78, 235]. Figures 8-2 and 8-3 illustrate the time history of the mid-span deflection for the linear solution case as well as four different nonlinear analyses representing the four failure criteria proposed for the failure and loading surfaces in Chapter 5. The central deflection history of the nonlinear cases was found to be in good agreement with that given in [78], and the deflection were 8% less compared with those given in [235]. This slight difference may be attributed to the fact that the material models adopted for concrete and steel in [235] do not account for the strain rate effect as well as the post-cracking behaviour of concrete.

The following conclusions can be drawn from Figure 8-2 and Figure 8-3 regarding the nonlinear response:

* An increase of the maximum deflection by almost 50% compared with the linear elastic case.
* An elongation of the fundamental period by nearly 25% compared with the linear solution.

* The energy dissipative characteristics of concrete due to cracking and viscoplastic behaviour in the nonlinear case diminish the amplitude of oscillations.

* All the proposed functions for loading surfaces predict the same deflection history which indicates that concrete cracking is the main cause of the nonlinear action in this case.

* The influence of material nonlinearities is more important in the vicinity of the critical regions. The first deviation of the nonlinear case from the linear one is due to cracking over the central part of the beam at the tension side.

Despite the spreading of tension cracks, the *structure is* found to be still capable, thanks to stress redistribution, of further load to reach the failure stage. Similar observation has been reported in [78, 235].

b) Deformation and cracking history

The beam topology is traced in Figure 8-4 which shows the deformed shape of the member and how the cracks spread in concrete at different time stations. The deformed beam elevation is represented considering the horizontal and vertical displacements magnified 20 times. In the figure, cracks are denoted by lines representing the direction of the cracks. As already mentioned in Chapter 5, the adopted smeared crack modelling will simulate discrete physical cracks by spreading their effect over that part of an element related to an integration point. Thus, each of the single cracks represented in Figure 8-4 stands for an several of parallel fissures covering one quarter of each 8-node isoparametric element.

The numerical patterns of Figure 8-4 display only full cracks, i.e. cracks for which the normal crack strain is beyond the ultimate strain of the tensile softening branch.

Partial cracks as well as closing ones have been ignored in that Figure. To define the ultimate tensile strain, the exponentially decaying softening curve adopted here is approximated by a linear descending one. The limiting value, ε_{tu}, is related to concrete fracture energy, G_f, concrete tensile strength σ'_{ts} and crack characteristic length, L_c, by $\varepsilon_{tu} = 2\ G_f\ /\ \sigma'_{ts}\ L_c$. It has been found that plotting all cracks can be misleading. Displaying only full macro-cracks correctly reveals only fracture localization. Similar findings have been reported in several recent studies [94, 236, 237].

Tracing the cracking history, the beam behaviour is linear elastic in the initial stages. At time, t = 0.00298 sec, cracking commences near the bottom surface of the beam. With increasing deflection, the cracks develop on the underside of the central part of the beam. The cracking patterns indicate that flexural deformations produce the cracks which are all perpendicular to the tension face at initiation. As the cracks propagate further into the beam the compressive strain combines with the shear strain and alters the inclination of the principal tensile strain so that the cracks incline towards the horizontal. The predicted crack patterns in the present analysis are found to be in good agreement with those reported elsewhere [78].

The horizontal and vertical displacement fields of half the beam span at different time stations are illustrated in Figure 8-5 and Figure 8-6 respectively. The displacements are represented by contours of constant value and all dimensions are in mm. The mid-span transverse section keeps its initial geometry in the horizontal direction since the x-displacements are restrained in this direction. Figure 8-6 shows that the concrete elements in the central zone of the beam, experience vertical deflections consistent with the constant bending moment in this zone. The significant increase in displacements with time reveals the fact that

the main factor contributing to the nonlinear behaviour is the cracking of concrete.

c) Distribution of concrete stresses and effective strain rate

Contours through points of equal values of the stress components as well as the principal stresses at time intervals 2.5, 7.5, 12.5 msec are shown in Figures 8-7 to 8-11. Just prior to cracking (time = 2.5 msec) the following observations from these figures can be made:

1 - The uniform spacing of stress contours in the longitudinal direction (Figure 8-7) across the beam depth indicates an approximately linear variation of the longitudinal stress with neutral axis located at about half the depth from the compression face.

2 - In the linear elastic stage, the tensile concrete stresses (Figure 8-7 and Figure 8-10) are found still to make a substantial contribution to the internal resistance of the beam.

3 - The maximal compressive stresses (Figure 8-7, Figure 8-11) are found mainly in the region closest to the applied concentrated load and over the top part of mid-span. The impulsively applied force appears to yield the largest tensile stresses (Figure 8-7, Figure 8-10) in remote face of central part of the beam. The shear stresses are locally higher underneath the applied force and also close to the support.

For higher time levels, the stress patterns are explained in respect of the crack patterns (Figure 8-4) which lead to the following points:

1 - After formation of the cracks and the associated destruction of concrete tensile stresses, the distributions in all plots show large gradients of stresses which indicate a concentration of compressive stresses at the head of cracked zones (Figure 8-7, Figure 8-11). Such concentration above a cracked region causes a fluctuation of the neutral

axis position.

2 - As a consequence of pronounced vertical flexural cracks in the fractured region, the longitudinal stresses drop gradually to zero (Figure 8-7) in this zone. The transfer of tensile stresses to the reinforcement and the shifting of the position of the neutral axis is well predicted.

3 - From the principal stress distributions (Figure 8-10, Figure 8-11), arching action from the support to the loaded region is clear at later time stations.

4 - Figure 8-8 gives almost similar stress patterns before and after cracking where the transverse stress component is generally increasing with time increase.

5 - From Figure 8-9, the determination of the shear stresses across the cracked zone as well as the higher shear stress levels at the head of cracks can be clearly seen, especially close to the support.

6 - It is noted that viscoplastic yielding of concrete occurs mainly in the central region close to the top of the beam (Figure 8-7). However, the compression stresses remain well below the proposed failure surface.

The effective strain rate distribution at different time stations is shown in Figure 8-12. In the linear elastic stage (time = 2.5 msec), the effective strain rate field shows higher gradients close to the applied load and over the central part of the beam. After cracking, the importance of rate effects on crack initiation and propagation is noteworthy. Significant concentrations of strain rate contours are found at the tip of the cracks and near the support.

d) Steel stress and effective strain rate distribution

The history of the computed axial stress and effective strain rate along the main reinforcing steel is shown in Figure 8-13 and Figure 8-14 respectively. It can be

observed that both the steel stress and the associated strain rate along the span increase for higher time intervals. Starting from the time station 0.005 sec, the influence of open cracks in concrete is clearly seen. In places where the cracks develop near the reinforcing steel, a large increase in the steel stress and strain rate occurs. The numerical results shown in Figure 8-13 also indicate that the calculated stress in the middle zone of the span is the highest stress level and exhibits almost the same distribution on the right hand side of the applied concentrated load. This may be explained as a consequence of the fact that the bending moment is constant and maximum over this area and more flexural cracks have developed there. No yielding has been observed in the reinforcing steel. The maximum computed stress is in the middle zone and equals 220.0 MN/m^2.

From Figure 8-14, it can also be seen that the concrete cracking allows the steel effective strain rate values to fluctuate along the beam span as a result of the localized fracture in concrete and the resulting stress concentration in concrete and steel.

8.3 CLAMPED CIRCULAR REINFORCED CONCRETE SLAB UNDER UNIFORMLY DISTRIBUTED JET FORCE

8.3.1 GENERAL BACKGROUND

Reinforced concrete slabs are best suited to withstand various types of short duration severe forces as a result of their relatively large masses and high energy absorption capacity due to ductility. Impact by deformable objects or rigid missiles on target slabs can be modelled by concentrated loads. Explosive charges detonated in contact with the slab may also lead to concentrated forces. Distributed loads can be used to simulate differential pressure of air or remote detonation of explosives. The reinforced concrete circular slab shown in Figure 8-15, which is subjected to a uniformly distributed load, was

selected for a study using the proposed numerical model. This problem has been previously analysed by several investigators [34, 78, 238] for checking their material modelling approaches.

8.3.2 GEOMETRY, MATERIAL PROPERTIES AND LOADING

The reinforced concrete slab has a radius of 10.0 m and a thickness of 1.0 m. The slab is isotropically reinforced in the upper and lower position by one percent of the reinforcement in both the radial and tangential directions. The plate geometry and reinforcing steel are shown in Figure 8-15. The material properties employed in the present study are specified in Table 8-2 which are the same as those defined in [78, 238]. The fluidity parameters of concrete and steel are evaluated on the basis of the emperical relations proposed in Chapter 5.

The uniformly distributed load is perpendicular to the middle surface of the plate and of intensity 137.3 kN/m^2. The load is applied with a rise time equal to half of the fundamental period of the plate ($T \approx 0.06$ sec) [238].

8.3.3 NUMERICAL MODEL

Axisymmetric conditions were assumed in the theoretical analysis. The finite element mesh of the reinforced concrete plate in the R-Z plane is shown in Figure 8-15 which has 24 elements and 101 nodal points. Due to symmetry, only a quadrant of the structure was modelled using the 8-node isoparametric elements. The reinforcement nets were simulated as axisymmetric membranes with Poisson's ratio $\nu = 0.0$, which in the adopted model implies four steel layers, two each placed near the top and bottom of the slab. The equivalent thickness of each steel layer is 1.0 cm. The finite element mesh and the loading and boundary conditions assumed in the analysis are defined in Figure 8-15.

The lumped mass matrix is evaluated using the 3x3

integration order while 2 × 2 rule is employed for the calculation of internal resisting forces. The material behaviour of concrete and steel are modelled using the rate dependent material models proposed in Chapter 5. The explicit central difference scheme is employed to solve the dynamic equations, with a time step length of 0.000005 sec. No viscous damping is considered.

8.3.4 RESULTS

a) Mid-span deflection history

As a first step, a linear elastic dynamic analysis is carried out to check the main input data. The linear elastic deflection curve was qualitatively and quantitively the same as the analytical results reported in [78, 238]. The time history of the mid-span deflection for the linear analysis as well as the nonlinear response for two different levels of the concrete cracking strain are plotted in Figure 8-16. The curve obtained for $\varepsilon_{ts}^{\backslash}$ = 0.00018 is almost identical to the response in [78]. However, unlike the results in [238], no decay of the subsequent peak amplitude is observed. This is probably due to the fact that a smaller time step was used in the present analysis, thus avoiding numerical damping. A similar finding has been reported in [78]. It is clear from these results that the resulting central deflection varies significantly with the analysis type (linear and nonlinear) as well as with the value of the cracking strain. The general trends observed in the previous example are confirmed. Nonlinear effects amplify displacements and elongate the period of vibration. As shown in the Figure, the displacements increase with decreasing cracking strain and the significant variation in responses obtained indicates that tensile cracking is the most sensitive dissipative mechanism for this concrete structure. The influence of such material nonlinearity is more important in the vicinity of the critical tension regions of concrete since concrete in the compressive zones remains within the elastic range throughout the analysis.

Despite the spreading of cracks in the radial and hoop directions, the slab is found to be still capable of resisting, higher load intensity to reach the failure stage, especially in compression zones. Similar conclusion has been drawn elsewhere [34, 238].

b) Deformation and cracking history

At different time intervals, the deformed slab profiles of one half of the structure and the spread of the crack zones through the thickness in the radial and hoop directions are shown in Figure 8-17 where the deformations are enlarged 20 times. In the initial stages (time = 0.024 sec), the slab behaviour is linear elastic. At time, t = 0.032 sec., the nonlinear analysis leads to cracking in the tangential direction in the vicinity of the built-in section at the top of the slab. The first circumferential cracks are predicted at the bottom of the centre of the slab at time, t = 0.0366 sec. With increasing time, the radial cracks spread to the top of the slab at mid-span and to the bottom of the slab at the fixed edge. On the other hand, the hoop cracks extend from the lower face towards the centre at the top of the slab. Cracks also propagate in the central zone. Such propagation of cracks as indicated by the computer program FEABRS is consistent with the fact that the flexural stresses in tension are maximum at the upper face near the clamped edge and also at the lower face in the central region. Shear induced diagonal cracks have not been observed, which is not unexpected considering that the slab is 1 m deep. This description compares favourably with the observations of previous analyses [78, 238].

Figure 8-18 and Figure 8-19 illustrate the distribution of displacement fields along the horizontal and vertical directions respectively. The deflections are represented by contours which are dimensioned in mm. The end-supported section keeps its initial geometry since the vertical and horizontal displacements are restrained in this section.

The mid-span transverse section is free to displace only in the vertical direction. As shown in the figures, the displacements generally increase with increasing time, compared with the elastic results at time = 0.016 sec. In Figure 8-18, a similar behaviour is observed in tension and compression before cracking, but the biaxial symmetry is lost for the plate due to change of stiffness after tensile cracking (time = 0.032, 0.048 sec). An interesting phenomenon can be observed at time = 0.048 sec, when a pronounced increase in concrete cracks is computed (Fig 8-17). At this point, it can be seen from Figure 8-19 that the increase in deformations is mainly determined by the increasing displacements in the cracked zones.

c) Distribution of concrete stresses and effective strain rate

Before and after cracking, the variation of concrete stress components and the corresponding principal stresses along the discretized part of the slab are illustrated in Figures 8-20 to Figure 8-25. The distribution of stresses in these diagrams together with the cracking patterns (Fig 8-17) support the following concluding remarks:

1 - In the elastic domain (time = 16 msec), the plots show similar behaviour in compression and tension zones with the neutral plane positioned at almost half the slab thickness, as expected. The maximal values of stresses are found close to clamped support or at the central part of the slab depending on the type of the stress component.

2 - After cracking, the biaxial symmetry is lost for the isotropically reinforced concrete plate and the neutral plane does shift due to change of concrete stiffness after cracking which follows the progression and orientation of cracks.

3 - At time = 32 msec, cracking was locally contained in the region of maximum moment in the vicinity of the fixed edge and most of the slab remained elastic. The compressive

and tensile stress contours indicated in the diagrams of main stress components follow uniform distribution. At time = 0.048 sec, the compression zone contours dominate in the bottom of support region and in the compression zone in the mid-span (Figure 8-20, Figure 8-25).

4 - Figure 8-24 and Figure 8-25 show respectively the maximum and minimum principal stress field history. It is noted that very large stress gradients exist in the regions close to the clamped edge and the central part of the slab. However, the maximal compressive stresses are approximately equal in these critical zones at time = 0.048 sec.

5 - Another stress component having major influence on the load carrying capacity of the slab is the circumferential stress which is plotted in Figure 8-23. At time = 0.048 sec, an extensive hoop cracking is developed at the lower central part which originates a significant redistribution of this stress component, decreasing the maximum relative values in this fractured zone.

6 - The diagrams of the distributions of shear stress (Figure 8-22) and transverse stress (Figure 8-21) are self-explanatory with respect to the crack patterns shown in Figure 8-17. Smooth distribution of such stress components are only obtained in unfractured concrete.

7 - At any time level, no viscoplastic response is predicted in concrete as the compressive stresses maintained within the initial dynamic yield surface.

The fluctuation of the concrete effective strain rate values at different time intervals is presented in Figure 8-26. Prior to cracking time (time = 16 msec), the strain rate distribution is uniform and well predicted. For higher time levels, the concrete cracking results in a significant redistribution of contours and high strain rate values in fractured zones. It can be further observed that the peak values alter their position following the progression and position of concrete cracking.

d) Distribution of steel stress and effective strain rate

At different time levels, the variation of the axial stress is shown in Figure 8-27 and Figure 8-28 along the radial and hoop reinforcing steel membranes, respectively. The corresponding effective strain rate distributions are shown in Figure 8-29 and Figure 8-30. In these diagrams, the stress and strain variations in the linear elastic stage are compared with those in the nonlinear stages. Prior to cracking in both the radial and the hoop direction, the distribution of the stress and the effective strain rate of the top reinforcing membranes is almost identical to that of the bottom ones. After cracking, the following phenomena can be observed from the redistribution of the stress and strain rate illustrated in the plots:

1 - The oscillating stress distribution along the reinforcement indicates that the more flexible concrete causes the hoop and radial reinforcement to carry more force resulting in higher strain rates and stresses where the concrete cracks are open.

2 - The numerical results give higher strain rate values in the reinforcement at the middle zone as well as near the fixed edge since more cracks have developed there. As shown, the peak strain rate value changes its position as the cracks propagate.

3 - Following a space truss analogy in cracked slab, the increase in stress and strain rate of reinforcement in tension zones leads to a similar effect in steel in compression side.

4 - No yielding has been predicted in the reinforcing steel. At time = 0.048 sec, the maximum computed stresses are 180.1 MN/m^2 for radial reinforcement at the fixed edge and 146.9 MN/m^2 for hoop reinforcement in the middle of the slab.

8.4 REINFORCED CONCRETE BEAM SUBJECTED TO UNIFORMLY DISTRIBUTED BLAST LOADING

8.4.1 COMPARISON WITH EXPERIMENTS

Experimental results on beams subjected to blast loading have been reported by Seabold [239]. In that study, eight reinforced concrete beams were tested to study shear and diagonal tension in beams under blast loads. These tests constituted the second phase of a programme to determine criteria for the minimum amount of shear reinforcement required for developing the ultimate resistance of beams as well as to determine the difference between these criteria for static and dynamic loading. Each beam was simply supported and all loads were uniformly distributed. The beams were tested in the NCEL blast simulator, shown in Figure 8-31 where dynamic loads were applied by generating expanding gases in the simulator from the detonation of Primacord explosive by means of blasting caps. The rise time is controlled by the holes in the firing tube, the peak pressure by the amount of Primacord, and the decay time by opening valves which vent the gases to the atmosphere.

One of the tested specimens, namely beam WE5, has been chosen here for the numerical simulation with FEABRS. This beam has been selected because dominant shear cracks characterised the behaviour of this beam. A good correlation with experimental results would be interpreted as validation of the numerical method proposed.

8.4.2 DESCRIPTION OF THE STRUCTURE AND MATERIAL PROPERTIES

The overall dimensions and supports of beam WE5 are shown in Figure 8-32. The dotted lines in the diagram show the location of the main reinforcement. The beam is doubly reinforced by 774.2 mm^2 (1.2 in^2) steel area in the top position and by 1290.3 mm^2 (2.0 in^2) steel area in the lower zone. The main material properties of concrete and steel employed in the analysis are based on those reported in [239]. All the necessary properties are listed in Table

8-3. The empirical relations proposed in chapter 5 have been adopted to calculate the constants of the rate dependent fluidity parameters of concrete and steel. The parameter governing the compressive softening of concrete is assumed to equal 10. For the post-cracking behaviour, the concrete fracture energy is taken as 60.2 Nm/m^2 and the shear transfer factor as 1.00.

8.4.3 NUMERICAL MODELLING OF THE PROBLEM

The beam is discretized using plane stress isoparametric elements with eight nodes. Using symmetry of the geometry and loading conditions, only one half of the complete structure has to be modelled. The finite element mesh and the boundary conditions are shown in Figure 8-32. The main reinforcement in tension and compression is simulated as perfectly bonded axial bars embedded in the surrounding concrete elements. Based on the numerical stability consideration discussed in Chapter 6, the time step length is chosen to be 0.000002 sec, for the central difference explicit time integration scheme. No viscous damping forces have been considered. The numerical modelling of concrete and steel is based on the history and rate dependent models developed in Chapter 5.

8.4.4 EXPLOSION LOADING DATA

The applied overpressure was measured at about 508 mm (20 ins) above the top surface of the beam at three locations along the span. From the experiment it was possible to identify the following characteristics of a pressure-time history due to blast loading (Fig 8-32):

1 - The arrival time of the shock front is 0.75 msec from the instant of detonation of Primacord which means that the shock wave travels at an average speed of about 700 m/sec.

2 - The shock front is not vertical, i.e. the pressure rise from the ambient to peak pressure is not instantaneous. The pressure rise time is about 2 msec.

3 - The width of the load was 205.74 mm (8.10 ins) and the entire cross-section of the pressure chamber on the beam top surface was considered to be entirley filled with combustible gas, therefore, the overpressure which is given in stress units, 0.4137 N/mm^2 (60.0 psi) has been multiplied by this width to obtain the load per unit length of the beam. The measured peak overpressure was about 85.115 $N/mm^{\backslash}$, (486.0 $lb/in^{\backslash}$).

4 - The peak overpressure remains approximately constant forming an overpressure plateau. The duration of the applied load was 28 msec.

5 - No decay of the peak pressure was reported at the end of overpressure plateau.

Based on this information, the analytical bilinear loading function, which closely approximated the experimentally applied blast load is shown in Figure 8-32 from the instant of application of the load on the beam.

8.4.5 ANALYTICAL RESULTS OF THE PROBLEM

a) Time history response of the beam at mid-span

The computed and experimental displacement-time histories at mid-span are shown for comparison in Figure 8-33 which shows a good agreement. The peak experimental response of 28.5 mm was recorded at 19.5 msec, which agrees closely with the analytical results, for which the computed peak displacement of 28.0 mm is reached in 18.0 msec. The recorded permanent deformation of this beam was 20.8 mm, and it also compared well with the predicted deflection of 19.7 mm. The computed mid-span velocity-time history is compared in Figure 8-34 with experimentally observed velocity. Again there is good agreement with the peak velocity and the corresponding time, as well as the time when the velocity returns to zero.

The experimental and computed top compressive strain histories of concrete at beam mid-span are presented in

Figure 8-35. There is good agreement as the variations observed are within the dispersion often encountered in experimental results. In addition, the time history of strains of the top and bottom reinforcing steel of beam WE5 are plotted in Figure 8-36. It can be noticed that the numerical analysis reasonably agrees with the observed experimental behaviour up to about 9 msec for the tension steel and 12 msec for the compression steel. For higher time history, the measured compressive and tensile strains oscillate resulting in a lower value than the computed ones. The reason for this discrepancy is not clear. To investigate a possible explanation, the strain time history of the main reinforcement of another beam of the test series, namely WE2 was computed. The geometry and loading conditions as well as the material properties of beam WE2 are similar to those of beam WE5, except that the compressive strength of concrete is slightly higher (by 4%). As shown in Figure 8-37, very good agreement is obtained.

The computed response in the most critical zone of the beam shows that a good numerical simulation of the experimental observation is possible using the present nonlinear numerical method despite the highly variable nature of the loading conditions. It is worth mentioning that although significant numbers of integration points show cracking up to time 0.015 sec, yet the analysis agrees very well with the structural response at each time step. The use of explicit central difference scheme, together with the energy balance tolerance of 0.001 gives satisfactory results.

b) Support reaction-time history

Comparison between the time history of the measured reaction at the left support of the beam and that of the calculated reaction is shown in Figure 8-38 which indicates a satisfactory agreement. The peak measured dynamic support reaction of 24.3 kN at 15.0 msec is in good agreement with computed support reaction of 27.0 kN that occurred at 17.0

msec. The slight discrepancy between theory and experiment may be attributed to the following factors:

1 - From the documentation of the experiment, it was diffcult to determine to what degree of accuracy the measurements have been made. It is also mentioned in [239] that the documented reaction measurements have been corrected for the effects of the overhang of the beam to determine the total shearing force at the supports.

2 - The monotonically applied blast loading used in the analysis is a close approximation of the experimental applied pressure.

3 - It may be expected that the moment and shear forces redistribution due to cracking affects the results at support zone in a way that was difficult to reproduce analytically in an accurate manner, since the representation of the boundary conditions in the adopted explicit time integration scheme is based on employing very large virtual nodal masses to simulate the fixed degrees of freedom.

4 - The analytical reaction-time history has been computed by multiplying the vertical acceleration-time history at the support by the assumed virtual nodal mass in that direction.

c) Deformation and cracking history

The deformed shape of beam WE5 at different time intervals is plotted in Figure 8-39 in which the open cracks of concrete at various stages in the loading history of the beam are also displayed. The deformations in the vertical and horizontal directions are magnified 10 times. In the initial stages (time = 3 msec), the beam behaviour is linear elastic as shown in the Figure. Then, flexural cracks developed and continued to propagate up to time 6 msec. After this, little further vertical crack development took place. Diagonal cracks appeared in the web at time 6-9 msec, some as isolated cracks and some propagating from flexural ones. For time higher than 9 msec, these inclined

cracks spread towards the beam top surface and towards the beam support. Similar to the experimental behaviour, concrete crushing does not occur.

In the experiment, it was observed that at first concrete exhibits a number of flexural cracks which are suddenly overshadowed by the occurence of major diagonal cracks. Particularly challenging for a numerical simulation are many physically observed phenomena such as localisation, opening and closing of cracks and mixed-mode effects. The results in Figure 8-39 match the experimentally recorded crack pattern quite well since diagonal cracks leading to failure are correctly obtained. It may be further observed that although there is some diffusion in the crack pattern, as in all smeared crack analyses [94, 236], strain localisation is clearly monitored. This becomes even more apparent when it is observed that almost all diagonal cracks are wide open, and open further with increasing time. This observation is also valid, though to a lesser extent, for flexural cracks. The difference between the plotted cracking patterns reveals that following time increase, some Gauss points exhibit flexural cracks. Once formed, these cracks did not fully develop but were arrested or even closed later in the process. This aspect is a typical feature of fracture localisation problems as such problems always involve simultaneous loading and unloading of adjacent elements.

The relatively smooth spread of crack zone is shown in Figure 8-39. This appears to be a basic feature of isoparametric elements. Even more remarkable is the ability of one element to reproduce two different types of cracking modes, namely flexural and diagonal cracks, during the transient analysis. From the crack development history, another important conclusion may be drawn is that the longitudinal reinforcement stabilises each crack originating at the tensile face of the reinforced concrete beam. The term stability here means limiting the crack propagation. However, the curved nature of cracks in a region of combined

moment and shear leads such cracks to zones of higher strains and instability of cracks may take place. The curved crack that has started nearest to the point of contraflexure is also the least stable for the same reason.

The distribution of the horizontal and vertical displacements of the discretized mesh are shown in Figure 8-40 and Figure 8-41 respectively. The displacements are represented by contours of constant value and all dimensions in mm. Since the x-displacements of the mid-span transverse section are restrained due to symmetry, the initial geometry of this section is maintained in the horizontal direction. In these figures, the displacements in the linear elastic stage (time = 3 msec) are compared with those in the nonlinear stages (time = 9, 18 msec). The significant increase in the deformation locally and globally for higher instants indicates the influence of concrete cracking in tension as well as the viscoplastic straining of concrete in compression.

d) Distribution of concrete stresses and effective strain rate

The distributions of the stress components and the corresponding principal stress values along one half of the beam span are plotted in Figure 8-42 to 8-46. The concrete stress contours in these figures are given in MN/m^2. The contours in the linear elastic stage (time = 3 msec) are compared with those in the cracking stage (time = 9, 18 msec). Before cracking, the variation of stresses indicates the previously observed phenomena in the first numerical example which are here even more clearly seen. The longitudinal stress varies linearly across the beam depth (Fig 8-42). As expected at this time level, maximum tensile and compressive stresses occured at mid-span section while maximum shear stresses are found near the support. On the other hand, after cracking, a significant redistribution of stresses has been computed. From the stress patterns, the

following main points can be stated:

1 - With increasing time, the tensile stresses (Fig 8-42, Fig 8-45) have generally disappeared due to cracking, and a pronounced thrust arch can be observed which equilibrates the mid-span tensile reinforcement stresses. This action represents a tied-arch equilbrium system.

2 - A concentration of the compressive stresses was found at the head of the cracked zone. However, the minimum principal stress (Fig 8-46) is approximately equal to the longitudinal stresses (Fig 8-42). This indicates the importance of cracking as a mechanism of energy dissipation.

3 - For a more quantitative understanding of the compressive principal stress distribution (Fig 8-46), the variation of this principal stress component can be considered at two different locations. At the section closest to the mid-span, a concentration of the stress occured near the top surface of the beam. In contrast, at the section closer to the support, the peak value of the stresses arises at some distance from the top of the beam. The manner in which these stresses are distributed can be understood by referring to the pattern of cracking (Figure 8-39).

4 - The distribution of transverse stresses shown in Figure 8-43 indicates higher gradients in the vicinity of the support before and after cracking. At time = 0.018 sec, these stresses are nearly zero in lower part of the middle zone as a result of some partially opened secondary cracks in this area.

5 - The redistribution of shear stresses due to cracking, shown in Figure 8-44, indicate that shear stresses vary rapidly in the regions where diagonal cracks are developed (Fig 8-39). Over the middle zone, the shear stresses are nearly zero.

6 - The viscoplastic behaviour of concrete in compression has been demonstrated (Fig 8-42 and Fig 8-46) over the middle region close to the upper beam surface

(time = 9 msec) The viscoplastic zone grows gradually down the depth mainly due to compressive stresses exceeding the elastic limit. Only at time = 0.018 sec., the maximum compressive stress is located very close to the rate dependent failure surface.

The variation of the concrete effective strain rate field along the beam is shown in Figure 8-47 in the linear and nonlinear stages. Before cracking (time = 0.003 sec), the strain rate is increasing gradually from the neutral axis towards the top and bottom surfaces of the beam in a uniform distribution across the beam depth. Due to progressive fracture, the distortion of the effective strain rate distribution is clearly seen in the Figure where high strain rate gradients exist in the cracked zones as well as the top part of the compression zone. The concentration of strain rate in the vicinity of the fractured zones highlights the importance of including the rate effects.

e) Distribution of steel stress and effective strain rate

The variation of the axial stress and the effective strain rate with time along the top and bottom reinforcing steel is shown in Figure 8-48 and Figure 8-49. The first observation that may be made is that the steel stress as well as the strain rate increase in parallel with the increase in deformation with time. At time station 3 msec., where the beam response is linear elastic, the variation of both the stress and effective strain rate for the tensile and compression reinforcement indicates almost the same distribution, as expected, with maximum values located at mid-span. After cracking (time > 3 msec) the steel stress plots clearly show the position of the dominant cracks in concrete. These plots show that the axial stress in the bottom steel increases significantly where the cracks intersect the reinforcing bars. It can be further observed that the amount of the tensile force transferred from cracked concrete to steel is higher for flexural cracks

compared with the shear ones. Taking the strain rate effect into consideration, the stresses in the lower reinforcement over the middle point of the span reach the yield level at time 0.015 sec. The maximum calculated stress level is in the mid-span section and equals 724.0 MN/m^2 corresponding to a gain in strength by a factor of aboout 1.50 due to dynamic effects. On the rebound stage of the beam response (time ≥ 18.0 msec), the stress in steel gradually decreases below the yield stress. From the difference between the strain rate distribution plots of Figure 8-49, it can be seen that concrete cracking allows the steel strain rate to fluctuate along the reinforcement bars. The peak strain rate value changes its location as the cracks spread. Between the cracks, the decrease of steel strain may be attributed to the perfect bond assumption in the present analysis.

8.5 PARAMETRIC STUDY OF CONCRETE NONLINEARITY

In finite element analysis of reinforced concrete structures, a large number of different combinations of geometric and material parameters can be considered. It is possible that, although markedly different combinations are considered, compensating factors may occur which result in similar predicted structural response. For this reason, it is desirable to perform a sensitivity analysis on at least the parameters which may be expected to influence the analytical response. In the present work, a special emphasis has been placed on the parameters governing the rate dependency of concrete, the cracking process and the strain hardening of concrete in compression. The numerical applications discussed in sections 8.2 and 8.4 have been selected for the numerical experimentation. The implications of the results of the parametric study are discussed with respect to modelling of reinforced concrete structures.

8.5.1 STRAIN RATE DEPENDENCY EFFECT

The performance of the rate independent modelling is compared with the rate dependent response of the concrete beam under impulsive concentrated load [235] in Figure 8-50, and with the experimental results of the concrete beam subjected to uniform blast loading [239] in Figure 8-51. The central deflection time history curves are shown together with the elastic response. Both the peak displacement and the time corresponding to the peak deflection vary with rate sensitivity consideration. As can be seen from Figure 8-50, ignoring the strain rate effect results in an over-estimate by almost 12% of the maximum deflection obtained for the rate dependent case, and by approximately 64% compared with the elastic case, an elongation of the natural period can also be noticed. The increase of central deflection by about 18% as well as the deviation of numerically predicted response from the test results reported in [239] at an early stage of the loading history, can be observed in Figure 8-51.

Based on the formulation of the proposed concrete constitutive modelling to simulate the experimentally observed phenomena under dynamic loading, two differences exist between the rate-dependent and rate-independent models that may account for discrepancies observed in the deflection history. First, the inclusion of strain rate dependency effect results in stress-strain diagrams which indicate higher strength and greater energy absorption before concrete fracture, than those in the rate-independent case. Second, the adopted rate dependent crack initiation criterion introduces numerically crack arresting mechanisms associated with the higher limiting cracking strain.

8.5.2 CONCRETE ELASTIC LIMIT IN COMPRESSION

The nonlinear response of the Bathe beam [235] for two different values of the concrete elastic limit in compression (0.3, 1.0) is illustrated in Figure 8-52. It

can be seen from the central deflection history curves shown in the Figure that increasing the elastic limit above the more realistic value of 0.3 decreases the maximum deflection by almost 13%. In the case where the elastic limit equals 1.0, i.e. strain hardening in compression is not included, no viscoplastic behaviour is observed, and hence the nonlinear effects are only due to the cracking of concrete.

The results of elastic limit parametric study for Seabold beam [235] given in Figure 8-53 confirms the above conclusions. The computed peak of the central deflection of the beam for the case of elastic limit = 1, *is lower* by nearly 10% than that of test results. The shortening of the time corresponding to peak displacement can also be noticed. A relatively good match between the two cases is achieved on the ascending branch of the curve until about 80% of the observed peak deflection level. However, the descending branch for the numerical model is significantly different. The deviation from the experimental results for the pre- and post-peak displacement history can be attributed to the absolute linear modelling of the concrete up to the failure surface, that is, the compressive strength level. This discrepancy can easily be eliminated by using the elasto-viscoplastic formulation with a rate dependent hardening function to model nonlinear behaviour of concrete in compression as shown in Figure 8-33.

8.5.3 CONCRETE CRACKING STRAIN EFFECT

For two different values of the cracking strain (0.0000613, 0.000075), the nonlinear response is plotted in Figure 8-54 for the Bathe beam [235]. It is clear from these results that the central deflection varies significantly with the value of the cracking strain. The decrease in the cracking strain by 20% results in an increase in the mid-span deflection by 10% as well as an elongation of the period. It is evident that the decrease in concrete cracking strain forces the cracks to propagate more rapidly. It was also

found that both the orientation and the number of cracks that develop in a concrete structure are highly affected by the cracking strain values used in the analysis.

Similar conclusions can be drawn from Figure 8-55 where the mid-span deflection history obtained from the finite element computations with a cracking strain = 0.000100, are compared with the test results of Seabold beam [239]. The peak value of the deflection is higher by 12% as a result of decreasing the crack initiation strain from 0.000129 to 0.00010. The discrepancy between the observed and the measured responses starts from an early stage. As expected, the cracking patterns obtained at different time stations were different from those shown in Figure 8-39. Incorrectly calculated direction of cracks may cause the stiffness and ductility of a structure to be underestimated. In turn, prediction of the deflection history and failure mode may also be in error.

8.5.4 CONCRETE FRACTURE ENERGY

In the analyses used to study the sensitivity of the Bathe beam [235] response to variations in the fracture energy, the nonlinear tension softening representation is employed and G_f varied between 105.1 and 150.6 Nm/m^2. Figure 8-56 highlights the influence of the concrete fracture energy upon the nonlinear response of the beam deflection history. It can be observed that the consequence of reducing this material property is an amplification of the effect of concrete cracking which results in an increase in deflection and an elongation of the period. However, the increase in the deflection is not proportional to the change in the fracture energy. As the fracture energy is increased by 50%, the maximum deflection decreases by only 10%.

The effect of the G_f concept on the computational results of Seabold beam [239] is shown in Figure 8-57. For lower value of G_f (= 40.1 Nm/m^2), the peak of mid-span deflection

increases by 12% while the time needed to reach the peak displacement decreases by a similar percentage. The deviation of the structural response in the pre- and post-peak deflection zones compared with the test results can also be observed. It is evident that the decrease in fracture energy forces the cracks to propagate more rapidly with significant increase in the crack widths.

The computed structural response clearly depends on the post-peak tensile behaviour of concrete through the fracture energy. The difference in deflection response for lower values of G_f seems to be a direct consequence of the decrease of the effective load-carrying area of concrete in tension. As the slope of the descending branch of the tensile stress-strain curves reduces for higher values of G_f, the cracks propagate more slowly and the load capacity of the structural member increases. The insensitivity of the response to small changes in fracture energy may be due to the fact that increasing the fracture energy primarily stiffens and not strengthens the structural element.

8.5.5 CONCRETE TENSION SOFTENING

The effect of tension softening in the post-cracking behaviour of concrete on the nonlinear response of Bathe beam [235] is considered in Figure 8-58. It is shown that the inclusion of tension softening reduces the deformation and the fundamental period considerably. Upon cracking the tension softening effect plays a major role in the prediction of stiffness of concrete elements. The mid-span deflection for the case with tension softening is reduced by 12% when compared with the case where it has not been included. It can also be concluded that the simulation of the tension softening effect by assigning a fracture energy based softening branch to the stress-strain curve of concrete in tension produces satisfactory results.

Figure 8-59 illustrates the sensitivity of the response of

Seabold beam [239] to concrete tension softening. The numerical analysis shows the same trend as Bathe beam where the peak and the post-peak response is much more ductile compared with the experimental results. The residual post-peak tensile strength of the concrete beam is considerably underestimated as a result of ignoring the tension softening.

Two main reasons may be suggested for this discrepancy:

1 - The influence of eliminating tension softening results in a greater flexibility on the global behaviour due to the decrease in the loading capacity of concrete in tension. As a consequence, the cracking is more widespread with an abrupt development.

2 - As a consequence of excluding tension softening effect, the neutral axis of the structural element experiences a shift towards the compression zone more than that would be obtained if concrete was treated as a linear elastic softening material in tension. This may result in an overestimate of the steel stresses, especially in critical zones.

8.6 DISCUSSION AND CONCLUDING REMARKS

Numerical solutions of three dynamic problems obtained using the proposed rate and history dependent material models which are implemented in the computer program FEABRS, are presented and compared with experimental and numerical results from other sources. These applications represent plane and axisymmetric structures characterised by different impulsive loadings, boundary conditions and geometrical factors. In addition to the specific concluding remarks made within the presentation of each example and the parametric study, some general conclusions from the numerical results obtained can also be drawn.

1 - The finite element formulation in conjunction with the proposed constitutive material models is a good tool for

simulating the complex behaviour of reinforced concrete structures under impulsive and blast loading. The numerical results indicate that one of the most dominant factors in the nonlinear response is the tensile cracking.

2 - The explicit time integration schemes outlined in Chapter 6 and implemented in program FEABRS have proved efficient in tackling complex material models and are also economical in computational effort.

3 - In common with other nonlinear analyses, the avergae computer time consumed for each problem is not small. Depending on the computer technology, the computer time will decrease. However, the effort needed for interpreting the computational results will remain the same. The effort expended in performing nonlinear analyses should be weighed against the information needed.

4 - The assumption of perfect bond between steel and concrete requires further validation in the vicinity of cracked parts. The concluding chapter of this thesis contains suggestions for further work in the material modelling aspects.

Table 8-1 Material properties of Bathe's reinforced concrete beam [235]

* Concrete		
Young's modulus		42059.5 MN/m^2
Poisson's ratio		0.2
Compressive strength		25.8 MN/m^2
Corresponding strain		0.00123
Crushing strain		0.00350
Tensile strength		3.2 MN/m^2
Cracking strain		0.000075
Elastic limit		0.3
Fracture energy		105.1 Nm/m^2
Fluidity parameters	B_1	-0.061
	B_2	0.906
Shear transfer parameter		1.00
Mass density		0.00190 MN sec^2/m^4
* Steel		
Young's modulus		206850.0 MN/m^2
Yield stress		303.4 MN/m^2
Hardening modulus		0.0
Fluidity parameters	K_1	-0.909
	K_2	0.954
Ultimate strain		0.015
Mass density		0.00641 MN sec^2/m^4

Table 8-2 Material properties of reinforced concrete circular slab [238]

* Concrete		
Young's modulus		19614.0 MN/m^2
Poisson's ratio		0.167
Compressive strength		34.325 MN/m^2
Corresponding strain		0.0023
Crushing strain		0.00350
Tensile strength		3.531 MN/m^2
Cracking strain		0.00018
Elastic limit		0.4
Fracture energy		196.14 Nm/m^2
Fluidity parameters	B_1	0.568
	B_2	0.920
Compressive softening parameter		10.0
Shear transfer parameter		1.00
Mass density		0.0024 MN sec^2/m^4
* Steel		
Young's modulus		20594.7 MN/m^2
Yield stress		451.122 MN/m^2
Hardening modulus		0.0
Fluidity parameters	K_1	-0.909
	K_2	0.954
Ultimate strain		0.015
Mass density		0.0

Table 8-3 Material properties of Seabold's reinforced concrete beam [239]

* Concrete		
Young's modulus		24132.5 MN/m^2
Poisson's ratio		0.2
Compressive strength		26.959 MN/m^2
Corresponding strain		0.002234
Crushing strain		0.004
Tensile strength		2.7235 MN/m^2
Cracking strain		0.0001129
Elastic limit		0.4
Fracture energy		60.2 Nm/m^2
Fluidity parameters	B_1	-0.143
	B_2	0.904
Compression softening parameter		10.0
Shear transfer parameter		1.00
Mass density		0.002 $MN\ sec^2/m^4$
* Steel		
Young's modulus		199955.0 MN/m^2
Yield stress		483.00 MN/m^2
Hardening modulus		0.0
Fluidity parameters	K_1	-0.909
	K_2	0.954
Ultimate strain		0.015
Mass density		0.00675 MN sec^2/m^4

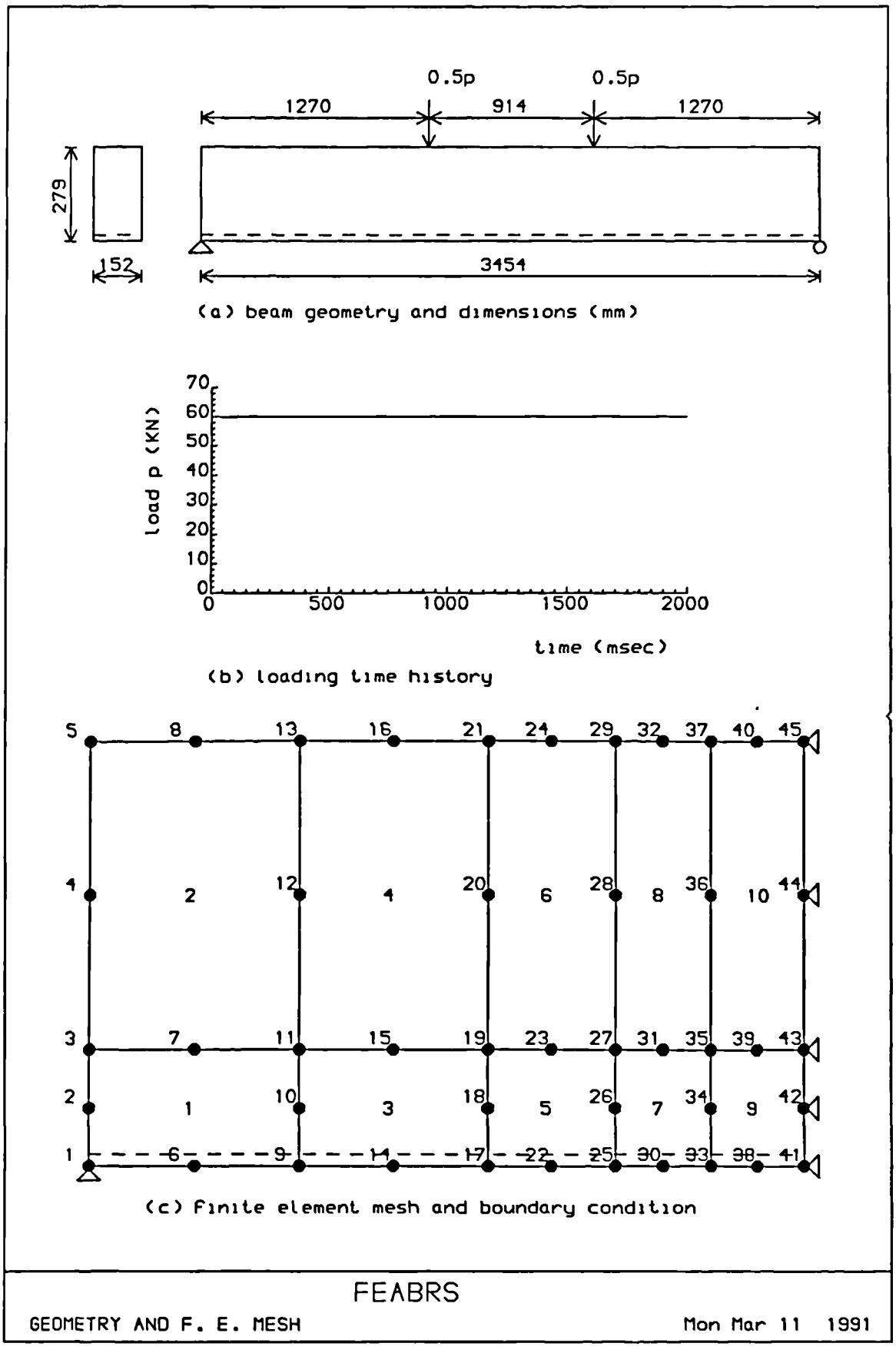

Figure 8.1: Bathe's beam details and finite element idealization

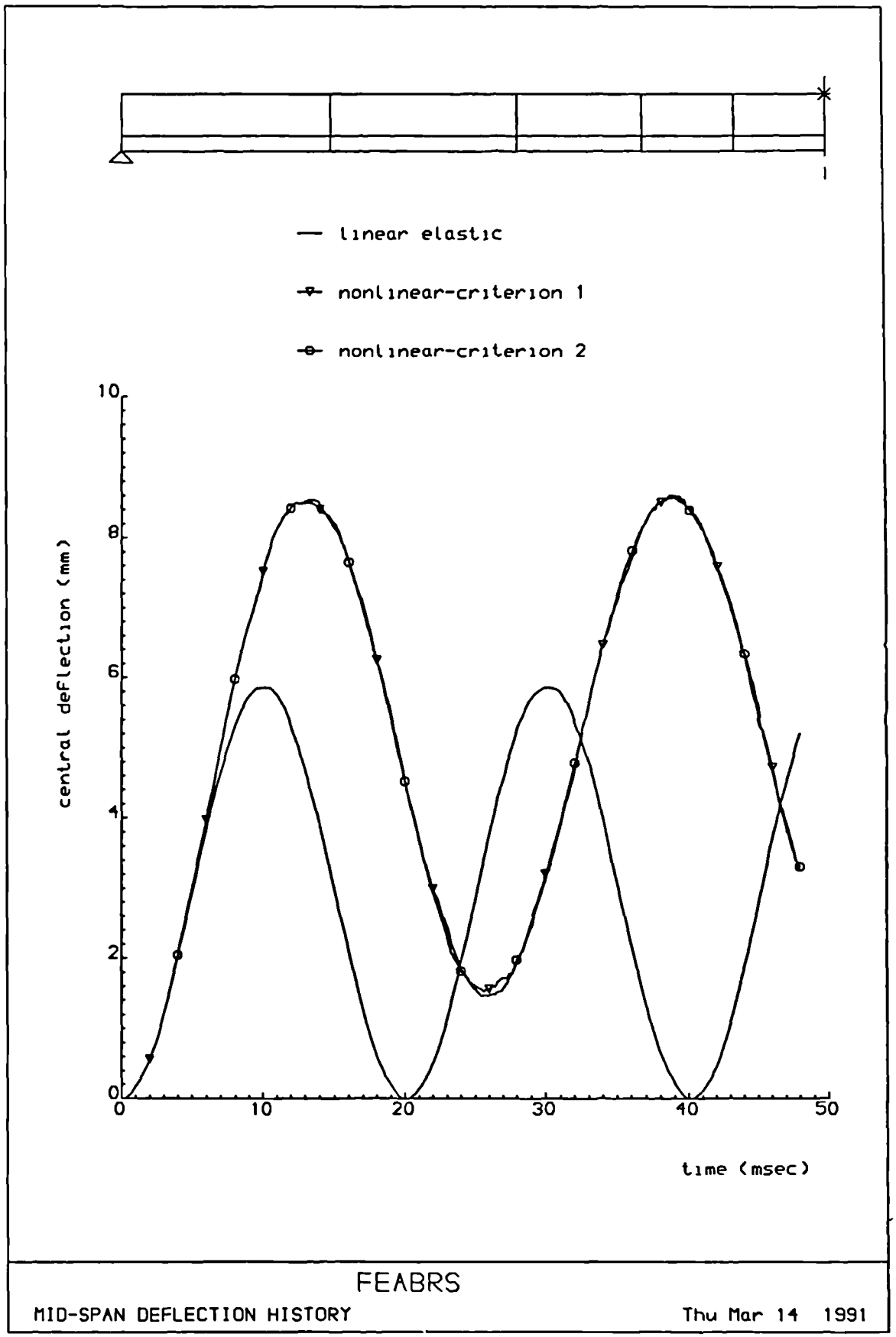

Figure 8.2: Nonlinear dynamic response of Bathe's beam (criteria 1 and 2)

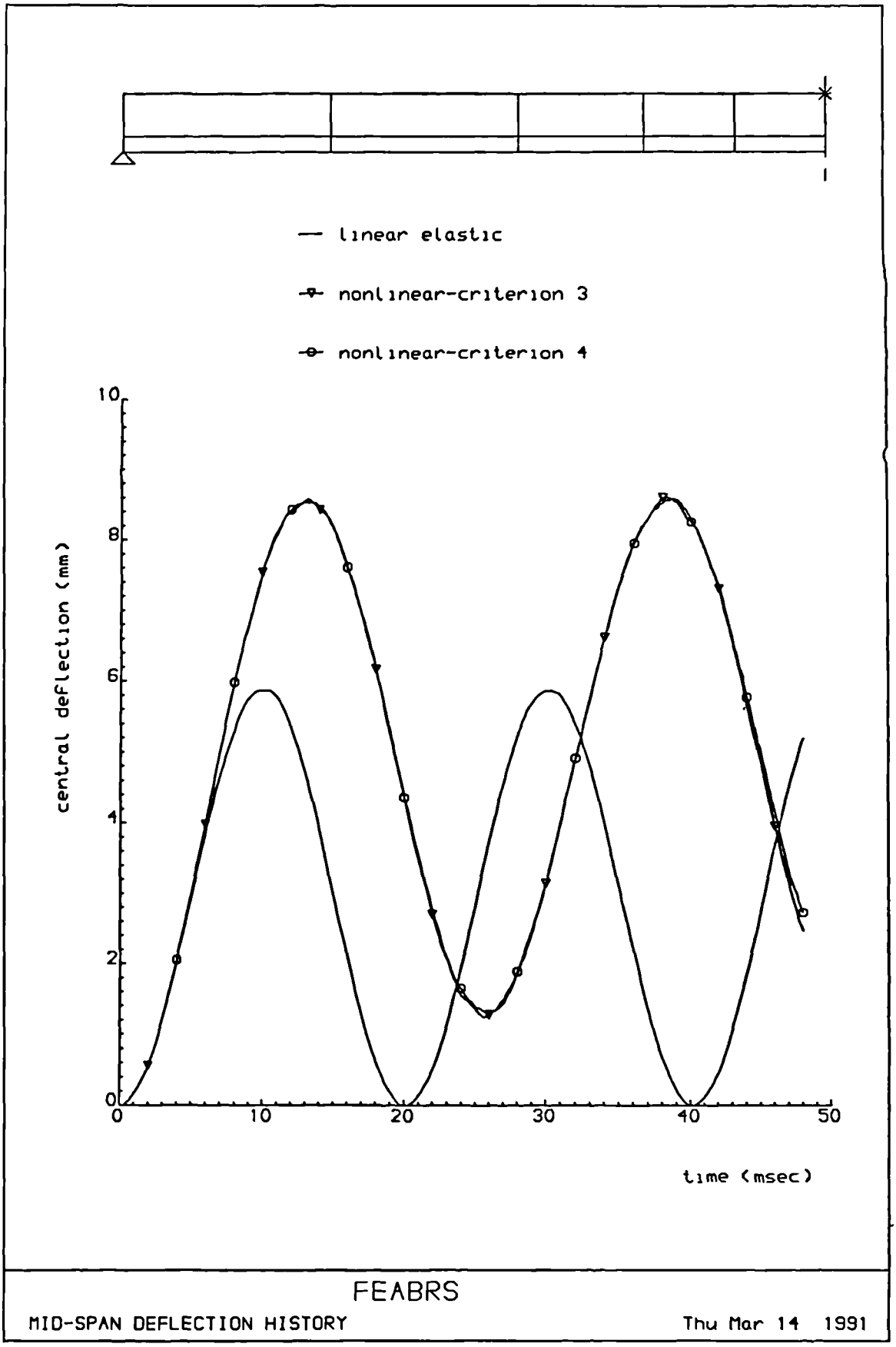

Figure 8.3: Nonlinear dynamic response of Bathe's beam (criteria 3 and 4)

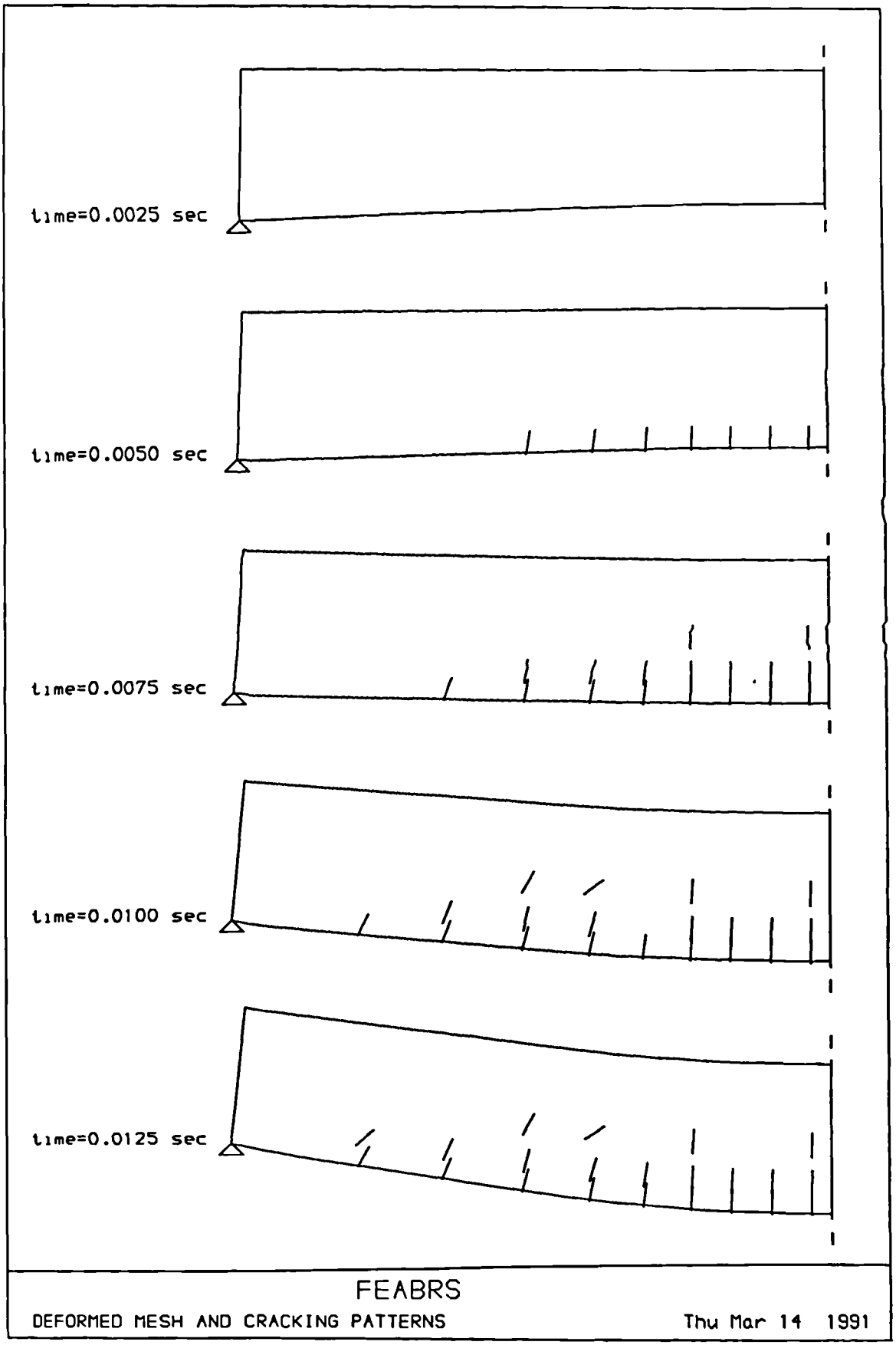

Figure 8.4: Deformation and cracking history of Bathe's beam

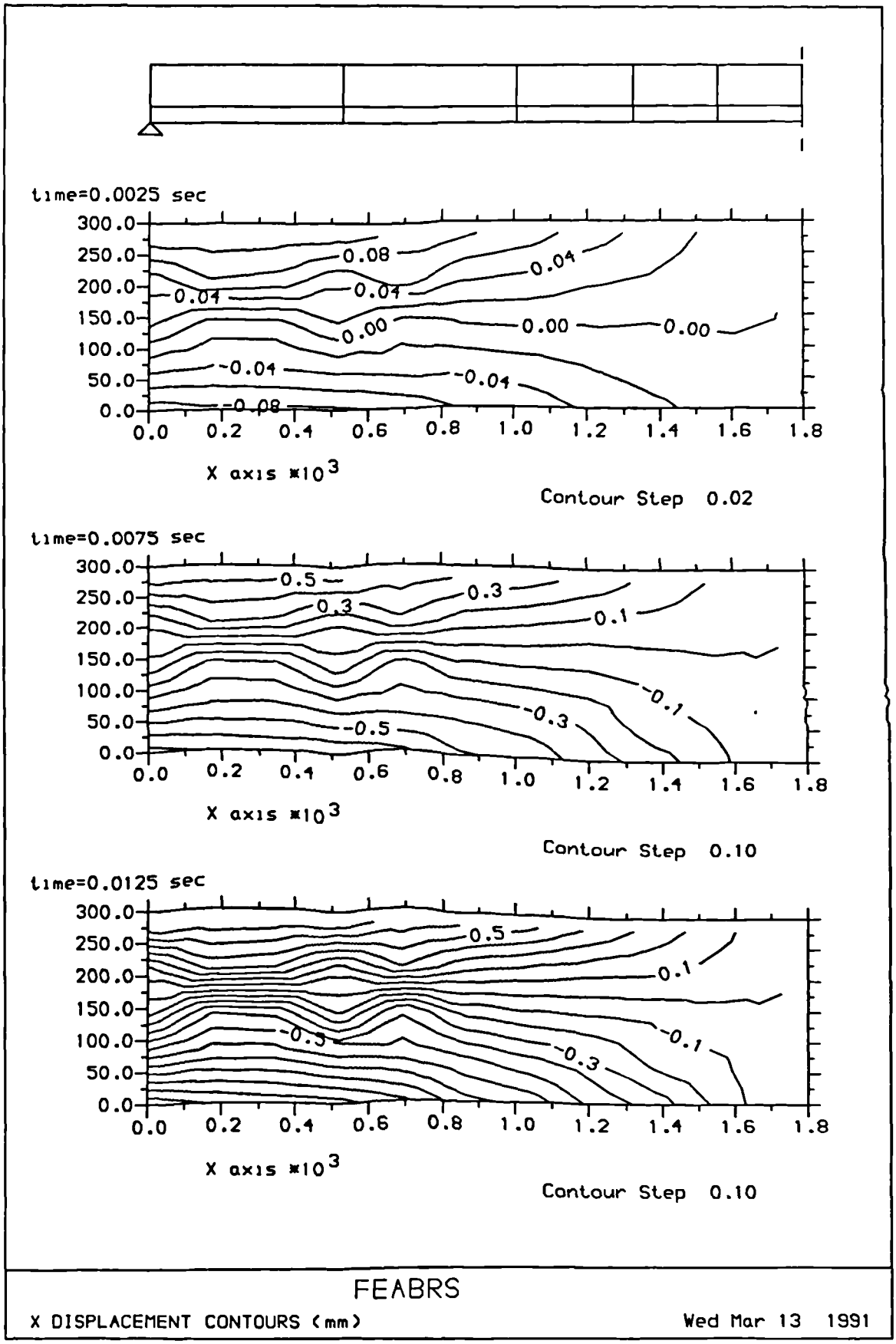

Figure 8.5: Horizontal displacement distribution along Bathe's beam at respective times

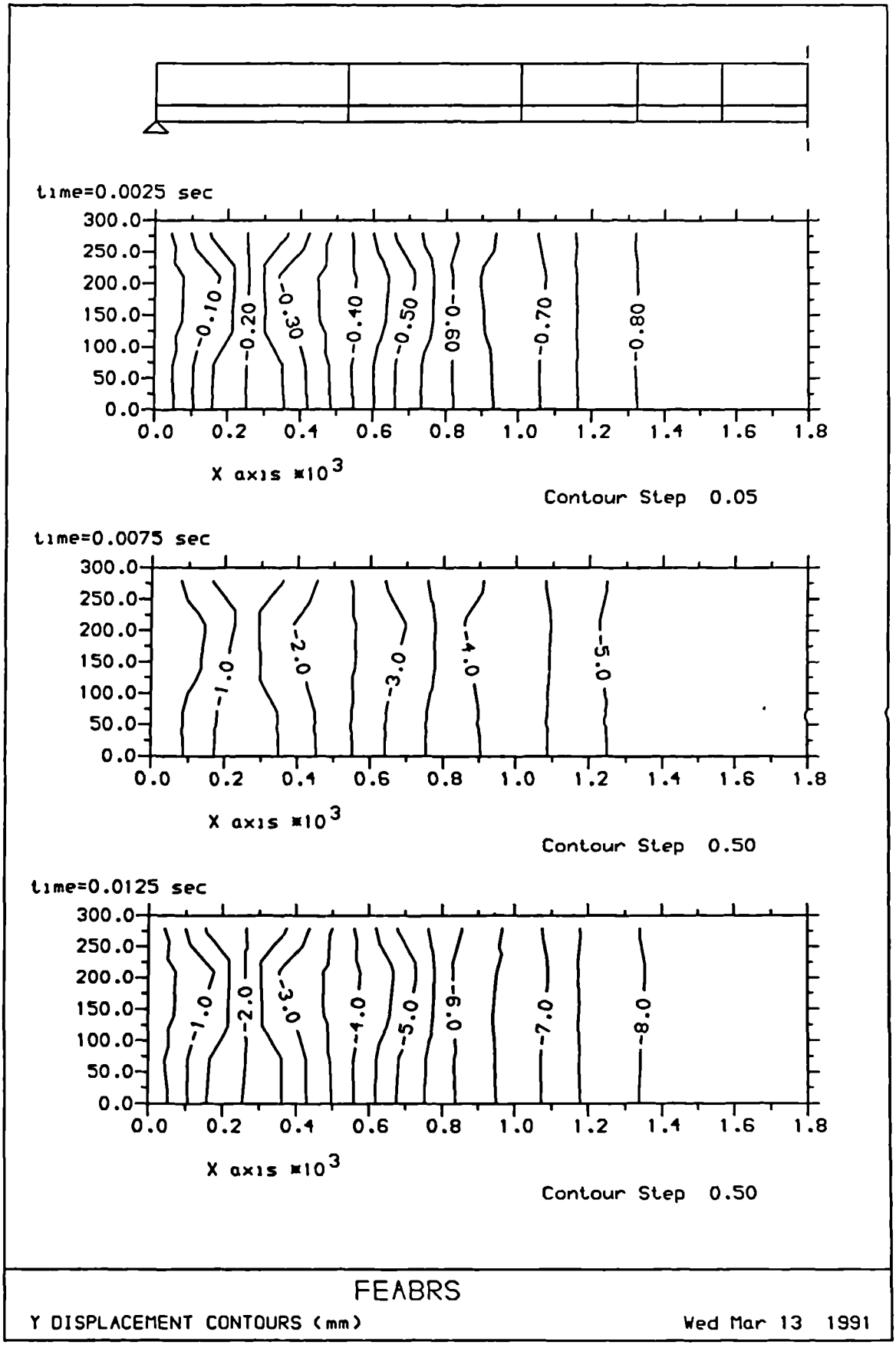

Figure 8.6: Vertical displacement distribution along Bathe's beam at respective times

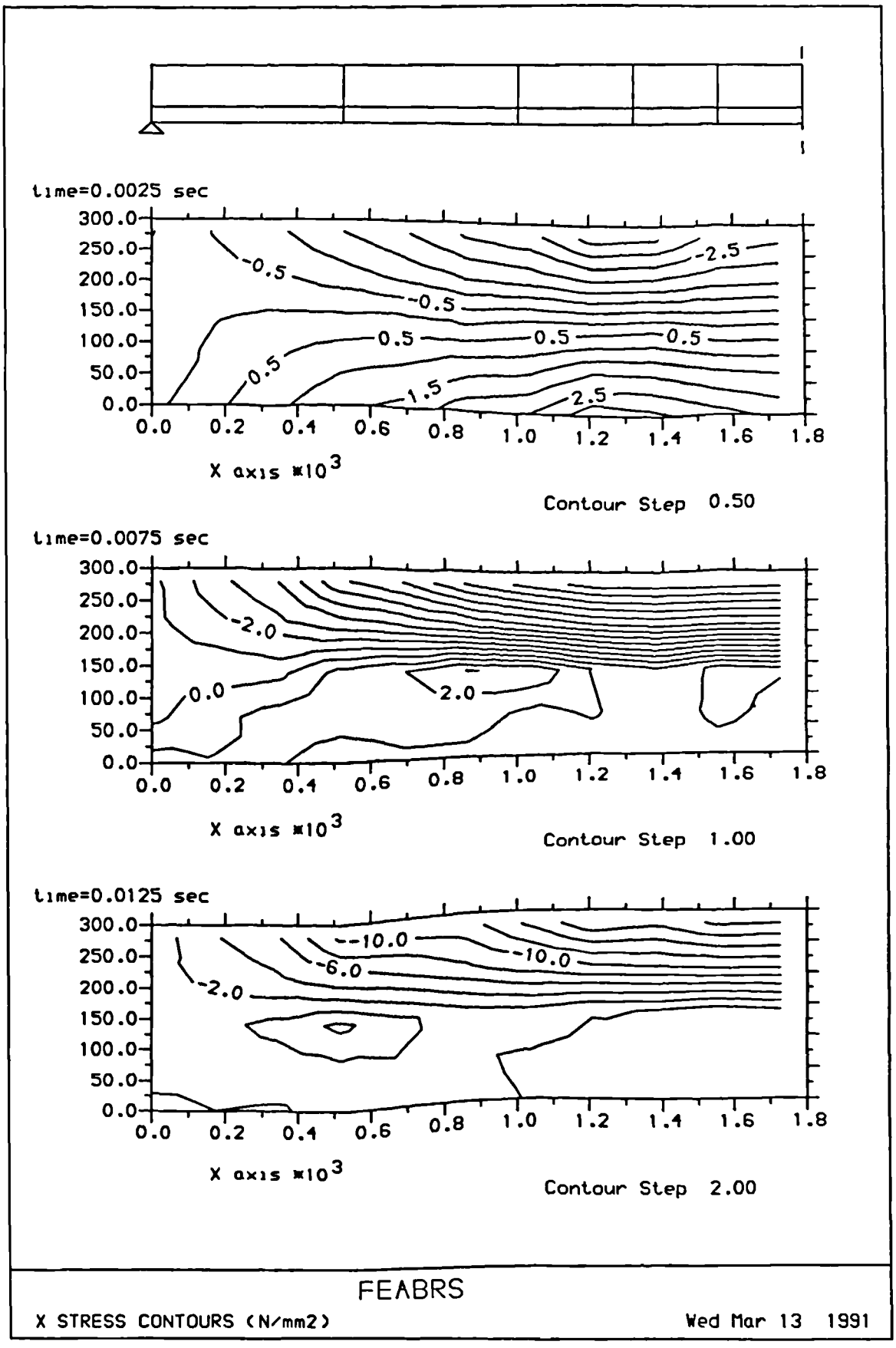

Figure 8.7: Longitudinal stress distribution along Bathe's beam at respective times

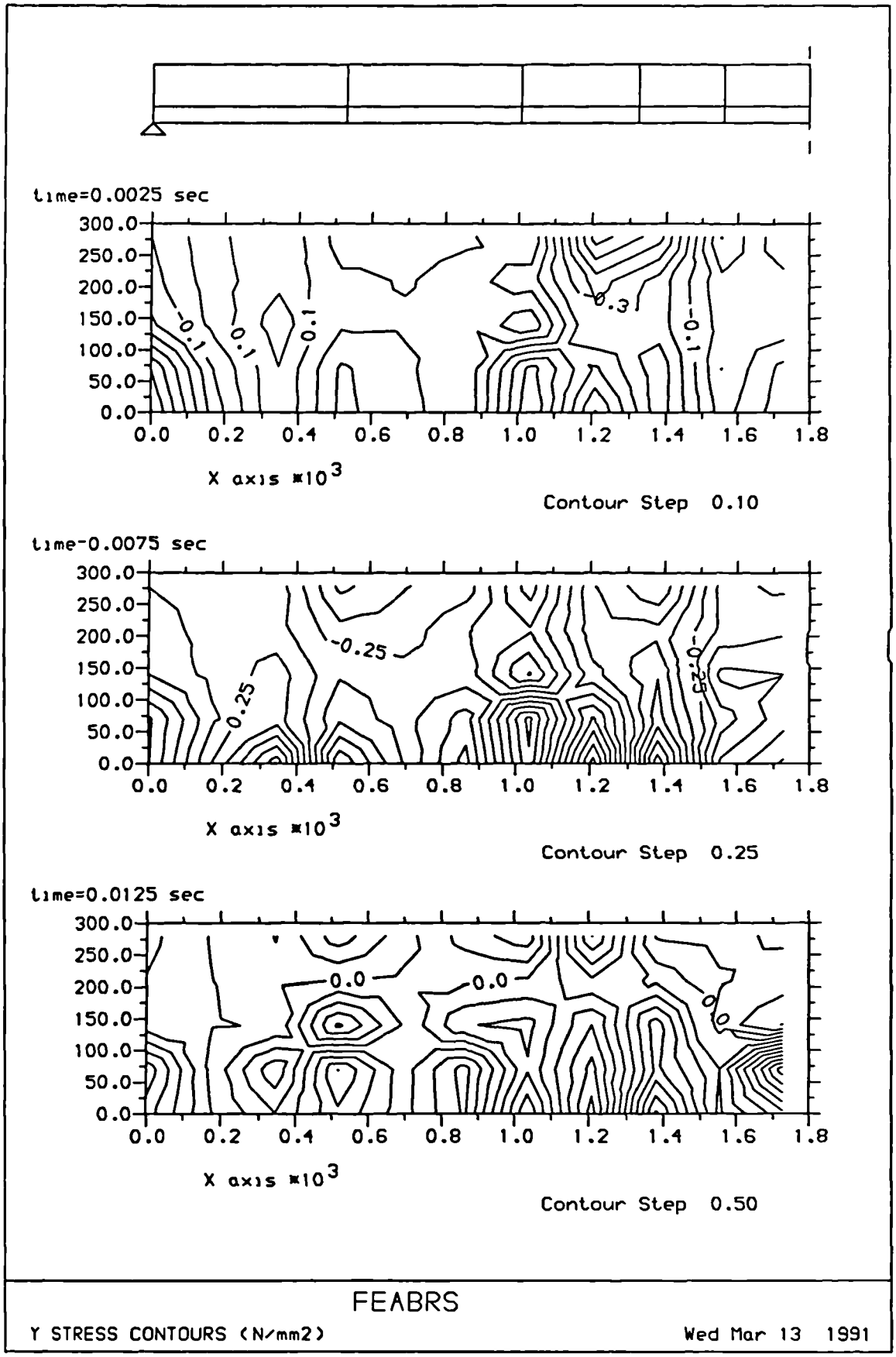

Figure 8.8 Transverse stress distribution along Bathe's beam at respective times

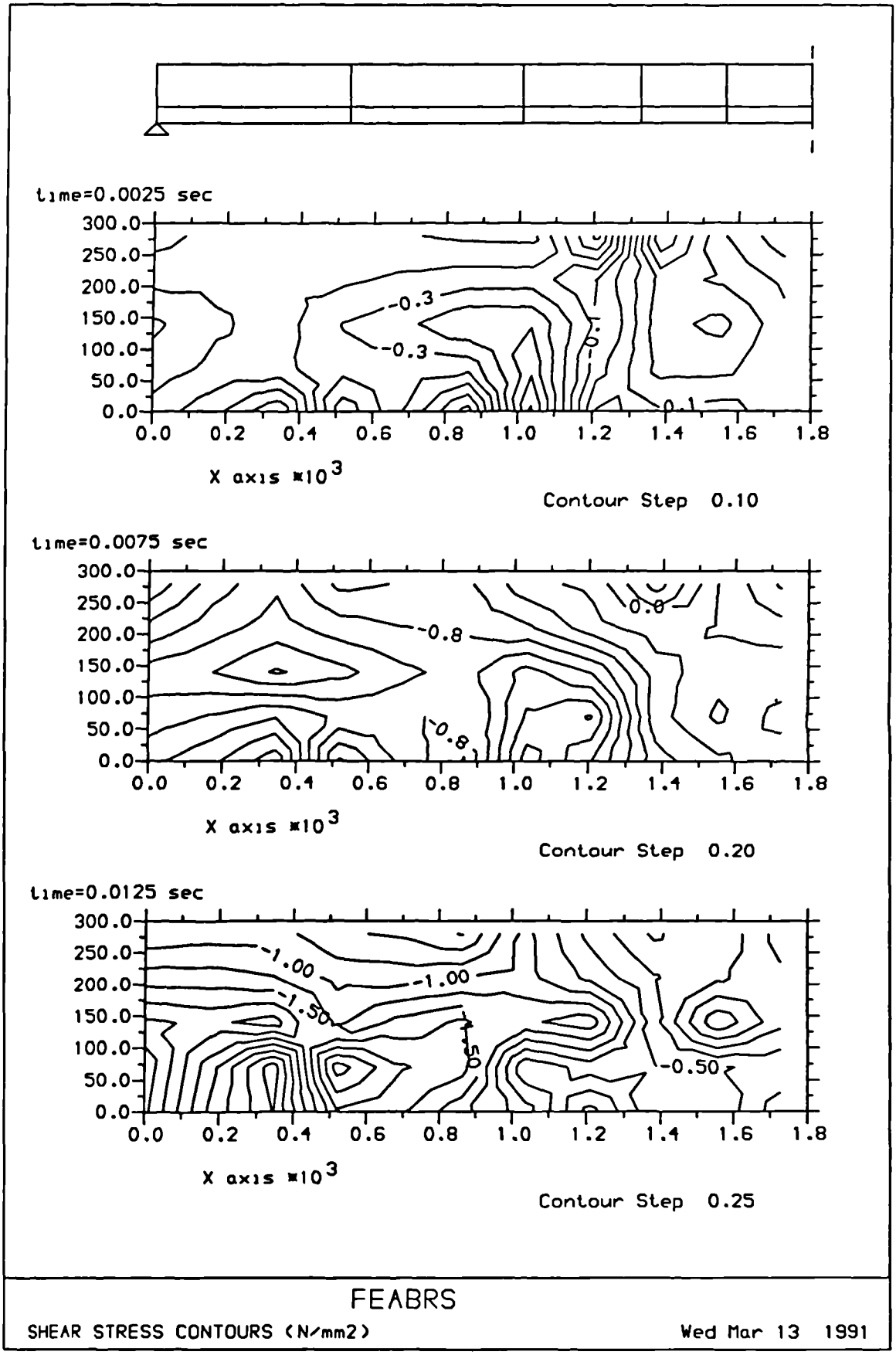

Figure 8.9 Shear stress distribution along Bathe's beam at respective times

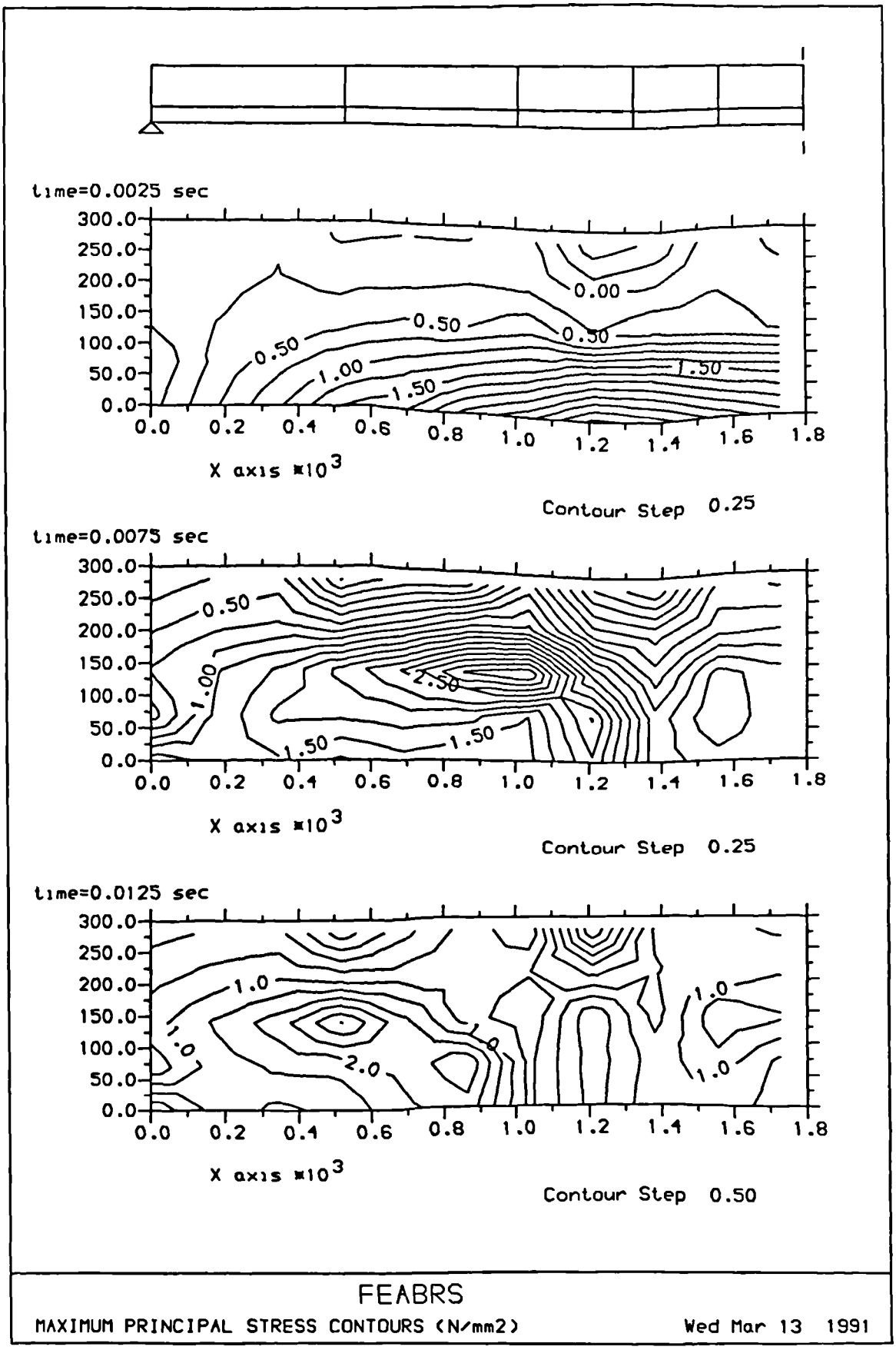

Figure 8.10: Maximum principal stress distribution along Bathe's beam at respective times

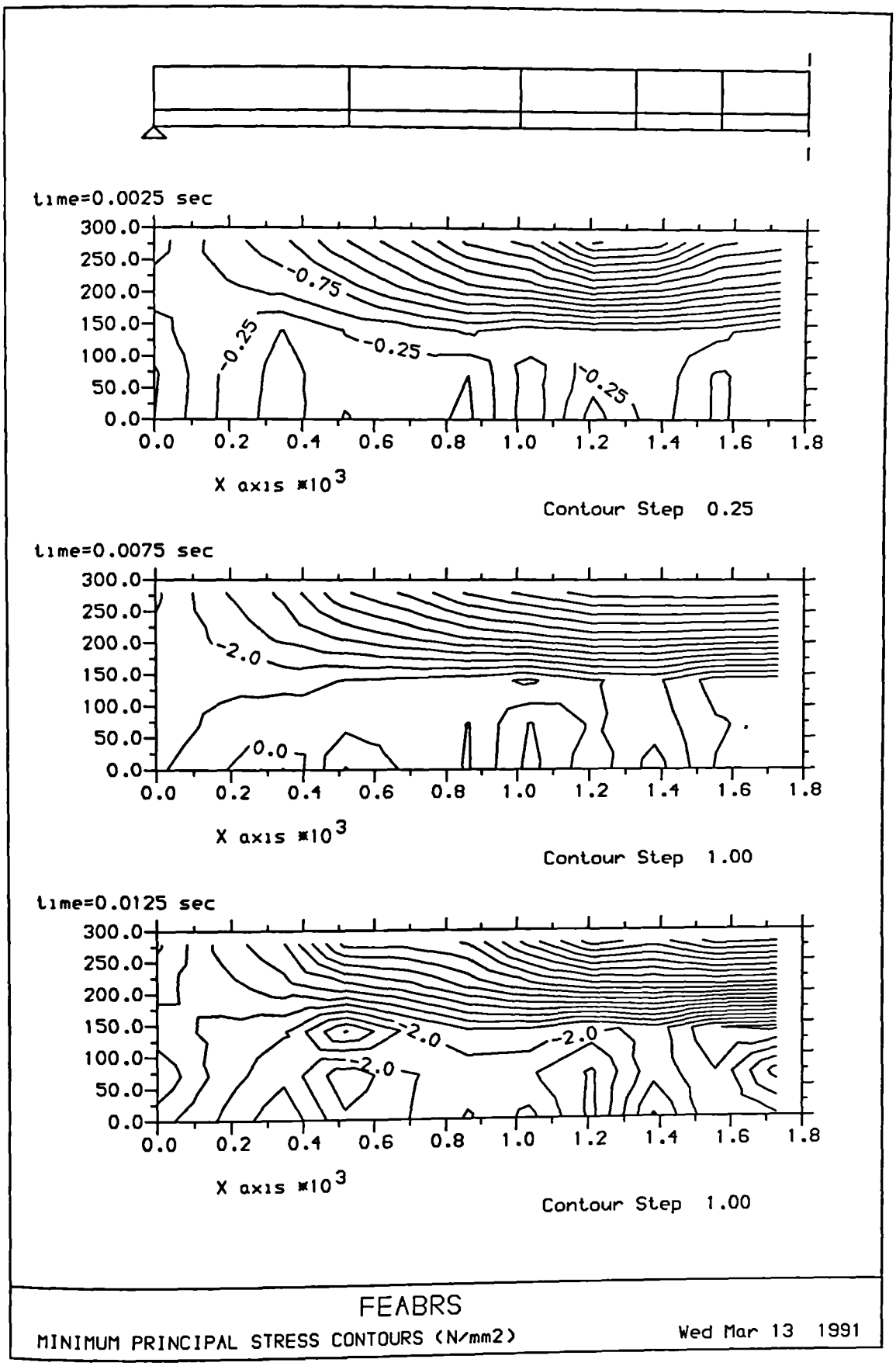

Figure 8.11: Minimum principal stress distribution along Bathe's beam at respective times

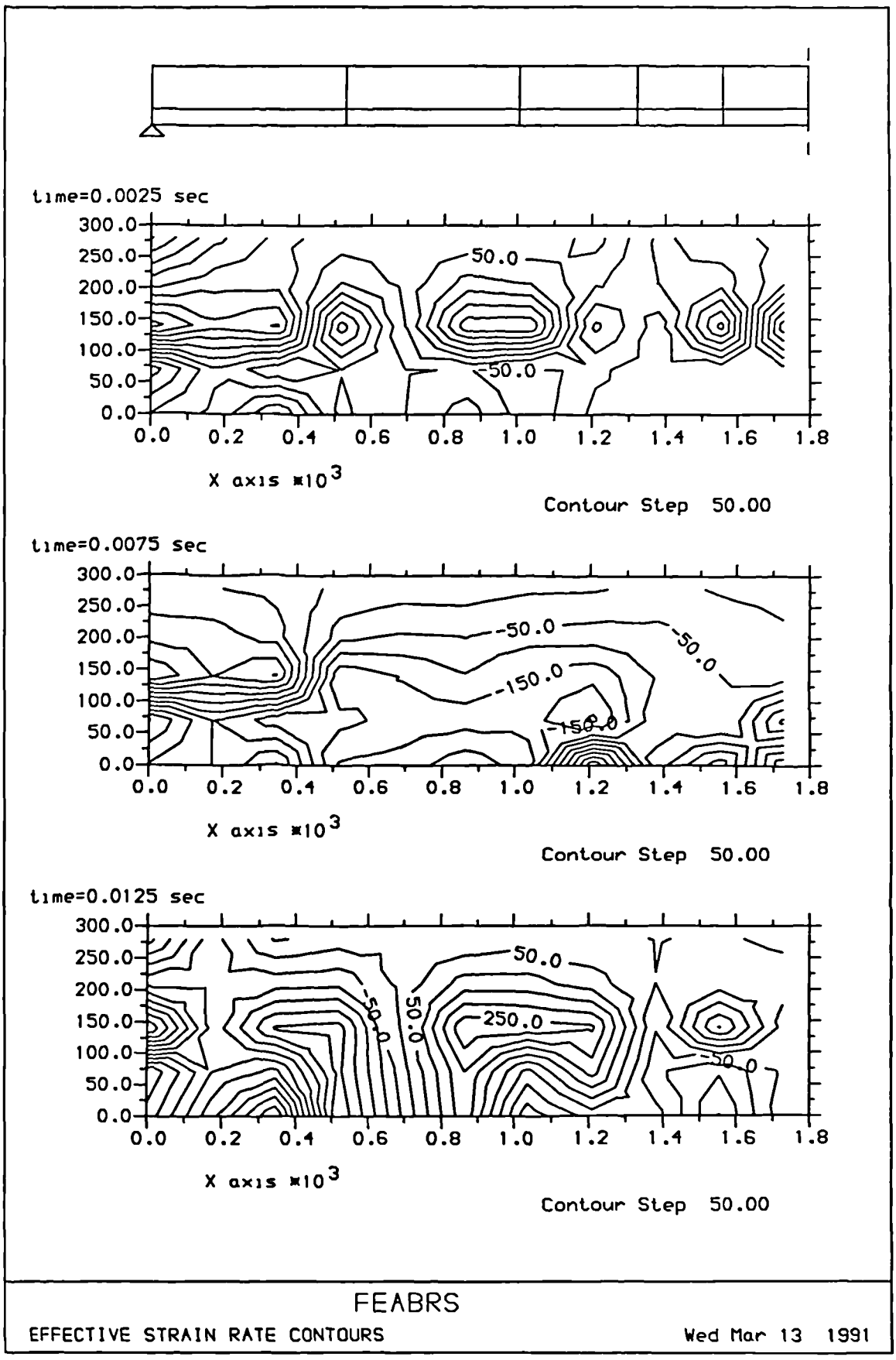

Figure 8.12: Effective strain rate distribution along Bathe's beam at respective times

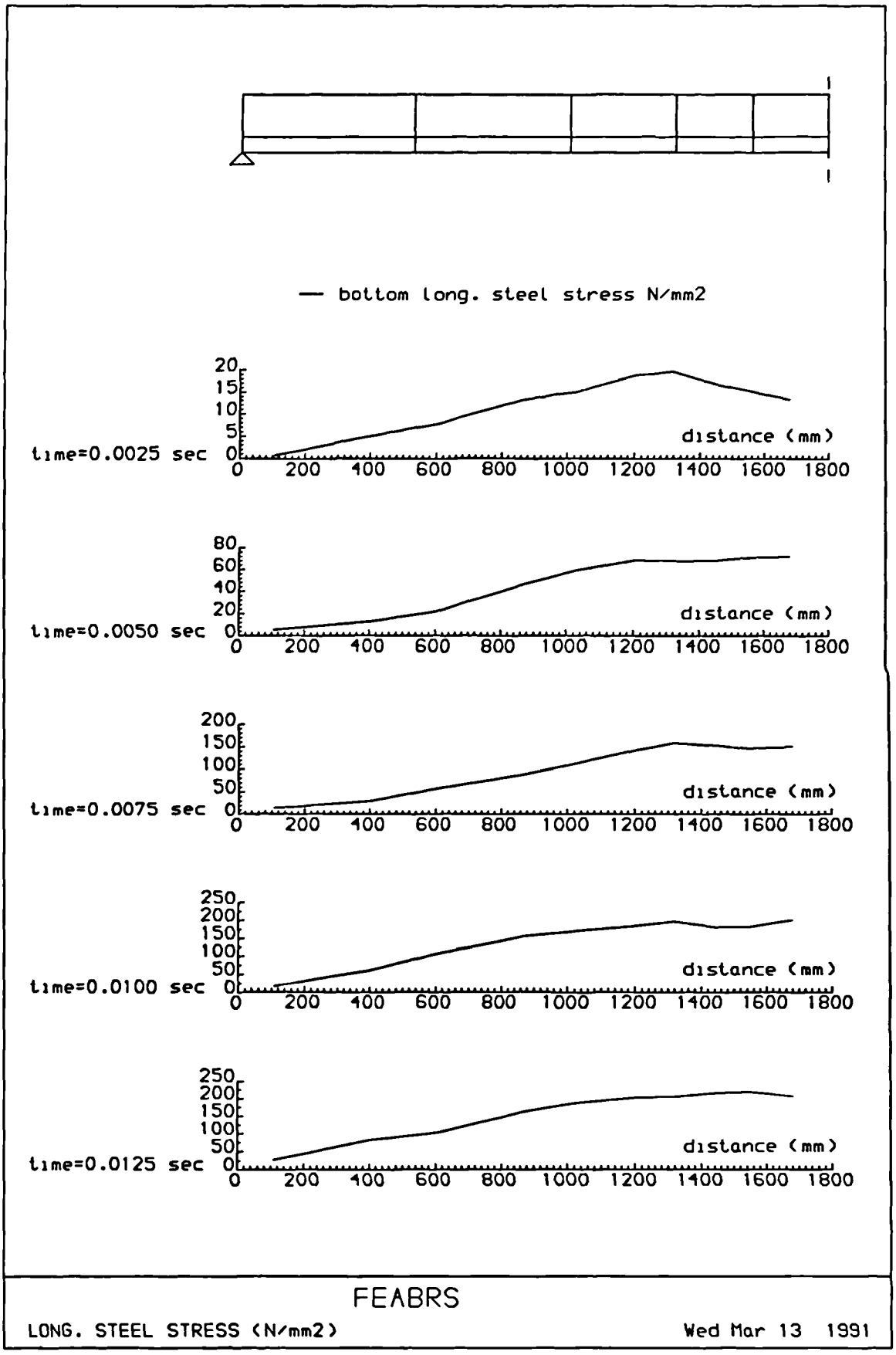

Figure 8.13: Stress distribution of reinforcing steel of Bathe's beam at various time stations

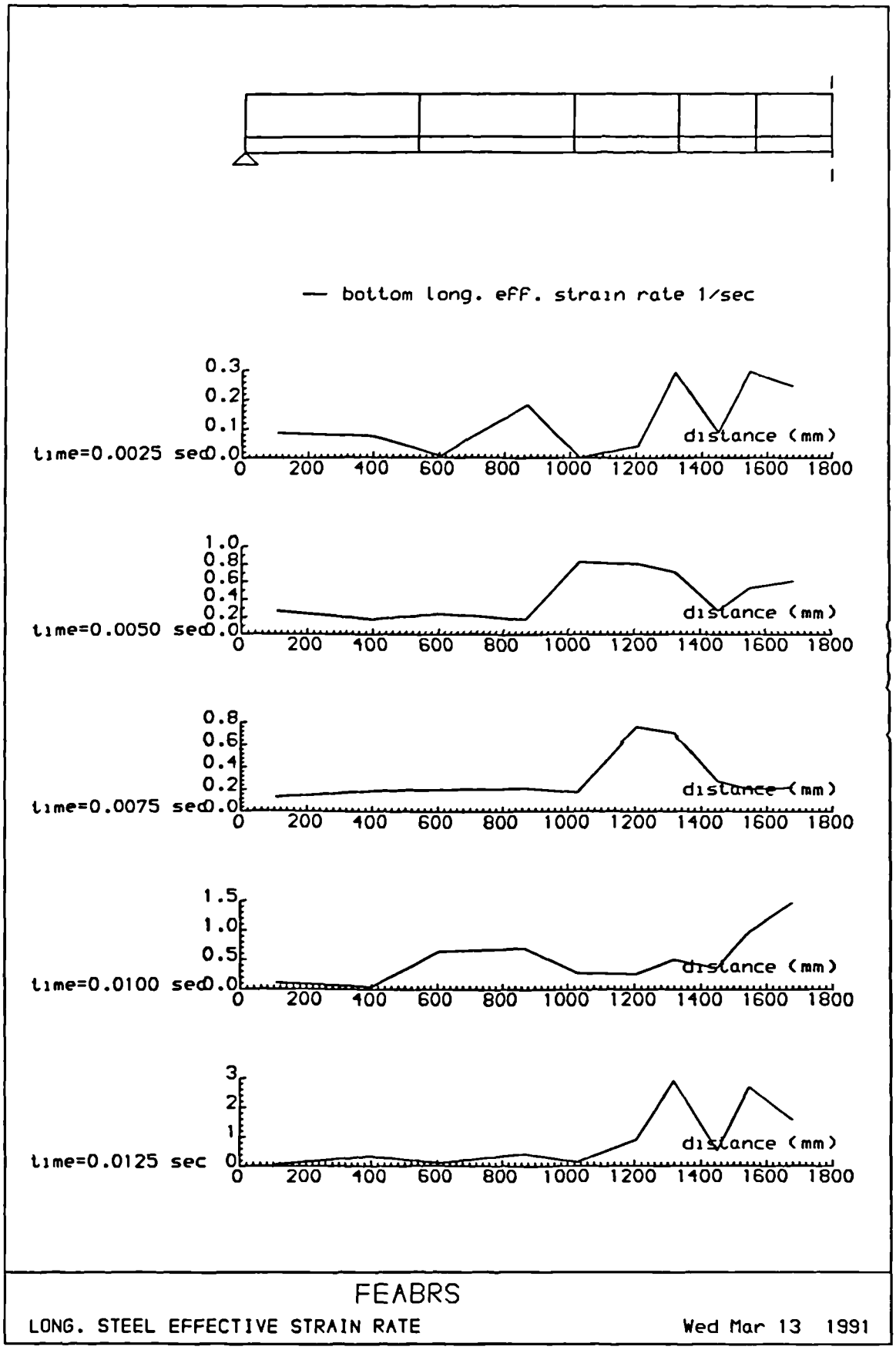

Figure 8.14: Effective strain rate distribution of reinforcing steel of Bathe's beam at various time stations

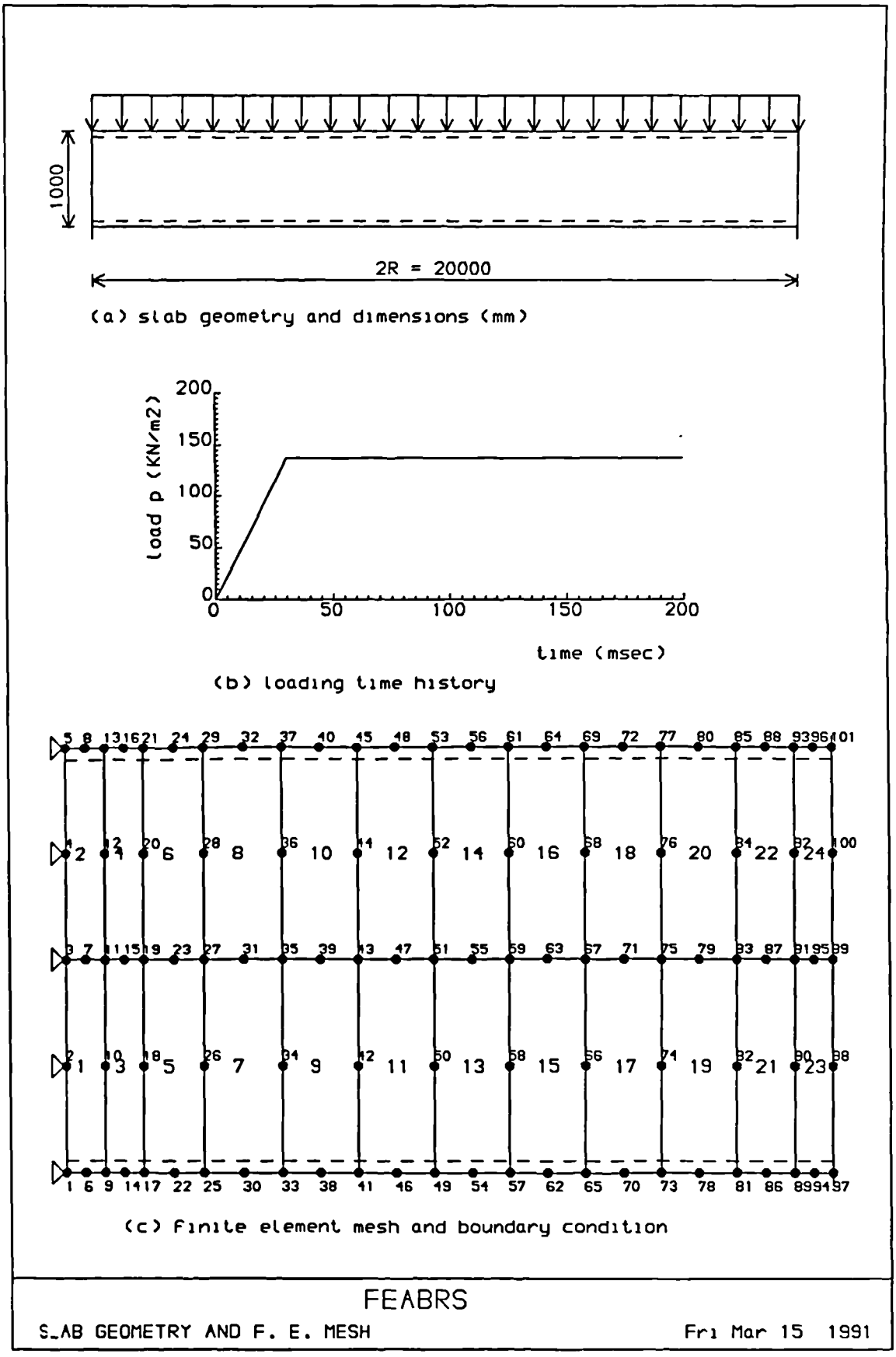

Figure 8.15: Circular slab details and finite element model

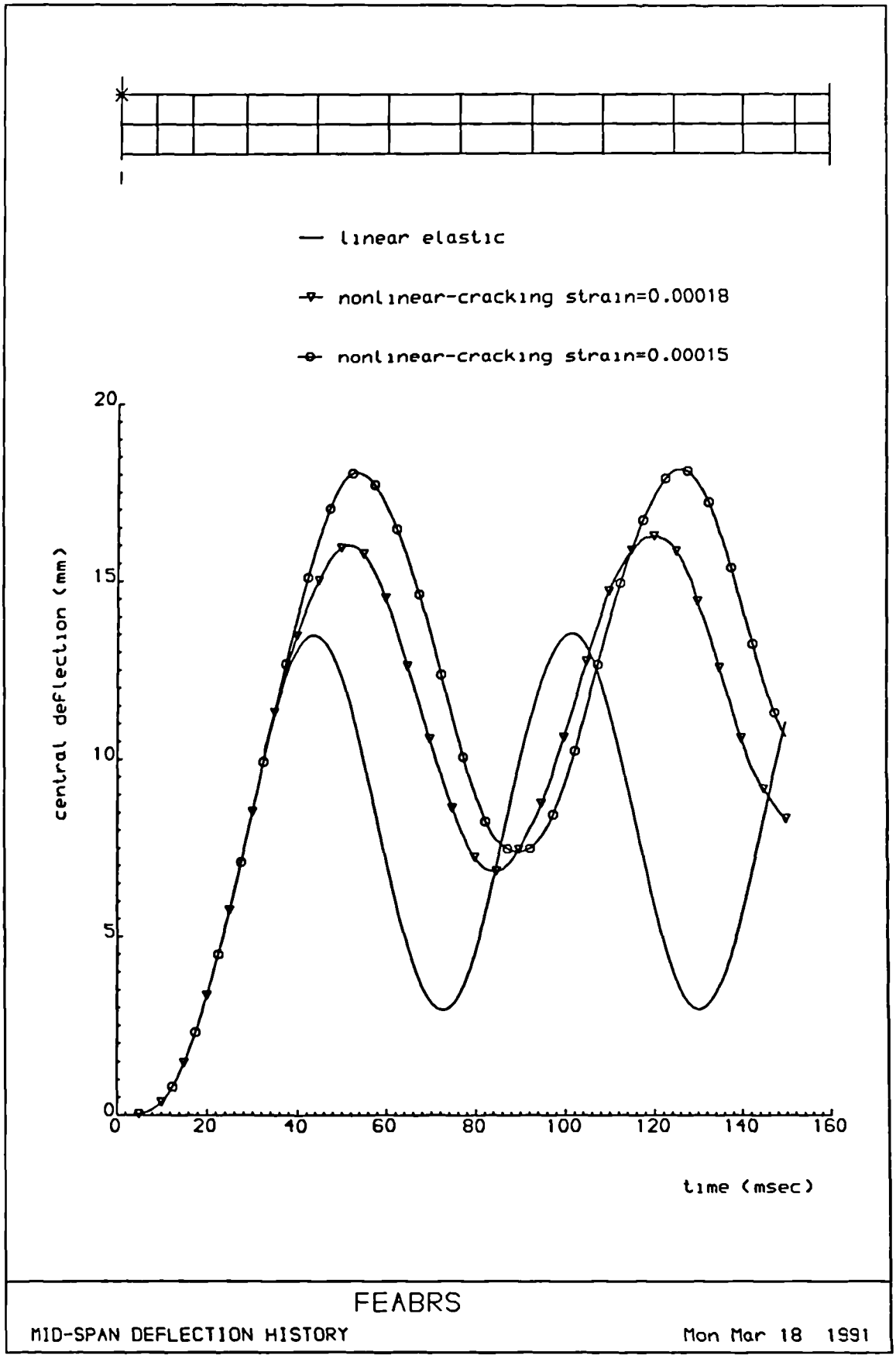

Figure 8.16: Nonlinear response of circular plate

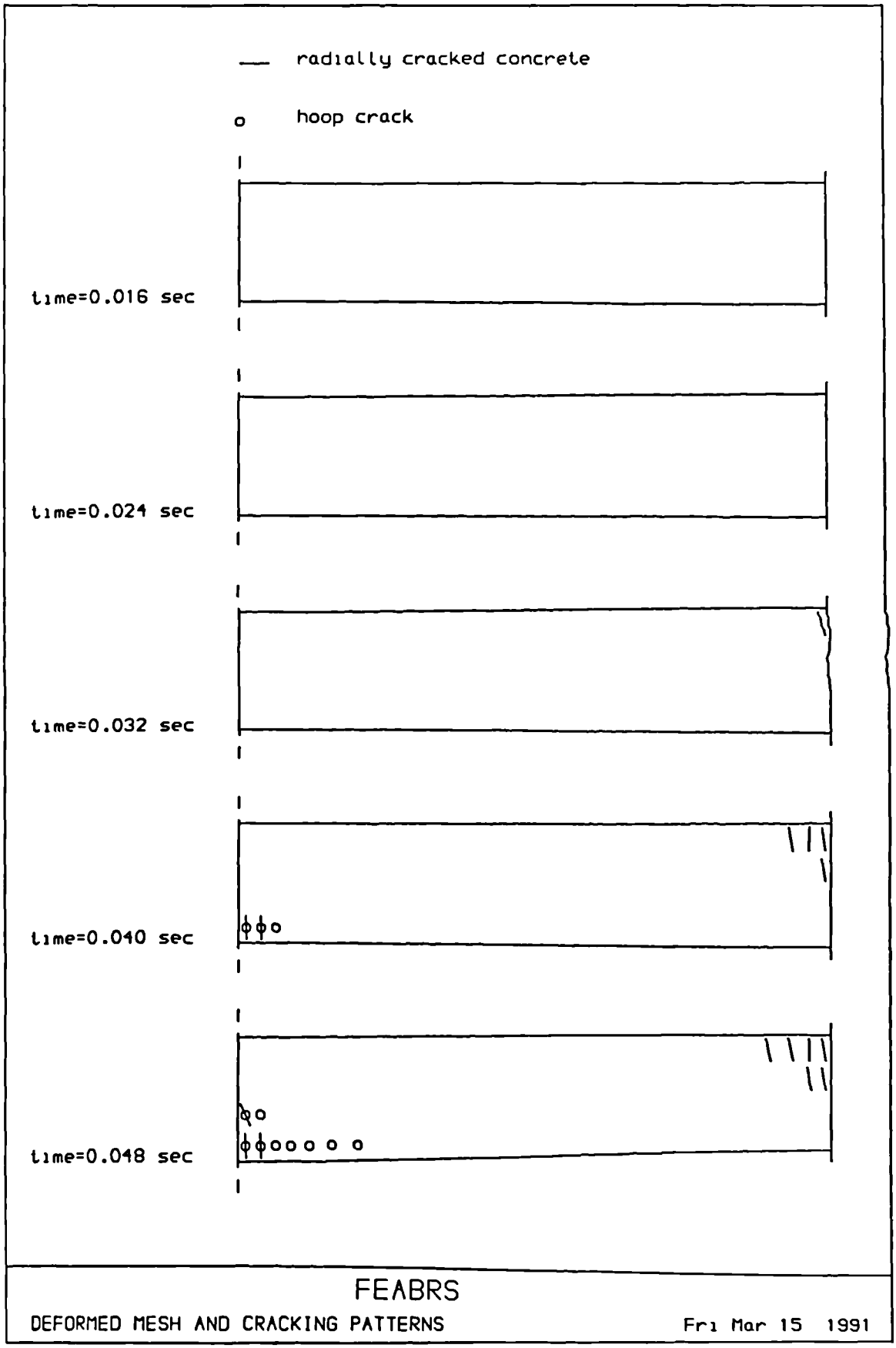

Figure 8.17: Deformation and cracking history for circular slab

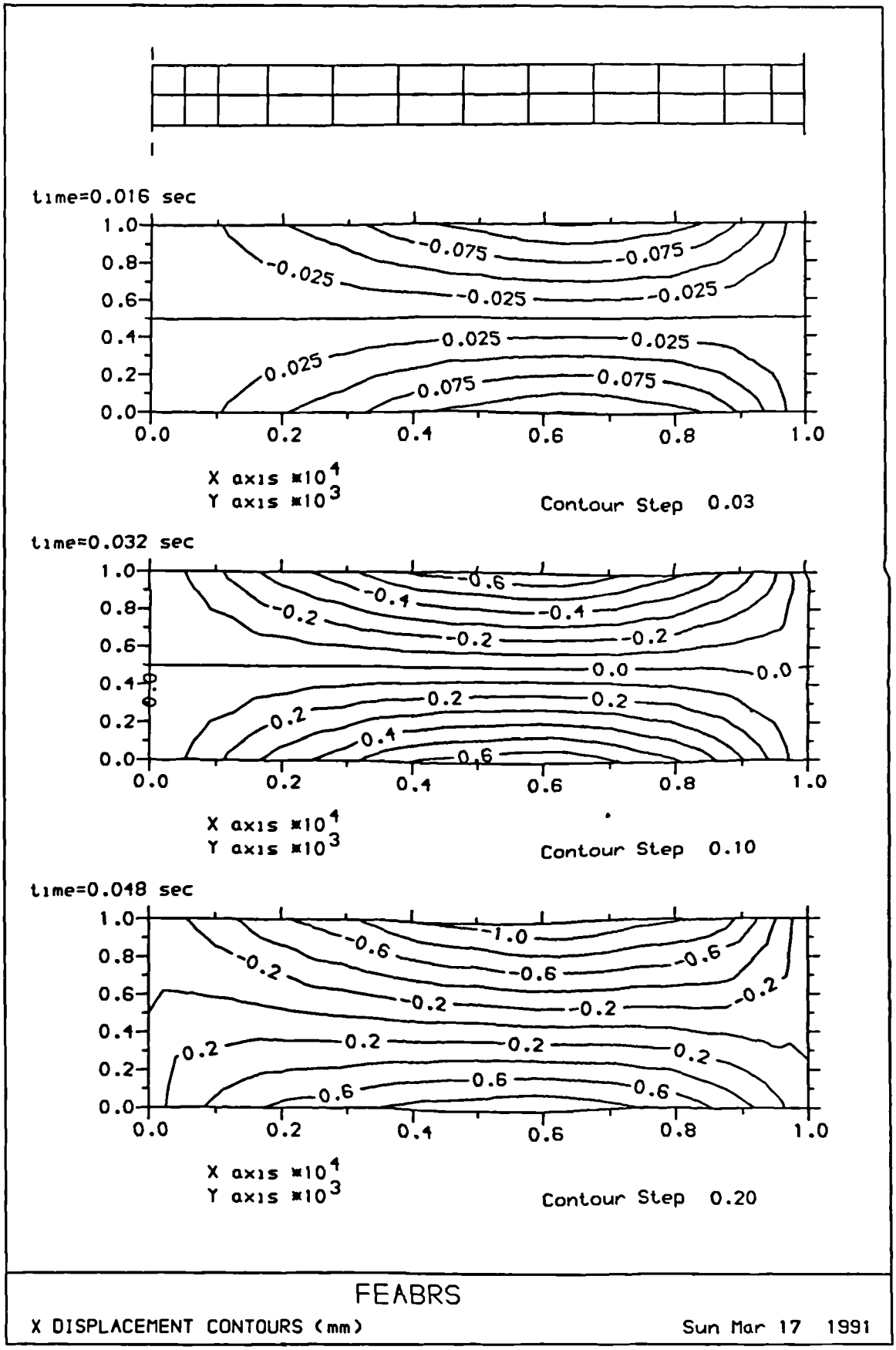

Figure 8.18: Horizontal displacement distribution of the slab at respective times

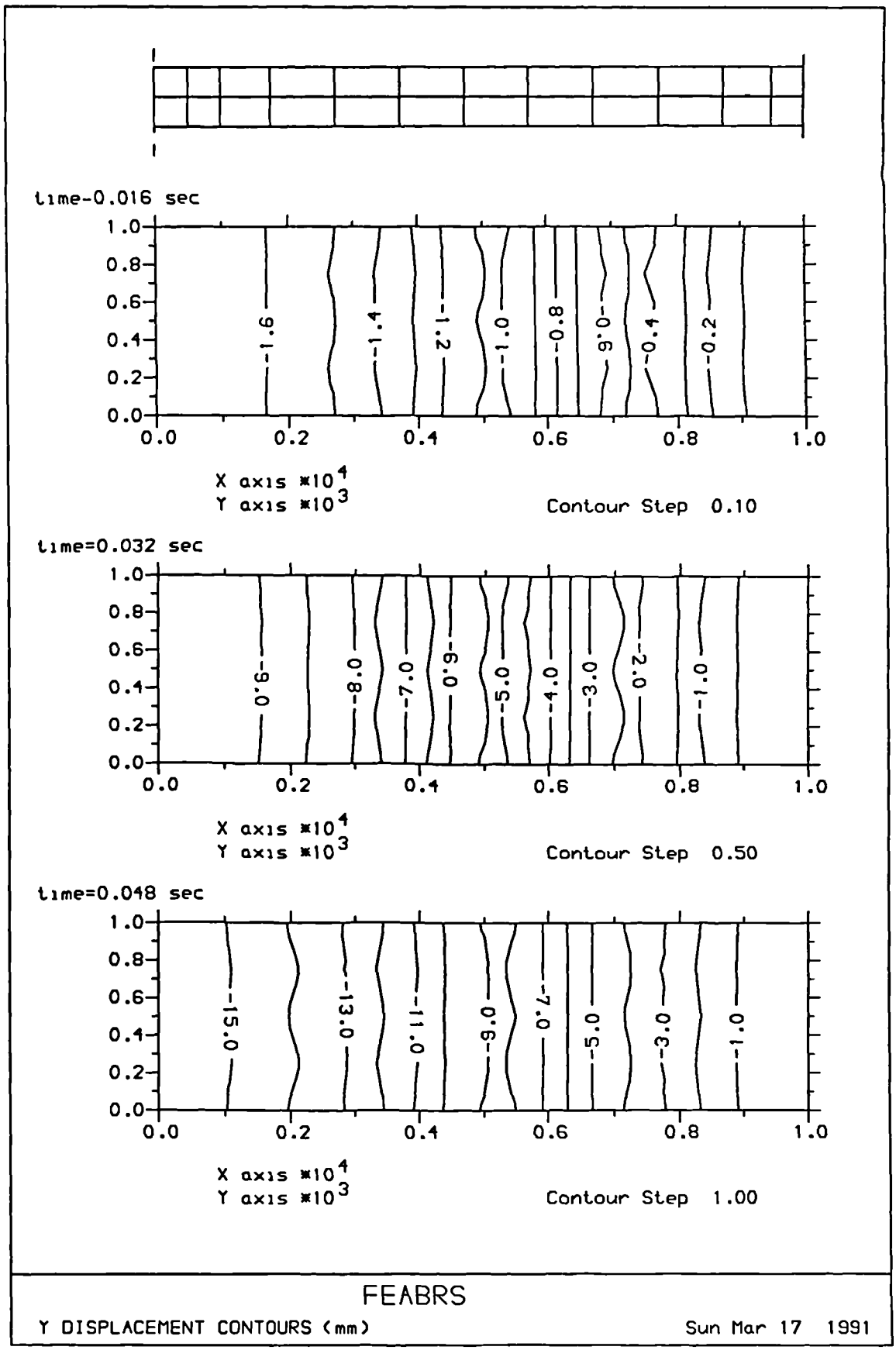

Figure 8.19: Vertical displacement distribution of the slab at respective times

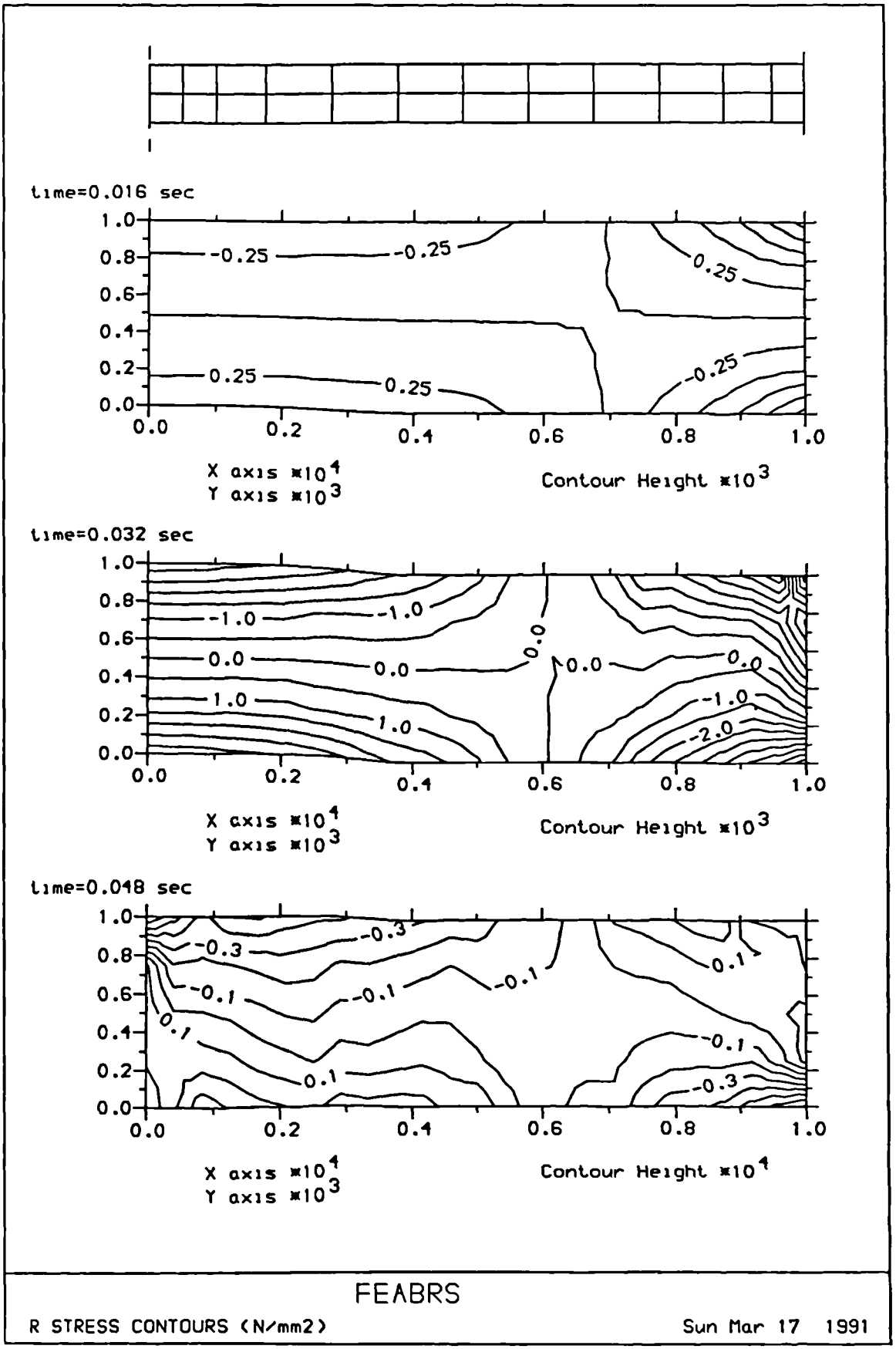

Figure 8.20: Radial stress distribution in r-direction of the slab at respective times

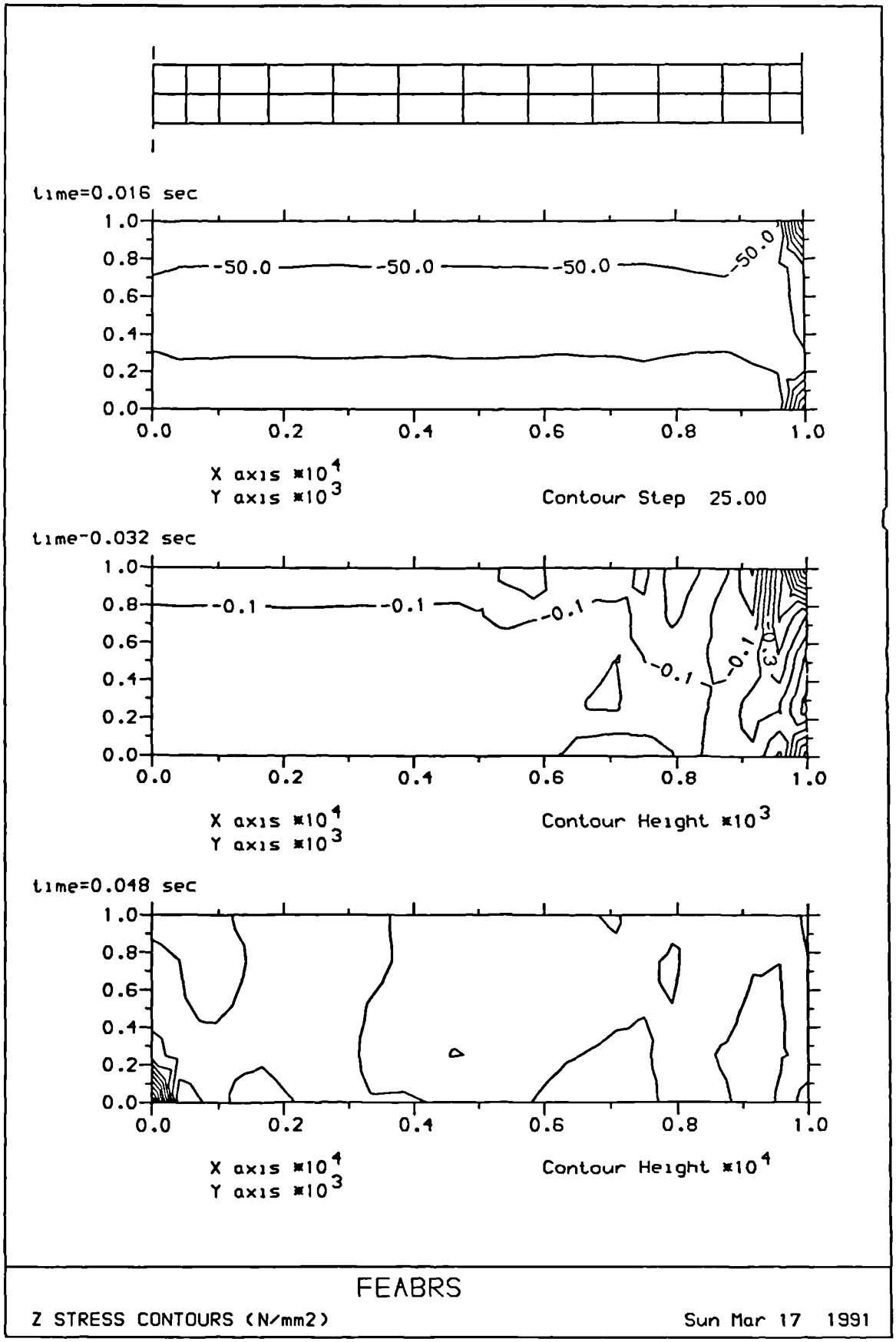

Figure 8.21: Radial stress distribution in z-direction of the slab at respective times

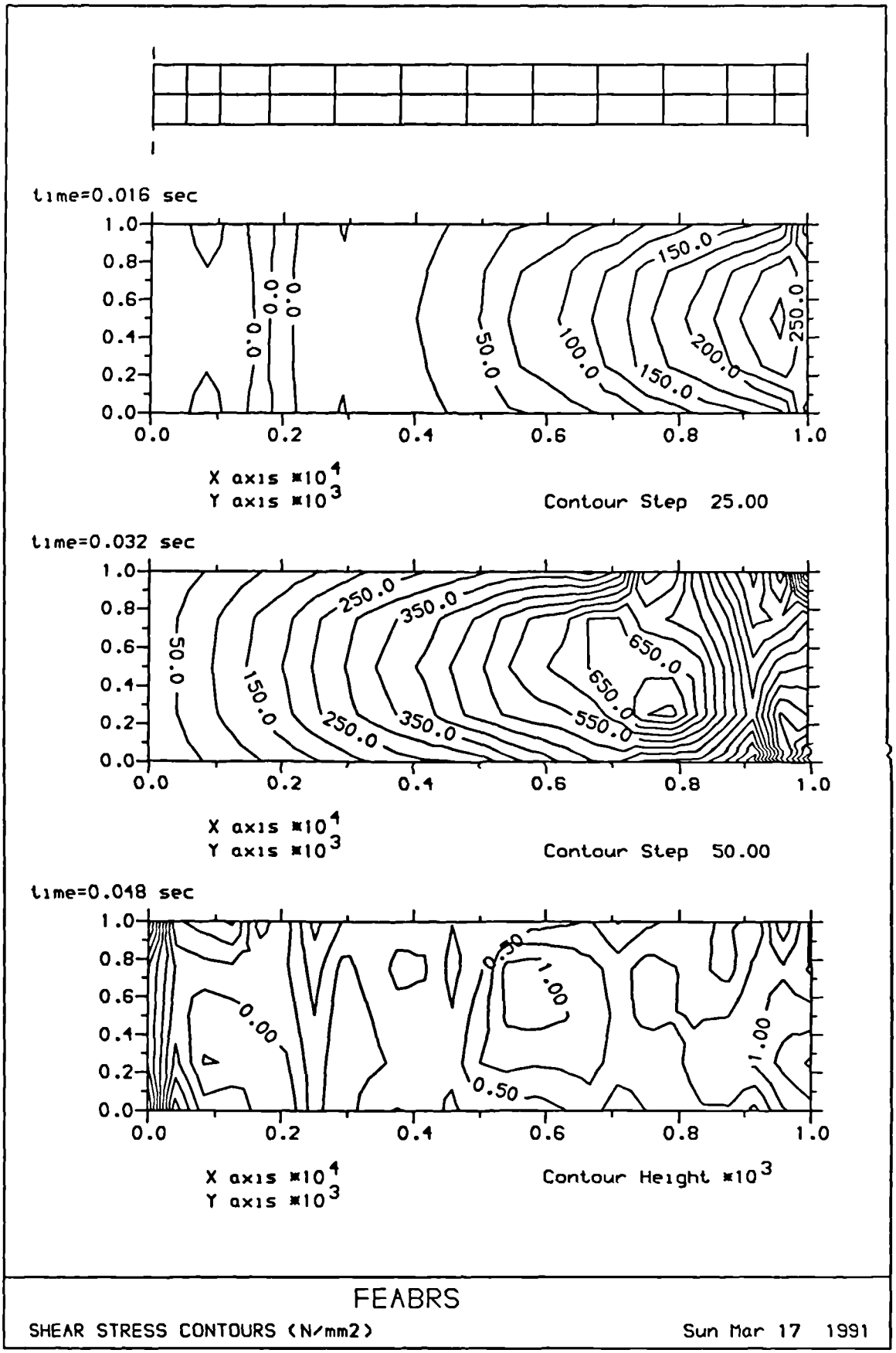

Figure 8.22: Shear stress distribution of the slab at respective times

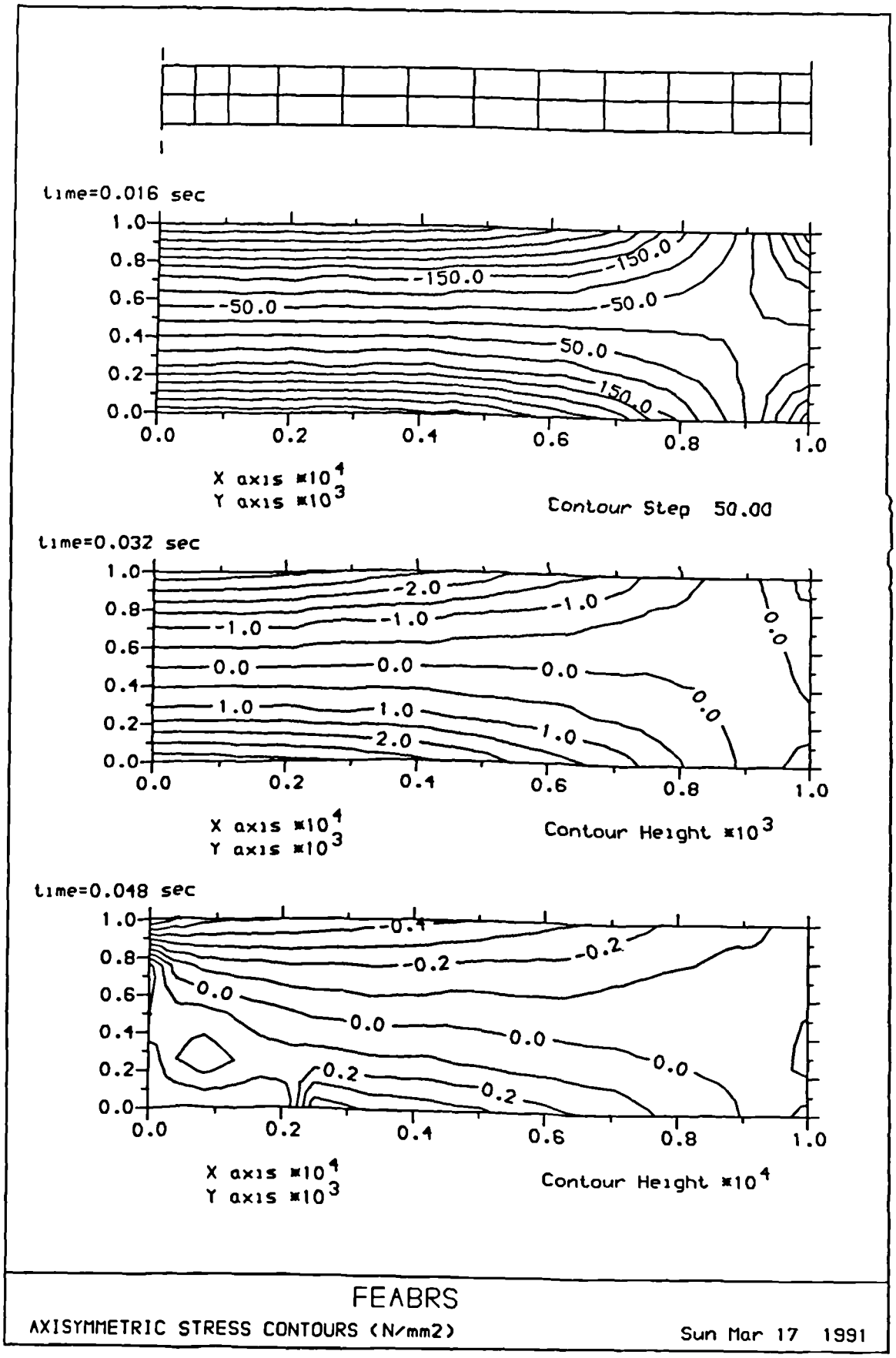

Figure 8.23: Hoop stress distribution of the slab at respective times

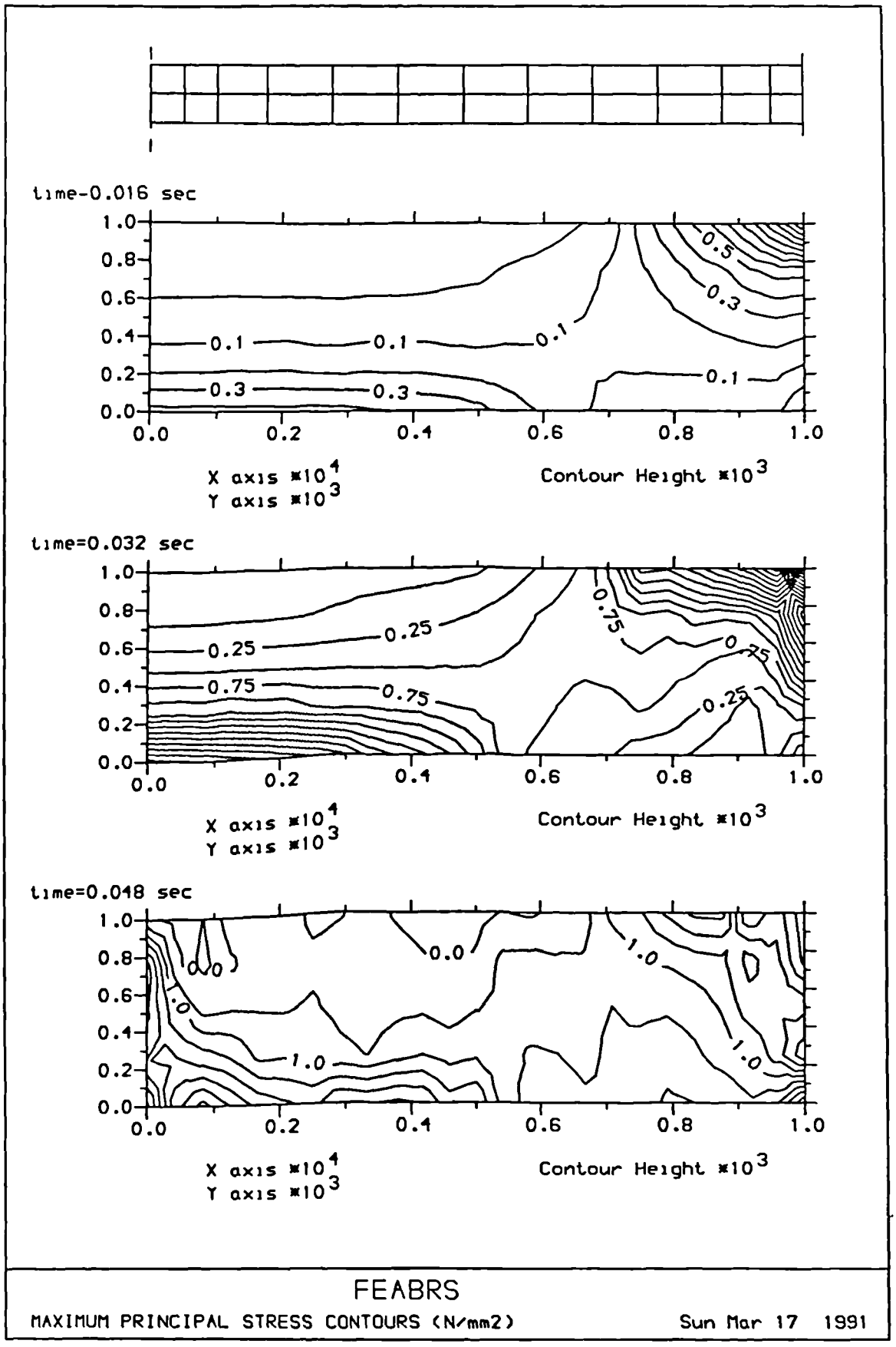

Figure 8.24: Maximum principal stress distribution of the slab at respective times

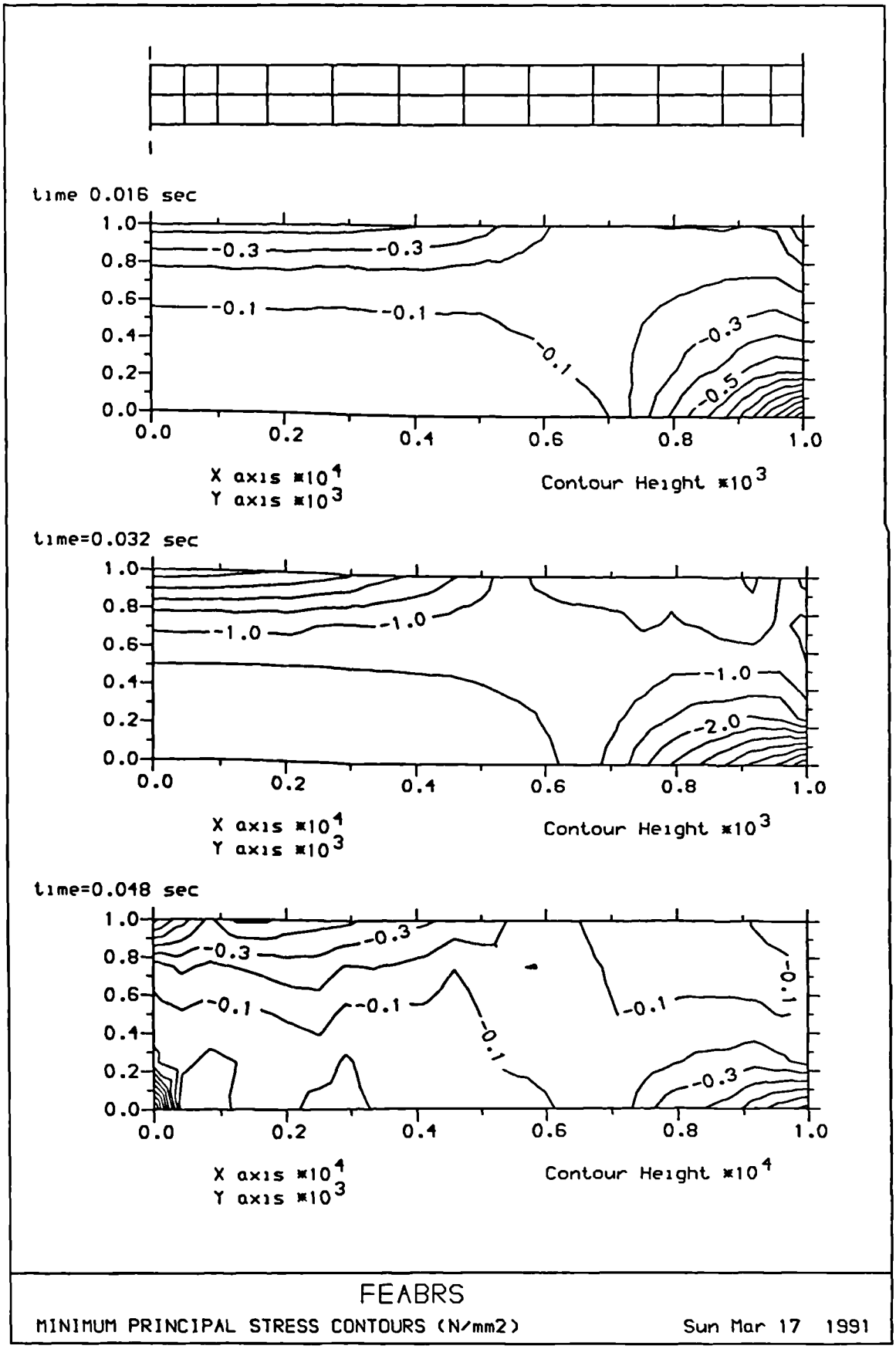

Figure 8.25: Minimum principal stress distribution of the slab at respective times

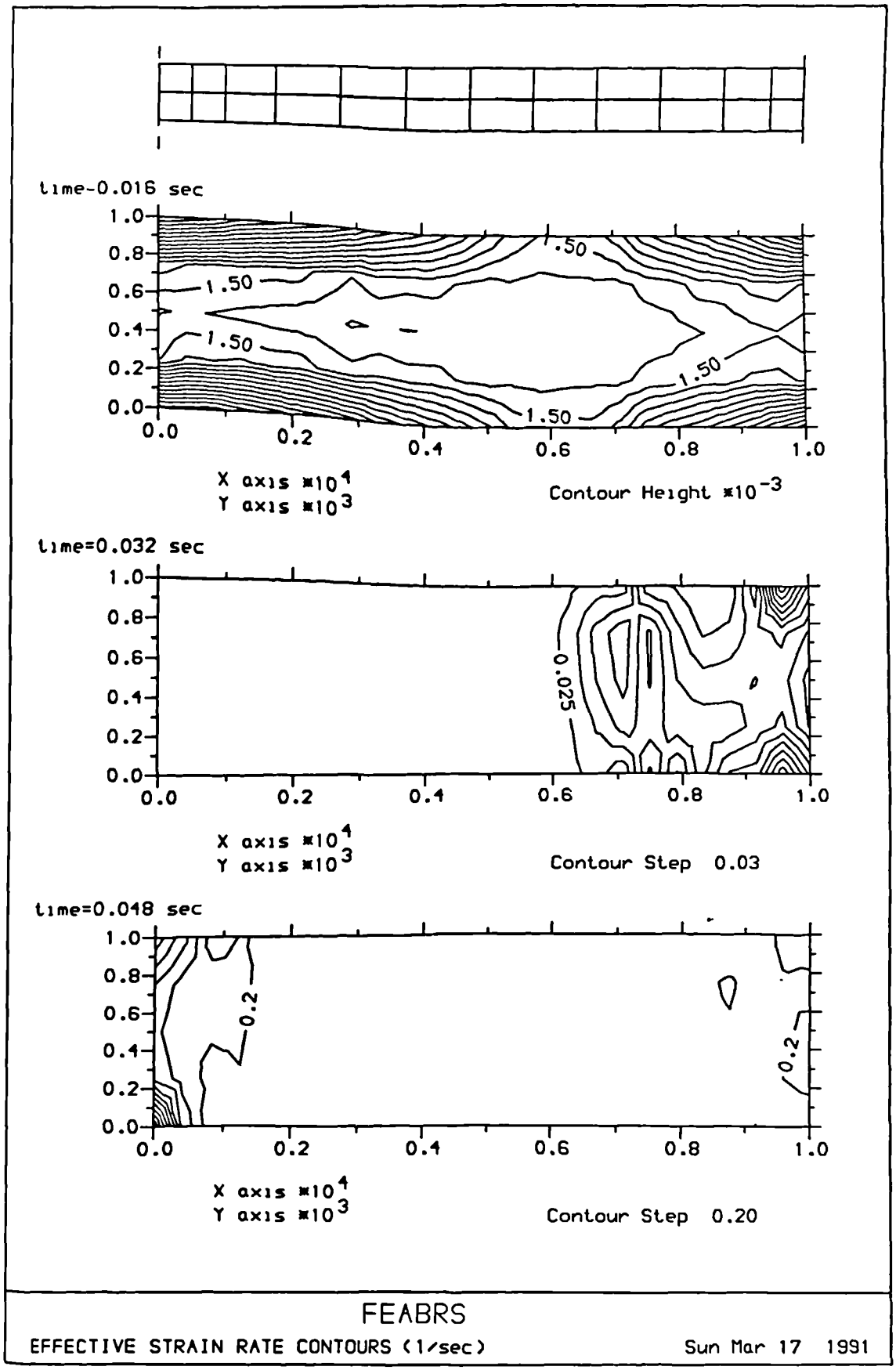

Figure 8.26: Effective strain rate distribution of the slab at respective times

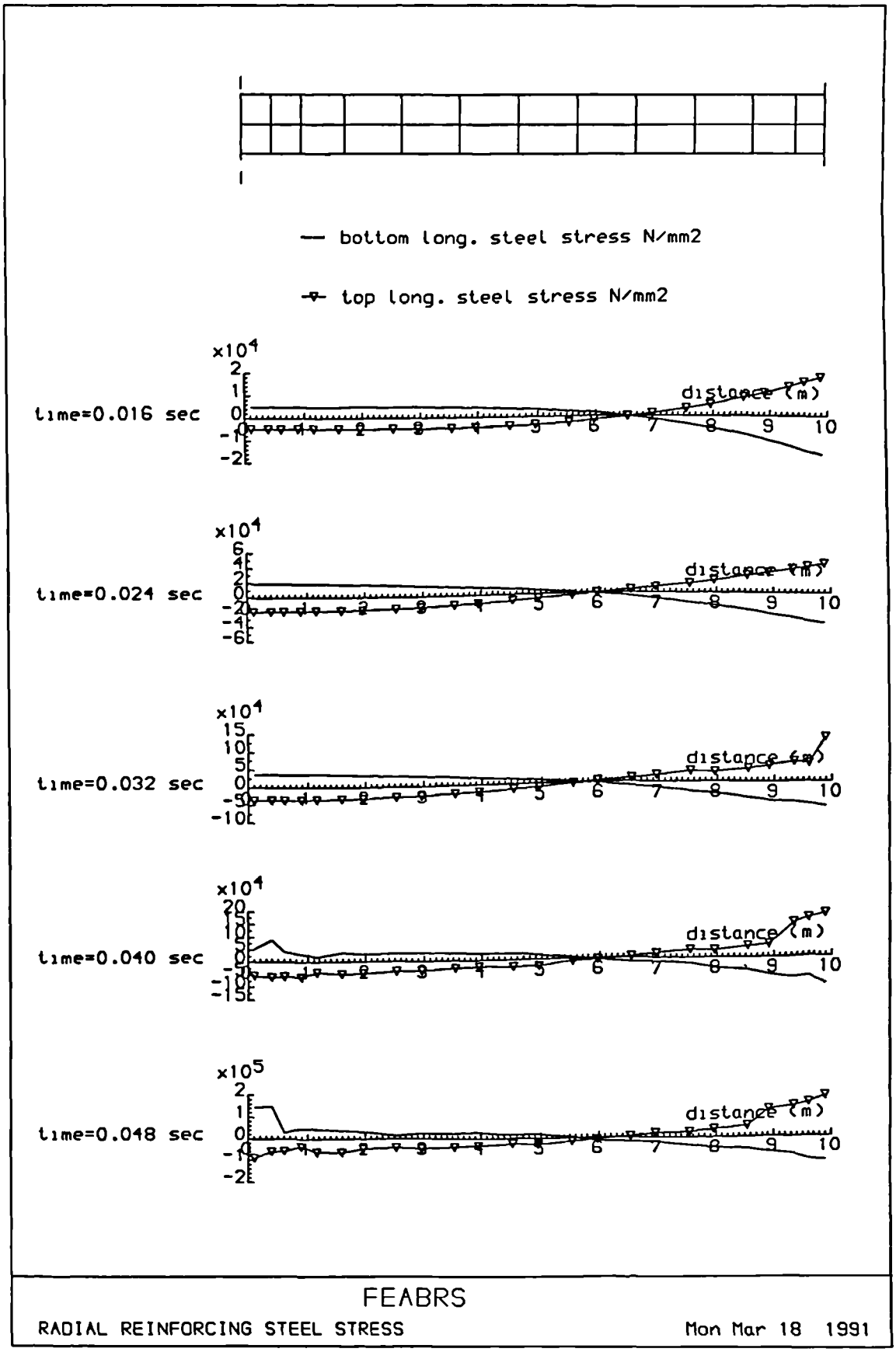

Figure 8.27: Stress distribution in the radial reinforcing steel of the plate at various time stations

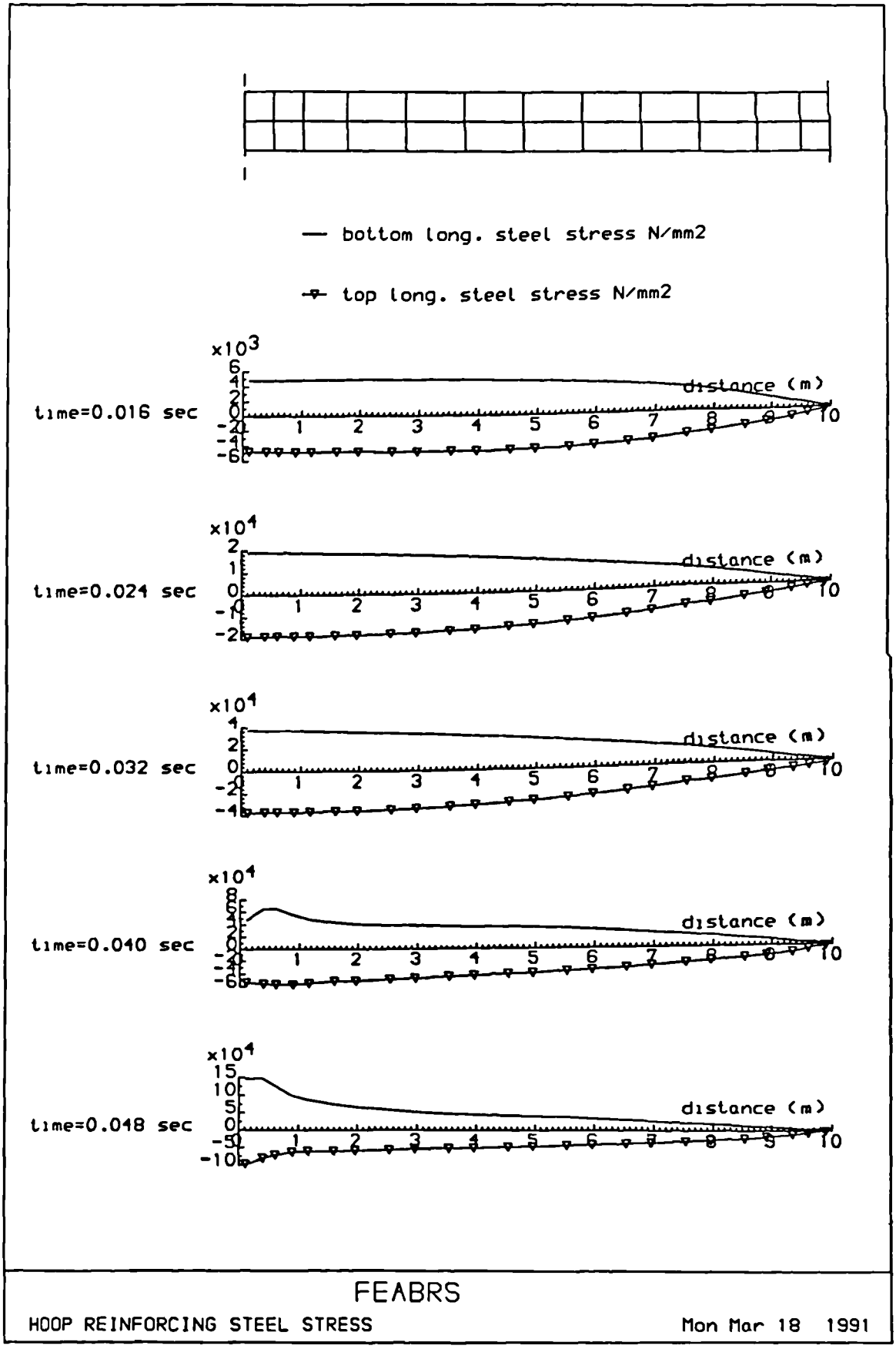

Figure 8.28: Stress distribution in the hoop reinforcement of the slab at various time stations

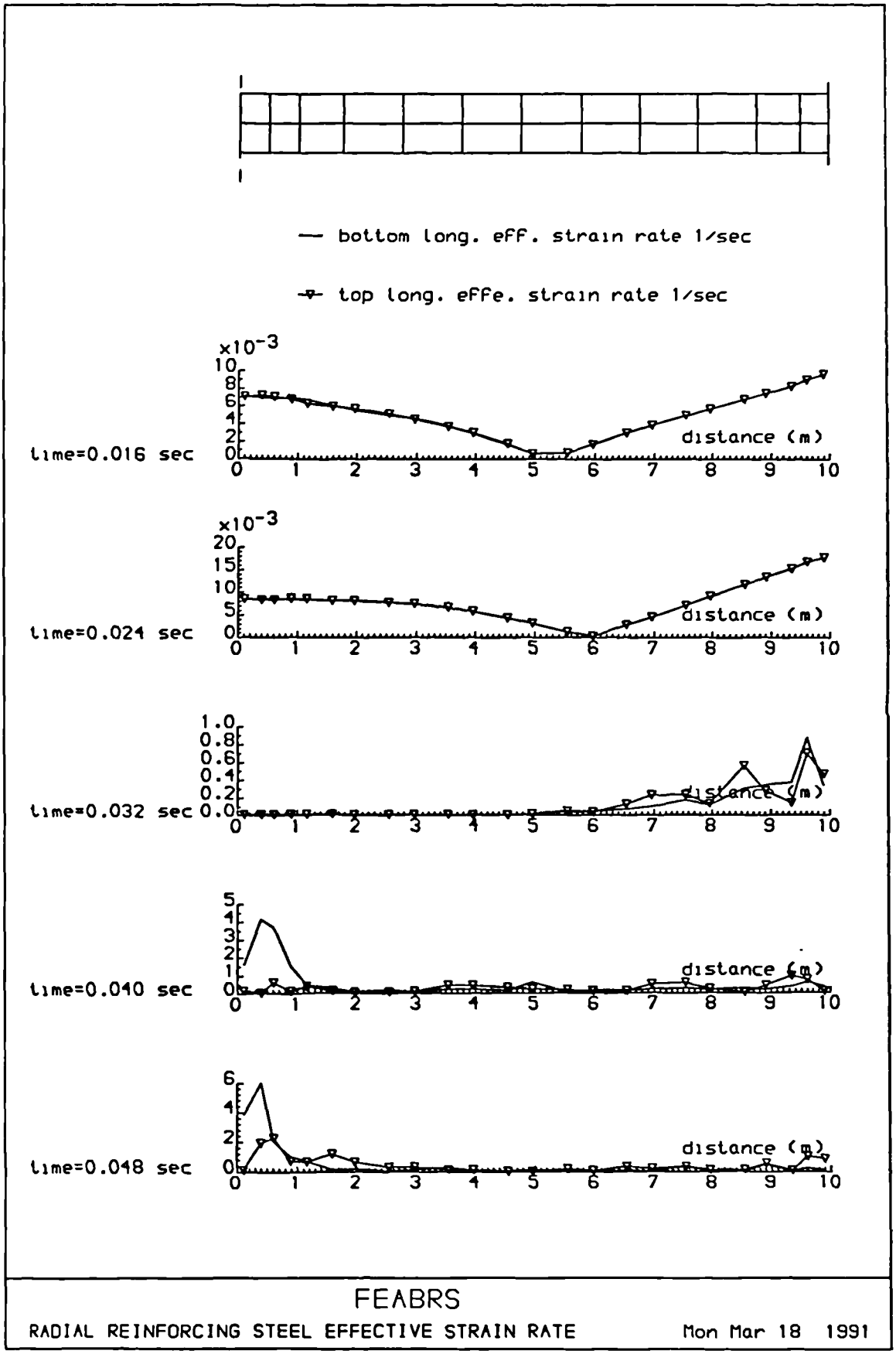

Figure 8.29: Effective strain rate distribution along the radial reinforcement of the plate at various time stations

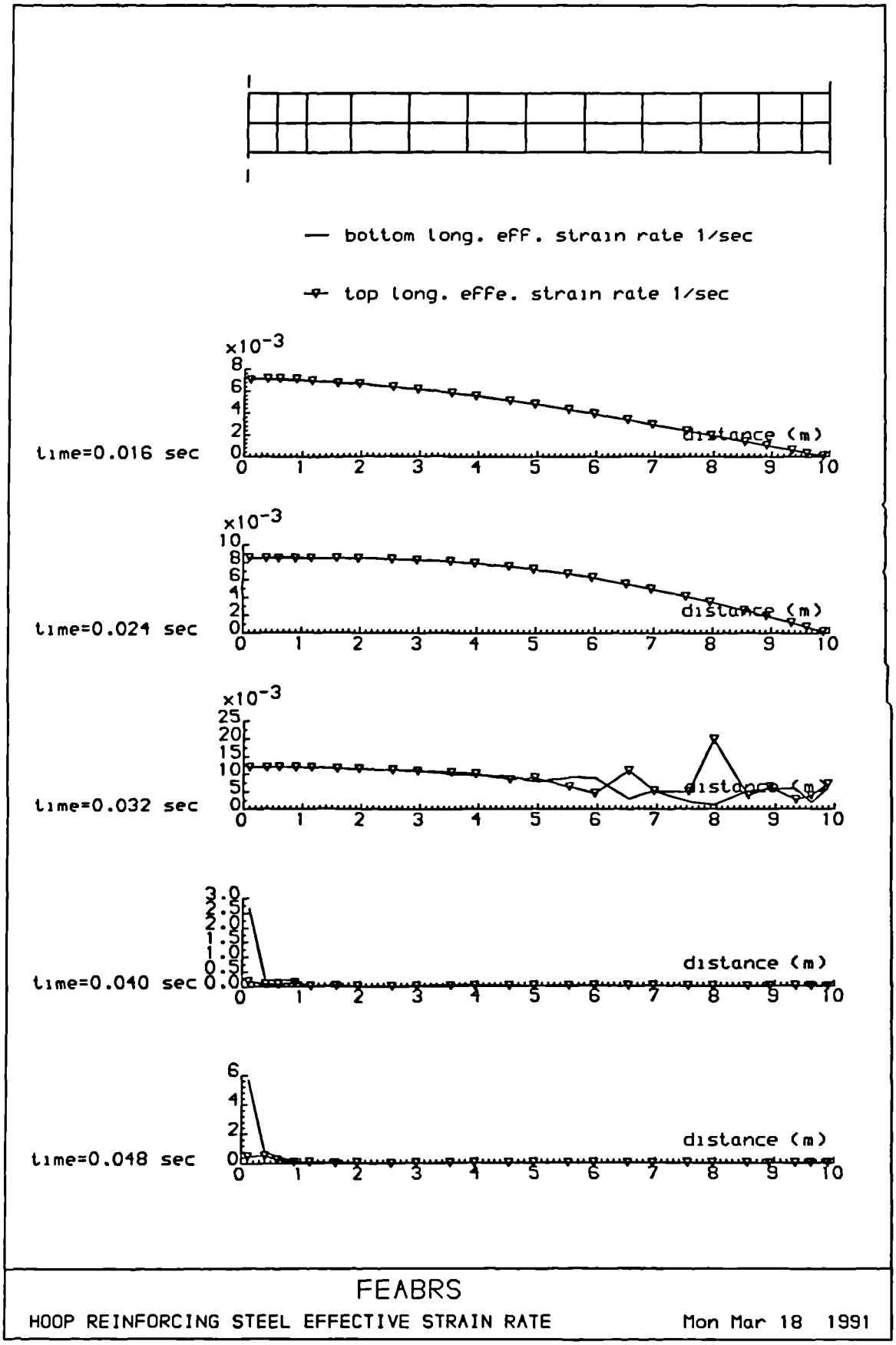

Figure 8.30: Effective strain rate distribution along the hoop reinforcement of the plate at various time stations

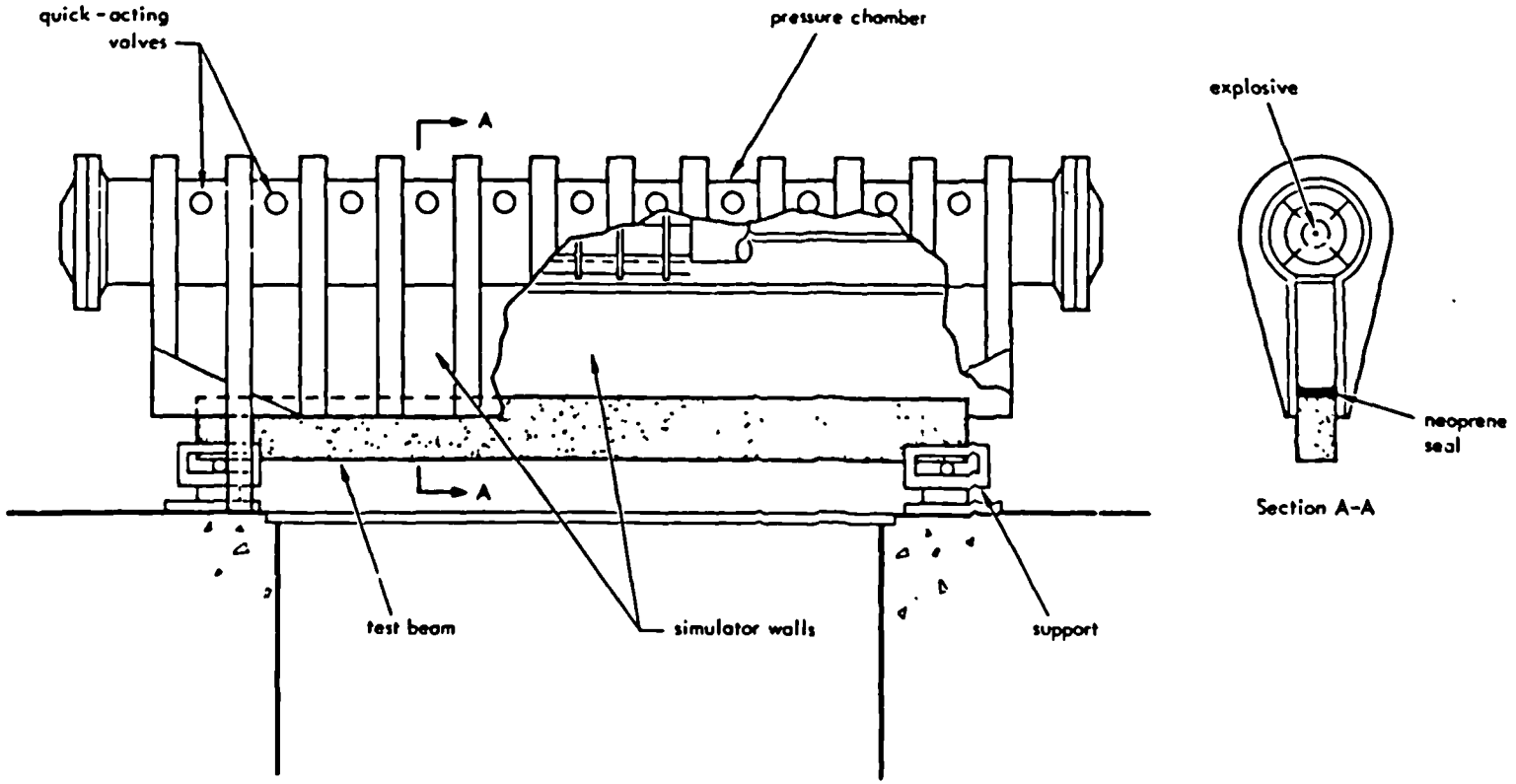

Figure 8.31: Schematic of beam in NCEL blast simulation

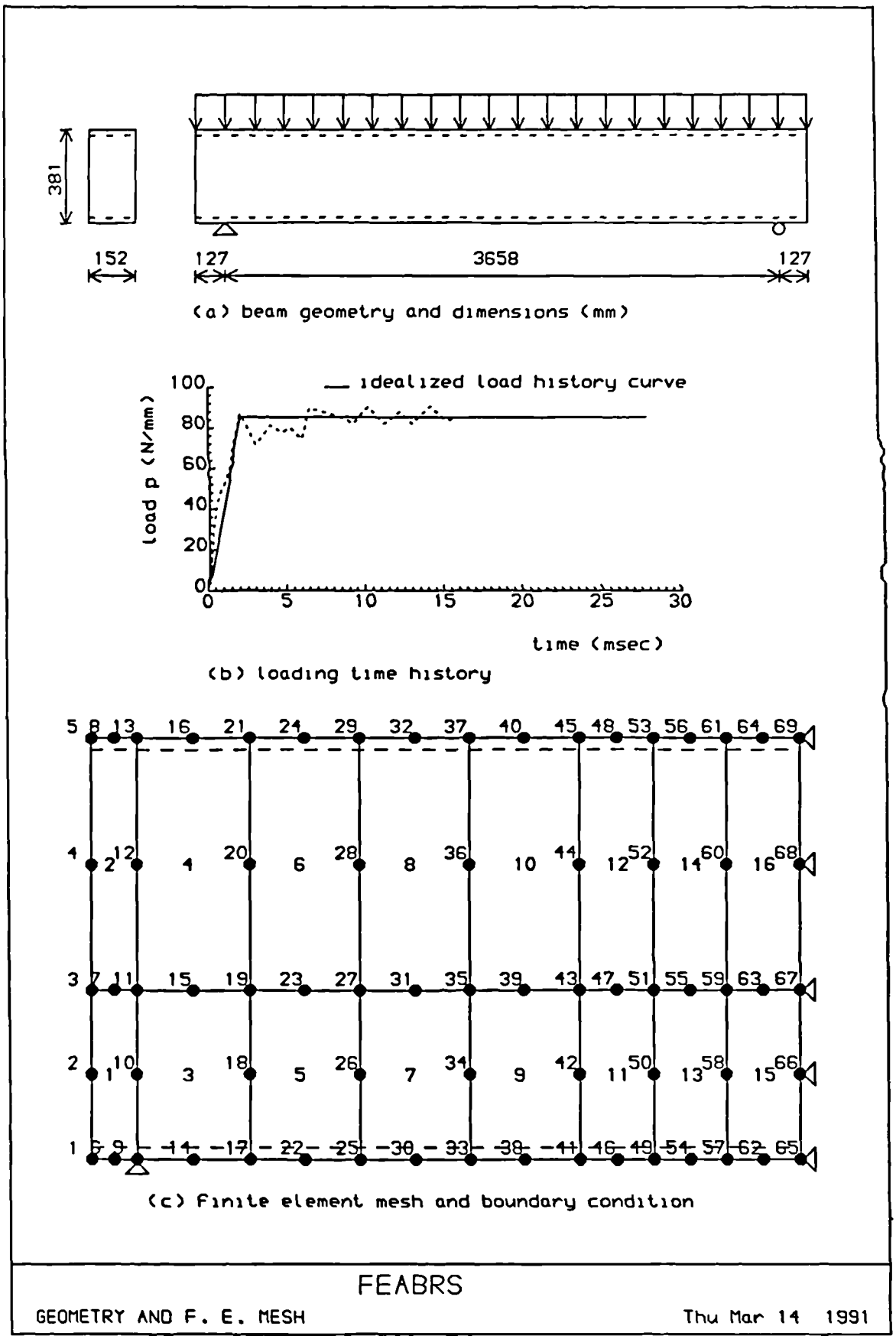

Figure 8.32: Details of Seabold's beam and finite element idealization

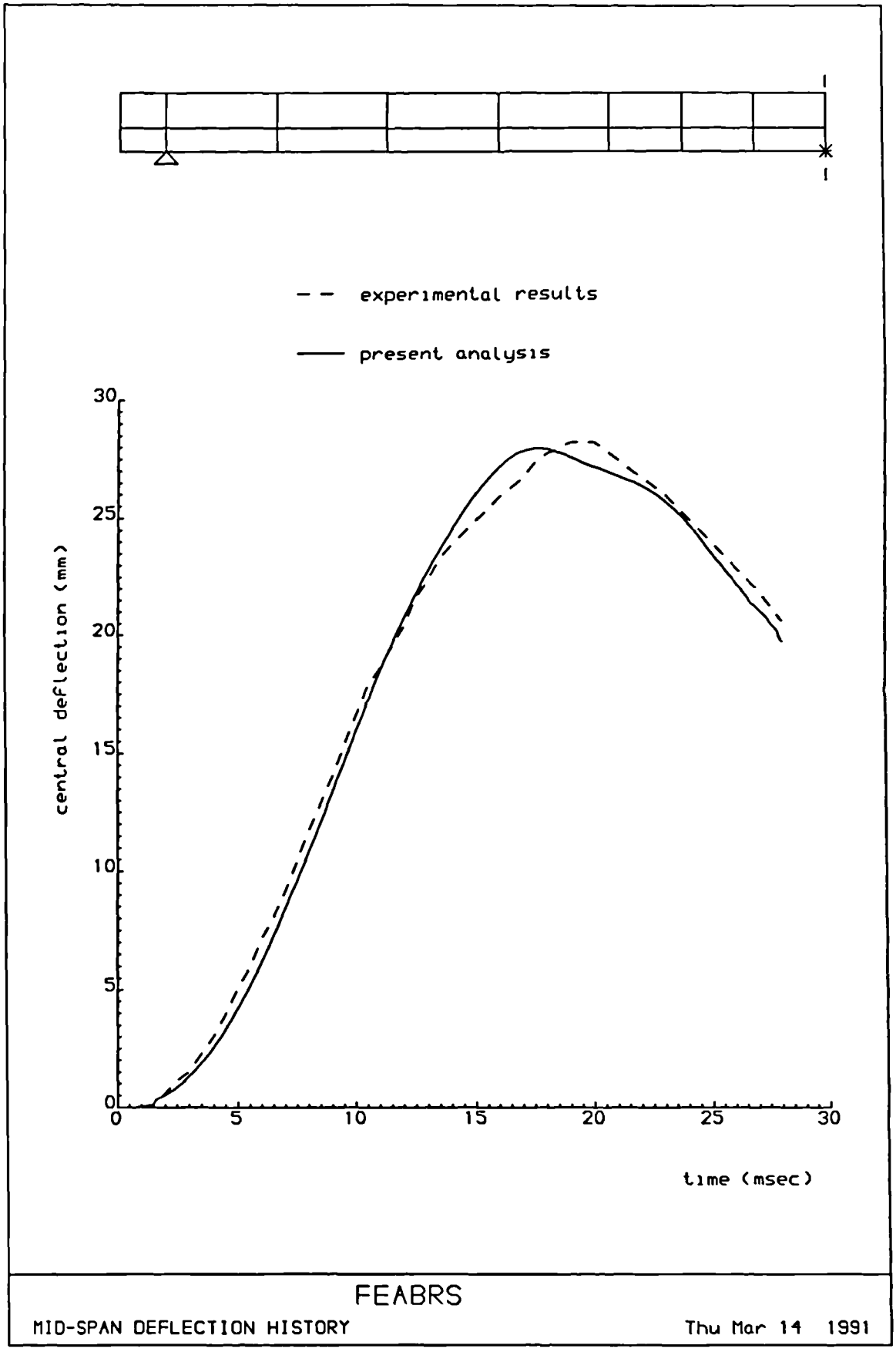

Figure 8.33: Comparison of the predicted and measured central deflection-time history

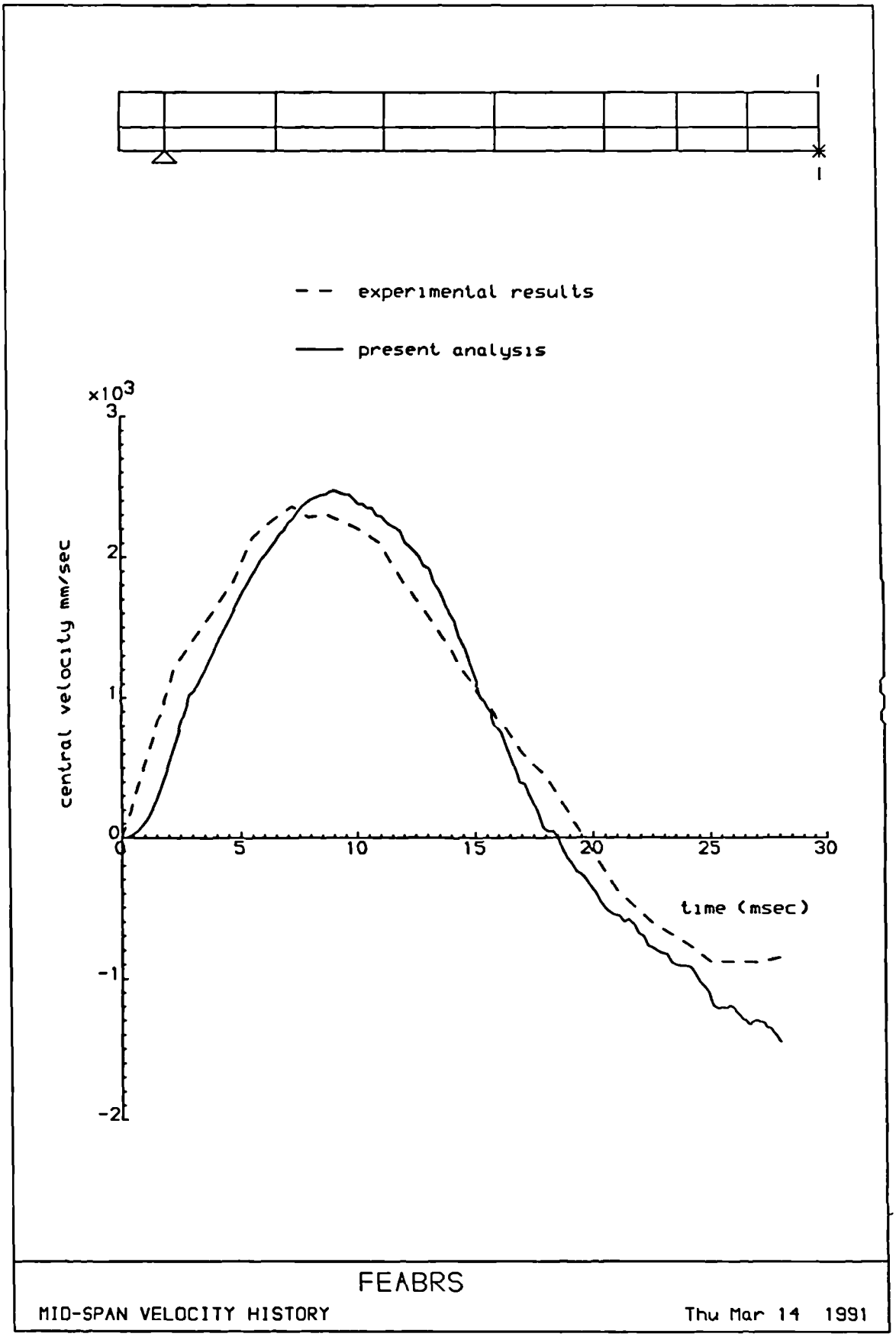

Figure 8.34: Comparison of the analytical and experimental mid-span velocity history of the beam

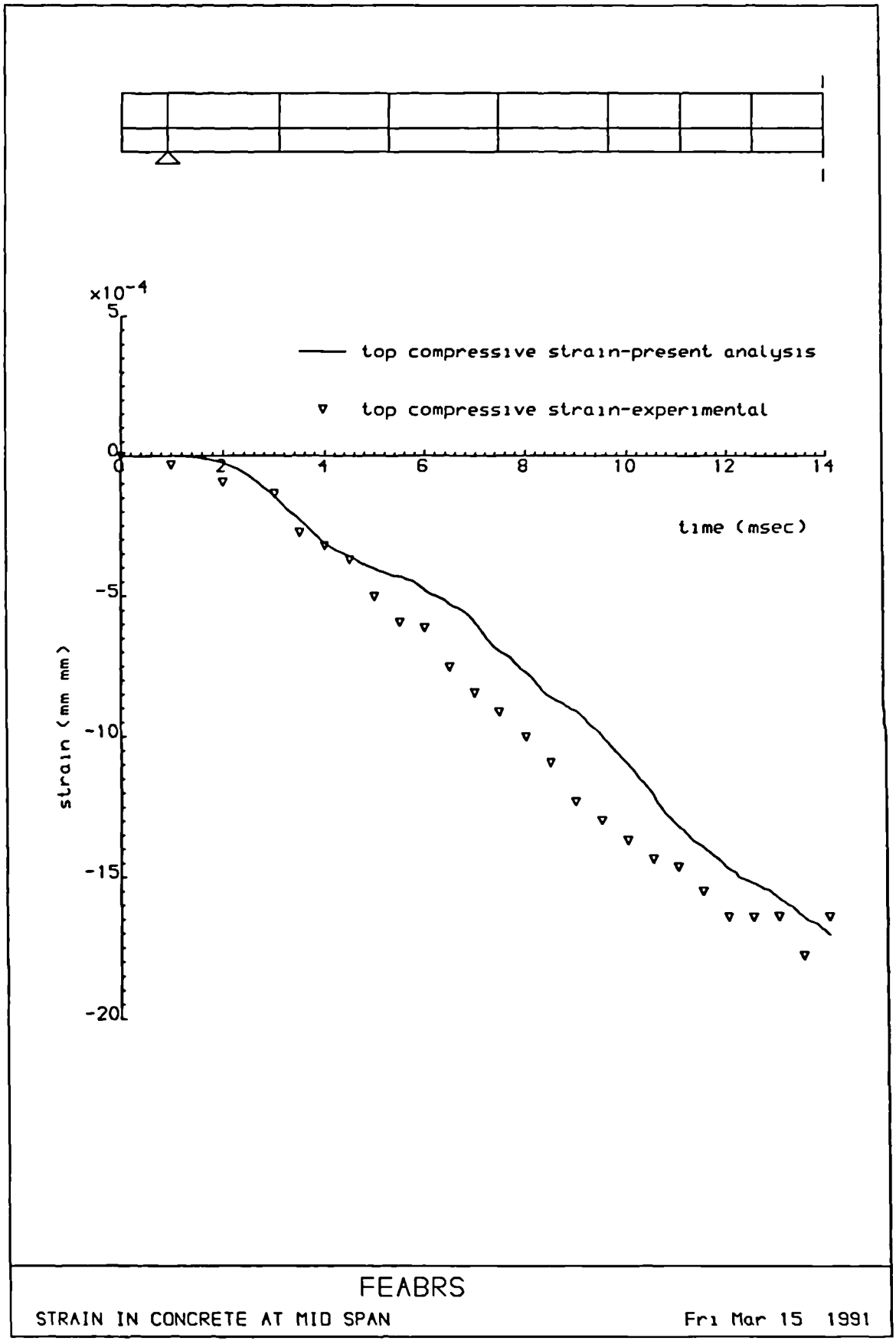

Figure 8.35: Comparison of the predicted and measured compressive strain history of concrete at beam mid-span

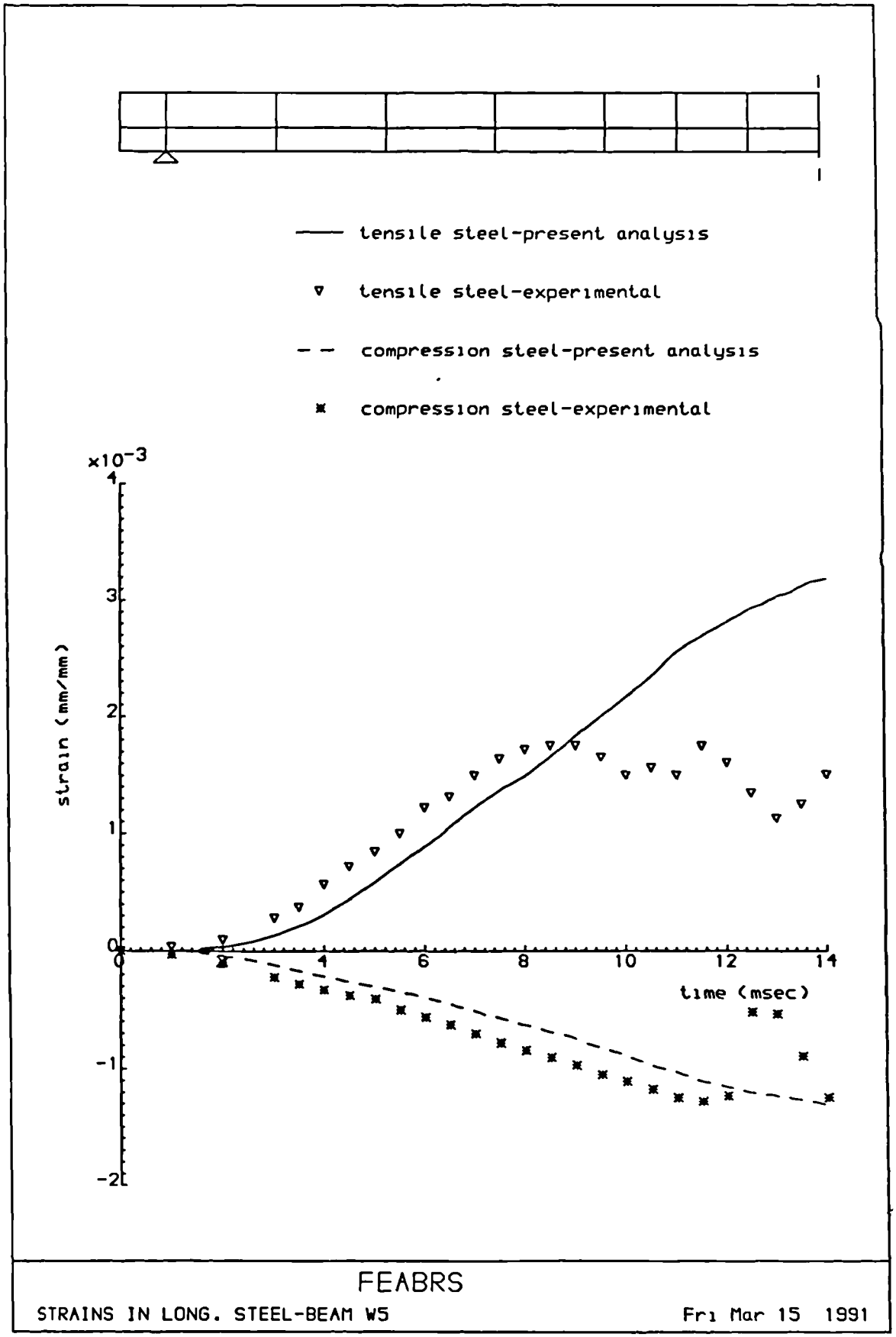

Figure 8.36: Comparison of the predicted and measured stress history of main reinforcement at mid-span of beam WE5

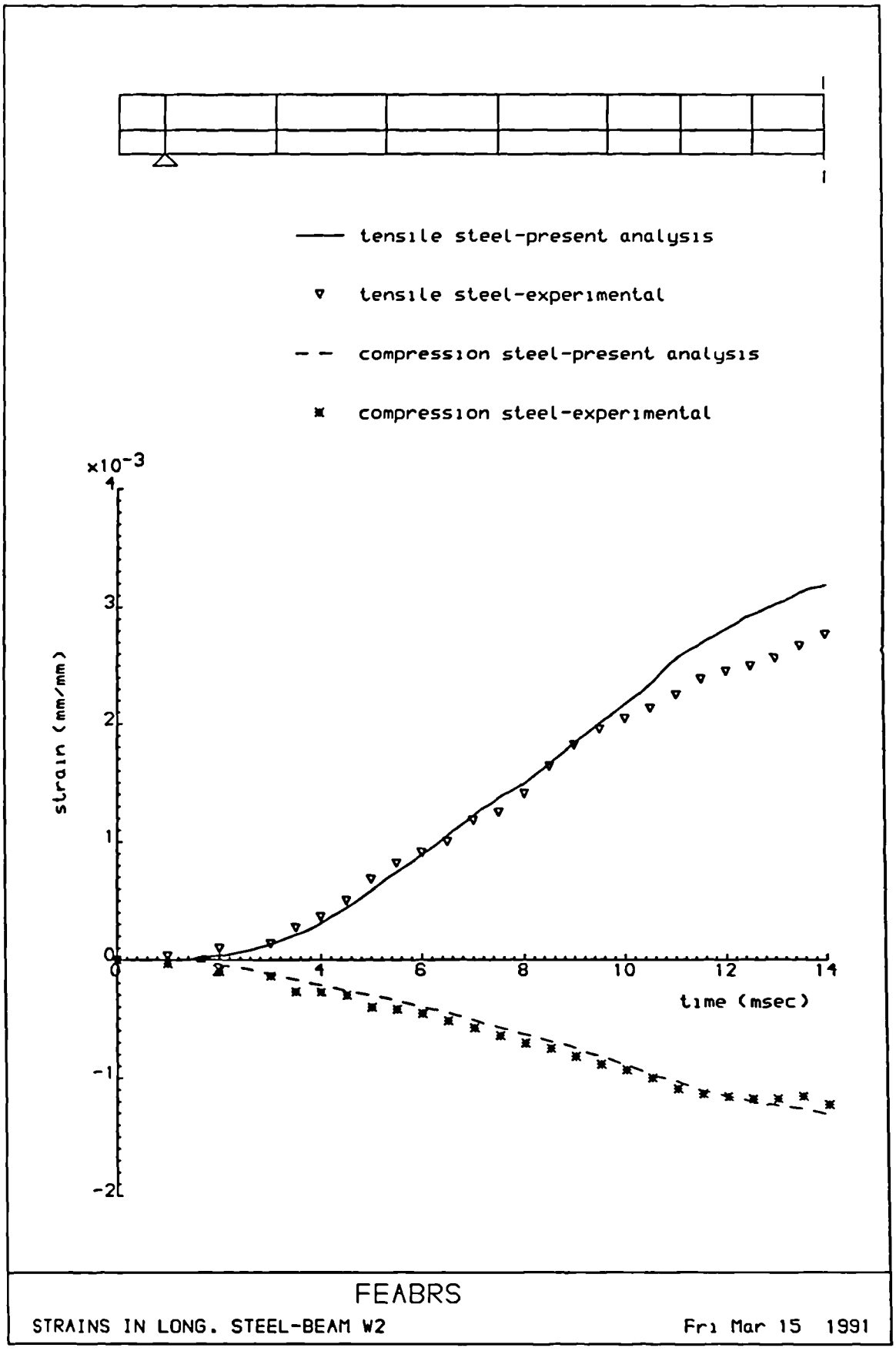

Figure 8.37: Comparison of the predicted and measured stress history of main reinforcement at mid-span of beam WE2

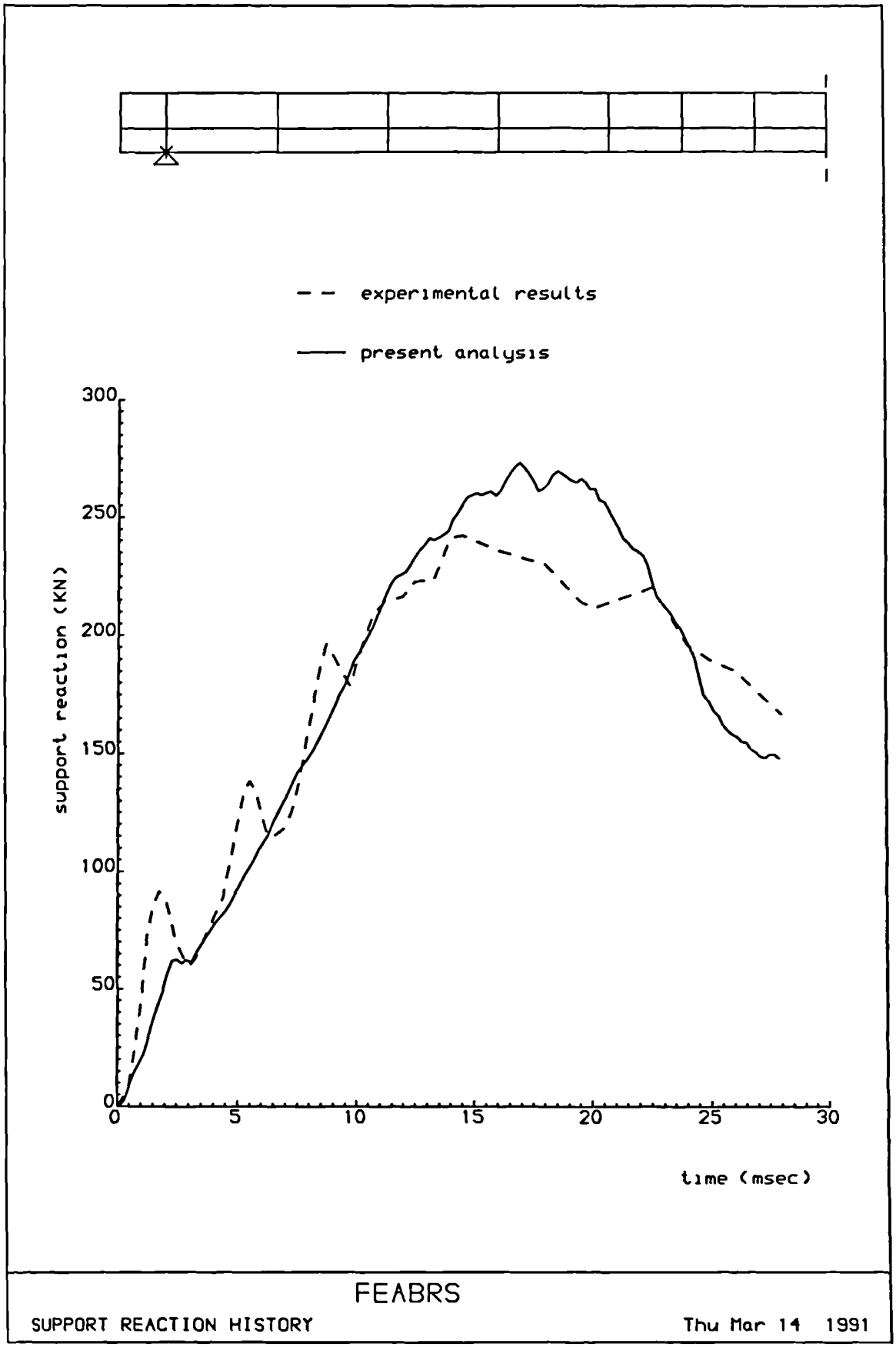

Figure 8.38: Comparison of the numerical and experimental reaction history at left-hand support

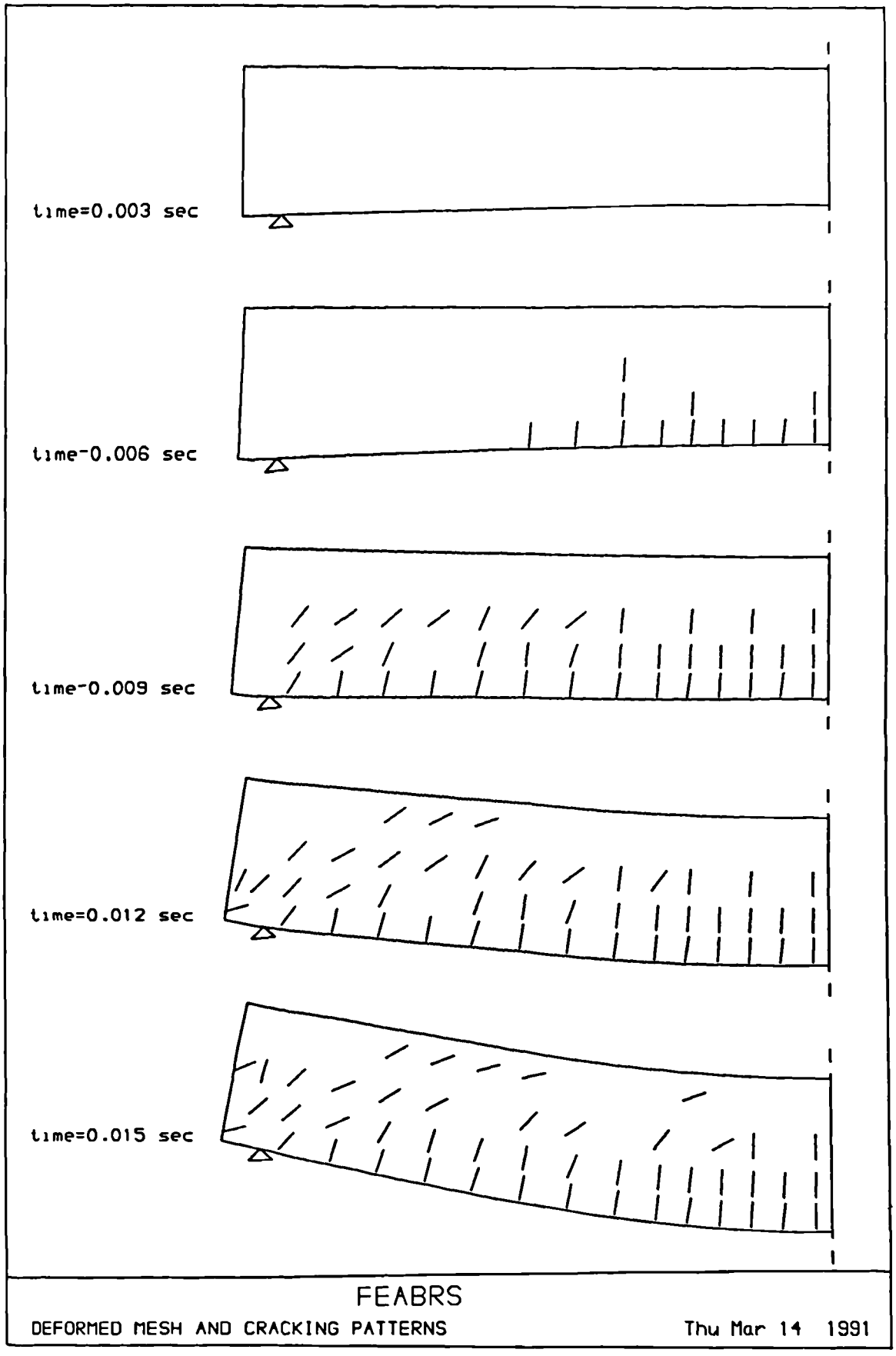

Figure 8.39: Deformation and cracking history for Seabold's beam

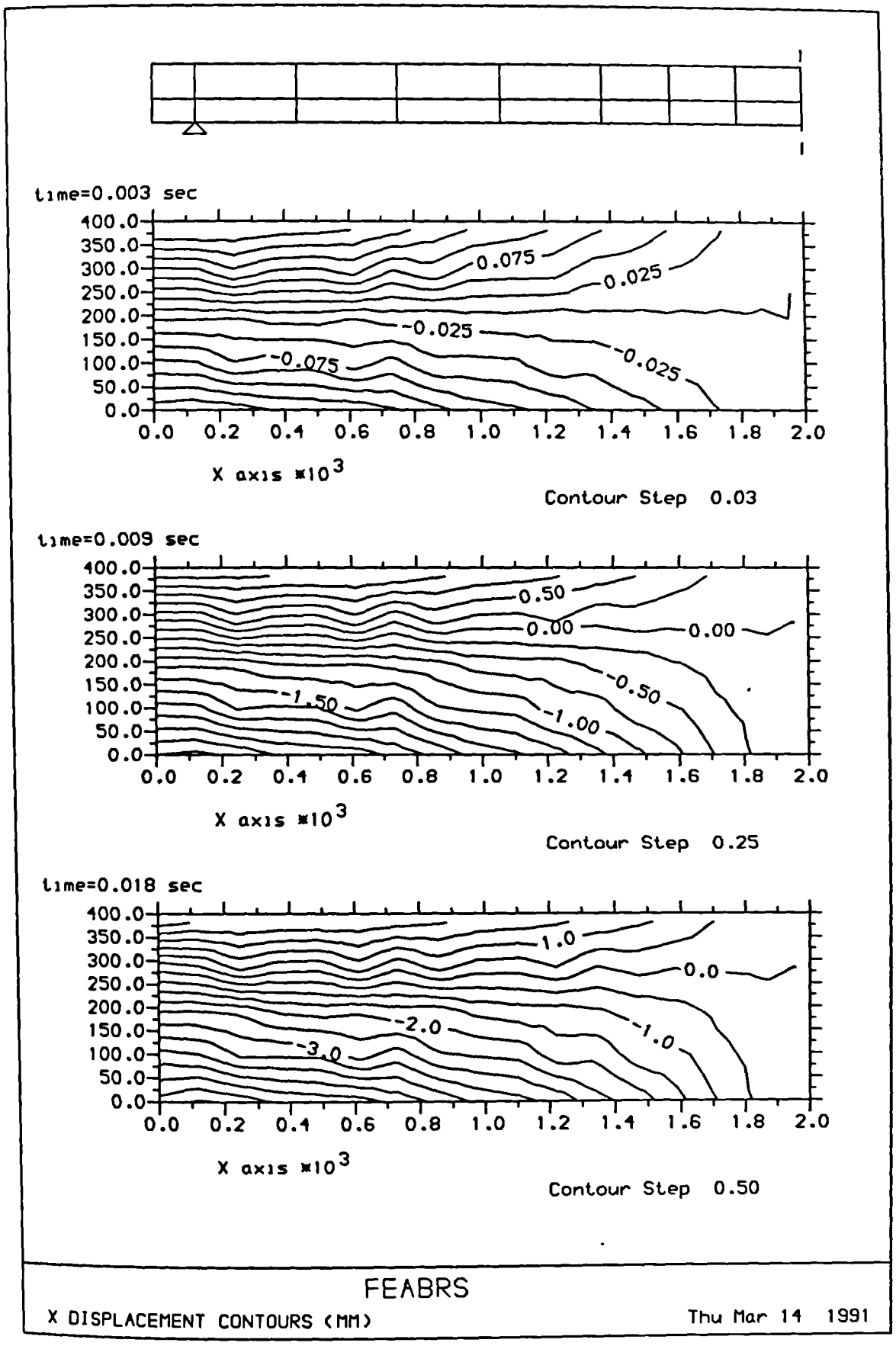

Figure 8.40: Horizontal displacement distribution along Seabold's beam at respective times

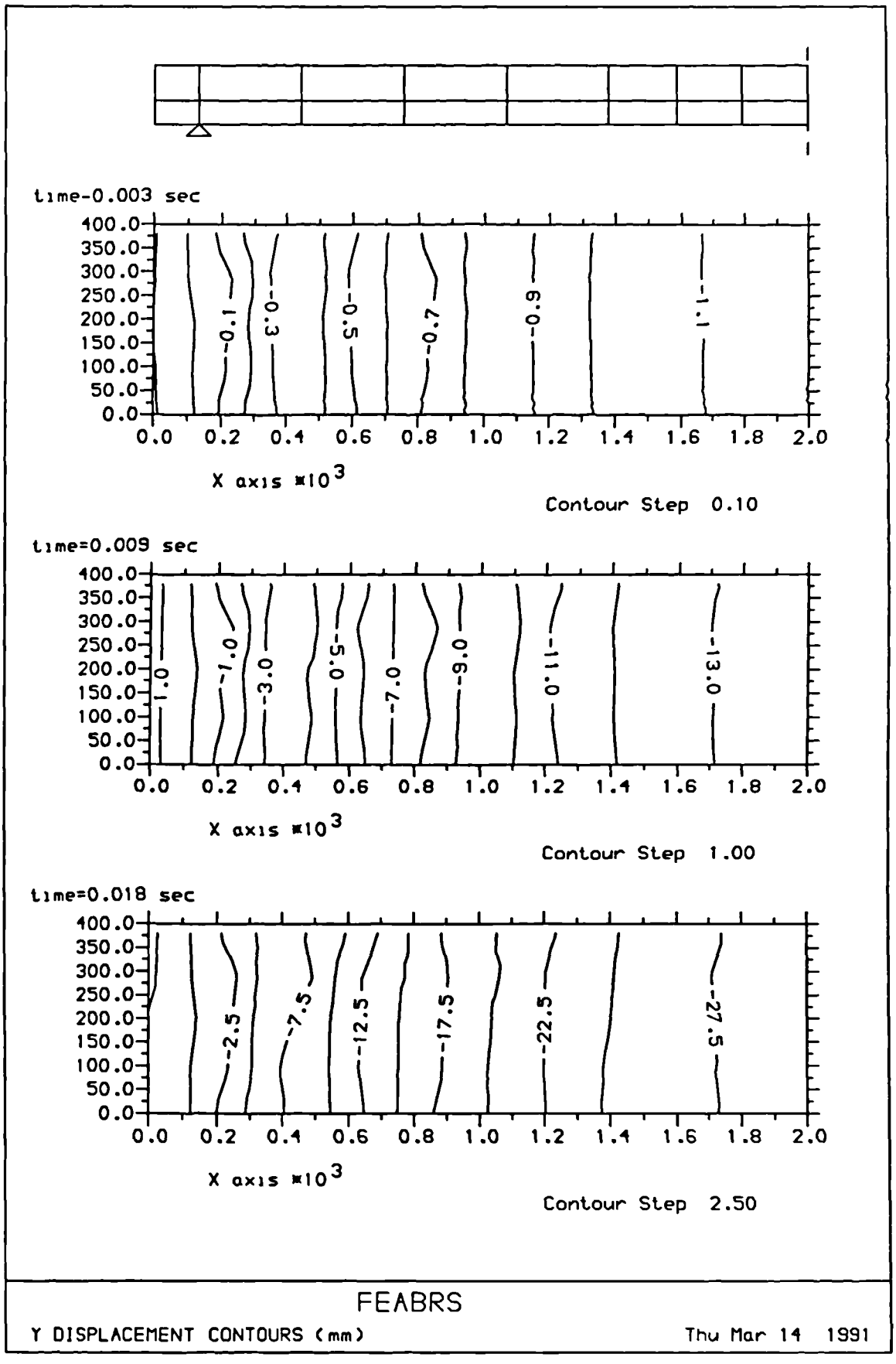

Figure 8.41: Vertical displacement distribution along Seabold's beam at respective times

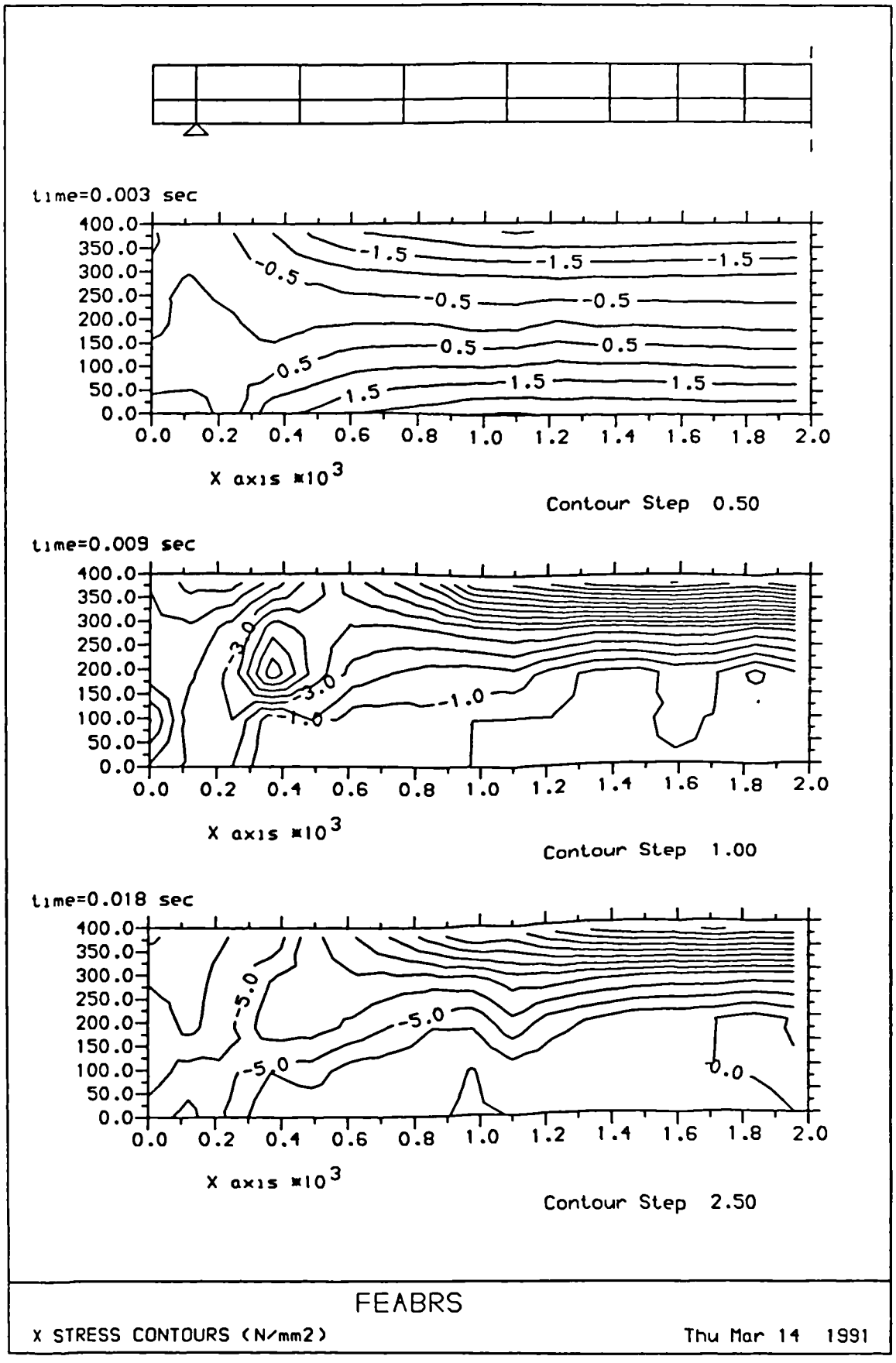

Figure 8.42: Longitudinal stress distribution along Seabold's beam at respective times

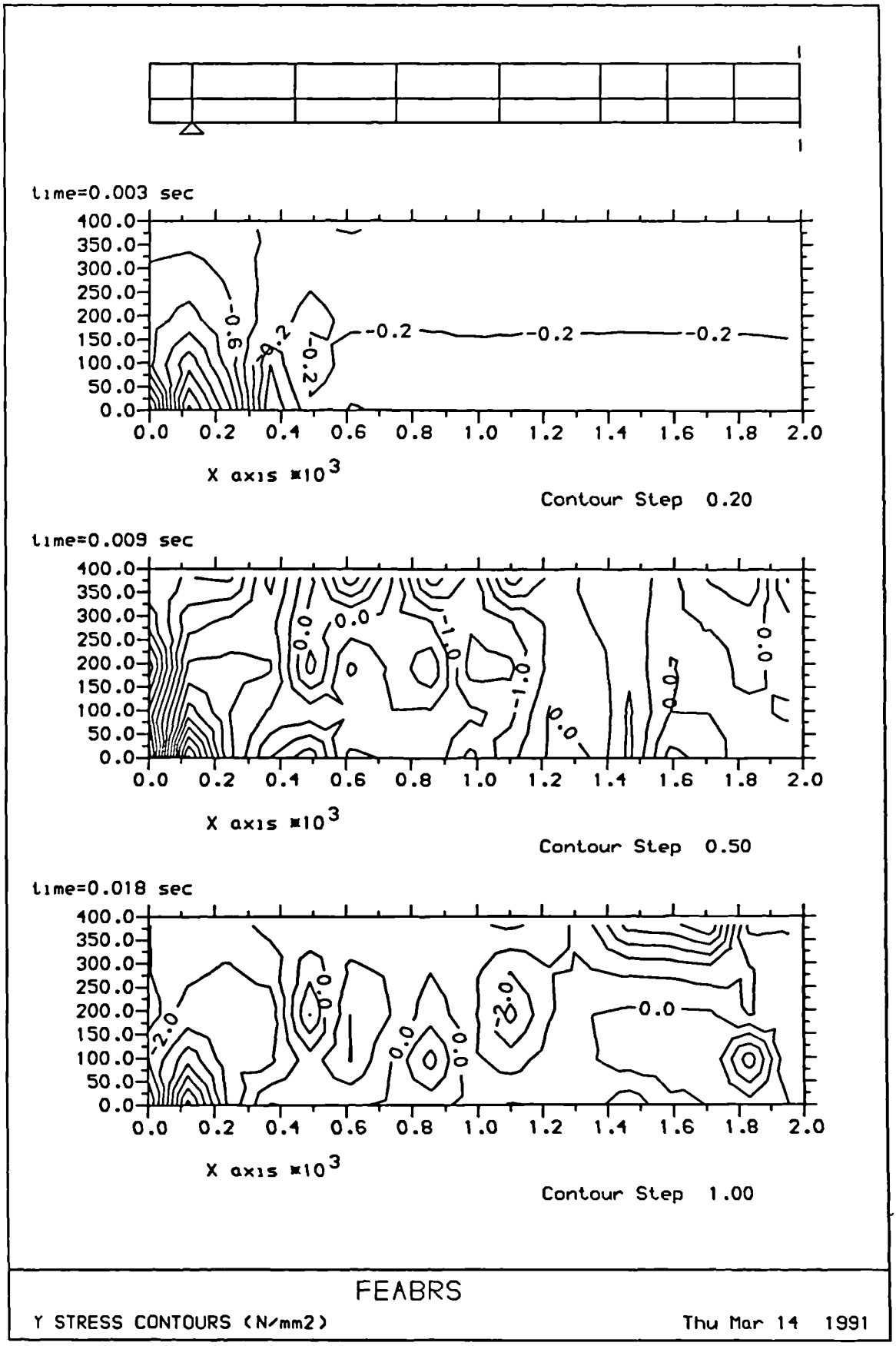

Figure 8.43: Transverse stress distribution along Seabold's beam at respective times

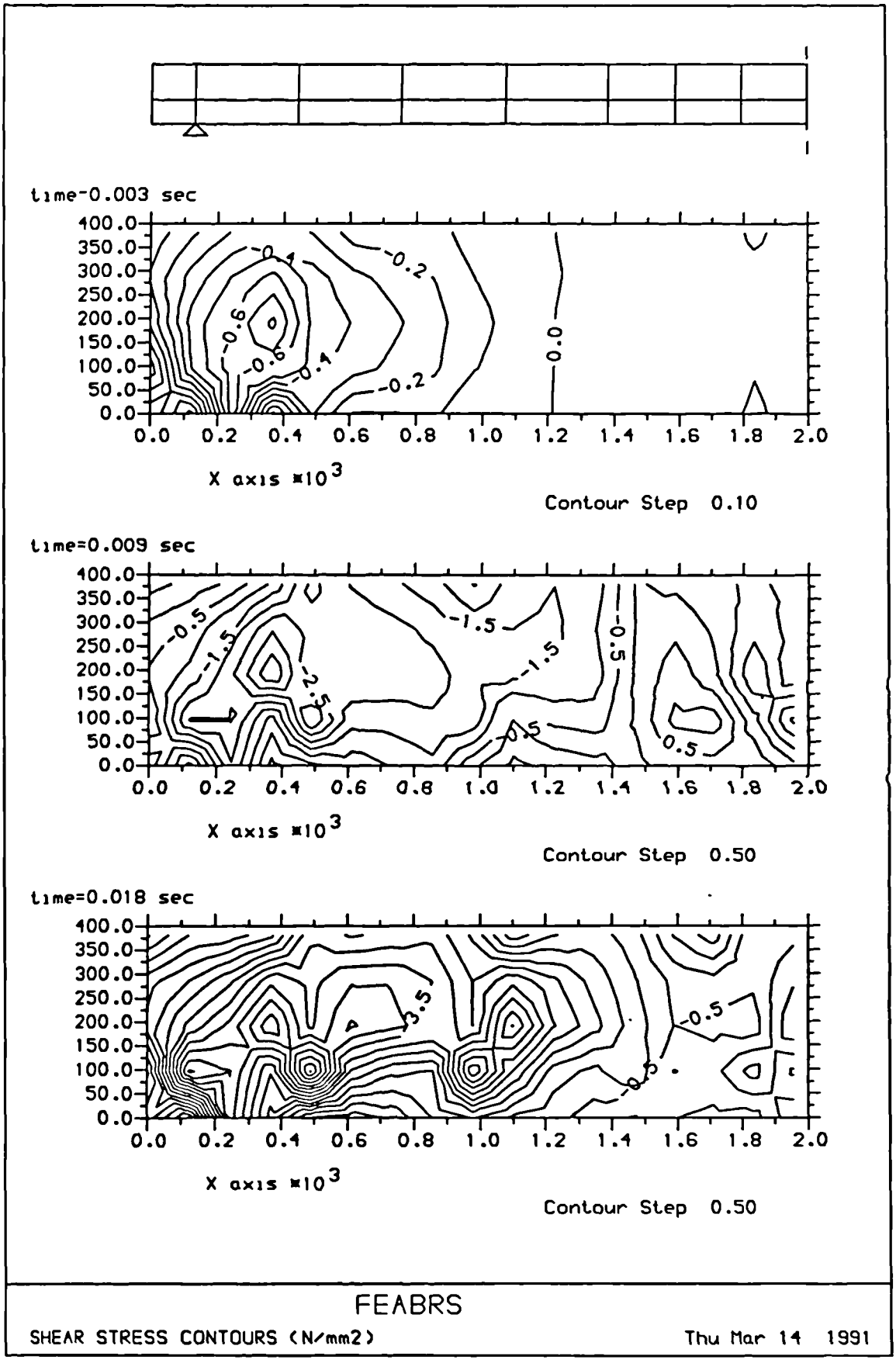

Figure 8.44: Shear stress distribution along Seabold's beam at respective times

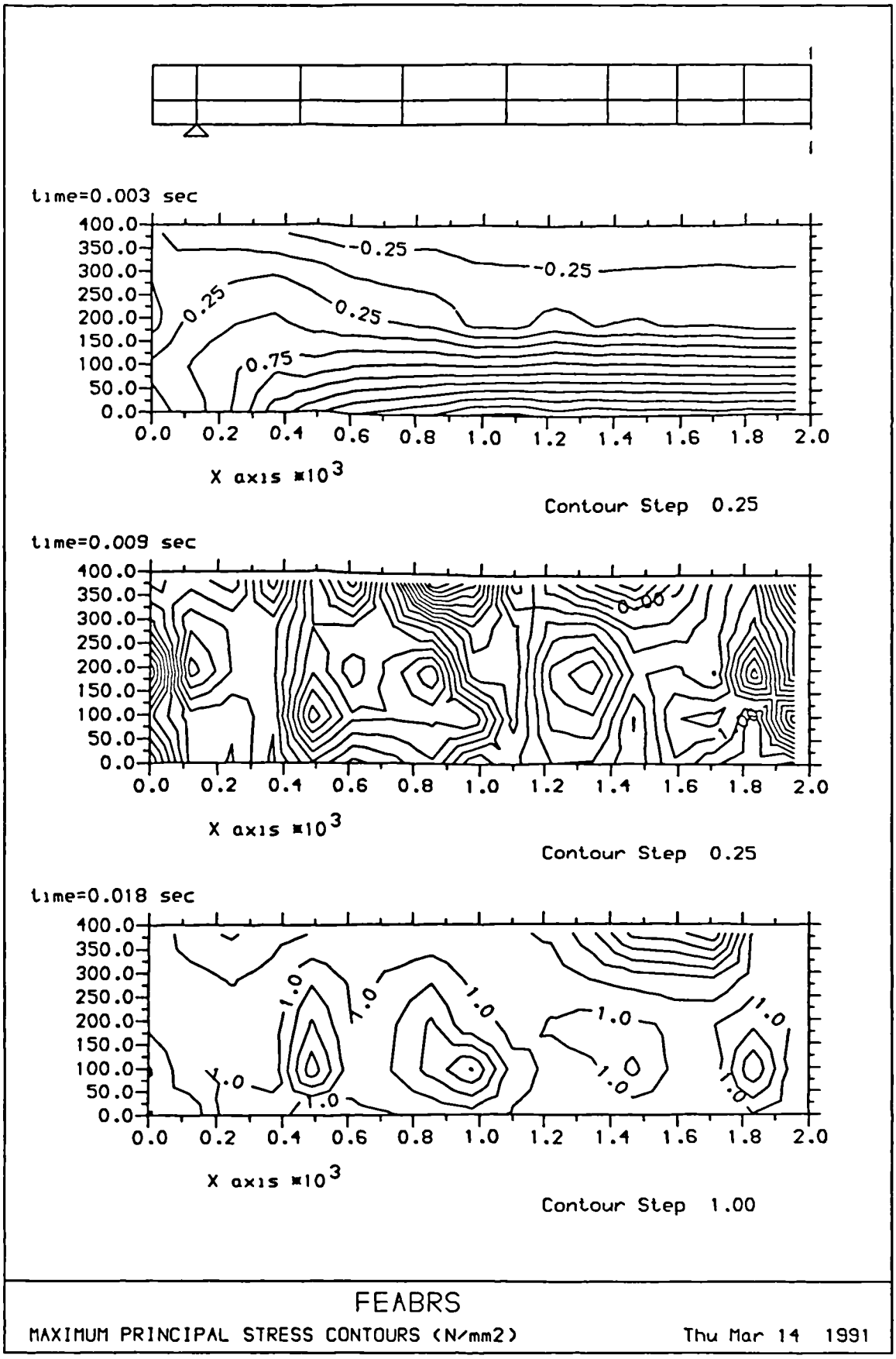

Figure 8.45: Maximum principal stress distribution along Seabold's beam at respective times

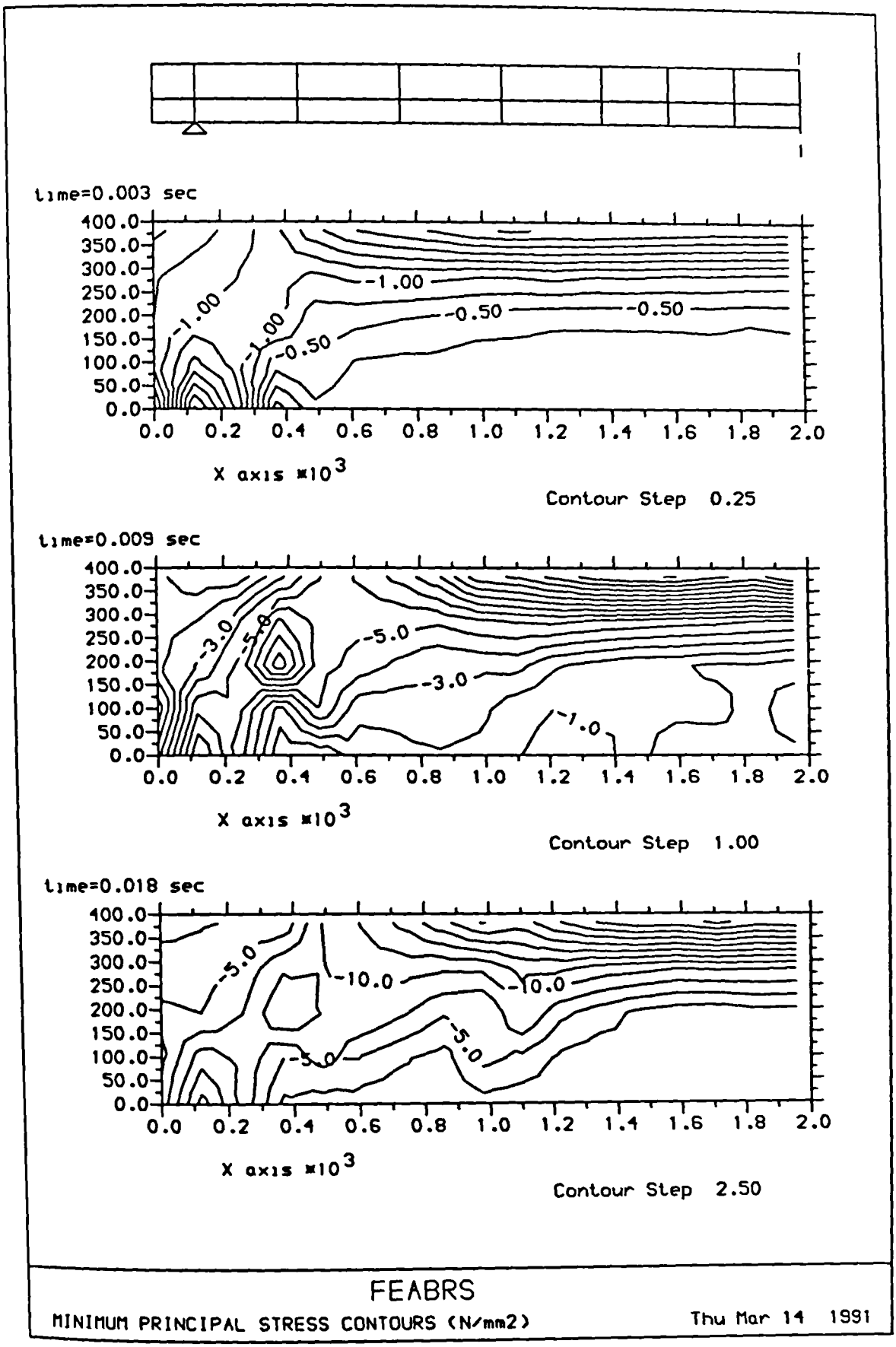

Figure 8.46: Minimum principal stress distribution along Seabold's beam at respective times

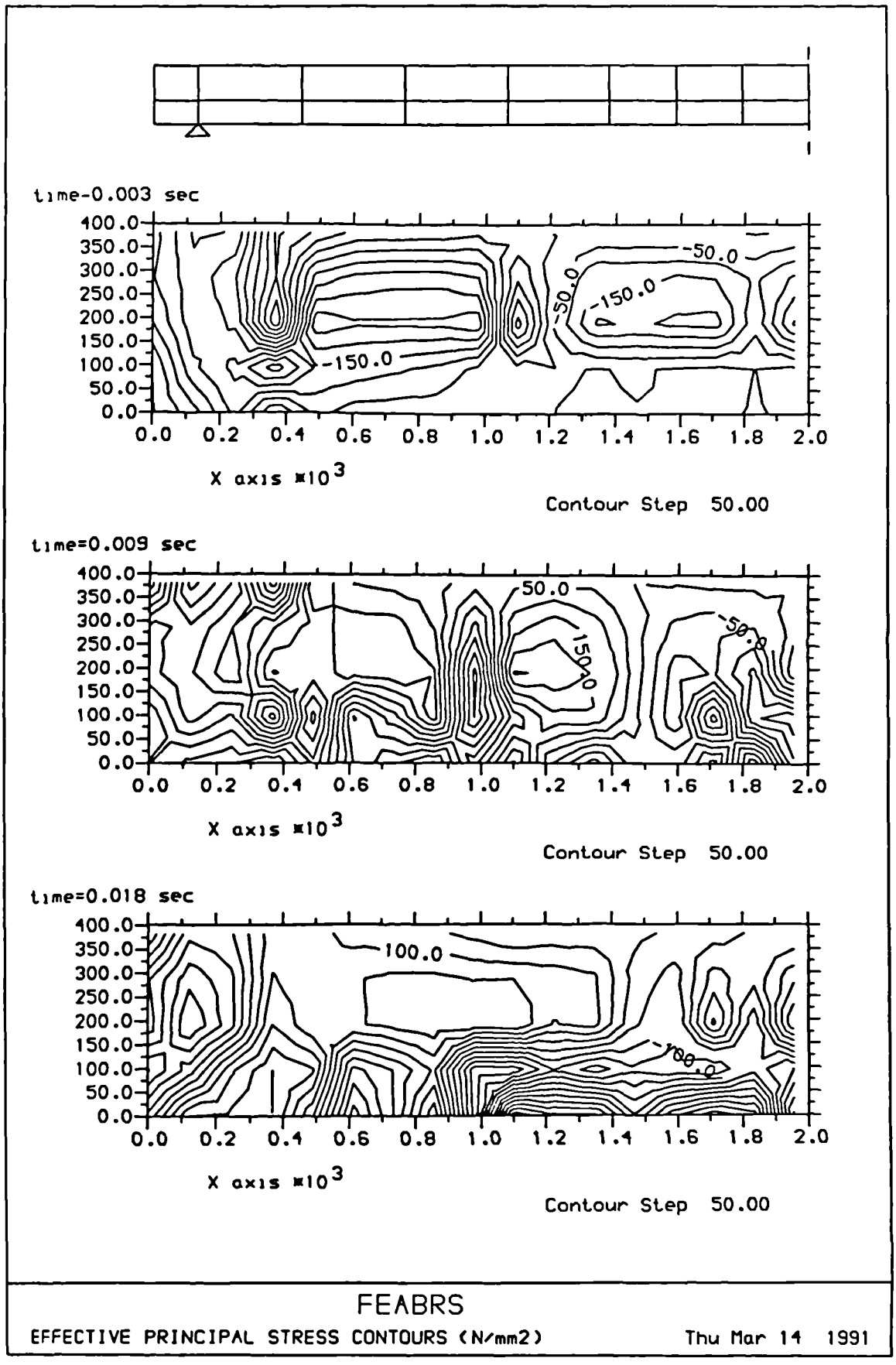

Figure 8.47: Effective strain rate distribution along Seabold's beam at respective times

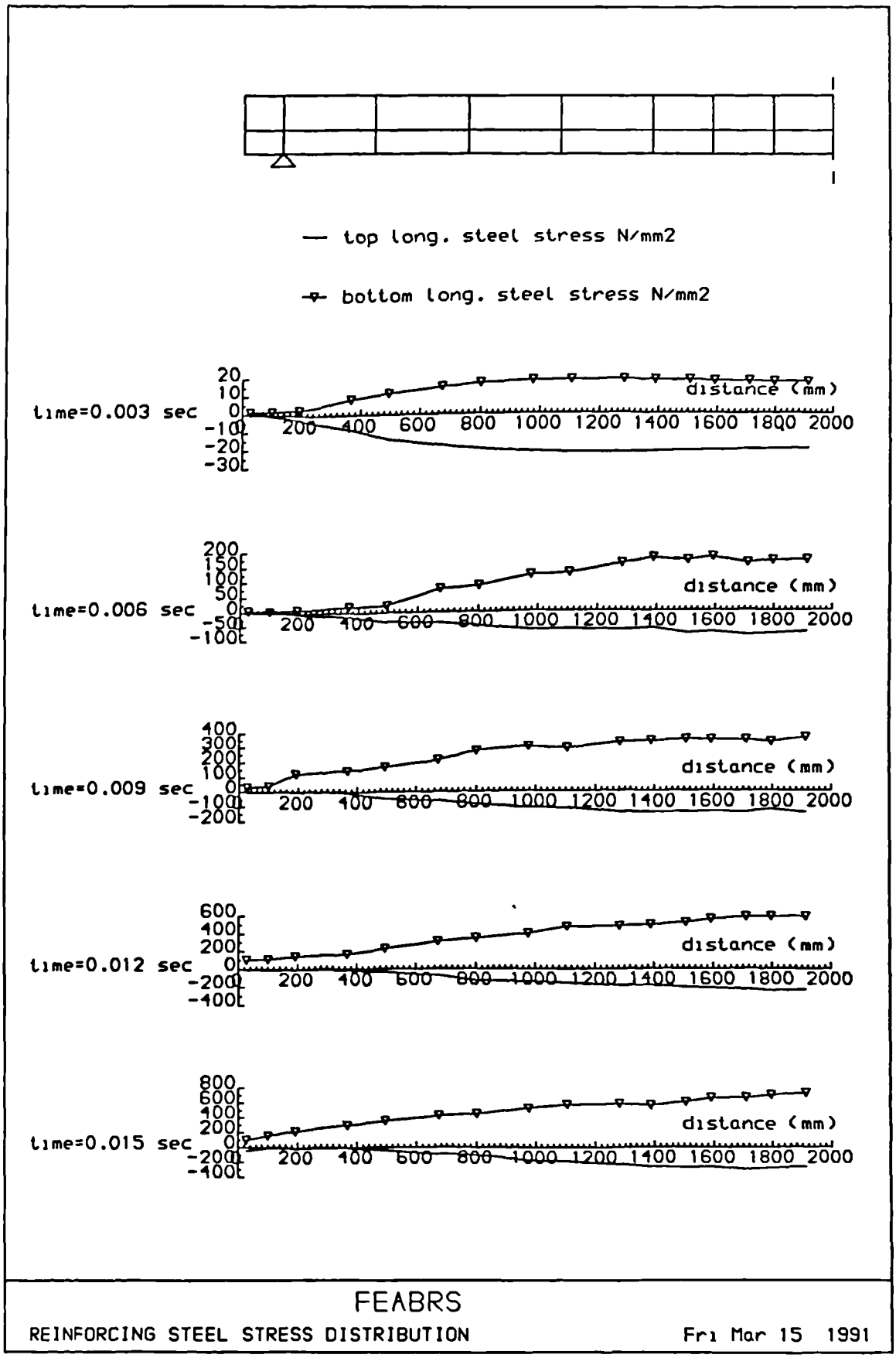

Figure 8.48: Stress distribution of reinforcing steel of Seabold's beam at various time stations

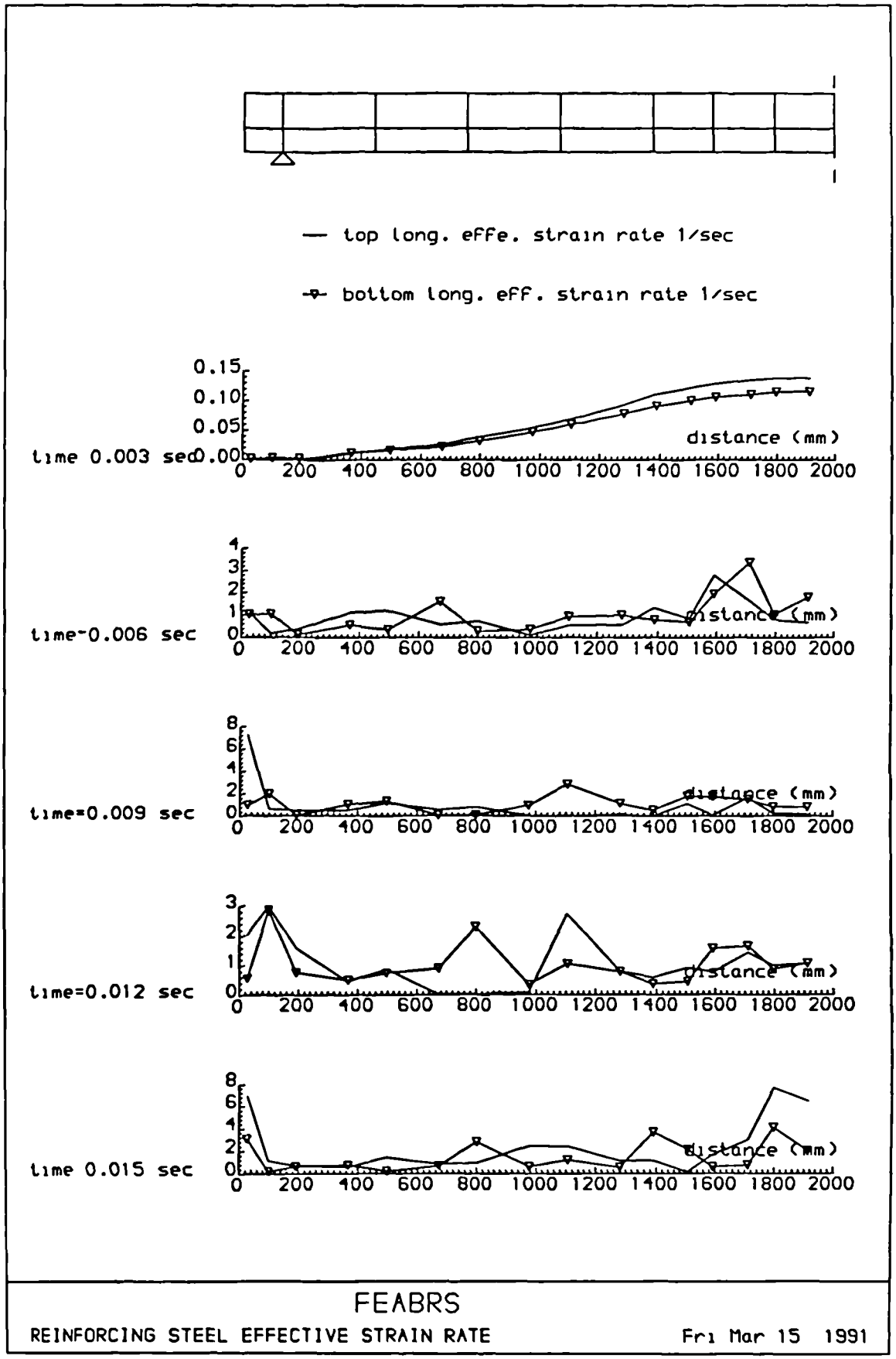

Figure 8.49: Effective strain rate distribution of reinforcing steel of Seabold's beam at various time stations

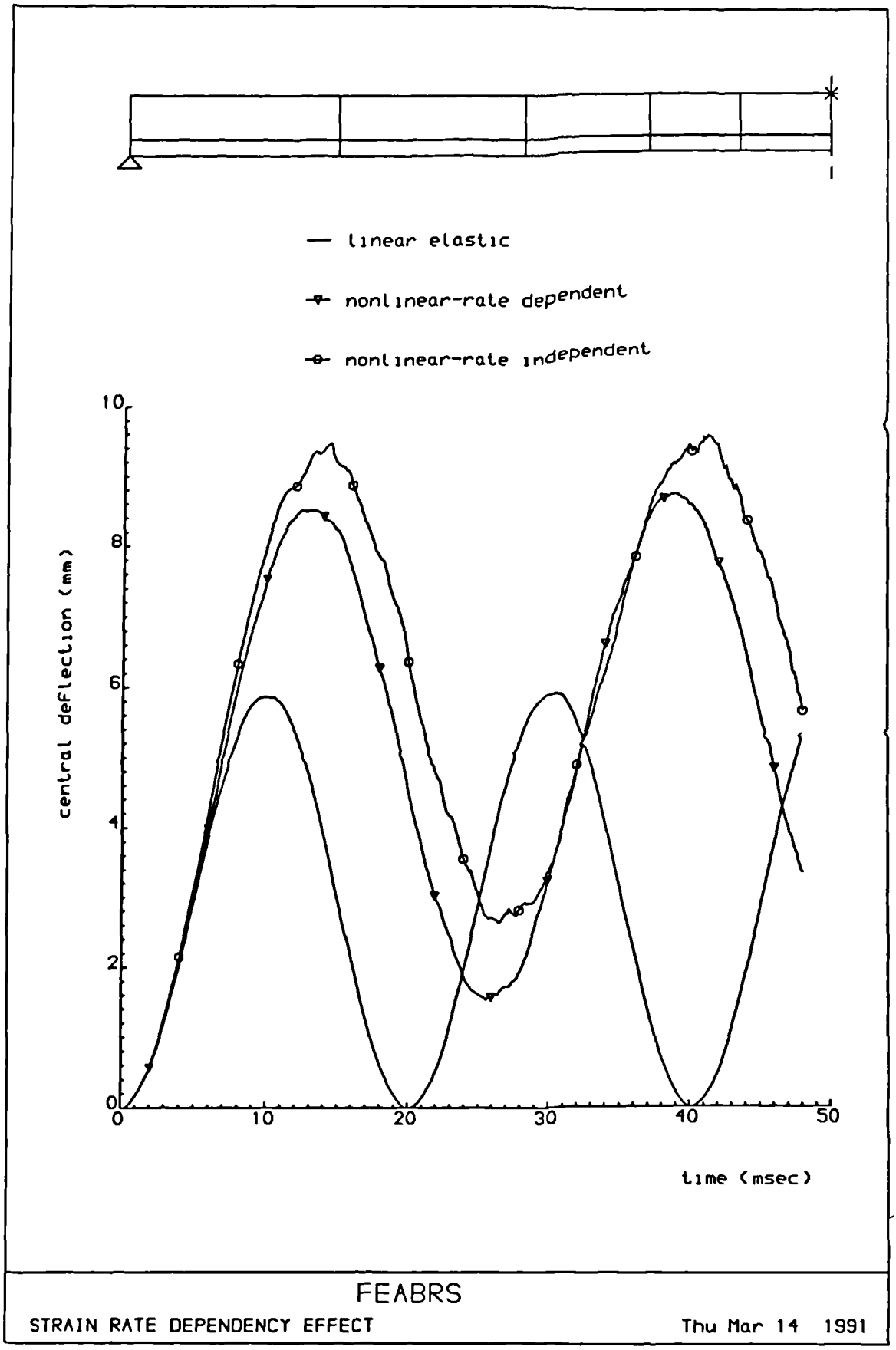

Figure 8.50: The effect of strain rate on the nonlinear response of Bathe's beam

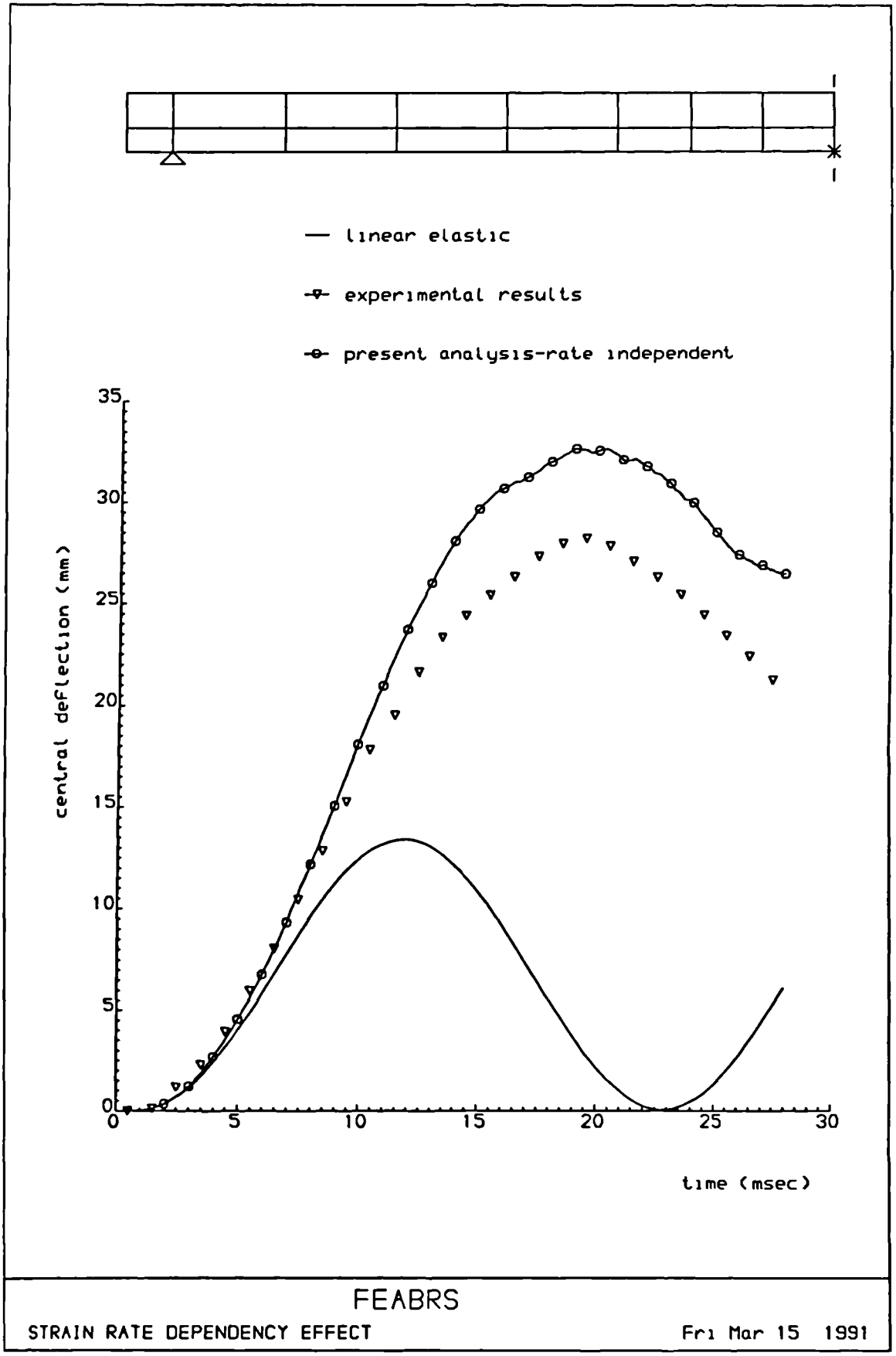

Figure 8.51: The effect of strain rate on the nonlinear response of Seabold's beam

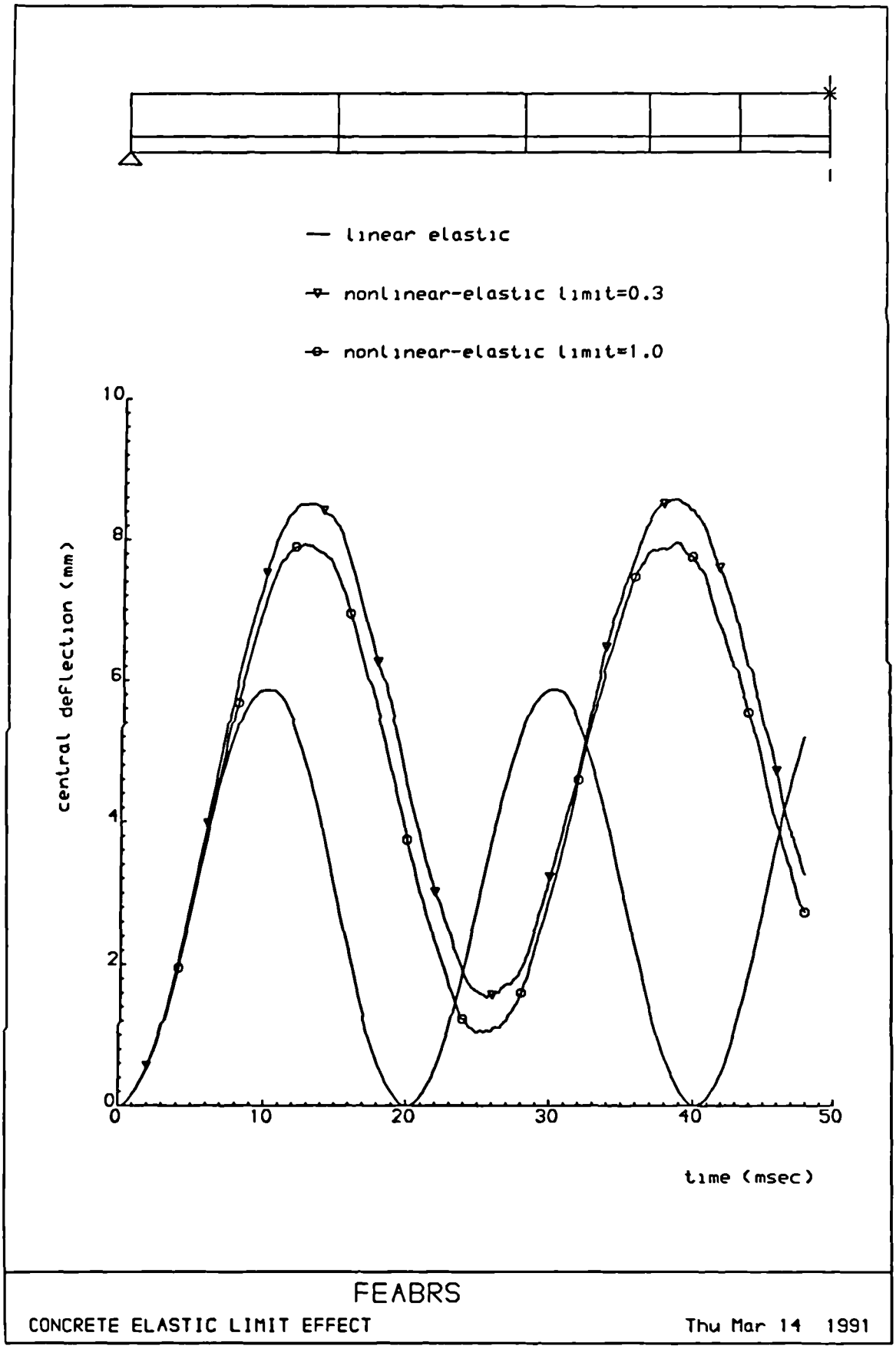

Figure 8.52: Influence of the elastic limit on the nonlinear response of Bathe's beam

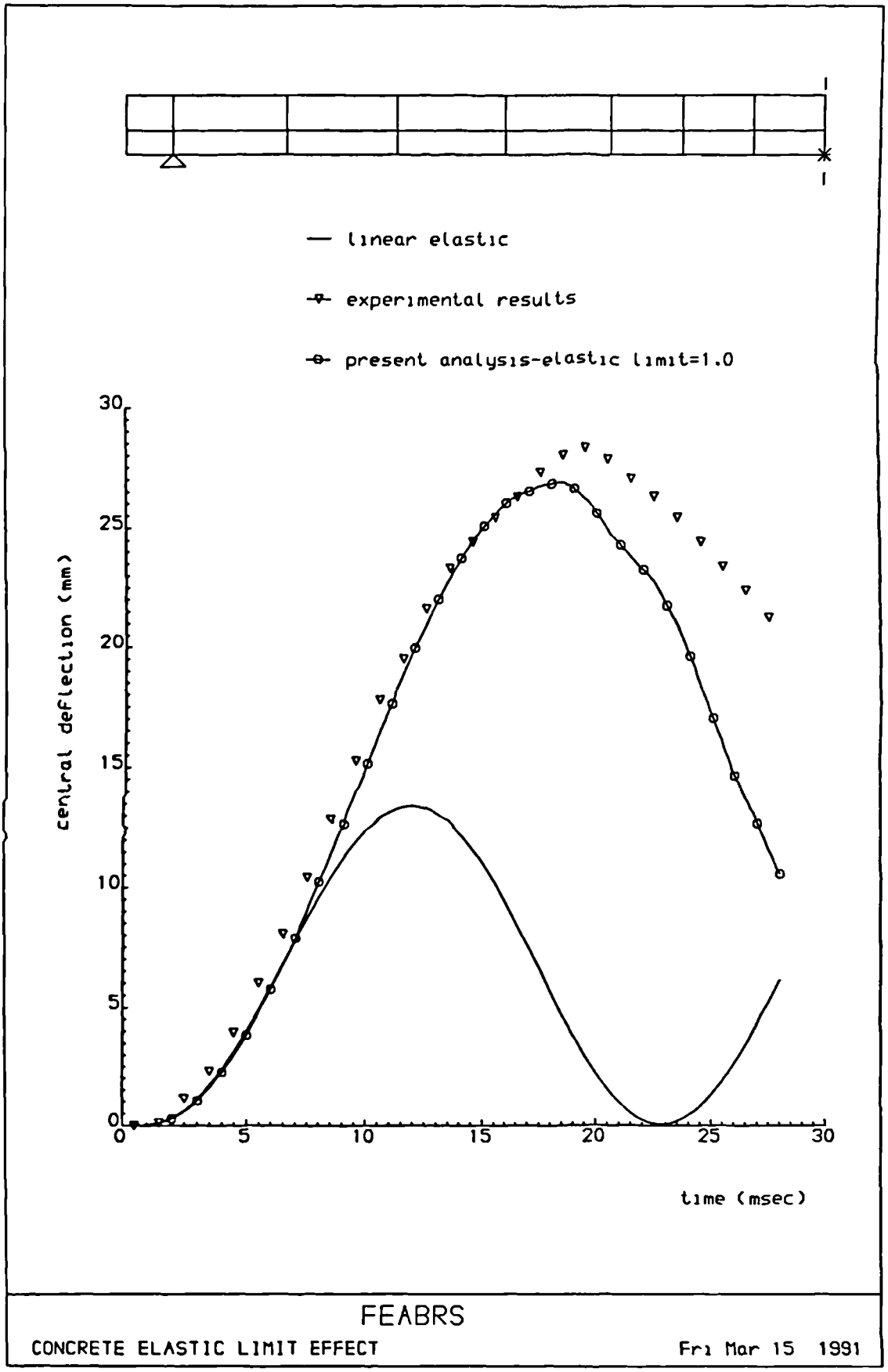

Figure 8.53: Influence of concrete elastic limit on the nonlinear response of Seabold's beam

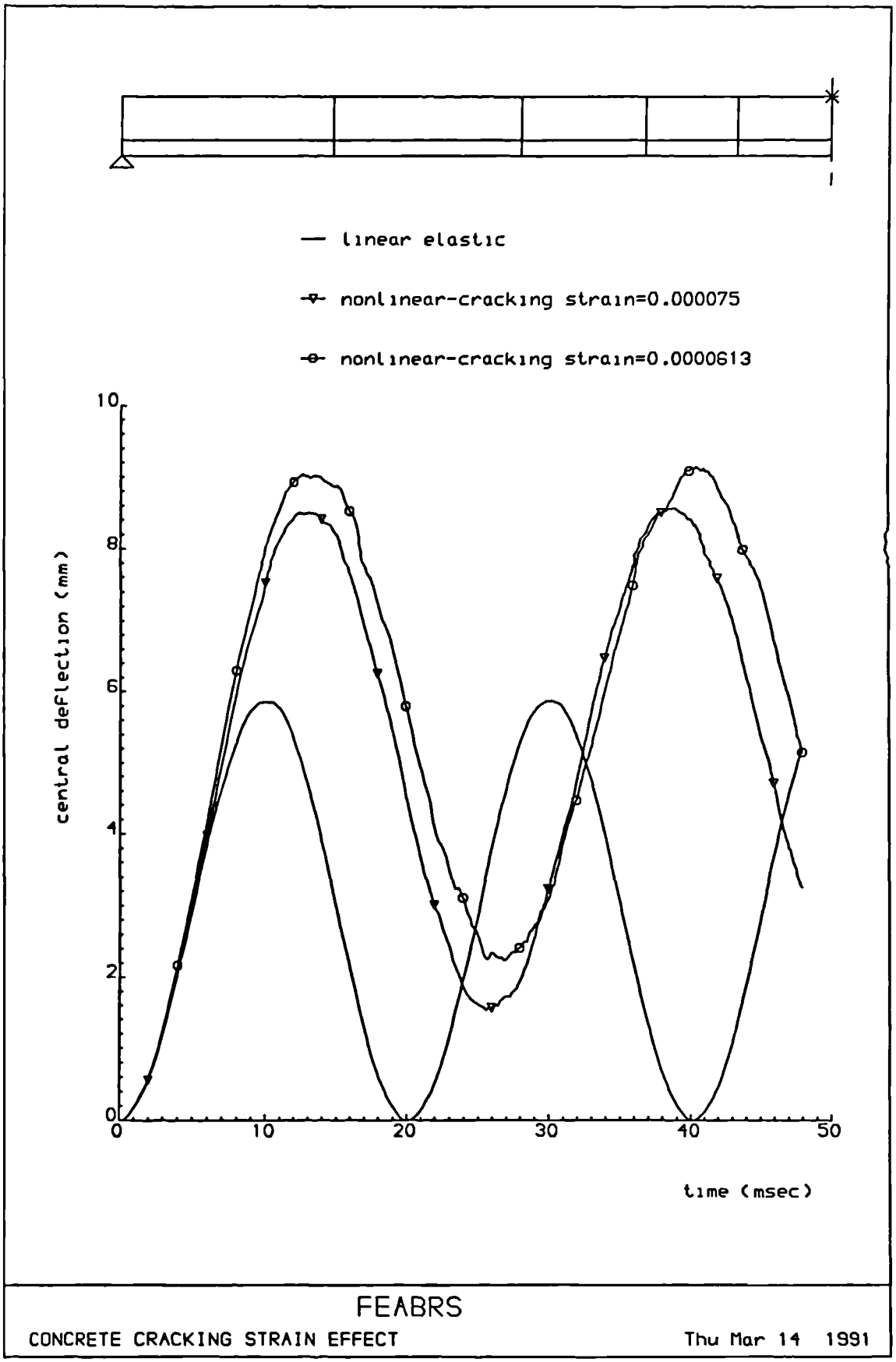

Figure 8.54: Nonlinear response of Bathe's beam for different cracking strains

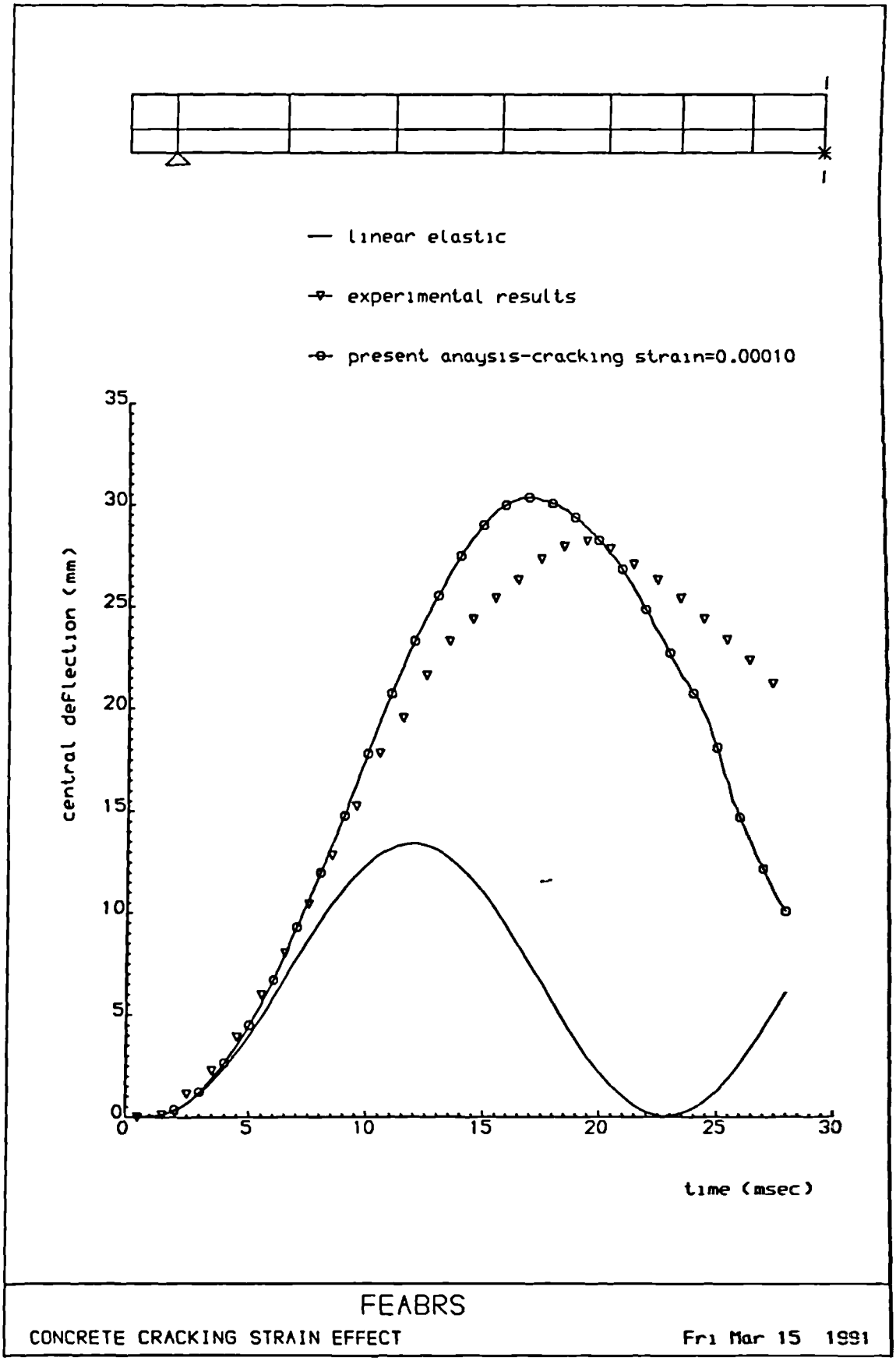

Figure 8.55: Nonlinear response of Seabold's beam for different cracking strains

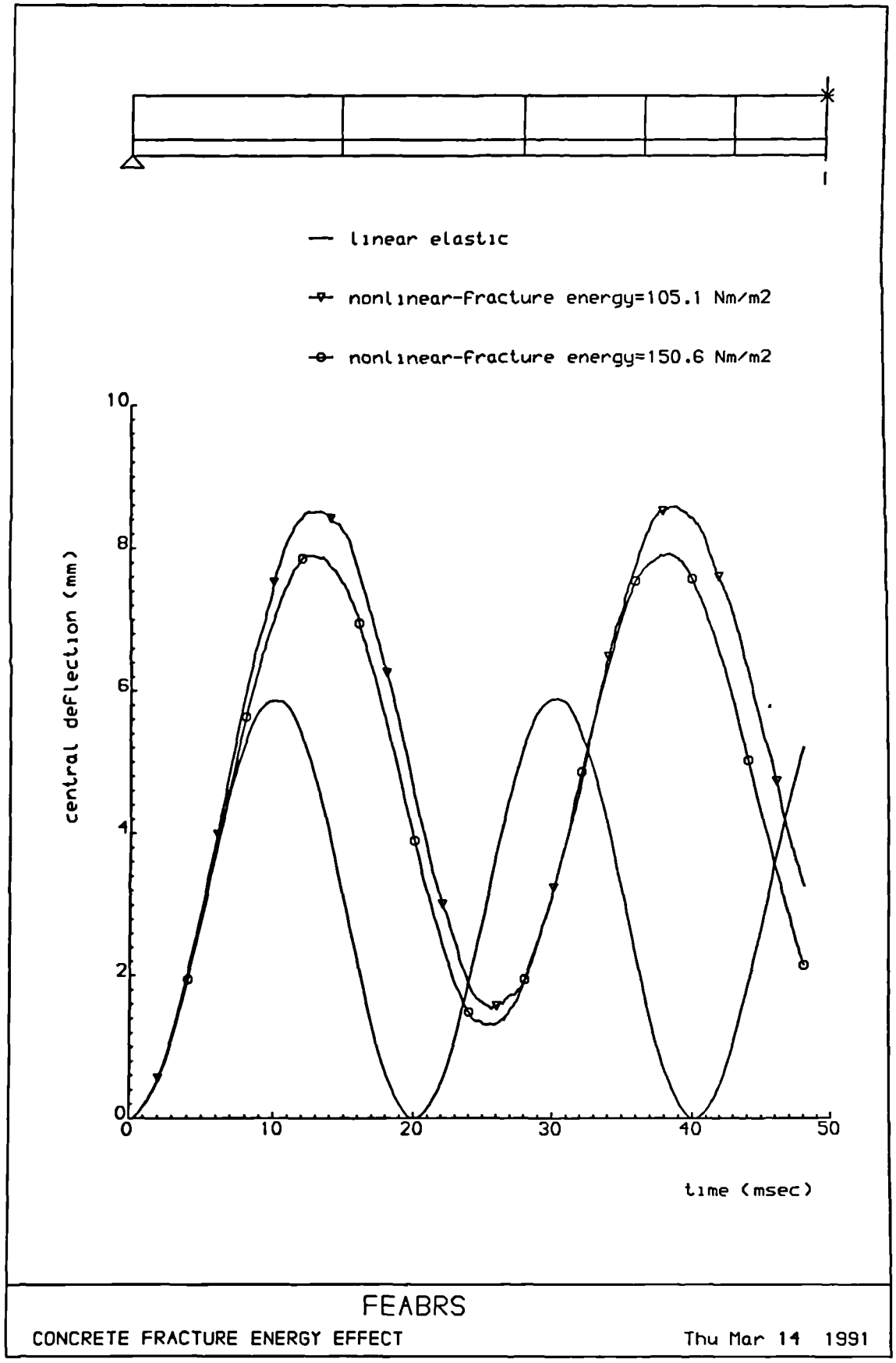

Figure 8.56: Influence of concrete fracture energy on nonlinear response of Bathe's beam

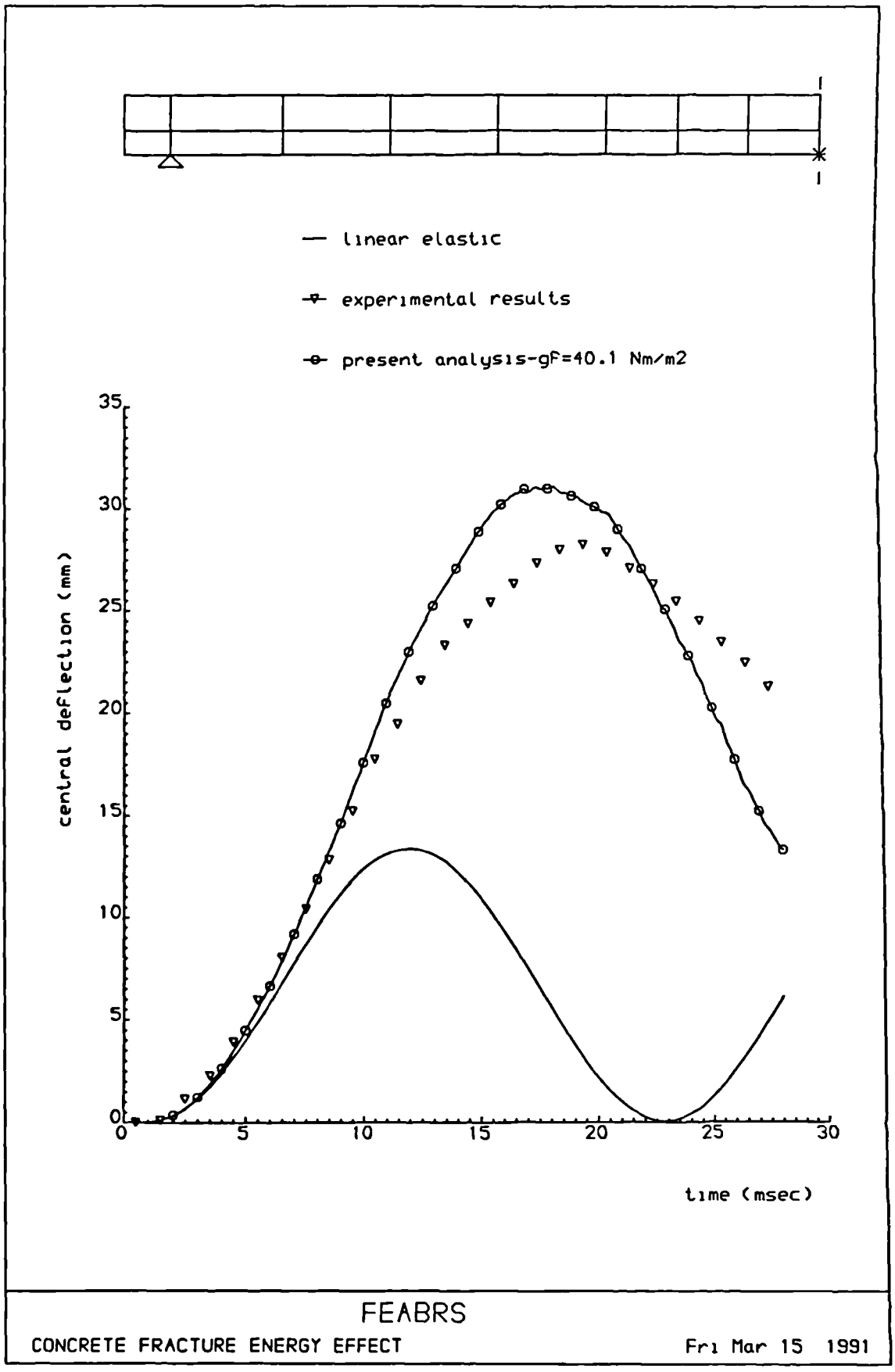

Figure 8.57: Influence of concrete fracture energy on nonlinear response of Seabold's beam

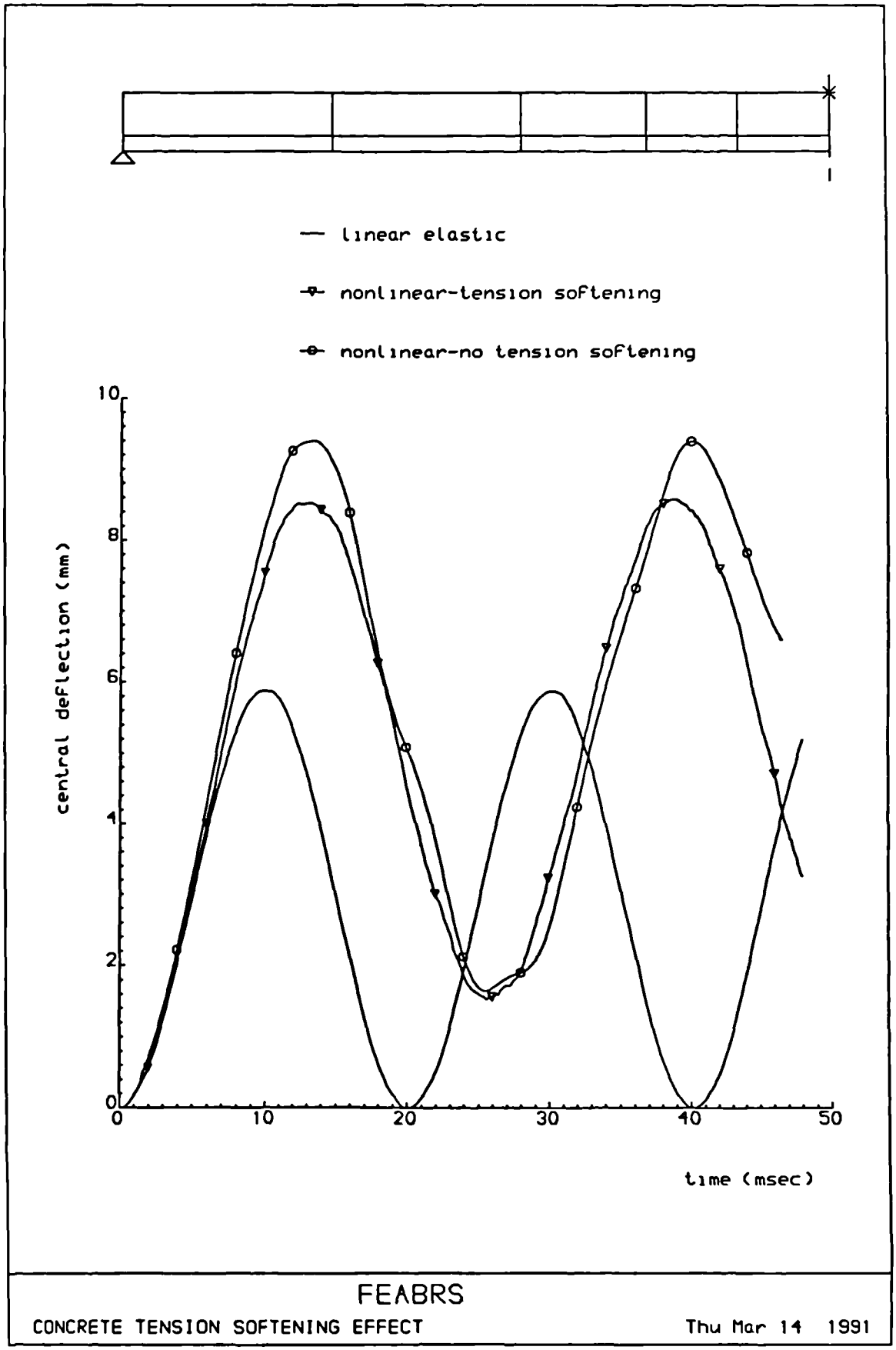

Figure 8.58: Nonlinear response of Bathe's beam as influenced by tension softening

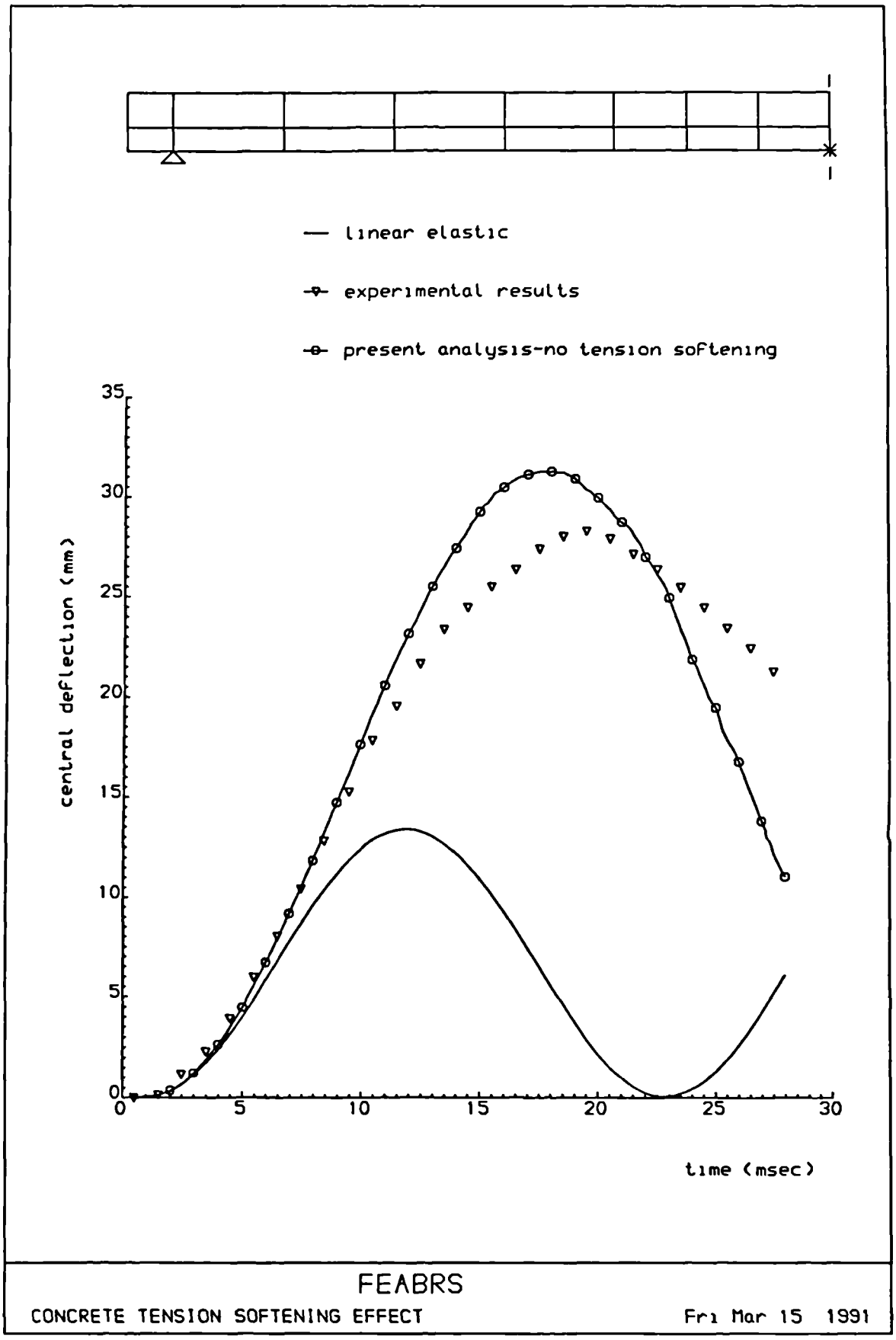

Figure 8.59: Nonlinear response of Seabold's beam as influenced by tensioning softening

CHAPTER 9

CONCLUSIONS AND RECOMMENDATIONS

9.1 GENERAL CONCLUSION

Finite element techniques for predicting the nonlinear dynamic response of plane and axisymmetric reinforced concrete structures subjected to blast and impulsive loading have been developed in this thesis. To establish the relationship between the physical structural system and the numerical model, the associated aspects of the engineering modelling process were examined and several contributions have been made in the areas which are less clearly understood. The main attention was focused on the development of appropriate history and rate dependent constitutive material models for concrete and steel. Methods for modelling blast loads have been extensively reviewed. Finite element procedures for the spatial discretization of the nonlinear dynamic equilibrium equations are adopted in accordance with isoparametric formulations. The explicit time integration schemes for the solution of equations of motion and the time rate dependent constitutive equations of concrete and steel have been derived. Numerical stability is ensured using energy balance check and suitable time increments throughout the step-by-step numerical integration process.

On the basis of the structures analysed it is concluded that the behaviour of typical planar and axisymmetric reinforced concrete structures under blast and impulsive loads are well simulated by the proposed computational models and solution procedures. The computer program, FEABRS, developed during the course of this work enables solution of various dynamic problems with confidence. In particular the deformations, stresses, strains, end reactions, cracking patterns, progressive fracture in concrete and yielding of steel at any stage of the loading-time history are determined with sufficient accuracy, subject only to a good knowledge of

the basic material properties. Material nonlinearities, namely crack propagation, stress and strain history dependency, concrete crushing, biaxial failure of concrete and post-failure residual strength, as well as the strain rate effects on the response of concrete and steel are allowed for in the method of analysis, consistent with expected modes of dynamic behaviour.

9.2 SPECIFIC CONCLUSIONS

9.2.1 MODELLING OF BLAST LOADS

1. General airblast phenomenon is presented along with discussion of TNT equivalency and blast scaling laws. From reviewing the available unclassified literature, prediction methods for modelling blast effects are considered. Blast due to nuclear weapons, conventional detonations, unconfined vapour cloud explosions, and confined gas and dust cloud deflagrations, are all reviewed.

2. The types of blast loads that can be produced on a concrete structure by an external explosion due to nuclear or conventional source are established as

* Side-on overpressure due to incident shock wave.
* Reflected overpressure on structure surfaces located in the direction of wave propagations.
* Dynamic pressure caused by the wind behind the wave front.
* Directly transmitted and airblast-induced ground shocks.

A number of commonly used formulae for predicting these loading components in the free field are presented along with their practical limitations. The distribution of the combined airblast pressures is defined for rectangular structures positioned above the ground surface. Given the expected difference in the time arrival of the various shocks to the structure, the directly transmitted ground shock can be ignored. For practical applications,

airblast-induced ground motion must necessarily be included.

3. The internal blast loads that can be caused by confined explosions are described as

* Short duration shock wave loading (for high explosives).
* Relatively long duration gas venting pressure (for high and low explosives).

The procedure and the necessary mathematical relationships are summarised for the prediction of the loading time histories. The effects of explosion containment and the venting process are included in such relations. The loading that arises from contact explosion on a structure and the minimum thickness of concrete required to resist spalling are given.

9.2.2 SPATIAL DISCRETIZATION

1. The development in this thesis has been limited to two-dimensional reinforced concrete structures.

2. The plane 8-noded isoparametric elements with quadratic variations of the field variables within each element have been chosen. Interpolation is based on Serendipity shape functions. In particular, special attention was paid to a correct simulation of crack propagation. Of special note is the smooth spread of cracking zones obtained and the ability of one element to reproduce two independent types of cracking modes during the analysis.

3. The use of Gaussian quadrature technique with the reduced 2 x 2 order for the numerical integration of the element forces proved to be a successful and computationally economical means of handling elastic and inelastic spatial domains within the same element. Moreover, it gives reasonable cracking patterns formed as a result of the partial release of the continuity requirements imposed by the shape functions.

4. The concept of reinforcing steel representation by embedded bars passing through the basic concrete elements was shown to give good results for a variety of dynamic analyses despite the perfect bond assumption. The use of equivalent membrane elements to simulate reinforcement under axisymmetric conditions was similarly proved valid.

9.2.3 MODELLING OF MATERIAL NONLINEARITY

To simulate the observed experimental evidence in the context of dynamic loading, it was found from the literature that the feasible classical theories for a realistic constitutive modelling of concrete or steel are the viscoplasticity and endochronic theories. For blast loading, rate and history dependent elasto-viscoplastic material models for concrete and steel have been developed in the thesis, along with a computational strategy for the concrete cracking process in which the effects of strain rate and post-cracking residual strength were included. Some numerical results have been presented which demonstrate the good performance of the proposed constitutive models and computer implementation. From the presentation of the examples, the following conclusions can be made:

1. It has been shown that detailed information about deflections, crack patterns, viscoplastic zones, principal stress fields, strain fields, etc, can be satisfactorily obtained. The results obtained were in good agreement with the results from previous numerical and experimental studies. A reasonable numerical simulation of the flexural and shear behaviour of planar and axisymmetric reinforced concrete structures under blast loading proved to be possible. It was concluded that compared with linear elastic response, material nonlinearities amplify displacements and elongate the effective period of vibration.

2. The inclusion of strain rate effects on the constitutive models of concrete and steel as well as the

strain rate-induced anisotropic influence, that is the difference in rate dependence in compression and tension for concrete, is essential for realistic nonlinear dynamic analysis of reinforced concrete structures under rapid loading conditions.

3. The modified theory of viscoplasticity developed within this thesis proved to be suitable for simulating the dynamic compressive behaviour of concrete. Viscoplastic response is controlled by two rate dependent bounding loading surfaces combined with rate sensitive hardening, softening and flow rules. The proposed loading criteria and the different rules governing the pre-failure and post-failure regimes are derived in simple mathematical form and predict stress-strain behaviour which is in good agreement with experimental results involving uniaxial and biaxial stress states [37]. Excluding the strain rate effect or including the strain hardening increases the predicted deflection and elongates the period of the structure.

4. The numerical results indicate that the modelling of concrete cracking process appears to be by far the most important source of material nonlinearity in the final model. Its representation is controlled by rate dependent crack initiation criterion and a fracture energy based nonlinear tension softening rule. The main advantage of such softening function is the objectivity of results with respect to element sizes. The parametric study showed that the structural response is sensitive to the crack initiation parameters (cracking strain and strain rate dependency) and the crack propagation parameters (fracture energy and tension softening). Decreasing the limiting cracking strain or fracture energy or ignoring the tension softening or strain rate effect results in higher deflections and longer periods.

5. Considering the spread of cracks through the reinforced concrete structures analysed in this work, at

different time stations, the algorithm developed for predicting and monitoring cracks produces reasonable crack patterns and operates with a relatively high degree of robustness. The development of vertical flexural cracks and diagonal shear cracks are in a good agreement with those reported in other sources, [78, 239].

6. Examinations of the crack development history in the numerical analyses supports the following conclusions:

a) Displaying only full cracks, i.e. cracks for which the normal strain is beyond the ultimate strain of the tensile softening branch, may be necessary to reveal any fracture localisation in the structure behaviour as well as to avoid any misunderstanding in the interpretation of predicted numerical crack patterns.

b) The proposed smeared crack formulation was capable of predicting strain localisation phenomenon which was in close agreement with the experimental observations, [239]. It was noticed that at first concrete exhibited a number of flexural cracks which were suddenly overshadowed by the occurrence of major shear cracks. Later, some integration points may exhibit secondary flexural cracks which were arrested or even closed further in the analysis as a result of simultaneous loading and unloading associated with the fracture localisation problems.

c) The presence of reinforcement in a concrete member stabilises each tensile crack by limiting its propagation. An example of a stable crack is the vertical crack originating at the tensile face of a beam in a region of pure moment. In a region of combined moment and shear, a typical crack originates in flexure in a stable manner, but the curved nature of cracks in this region leads such cracks to zones of higher stresses and strains and instability of the crack propagation may occur.

7. The plotted contour maps indicate that redistribution of stress components and strain rate field was well predicted with the process of cracking in concrete. For beams, a pronounced thrust arch is observed in concrete and is in equilibrium with the main tensile reinforcement. This action represents a tied-arch equilibrium system.

8. The validity of the proposed model for steel as a strain rate dependent uniaxial elasto-viscoplastic material with linear strain hardening was demonstrated through the analyses of reinforced concrete beams and a circular slab. The history of steel stress, strain and strain rate as well as the influence of concrete cracking on the variation of reinforcement stress is satisfactorily simulated. As expected, peak steel stresses and high strain rate values were found near the critical regions of the structure and at the cracked cross-sections.

9.2.4 TIME DISCRETIZATION AND SOLUTION TECHNIQUES

1. A modified form of explicit central difference operator was developed for the time integration of semi-discretized dynamic equilibrium equations in order to advance the nodal displacements, velocities and accelerations. Such scheme has been extensively employed in this thesis for the linear and nonlinear dynamic analysis of reinforced concrete structures with success. In addition to the generality, it also results in efficient and economic architecture for programming.

2. For path and rate-dependent materials proposed here, reduced values of the limiting time steps, postulated by previous researchers for the numerical stability of explicitly integrated equations of motion, have been used. From many computations carried out, a reduction factor varying between 0.2 and 0.4 was found to be necessary to account for the discretizing effects, of round-off errors, and rapidly varying material properties as well as to limit the speed with which the cracks spread throughout the structure. However, the inclusion of energy balance check

to guard against arrested instability errors induced by dissipative mechanisms of concrete and steel behaviour was essential.

3. The Euler explicit time integration scheme for the first order time rate dependent constitutive equations of concrete and steel in combination with suitable stability conditions for the definition of time increments proves to be efficient in tackling complex material behaviour and is also economical in computational effort.

4. Semi-empirical *a priori* stability criteria relating to the Euler explicit algorithm have been derived on the basis of the theoretical and experimental considerations for concrete and steel. In practice, such criteria represent an upper limit for the critical time step length which provides a stable and accurate solution for the elasto-viscoplastic response of reinforced concrete structures.

9.3 RECOMMENDATIONS FOR FUTURE WORK

Some recommendations for further improvement of the proposed numerical techniques, and possible extensions of these investigations are summarised below:

1. The applicability of the present numerical model for the plane and axisymmetric analyses could be extended by

   a) Introducing an initial loading procedure to account for the effect of prestressing, thus enabling dynamic analysis of prestressed concrete structures.

   b) Generalising the representation of steel components in axisymmetric problems by developing point and bar elements in addition to the membrane ones.

   c) Implementing geometric nonlinearity for thin structures sensitive to instability problems.

2. The application of the numerical model to general 3-dimensional cases, which would first require the development of constitutive material models and numerical

approach to cracking valid for such studies. Search for a new loading surface of the constitutive model presented here which fits the triaxial experimental data would also be needed. It may become necessary, at this stage, to consider the production of a simplified version of the computer program FEABRS since computing costs for nonlinear dynamic 3-dimensional problems are likely to rise sharply when compared with those relating to planar and axisymmetric applications.

3. The material models developed here can be extended to include some aspects of reinforced concrete behaviour not considered in this study, e.g.

a) The assumption of isotropic hardening can be too simple for pronounced cyclic deformation situations, and a more sophisticated hardening model may be necessary.

b) The significance of different hardening functions suited for steel reinforcement can be investigated.

c) The inclusion of a realistic law describing bond-slip behaviour between concrete and steel under dynamic loading may also be a subject for further work. However, this will require a reformulation of the bar and membrane elements used in this work. Also the relation between bond-slip effect and tension stiffening behaviour has to be investigated.

d) The aggregate interlock and dowel bar mechanisms used in the crack interface may be improved by employing more sophisticated models [240].

4. Some features of the constitutive concrete model presented in this thesis are clearly extrapolations from uniaxial state, where validity and limitations are not easy to define due to the complexity and insufficient knowledge of concrete behaviour under biaxial dynamic conditions. Investigation of the accuracy and efficiency of the present model can only be based on extensive experimental research

on concrete behaviour in biaxial state of stress under dynamic loading conditions. Experimental data for the rate and history-dependency of the material behaviour in the pre-failure and post-peak regimes should be made available.

5. Recently it has been recommended [241] that strain-rate dependent data can be characterised in strain space better than using traditional stress based failure criteria. Therefore, an experimental and analytical dynamic investigation is needed to generate more data in order to develop the criteria which would produce a family of response surfaces in strain space as a function of strain rate and strain history.

6. Since the solution procedures of reinforced concrete structures at present are relatively expensive in terms of computer time, alternative approaches may be used for improving the efficiency of the dynamic analysis computations.

a) Mixed time integration schemes such as explicit-explicit subcycling procedure [222] can be employed for the finite element dynamic analysis. This is accomplished by separating the elements or nodes into element size based-groups and assigning a different time step to each group which is dependent only on the frequencies of the elements in that group.

b) For large scale reinforced concrete structures, the nonlinear dynamic analysis using substructure technique [93] may be adopted in which the method of analysis takes advantage of direct time integration and modal analysis in such a way that the computational work is focused on the important parts of the structure.

c) One point integration technique may be used to evaluate each element matrices and contributions in the analysis. Such a procedure has been successfully used with the linear quadrilateral isoparametric element [242]. However, the principal disadvantage of

this technique is the generation of unstable zero-energy deformation modes. The inclusion of the hourglass control techniques is unavoidable for numerical stability.

7. Undoubtedly, it is possible to refine and extend the computer program FEABRS in several ways in order to make it more efficient and versatile. Some useful modifications may be mentioned here:

a) An interactive system identification module, with graphical displays, needs to be developed to enable proper description of model behaviour.

b) A post-processing module, with interactive graphics, needs to be developed so that the results of the response analysis may be visualised in a graphical form.

c) Extension of the computer code by including the well known material models of cracking and compressive behaviour so that any combinations could be selected at will.

8. There is considerable research to be done to enable a reasonable assessment to be made of the loading function for confined gas and dust cloud deflagrations as well as unconfined vapour cloud explosions. Containment of explosions and venting will necessarily depend upon the structural system but a great deal of information is needed for careful analysis.

9. When the blast wave due to high explosive impinges upon a structural system, it is immediately modified by reflection enhancement followed by vortex formation and rarefaction wave movements as the blast wave moves over the structure. As a result of complexity of the process, further research is needed to make a reasoned judgment of the variations of pressure with time and space for response analysis.

REFERENCES

1. *Hopkinson, B.* (1915). "British Ordnance Board Minutes 13565".

2. *Christopherson, D.G.* (1945). "Structural Defence", British Ministry of Home Security.

3. *White, M.T.* (1946). "Effects of Impacts and Explosions", Summary Technical Report of Division 2, National Defence Research Council, Volume 1, Washington, D.C., AD221-586.

4. *Whitney, C.S., Anderson, B.G., and Cohen, E.* (1955). "Design of Blast Resistant Construction for Atomic Explosions", ACI Journal, Volume 51, No.7, pp. 589-684.

5. *Newmark, N.M.* (1956) "Analysis and Design of Structures to resist Atomic Blast", Bulletin, Virginia Polytechnic Inst. Eng. Experiment Station, Volume 106, Part 2, pp. 49-77.

6. *Ngo, D., and Scordelis, A.C.* (1967). "Finite Element Analysis of Reinforced Concrete Beams", ACI Journal, Volume 64, No.3, pp. 152-163.

7. *Mainstone, R.J.* (1975). "Properties of Materials at High Rates of Straining or Loading", Material and Structures (Paris), Volume 8, No.44, pp. 102-116.

8. *Suaris, W., and Shah, S.P.* (1982). "Mechanical Properties of Materials subjected to Impact", Introductory Report, RILEM/IABSE/CEB/IASS Symposium on Concrete Structures under impact and impulsive loading, Berlin (West), pp. 33-61.

9. *Takeda, J., and Tachikawa, H.* (1971). "Deformation and Fracture of Concrete Subjected to Dynamic Load", Proceedings of the International Conf. on mechanical behaviour of materials, Volume IV, Kyoto, Aug. 15-20, pp. 267-277.

10. *Cowell, W.* (1966). "Dynamic Properties of Plain Portland Cement Concrete", Technical Report No. R447, U.S. Naval Engineering Laboratory, Port Hueneme, California.

11. *Mellinger, F.M., and Birkimer, D.L.* (1966). "Measurements of Stress and Strain on Cylindrical Test Specimens and Concrete under Impact Loading", Technical Report No. 4-46, Dept. of the Army, Ohio River Division Laboratories.

12. *Kormeling, H.A., Zielinski, A.J., and Reinhardt, H.W.* (1980). "Experiments on Concrete under Single and Repeated Impact Loading", Report No. 5-80-3, Delft Univ. of Technology, Stevin Laboratory.

13. *Hughes, B.P., and Gregory, R.* (1972). "Concrete subjected to high rates of Loading in Compression", Magazine of Concrete Research, Volume 24, No. 78, pp. 25-36.

14. *Sparks, P.R., and Menzies, J.B.* (1973). "The Effect of Rate of Loading upon the Static and Fatigue Strengths of Plain Concrete in Compression", Magazine of Concrete Research, Volume 25, No. 83, pp. 73-80.

15. *Atchley, B.L., and Furr, H.L.* (1967). "Strength and Energy Absorption Capabilities of Plain Concrete under Dynamic and Static Loading", ACI Journal, Volume 64, No. 11, pp. 745-756.

16. *Watstein, D.* (1953). "Effect of Straining Rate on the Compressive Strength and Elastic Properties of Concrete", ACI Journal, Volume 49, No. 8, pp. 729-744.

17. *Hatano, T., and Tsutsumi, H.* (1960). "Dynamical Compressive Deformation and Failure of Concrete under Earthquake Load", Proceedings, 2nd World Conf. on Earthquake Engng., Tokyo, pp. 1963-1978.

18. *Dilger, W.H., Koch, R., and Kowalczyk, R.* (1984). "Ductility of Plain Concrete and Confined Concrete under different Strain Rates", ACI Journal, Volume 81, No. 1, pp. 73-81.

19. *Scott, B.D., Park, R., Priestley, M.J.N.* (1982). "Stress Strain Behaviour of Concrete Confined by Overlapping Hoops at Low and High Strain Rates", ACI Journal, Volume 79, No. 1, pp. 13-27.

20. *Soroushian, P., Choi, K., and Alhamad, A.* (1986). "Dynamic Constitutive Behaviour of Concrete", ACI Journal, Volume 83, No. 2, pp. 251-259.

21. *Chen, W.F.* (1982). "Plasticity in Reinforced Concrete", McGraw-Hill.

22. *Neville, A.M.* (1977). "Properties of Concrete", Pitman, London.

23. *Popovics, S.* (1969). "Fracture Mechanism in Concrete: how much do we know?", J. Eng. Mech. Div., ASCE, Volume 95, No. 3, pp. 531-544.

24. *Wasteils, J.* (1979). "Behaviour of Concrete under Multiaxial Stresses - A Review", Cement and Concrete Research, Volume 9, pp. 33-44.

25. *Hsu, T.T.C., Slate, F.O., Sturman, G.M., and Winter, G.* (1963). "Microcracking of Plain Concrete and the Shape of the Stress Strain Curve", ACI Journal, Volume 60, No. 2, pp. 209-224.

26. *Shah, S.P., and Winter, G.* (1966). "Inelastic Behaviour and Fracture of Concrete", ACI Journal, Volume 63, No. 9, pp. 925-930.

27. *Damjanic, F.B.* (1983). "Reinforced Concrete Failure Prediction under both Static and Transient Conditions", Ph.D Thesis, C/Ph/71/83, Univ. College of Swansea, Dept. of Civil Engng.

28. *Nilsson, L.* (1979). "Impact Loading on Concrete Structures - A Constitutive Modelling - Finite Element Analysis and Experimental Study of Nonlinear Wave Propagation", Chalmers Univ. of Technology, Publication 79:1.

29. *Hsu, T.T.C.* (1963). "Mathematical Analysis of Shrinkage Stresses in a Model of Hardened Concrete", ACI Journal, Volume 60, No. 3, pp. 371-390.

30. *Hsu, T.T.C., and Slate, F.O.* (1963). "Tensile Bond Strength between Aggregate and Cement Paste of Mortar", ACI Journal, Volume 60, No. 4, pp. 465-486.

31. *Zielinski, A.J., and Reinhardt, H.W.* (1982). "Impact Stress-Strain Behaviour of Concrete in Tension", Proceedings of RILEM/CEB/IABSE/AISS Symposium on Concrete Structures under Impact and Impulsive Loading", Berlin (West), pp. 112-124.

32. *Kotsovos, M.D., and Newman, J.B.* (1977). "Behaviour of Concrete under Multiaxial Stress", ACI Journal, Volume 74, No. 9, pp. 443-446.

33. *Rusch, H.* (1960). "Researches towards a general Flexural Theory for Structural Concrete", ACI Journal, Volume 57, No. 1, pp. 1-28.

34. *Liu, G.Q.* (1985). "Nonlinear and Transient Finite Element Analysis of general Reinforced Plates and Shells", Ph.D Thesis, C/Ph/84/85, Univ. College of Swansea, Dept. of Civil Engng.

35. *Hughes, B.P., and Chapman, G.P.* (1966). "The Complete Stress Strain Curve for Concrete in Direct Tension", RILEM Bulletin, No. 30, pp. 95-98.

36. *Welch, G.B.* (1966). "Tensile Strains in Unreinforced Concrete Beams", Magazine of Concrete Research, Volume 18, No. 54, pp. 9-18.

37. *Kupfer, H., Hilsdorf, H.K., and Rusch, H.* (1969). "Behaviour of Concrete under Biaxial Stresses", ACI Journal, Volume 66, No. 8, pp. 656-666.

38. *Andenaes, E., Girstle, K., and Ko, H.Y.* (1977). "Response of Mortar and Concrete to Biaxial Compression", J.Eng. Mech. Div., ASCE, Volume 103, No. 4, pp. 515-526.

39. *Tasuji, M.E., Slate, F.O., and Nilson, A.H.* (1978). "Stress-Strain Response and Fracture of Concrete in Biaxial Loading", ACI Journal, Volume 75, No. 7, pp. 306-312.

40. *Gerstle, K.H. et al.* (1980). "Behaviour of Concrete under Multiaxial Stress States", J.Eng. Mech. Div., ASCE, Volume 106, No. 6, pp. 1383-1403.

41. *Wastiels, J.* (1979). "Failure Criteria for Concrete under Multiaxial Stress States", IABSE Colloquium on Plasticity in Reinforced Concrete, IABSE Report V29, Copenhagen, pp. 3-10.

42. *Figueiras, J.A.* (1983). "Ultimate Load Analysis Anisotropic and Reinforced Concrete Plates and Shells", Ph.D Thesis, C/Ph/72/83, Univ. College of Swansea, Dept. of Civil Engng.

43. *Chen, A.C.T., and Chen, W.F.* (1975). "Constitutive Relations for Concrete", J.Eng. Mech. Div., ASCE, Volume 101, No. 4, pp. 465-481.

44. *Richardt, F.E., and Brandtzaeg, A., and Brown, R.L.* (1928). "A Study of the Failure of Concrete under Combined Compressive Stresses", Bulletin No. 185, University of Illinois, Engng. Expt. Station, Urbana, pp. 1-102.

45. *Millis, L.L., and Zimmerman, R.M.* (1970). "Compressive Strength of Plain Concrete Multiaxial Loading Conditions", ACI Journal, Volume 67, No. 10, pp. 802-807.

46. *Green, S.J., and Swanson, S.R.* (1973). "Static Constitutive Relations for Concrete", Air Force Weapons Lab., Technical Report No. AFWL-TR-72-2, Kirtland, AFB, USA.

47. *Palaniswamy, R., and Shah, S.P.* (1974). "Fracture and Stress-Strain Relations for Concrete under Triaxial Compression", J. Struct. Div., ASCE, Volume 100, No. 5, pp. 901-915.

48. *Willam, K.J., and Warnke, E.P.* (1974). "Constitutive Model for the Triaxial Behaviour of Concrete", IABSE Seminar on Concrete Structures Subjected to Triaxial Stresses, Paper III-1, Bergamo, Italy.

49. *Ottoson, N.S.* (1977). "A Failure Criterion for Concrete", J.Eng. Mech. Div., ASCE, Volume 103, No. 4, pp. 527-535.

50. *Suaris, W.* (1983). "Dynamic Behaviour of Concrete - a Phenomenological Theory and Instrumented Impact Testing", Ph.D Dissertation, Northwestern Univ., Evanston, Illinois, Dept. of Civil Engng.

51. *Nelissen, L.J.M.* (1972). "Biaxial Testing of Normal Concrete", Heron, Volume 18, No. 1.

52. *Nilson, H.* (1968). "Nonlinear Analysis of Reinforced Concrete by the Finite Element Method, ACI Journal, Volume 65, No. 9, pp. 757-766.

53. *Kupfer, H.B., and Gerstle, K.H.* (1973). "Behaviour of Concrete under Biaxial Stresses", J.Eng. Mech. Div., ASCE, Volume 99, No. 4, pp. 853-866.

54. *Coon, M.D., and Evans, R.J.* (1972). "Incremental Constitutive Laws and their associated Failure Criteria with application to Plain Concrete", Int. J. Solids and Structures, Volume 8, pp. 1169-1183.

55. *Gerstle, K.H.* (1981). "Simple Formulation of Biaxial Concrete Behaviour", ACI Journal, Volume 78, No. 1, pp. 62-68.

56. *Gerstle, K.H.* (1981). "Simple Formulation of Triaxial Concrete Behaviour", ACI Journal, Volume 78, No. , pp. 382-387

57. *Ottosen, N.S.* (1979). "Constitutive Model for Short Time Loading of Concrete", J.Eng. Mech. Div., ASCE, Volume 105, No. 1, pp. 127-141.

58. *Liu, T.C.Y., Nilson, A.H., and Slate, F.O.* (1972). "Biaxial Stress-Strain Relations for Concrete", J. Struct. Div., ASCE, Volume 99, No. 5, pp. 1025-1034.

59. *Darwin, D., and Pecknold, D.A.* (1976). "Analysis of R/C Shear Panels under Cyclic Loading", J. Struct. Div., ASCE, Volume 102, No. 2, pp. 355-369.

60. *Elwi, A.A., and Murry, D.W.* (1979). "A 3D Hypoelastic Concrete Constitutive Relationship", J.Eng. Mech., ASCE, Volume 105, No. 4, pp. 623-641.

61. *Bazant, Z.P.* (1983). "Comments on Orthotropic Models for Concrete and Geometricals", J.Eng. Mech. Div., ASCE, Volume 109, No. 3, pp. 849-865.

62. *Pal, N.* (1976). "Seismic Cracking of Concrete Gravity Dams", J. Struct. Div., ASCE, Volume 102, No. 9, pp. 1827-1845.

63. *Pozzo, E.* (1970). "Rhelogical Model of Concrete in the Dynamic Field", Meccanica, pp. 143-158.

64. *Bazant, Z.P., and Oh, B.H.* (1980). "Strain Rate Effect in Rapid Nonlinear Triaxial Deformation of Concrete", Report No. 80-81/640S, Dept. of Civil Engng., Northwestern Univ., Evanston.

65. *Bazant, Z.P., and Kim, S.S.* (1979). "Plastic Fracturing Theory for Concrete", J.Eng. Mech. Div., ASCE, Volume 105, No. 3, pp. 407-428.

66. *Oh, B.H.* (1987). "Behaviour of Concrete under Dynamic Tensile Loads", ACI Journal, Volume 84, No. 7, pp. 8-13.

67. *Chen, W.F., and Ting, E.C.* (1980). "Constitutive Models for Concrete Structures", J.Eng. Mech. Div., ASCE, Volume 106, No. 1, pp. 1-19.

68. *Prager, W.* (1956). "A New Method of Analysing Stress and Strain in Work Hardening Plastic Solids", J.appl. Mech., Volume 23, pp. 493-496.

69. *Ziegler, H.* (1959). "A Modification of Prager's Hardening Rule", Qurt. Appl. Math., Volume 17, pp. 55-60.

70. *Dafalias, Y.F., and Popov, E.P.* (1975). "A Model of Nonlinearly Hardening Materials for Complex Loading", Acta Mechanica, Volume 21, pp. 173-192.

71. *Argyris, J.H., Faust, G., Szimmat, J., Warnke, E.P., and Willam, K.J.* (1974). "Recent Developments in the Finite Element Analysis of Prestressed Concrete Reactor Vessels", Nucl. Engng. Design, Volume 28, pp. 42-75.

72. *Han, D.J., and Chen, W.F.* (1985). "A Non-uniform Hardening Plasticity Model for Concrete Materials", Mech. of Materials, Volume 4, pp. 283-302.

73. *Chen, W.F., and Suzuki, H.* (1980). "Constitutive Models for Concrete", Computers and Structures, Volume 12, pp. 23-32.

74. *Buyukozturk, O.* (1977). "A Constitutive Model for Concrete in Compression", Proceedings of 3rd ASCE Engineering Mechanics Division Speciality Conf., Austin.

75. *Han, D.J., and Chen, W.F.* (1986). "Strain Space Plasticity Formulation Hardening-Softening Materials with Elastoplastic Coupling", Int. J. Solids and Structures, Volume 22, pp. 935-950.

76. *Perzyna, P.* (1966). "Fundamental Problems in Viscoplasticity", Advances in Applied Mechanics, Volume 9, Academic Press, N.Y., pp. 243-377.

77. *Bicanic, N.* (1978). "Nonlinear Finite Element Transient Response of Concrete Structures", Ph.D Thesis, C/Ph/50/78, Univ. College of Swansea, Dept. of Civil Engng.

78. *Cervera, M., Hinton, E., and Bicanic, N.* (1988). "Nonlinear Transient Dynamic Analysis of Three-dimensional Structures - A Finite Element Model for Steel and Reinforced Concrete Structures", in Numerical Methods and Software for Dynamic Analysis of Plates and Shells, ed. by E. Hinton, Pineridge Press, Swansea, U.K.

79. *Valanis, K.C.* (1975). "On the Foundation of the Endochronic Theory of Viscoplasticity", Archiuum Mechaniki Stossowomej, Volume 27, pp. 857-868.

80. *Bazant, Z.P., and Bhat, P.D.* (1976). "Endochronic Theory of Inelasticity and Failure of Concrete", J.Eng. Mech. Div., ASCE, Volume 102, No. 4, pp. 701-722.

81. *Dougill, J.W.* (1976). "On Stable Progressively Fracturing Solids", J. Applied Math. Phys., Volume 27, pp. 423-437.

82. *Kachamov, L.M.* (1958). "On the Creep Fracture Time" IZV AN SSSR, Otd, Tekhn, Nauk, No. 8, pp.26-31 (In Russian).

83. *Loland, K.E.* (1980). "Continuous Damage Model for Load Response Estimations of Concrete", Cement and Concrete Research, Volume 10, pp. 395-402.

84. *Mazars, J.* (1981). "Mechanical Damage and Fracture of Concrete Structures", in Advances in Fracture Research, 5th Int. Conf. on Fracture, Ed. D. Francois, Cannes, pp. 1499-1506.

85. *Bazant, Z.P., and Oh, B.H.* (1981). "Concrete Fracture via Stress-Strain Relations", Report No. 81-10/G 55C, Centre for Concrete and Geomaterials, Technological Institute, Northwestern University, Evanston.

86. *ACI Standard 318-77.* (1977). "Building Code Requirements for Reinforced Concrete", American Concrete Institute, Detroit.

87. *Chen, W.F., Suzuki, H., and Chang, T.Y.P.* (1980). "End Effects of Pressure Resistant Concrete Shells", J. Struct. Div., ASCE, Volume 106, No.4, pp. 751-771.

88. *Ngo, D., Scordelis, A.C., and Franklin, H.A.* (1970). "Finite Element Study of Reinforced Concrete Beams with Diagonal Tension Cracks", US-SESM, Report No. 70-19, Univ. of California, Berkeley.

89. *Al-Mahaidi, R.S.H.* (1979). "Nonlinear Finite Element Analysis of Reinforced Concrete Deep Members", Report 79-1, Dept. of Struct. Engng., Cornell Univ.

90. *Rashid, Y.R.* (1968). "Ultimate Strength Analysis of Prestressed Concrete Vessels", Nucl. Engng. and design, Volume 7, No. 4, pp. 334-344.

91. *Nilsson, L., and Oldenburg, M.* (1982). "Nonlinear Wave Propagation in Plastic Fracturing Materials - A Constitutive Modelling and Finite Element Analysis", IUTAM Symp. on Nonlinear deformation waves, Tallin.

92. *Bazant, Z.P., and Oh, B.H.* (1983). "Crack Band Theory for Fracture of Concrete", RILEM, Materiaux et Constructions, Volume 16, pp. 155-177.

93. *Glemberg, R.* (1984). "Dynamic Analysis of Concrete Structures - Constitutive Modelling, Dynamic Substructuring, Computer Implementation", Chalmers Univ. of Technology, Publication 84:1.

94. *Rots, J.G., Nauta, P., Kusters, G.M.A., and Blaauwendraad, J.C.* (1985). "Smeared Crack Approach and Fracture Localisation" in Concrete", Heron, Volume 30, No. 1, Delft.

95. *Bergan, P.G.* (1984). "Some Aspects of Interpolation and Integration in Nonlinear Finite Element Analysis of Reinforced Concrete Structures", in Computer aided analysis and design of concrete structures, ed. by F. Damjanic et al, pp. 301-316,, Pineridge Press, Swansea.

96. *Gustafasson, J.* (1985). "Fracture Mechanics Studies of Non-yielding Materials like Concrete", Ph.D Thesis, Univ. of Lund.

97. *Bazant, Z.P.* (1976). "Instability, Ductility and Size Effect in Strain Softening Concrete", J.Eng. Mech. Div., ASCE, Volume 102, No. 2, pp. 331-344.

98. *Bergan, P.G., and Holand, I.* (1979). "Nonlinear Finite Element Analysis of Concrete Structures", Comp. Meth. Appl. Engng., Volume 17/18, pp. 443-467.

99. *Scanlon, A., and Murray, D.W.* (1974). "Time Dependent Reinforced Concrete Slab Deflections", J. Struct. Div., ASCE, Volume 99, pp. 1911-1924.

100. *Lin, C.S., and Scordelis, A.C.* (1975). "Nonlinear of RC Shells of General Form", J. Struct. Div., ASCE. Volume 101, No. 3, pp. 523-538.

101. *Crisfield, M.A.* (1982). "Local Instabilities in the Nonlinear Analysis of Reinforced Concrete Beams and Slabs", Proc. Inst. Civ. Eng., Volume 73, Part 2, pp. 135-145.

102. *Gilbert, R.I., and Warner, R.F.* (1980). "Tension Stiffening in Reinforced Concrete Slabs", J. Struct. Div., ASCE, Volume 106, No. 4, pp. 751-771.

103. *Willam, K.J., Bicanic, N., and Sture, S.* (1984). "Constitutive and Computational Aspects of Strain Softening and Localisation in Solids", WAM84 Symposium on Constitutive equations: Micro, Macro and Computational aspects, New Orleans, L.A.

104. *Petersson, P.E.* (1981). "Crack Growth and Development of Fracture in Plain Concrete and Similar Materials", Ph.D Thesis, Univ. of Lund.

105. *Hofbeck, J.A., Ibrahim, I.O., and Mattock, A.H.* (1969). "Shear Transfer in Reinforced Concrete", ACI Journal, Volume 66, pp. 119-128.

106. *Walraven, J.C., Vos, E., and Reinhardt, H.W.* (1978). "Experiments on Shear Transfer in Cracked Concrete", in nonlinear behaviour of reinforced concrete spatial structures, IASS Symposium, Volume 1, Darmstadt.

107. *Fenwick, R.C., and Paulay, T.* (1968). "Mechanics of Shear Resistance of Concrete Beams", J. Struct. Div., ASCE, Volume 94, No. 10, pp. 2325-2350.

108. *Jimenez, R., White, R.N., and Gergely, P.* (1979). "Bond and Dowel Capacities of Reinforced Concrete", ACI Journal, Volume 76, No. 1, pp. 73-92.

109. *ASCE Task Committee on Concrete and Masonry Structures.* (1982). "Finite Element Analysis of Reinforced Concrete", State of the Art Report, ASCE, A.H. Nilsson, Chairman.

110. *Singh, A., Gerstle, K.H. and Tulin, L.G.* (1965). "The Behaviour of Reinforcing Steel under Reversed Loading", Mater. Res. Stand., Volume 5, No. 1.

111. *Nadai, A.* (1963). "Theory of Flow and Fracture of Solids", Volume 1-2, McGraw-Hill, N.Y.

112. *Owen, D.R.J., and Hinton, E.* (1980). "Finite Elements in Plasticity - Theory and Practice", Pineridge Press, Swansea, Wales.

113. *Baker, W.E.* (1973). "Explosions in Air", Univ. of Texas Press, Austin, Texas.

114. *Glasstone, S., and Dolan, P.J.* (1977). "The Effects of Nuclear Weapons", U.S. Dept. of Defence and U.S. Dept. of Energy, Third edition, Washington, D.C.

115. *Baker, W.E., Cox, P.A., Westine, P.S., Kulesz, J.J., and Strehlow, R.A.* (1983). "Explosion Hazards and Evaluation", Elsevier Scientific Publishing Company.

116. *Kinney, G.F., and Graham, K.J.* (1985). "Explosive Shocks in Air", Springer Verlag, N.Y. Inc.

117. *Biggs, J.M.* (1964). "Introduction to Structural Dynamics", McGraw-Hill Book Company, N.Y.

118. *Norris, C.H., Hansen, R.J., Holley, M.J., Biggs, J.M., Namyet, S., and Minami, J.V.* (1959). "Structural Design for Dynamic Loads", McGraw-Hill Book Company, N.Y.

119. *Rogers, G.L.* (1959). "Dynamics of Framed Structures", John Wiley & Sons, Inc. New York.

120. *Crawford, R.E., Higgins, C.J., and Bultman, E.H.* (1974). "The Air Force Manual for Design and Analysis of Hardened Structures", AFWL-TR-74-102, Air Force Weapons Laboratory, Albuquerque, N.M.

121. *Agbabian, M.S.* (1985). "Design of Structures to resist Nuclear Weapon Effects", ASCE Manual on Engineering Practice, No. 42, American Society of Civil Engineers, N.Y.

122. *TM5-1300,* (1969). "Structures to resist the Effects of Accidental Explosions", United States Departments of the Army, Navy and Air Force.

123. *Newmark, N.M., and Hansen, R.J.* (1961). "Design of Blast-resistant Structures", in Shock and Vibration Handbook, Volume 3, ed. by Harris and Crede, McGraw-Hill.

124. *Newmark, N.M.* (1963). "Design Structures for Dynamic Loads including the effects of Vibration and Ground Shock", in Symposium on Scientific Problems of Protective Construction, Swiss Federal Institute of Technology, Zurich, pp. 148-248.

125. *Newmark, N.M., and Haltiwanger, J.D.* (1962). "Air Force Design Manual: Principles and Practices for Design of Hardened Structures", SWL TDR-62-138, Air Force Special Weapons Centre, Kirtland, Air Force Base, N.M.

126. *Newmark, N.M.* (1972). "External Blast", Proceedings of Int. Conf. on the planning and design of tall buildings, Lehigh Univ., Volume Ib, pp. 661-676.

127. *Newmark, N.M.* (1953). "An Engineering Approach to Blast Resistant Design", Proceedings of ASCE, Volume 79, Separate No. 309. [Also, Trans. ASCE, Volume 121 (1956), pp. 45-64].

128. *HNDM-1110-1-2.* (1977). "Supressive Shields - Structural Design and Analysis Handbook", U.S. Army Corps. of Engineers, Huntsville, Alabama.

129. *Carpenter, H.J.* (1975). "On Nuclear Height of Burst Airblast at High Overpressures", RDA-TR-5900-015, R & D Associates, Marina del Rey, Calif.

130. *Tomlinson, W.R., and Sheffield, O.E.* (1971). "Engineering Design Handbook - Properties of Explosive of Military Interest", AMC Pamphlet No. 706-177, Headquarters, U.S. Army Material Command.

131. *Kingery, C.N.* (1966). "Airblast Parameters versus Distance for Hemi-spherical TNT Surface Bursts", BRL Report No. 1344, Aberdeen, Proving Ground, Maryland.

132. *Strehlow, R.A., and Baker, W.E.* (1976). "The Characterization and Evaluation of Accidental Explosions", Progress in Energy and Combustion Science, Volume 2, No. 1, pp. 27-60.

133. *TM5-855-1.* (1965). "Fundamentals of Protective Design (Non-nuclear)", U.S. Dept. of the Army Technical Manual.

134. *Mills, C.A.* (1987). "The Design of Concrete Structures to resist Explosions and Weapon effects", Proceedings of 1st Int. Conf. on Concrete for Hazard Protection, Edinburgh, pp. 61-73.

135. *Lees, F.B.* (1980). "Loss Prevention in the Process Industries-Hazard Identification, Assessment and Control", Volume 2, Butterworths, London.

136. *Lee, J.H., Guicrao, C.M., Chiu, K.W., and Bach, G.G.* (1977). "Blast effects from Vapour Cloud Explosions", Loss Prevention, Volume 11, pp. 59-70.

137. *PFortaser, H.* (1977). "Gas Cloud Explosions and Resulting Blast effects", *Nucl. Engng.* and Design, Volume 41, pp. 59-67.

138. *Koch, C., and Bokeneir, V.* (1977). "Phenomenology of Explosions of Hydrocarbon Gas-air mixtures in the Atmosphere", Nucl. Engng. and Design, Volume 41, pp. 69-74.

139. *Gugan, K.* (1978). "Unconfined Vapour Cloud Explosions", The Institute of Chemical Engineering, Rigley Wark, England.

140. *Jungclaus, D.* (1977). "Basic ideas of a Philosophy to protect Nuclear Plants against Shock Waves related to Chemical Reactions", Nucl. Engng. and Design, Volume 41, pp. 75-89.

141. *Strehlow, R.A., Luckritz, R.T., Adamczyk, A.A., and Shimpi, S.A.* (1979). "The Blast Wave generated by Spherical Flames", Combustion and Flame, Volume 35, pp. 297-310.

142. *Doering, W., and Buckhardt, G.* (1949). "Contribution to the Theory of Detonation", Translation from the German as Technical Report No. F-TS-1227-IA (GDAM A9-T-46), Headquarters, Air Material Command, Wright-Patterson Air Force Base, Ohio, AD 77863.

143. *Brode, H.L.* (1968). "Review of Nuclear Weapons Effects", Annual Review of Nuclear Science, Volume 18, pp. 153-202.

144. *Mainstone, R.J.* (1972). "Internal Blast", Proceedings of Int. Conf. on the planning and design of high buildings, Lehigh Univ., Volume Ib, pp. 643-660.

145. *Mainstone, R.J.* (1976). "The Response of Buildings to Accidental Explosions", Building Research Establishment Current Paper, CP 24/76 Garston, Watford, England.

146. *Mainstone, R.J., Nicholson, H.G., and Alexander, S.J.* (1978). "Structural Damage in Buildings caused by Gaseous Explosions and other Accidental Loadings 1971-1977", Building Research Establishment, Garston, Watford, England.

147. *Mainstone, R.J.* (1971). "The Hazard of Internal Blast in Buildings", Building Research Establishment Current Paper CP/26/71, Garston, Watford, England.

148. *Cubbage, P.A., and Marshall, M.R.* (1972). "Pressures Generated in Combustion Chambers by the Ignition of Air-gas Mixtures", I. Chem, E. Symposium, Series No. 33, Institution of Chemical Engineers, London, England, pp. 24-31.

149. *Rasbash, D.J.,* (1969). "The Relief of Gas and Vapour Explosions in Domestic Structures", The Structural Engineer (London), Volume 47, pp. 404-411.

150. *Rasbash, D.J., Palmer, K.N., Rogwski, Z.W., and Ames, S.* (1970). "Gas Explosions in Multiple Compartments", JERO Fire Research Note No. 847.

151. *Alexander, S.J., and Hambly, E.C.* (1970). "The Design of Structures to withstand Gaseous Explosions", Concrete (London), Volume 4, pp. 62-65, pp. 107-116.

152. *Dragosavic, M.* (1972). "Structural Measures against Explosions of Natural Gas in Multi-storey Residential Buildings", Report No. BI-72-6/04.3. 02.520, Institut TNO, Voor Bouwmaterialen en Bouwconstructies.

153. *Bradley, D., and Mitcheson, A.* (1978). "The Venting of Gaseous Explosions in Spherical Vessels", Combustion and Flame, Volume 32, pp. 221-236, pp. 237-255.

154. *Palmer, K.N.* (1973). "Dust Explosions and Fires", Chapman and Hall Ltd., London, England.

155. *Cross, J., and Farrer, D.* (1982). "Dust Explosions", Plenum Press, N.Y. and London.

156. *Bartknecht, W.* (1978). "Gas, Vapour and Dust Explosions - Fundamentals, Prevention, Control", Int. Symp. on Grain Elevator Explosions, U.S. National Research Council.

157. *Gibson, N., and Harris, G.F.P.* (1976). "The Calculation of Dust Explosion Vents", Chemical Engng. Progress, pp. 62-67.

158. *Morton, J.* (1985). "Accidental Damage - Robustness and Stability", Prepared for BS5628: The Structural use of Masonry, Part 1: Unreinforced Masonry.

159. *Wu, S.T., Jain, B.P., and Srinivasan, R.* (1975). "Blast effects on Safety Related Structures", Proceedings of 2nd ASCE Spec. Conf. on Struct. Design of Nuclear Plant Facilities, New Orleans.

160. *Zinkiewicz, O.C.* (1977). "The Finite Element Method" 3rd Edition, McGraw-Hill, London.

161. *Bathe, K.J. and Wilson, E.L.* (1976). "Numerical Methods in Finite Element Analysis", Prentice Hill.

162. *Yang, T.Y.* (1986). "Finite Element Structural Analysis", Prentice Hill.

163. *Kardestuncer, H. (Editor in Chief).* (1987). "Finite Element Handbook", McGraw-Hill, N.Y.

164. *US - Japan Seminar.* (1985). "Finite Element Analysis of Reinforced Concrete Structures", Tokyo, Japan.

165. *IABSE Colloquiuum.* (1981). "Advanced Mechanics of Reinforced Concrete Structures", Final Report, Delft.

166. *Ergatoudis, J.G., Irons, B.M., and Zienkiewicz, O.C.* (1968). "Curved Isoparametric, Quadrilateral Elements for Finite Element Analysis", Int. J. Solids and Structures, Volume 4, pp. 31-42.

167. *Zienkiewicz, O.C., Owen, D.R.J., Phillips, D.Y., and Nayak, G.C.* (1972). "Finite Element Methods for the Analysis of Reactor Vessels", Nucl. Engng. and Design, Volume 20, pp. 507-541.

168. *Phillips, D.V., and Zienkiewicz, O.C.* (1976). "Finite Element Nonlinear Analysis of Concrete Structures", Proc. Inst. Civil Eng., Part 2, Volume 61, pp. 59-88.

169. *Fried, I.* (1974). "Numerical Integration in the Finite Element Method", Computer and Structures, Volume 4, pp. 921-932.

170. *Zienkiewicz, O.C., Taylor, R.L., and Too, J.M.* (1971). "Reduced Integration Technique in general Analysis of Plates and Shells", Int. J. Num. Meth. Engng., Volume 3, pp. 275-290.

171. *Pawsey, S.F., and Clough, R.W.* (1971). "Improved Numerical Integration of Thick Shell Finite Elements", Int. J. Num. Meth. Engng., Volume 3, pp. 545-586.

172. *Malkus, D.S., and Hughes, T.J.R.* (1978). "Mixed Finite Element Methods - Reduced and selective Integration Techniques: a unification of concepts", Comp. Meth. Appl. Mech. Engng., Volume 15, pp. 63-81.

173. *Hughes, T.J.R., Cohen, M., and Haroun, M.* (1978). "Reduced and selective Integration Techniques in the Finite *Element Analysis* of Plates", Nucl. Engng. Design, Volume 46, pp. 203-222.

174. *Sandhu, R.S., and Singh, K.J.* (1978). "Reduced Integration for improved accuracy of Finite Element Approximations", Comp. Meth. Appl. Mech. Engng., Volume 14, pp. 23-37.

175. *Bicanic, N., and Hinton, E.* (1979). "Spurious Modes in Two-dimensional Isoparametric Elements", Int. J. Num. Meth. Engng., Volume 14, pp. 1545-1557.

176. *Beshara, F.B.A., and Virdi, K.S.* (1989). "Nonlinear Finite Element Dynamic Analysis of Two-dimensional Concrete Structures", in the Proceedings of the 4th Int. Conf., and Exhib., on Civil and Struct. Eng., Computing, Volume 1, pp. 329-343.

177. *Marques, J.M.M.C.* (1984). "Finite and Infinite Elements in Static and Dynamic Structural Analysis", Ph.D Thesis, C/Ph/78/84, Univ. College of Wales, Swansea.

178. *Clough, R.W.* (1971). "Analysis of Structural Vibration and Dynamic Response", in recent advances in Math. Mech. of Struct. Analysis and Design, pp. 441-485, Ed. by R.H. Gallagher et al, Univ. of Alabama Press.

179. *Tong, P., Pian, T.H.H., and Buciarelli, L.L.* (1971). "Mode Shapes and Frequencies by the Finite Element Method using consistent and Lumped Mass", Computers and Structures, Volume 1, pp. 623-638.

180. *Hinton, E., Rock, T., and Zienkiewicz, O.C.* (1976). "A note on Mass Lumping related Processes in the Finite Element Method", Int. J. Earth. Engng. Struct. Dyn., Volume 4, pp. 246-249.

181. *Shantarm, D., Owen, D.R.J., and Zienkiewicz, O.C.* (1976). "Dynamic Transient Behaviour of Two and Three-dimensional Structures including Plasticity, Large Deformation effects and Fluid Interaction", Int. J. Earth, Engng. and Struct. Dyn., Volume 4, pp. 561-578.

182. *Rock, T., and Hinton, E.* (1974). "Free Vibration and Transient Response of Thick and Thin Plates using the Finite Element Method", Int. J. Earth Engng. and Struct. Dyn., Volume 3, pp. 51-63.

183. *Fried, I., and Malkus, D.S.* (1976). "Finite Element Mass Matrix Lumping by Numerical Integration without Convergence Rate Loss", Int. J. Solids and Structures, Volume 11, pp. 461-466.

184. *Cook, R.D.* (1981). "Remarks about Diagonal Mass Matrices", Int. J. Num. Meth. Engng., Volume 17, pp. 1427-1429.

185. *Tanjine, T.* (1984). "Nonlinear Analysis of Reinforced Concrete Structures by Finite Element Method", Ph.D Dissertation, Univ. of Akron.

186. *Bedard, C.* (1983). "Nonlinear Finite Element Analysis of Reinforced Concrete Structures", Ph.D Thesis, Faculty of Engng. of the Univ. of London (Imperial College), England.

187. *Bedard, C., and Kotsovos, M.D.* (1986). "Fracture Processes of Concrete for NLFEA Methods", J. Struct. Eng., ASCE, Volume 112, No. 3, pp. 573-587.

188. *Ammann, W., Mohlematter, M., and Bachmann, J.* (1982). "Stress Strain Behaviour of Non-prestressed and Prestressed Reinforced Steel at high Strain Rates", Proceedings of RILEM/CEB/IABSE/AISS Symposium on Concrete Structures under impact and Impulsive Loading, Berlin, (West), pp. 146-156.

189. *Limberger, E., Brandes, K., and Herter, J.* (1982). "Influence of Mechanical Properties of Reinforcing Steel on the Ductility of Reinforced Concrete Beams with respect to High Strain Rate", Proceedings of RILEM/CEB/IABSE/AISS Symposium on Concrete Structures under Impact and Impulsive Loading, Berlin (West), pp. 134-145.

190. *Hardings, J.* (1972). "Effect of High Strain Rates on the Room Temperature Strength and Ductility of Five Alloy Steels", J. The Iron Steel Inst., pp. 425-432.

191. *Rots, J.G., and Blaauwendraad, J.* (1989). "Crack Models for Concrete - Discrete or Smeared?, Fixed, Multi-directional or Rotating?, Heron, Volume 34, No. 1.

192. *Taniguchi, H.* (1984). "Nonlinear Analysis of Reinforced Concrete Structures by Finite Element Method", Ph.D Dissertation, University of Akron.

193. *Bazant, Z.P., and Gambarova, P.* (1980). "Rough Cracks in Reinforced Concrete", J. Eng. Mech. Div., ASCE, Volume 106, pp. 819-642.

194. *Yankelevsky, D.Z., and Reinhardt, H.W.* (1989). "Uniaxial Behaviour of Concrete in Cyclic Tension", J. Struct. Engng., ASCE, Volume 115, pp. 166-182.

195. *Cervenka, V.* (1985). "Constitutive Model for Cracked Reinforced Concrete", ACI Journal, Volume 82, pp. 877-882.

196. *Symmonds, P.S.* (1965). "Behaviour of Materials under Dynamic Loading", Ed. N.J. Huffington, ASME, pp. 106-124.

197. *Reinhardt, H.W.* (1982). "Concrete under Impact Loading - Tensile Strength and Bond", Heron, Volume 27, No. 3.

198. *British Standards Institution.* (1985). "Structural use of Concrete - Part 2: Code of Practice for special circumstances", BS8110, Part 2, Section 7.

199. *Comite Euro-International Du Beton.* (1988). "CEB-FIP Model Code 1990 - First pre-draft 1988", Bulletin D' Information, No. 190a.

200. *Belytschko, T.* (1976). "A Survey of Numerical Methods and Computer programs for Dynamic Structural Analysis", Nucl. Engng. Design, Volume 37, pp. 23-34.

201. *Hughes, T.J.R., and Belytschko, T.* (1983). "A Precis of Developments in Computational Methods for Transient Analysis", J. Appl. Mech., Volume 50, pp. 1033-1041.

202. *Belytschko, T., and Hughes, T.J.R.* (1983). "Computational Methods for Transient Analysis", Volume 1 in Computational Methods in Mechanics, Elsevier Science Publishers.

203. *Bathe, K.J.* (1979). "Finite Element Formulation, Modelling and Solution of Nonlinear Dynamic Problems", in Numerical Methods of Partial Differential Equations, pp. 1-40, Academic Press, N.Y.

204. *Bathe, K.J.* (1982). "Finite Element Procedures in Engineering Analysis", Prentice Hill, N.Y.

205. *Tillerson, J.R.* (1975). "Selecting Solution Procedures for Nonlinear Structural Dynamics", The Shock and Vibration Digest, Volume 7, Part 4, pp. 2-13.

206. *Dokainish, M.A., and Subbaraj, K.* (1989). "A Survey of direct Integration Methods in Computational Structural Dynamics - I. Explicit Methods", Computers and Structures, Volume 32, pp. 1371-1386.

207. *Dokainish, M.A., and Subbaraj, K.* (1989). "A Survey of Direct Integration Methods in Computational Structural Dynamics - II. Implicit Methods", Computers and Structures, Volume 32, pp. 1387-1401.

208. *Park, K.C.* (1977). "Practical Aspects of Numerical Time Integration", Computers and Structures, Volume 7, pp. 343-353.

209. *Krug, R.D., and Key, S.W.* (1973). "Transient Shell Response by Numerical Time Integration", Int. J. Num. Meth. Engng., Volume 17, pp. 273-286.

210. *Mikkola, M.J., and Sinisalo, H.* (1981). "Comparison of Numerical Integration Methods in the Analysis of Impulsively Loaded Elastoplastic and Viscoplastic Structures", Computers and Structures, Volume 14, pp. 469-478.

211. *Belytschko, T., and Engelmann, B.E.* (1988). "Explicit Time Integration with Enhanced Stability for Structural Dynamics", Computers and Structures, Volume 29, pp. 587-590.

212. *Brackhus, J., and Aasen, J.O.* (1981). "Experiments with direct Integration Algorithms for ordinary Differential Equations in Structural Dynamics", Computers and Structures, Volume 13, pp. 91-96.

213. *Nilsson, L.* (1978). "Finite Element Analysis of Impact on Concrete Structures", in Finite Elements in Nonlinear Mechanics, Ed. by P.C. Bergan, Tapir, Trondheim.

214. *Marchestas, A.H., Fistedis, S.H., Bazant, Z.P., and Belytscko, T.* (1978). "Analysis and Application of Prestressed Concrete Reactor Vessels for LMFBR Containment", Nucl. Engng. Design, Volume 49, pp. 155-173.

215. *Mikkola, M.J. and Sinisalo, H.S.* (1980). "Finite Element Analysis of Transient Nonlinear Response of Reinforced Concrete Structures", Proceedings of the Europe - U.S. Workshop on Nonlinear Finite Element Analysis in Structural Mechanics, Ed. by Wunderlich and Bathe.

216. *Newmark, N.M.* (1959). "A Method of Computation for Structural Dynamics", J. Engng. Mech. Div., ASCE, Volume 85, No. 3, pp. 67-95.

217. *Wilson, E.L., Farhoom, I., and Bathe, K.J.* (1973). "Nonlinear Dynamic Analysis of Complex Structures", Earth Engng. and Struct. Dyn., Volume 1, pp. 241-252.

218. *Houbolt, J.C.* (1950). "A Recurrence Matrix Solution for the Dynamic Response of Elastic Aircraft", J. Aero. Sci., pp. 540-550.

219. *Park, K.C.* (1975). "An Improved Stiffly Stable Method for direct Integration of Nonlinear Structural Dynamic Equations", J. Appl. Mech., Volume 42, pp. 464-470.

220. *Belytschko, T., and Mullen, R.* (1976). "Mesh Partitions of Explicit-Implicit Time Integration", in Formulations and Comput. Algor. in Finite Element Analysis, Ed. by K.J. Bathe et al, MIT Press, Cambridge, pp. 673-690.

221. *Hughes, T.J.R., and Lui, W.K.* (1978). "Implicit-Explicit Finite Elements in Transient Analysis", J. Appl. Mech., Volume 45, pp. 371-378.

222. *Neal, M.O., and Belytschko, T.* (1989). "Explicit - Explicit Subcycling with Non-integer Time Step Ratios for Structural Dynamic System", Computers and Structures, Volume 31, pp. 871-880.

223. *Heifitz, J.H., and Costantino, C.J.* (1972). "Dynamic Response of Nonlinear Media at large Strains", J. Eng. Mech. Div., ASCE, Volume 98, pp. 1511-1528.

224. *Belytschko, T., Chiapetta, R.L., and Bartel, H.D.* (1976). "Efficient large scale Nonlinear Transient Analysis by Finite Elements", Int. J. Num. Meth. Engng., Volume 10, pp. 579-596.

225. *Zienkiewicz, O.C., and Cormeau, I.C.* (1974). "Viscoplasticity-Plasticity and Creep in Elastic Solids: A Unified Numerical Solution Approach", Int. J. Num. Meth. Engng., Volume 3, No. 8, pp. 821-845.

226. *Cormeau, I.C.* (1975). "Numerical Stability in Quasi-static Elasto-viscoplasticity", Int. J. Num. Meth. Engng., Volume 9, pp. 109-127.

227. *Belytschko, T., Holmes, N., and Mullen, R.* (1975). "Explicit Integration-Stability, Solution Properties, Cost", in finite element analysis of transient nonlinear structural behaviour, Ed. by T. Belytschko, Osias and Marcal.

228. *Belytschko, T.* (1978). "Explicit Time Integration of Structural Mechanical System", in advanced structural dynamics, Ed. by J. Donea, pp. 97-122.

229. *Holmes, N.A.* (1976). "Characteristics of Transient Finite Element Solutions", Ph.D Thesis, Univ. of Illinois at Chicago.

230. *Irons, B.M., and Treharne, G.* (1971). "A Bound Theorem in Eigenvalues and its Practical Applications", Proceedings of 3rd Conf. on Matrix Meth. Struct. Mechanics, Wright Patterson, pp. 245-254.

231. *Nagy, D.A.* (1978). "Software Engineering for Finite Element Analysis", J. Struct. Div., ASCE, Volume 104, No. 8 , pp. 1278-1298.

232. *Irons, B., and Ahmad, S.* (1980). "Techniques of Finite Elements", Ellis Harword, New York.

233. *Hinton, E., and Owen, D.R.J.* (1977). "Finite Element Programming", Academic Press, London.

234. *Gino Graphics Libraries.* (1990). "GINO-F, GINOGRAF, GINOSURF USER'S Manuals", Version 3.0, Bradley Associates Ltd., Berkshire, England.

235. *Bathe, K.J., and Ramaswamy, S.* (1979). "On Three-dimensional Nonlinear Analysis of Concrete Structures", Nucl. Engng. Design, Volume 52, pp. 385-409.

236. *Van Mier, J.G.M.* (1987). "Examples of Nonlinear Analysis of Reinforced Concrete Structures with DIANA", Heron, Volume 32, No. 3, Delft.

237. *Elfgren, L.* (1989). "Fracture Mechanics of Concrete Structures - from Theory to Applications", RILEM Technical Committee 90 - FMA Fracture Mechanics to Concrete Applications, Chapman and Hall.

238. *Rebora, B., and Zimmermann, T.* (1976). "Dynamic Rupture Analysis of Reinforced Concrete Shells", Nucl. Engng. Design, Volume 37, pp. 269-297.

239. *Seabold, R.H.* (1967). "Dynamic Shear Strength of Reinforced Concrete Beams, Part II", Naval Civil Engineering Laboratory, Port Hueneme, California, AD 644823.

240. *Frantzeskakis, C., and Theillout, J.N.* (1989). "Nonlinear Finite Element Analysis of Reinforced Concrete Structures with a particular strategy following the Cracking Process", Computers and Structures, Volume 31, No. 3, pp. 395-412.

241. *Galloway, R.G.* (1989). "Modelling Strain Rate Effects in Plain Concrete", Ph.D Dissertation, Univ. of New Mexico, Albuquerque, New Mexico.

242. *Hallquist, J.O.* (1983). "Theoretical Manual for DYNA3D", Univ. of Calif., Lawrence Livermore Laboratory, Report UCID-19401.